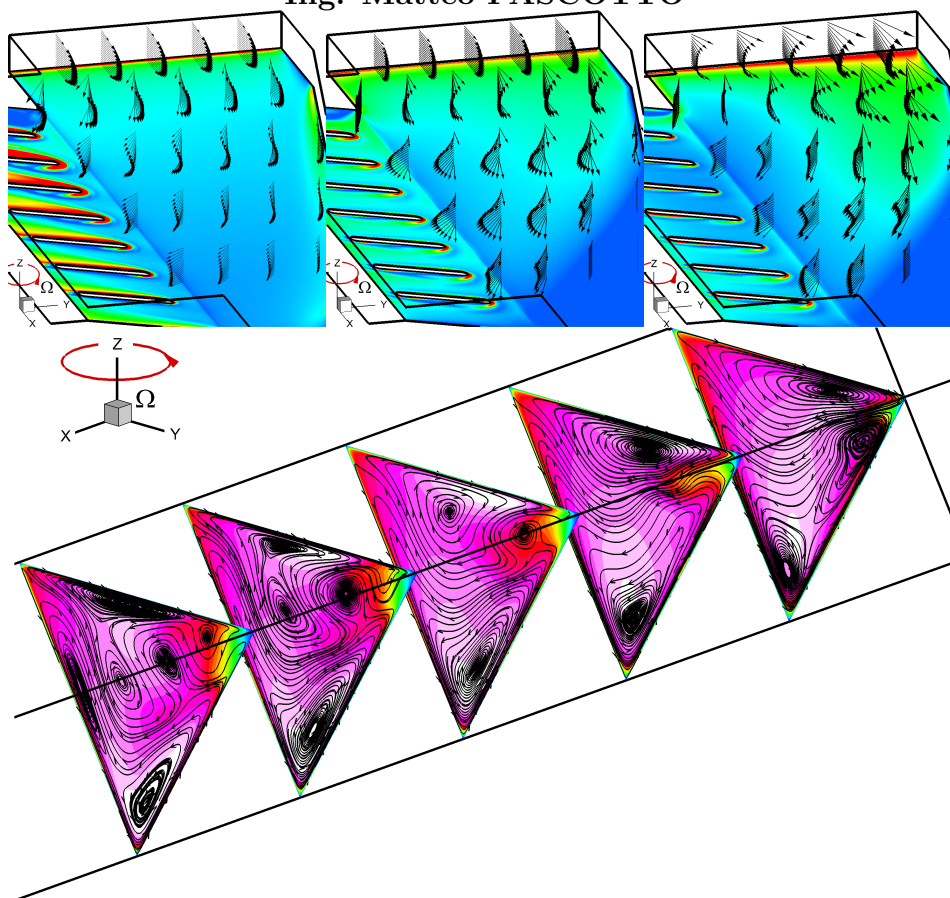




UNIVERSITÀ DEGLI STUDI DI UDINE  
GRADUATE EDUCATION IN  
TECNOLOGIE CHIMICHE ED ENERGETICHE

# Aero-Thermal Numerical Predictions of Trailing Edge and Leading Edge Cooling Channels

Ing. Matteo PASCOTTO



DOCTORAL COMMITTEE

---

Prof. Peter IRELAND	REVIEWER
Prof. Bruno FACCHINI	REVIEWER
Prof. Pietro POESIO	REFEREE
Prof. Cristian MARCHIOLI	REFEREE
Prof. Giuseppe PASCAZIO	REFEREE
Prof. Luca CASARSA	SUPERVISOR

---

Prof. Alfredo SOLDATI	CHAIR
-----------------------	-------

Author's Web Page: <http://www.linkedin.com/in/matteopascotto>

Author's e-mail: Office email: [matteo.pascotto@uniud.it](mailto:matteo.pascotto@uniud.it)  
Permanent email: [pascotto.matteo@gmail.com](mailto:pascotto.matteo@gmail.com)

Author's address:

Dipartimento di Ingegneria Elettrica  
Gestionale e Meccanica  
Università degli Studi di Udine  
Via delle Scienze, 106  
33100 Udine – Italia  
tel. +39 0432 558253  
fax. +39 0432 558251  
web: <http://www2.diegm.uniud.it/diegm/>

#### **COVERART**

**Top:** CFD velocity vectors distributions at  $x = -100, 10, 165, 320$  and  $470[mm]$  at  $Ro = 0$  (a),  $Ro = 0.23$ (b) and  $Ro = 0.46$  (c), G0 rotating configuration.

**Bottom:** CFD contour maps of the stream-wise velocity and stream-tracers at different channel locations at  $Re = 20000$ ,  $Ro = 0.4$ .

To my Father, Mother and Jules



# Acknowledgments

I thought that writing the following lines would be the easiest part of my thesis, but only now I realize that I was wrong. Many people strongly supported this work from the beginning till the end and I hope I will be able to fully express my gratitude to every single person who made this possible. I promise I will do my best!

First of all, I would like to say thank you to my supervisor Prof. Luca Casarsa who has given me the enthusiasm and suggestions for research since I was a master's student. Every day I spent with him I learn something new, from both a technical and human point of view. I will never forget his patience in answering to my huge amount of questions and his scientific expertise in dealing with many problems and solving them. It was really a pleasure to work with him. Many thanks also go to Dott. Ing. Alessandro Armellini for the long talks, suggestions and reliable feedback that were always very appreciated. Moreover, I wish to thank Prof. Piero Pinamonti and Prof. Pietro Giannatasio for their support and encouragement over these last few years. Special thanks go of course to my colleagues, and now friends, Alessandro Zanon, Claudio Mucignat, Dario Buoro, Silvia Daniotti, Luca Furlani, Luca Scarbolo and Enrico Pitton for the "scientific" conversations we had and the good time we spend together as well.

I would like to express my gratitude to Prof. Jens von Wolfersdorf for giving me the opportunity to spend seven months at the I.T.L.R. in Stuttgart. Here I met Dr. Ing. Sebastian Spring who taught me how to see the world in the form of hexahedral meshes and with whom I had a great/wonderful time sharing my/our big passion for cars.

Moreover, this thesis has been improved in quality and clearness thanks to the useful observations made by Prof. Peter Ireland and Prof. Bruno Facchini. I'm proud they really appreciated my work.

Special thanks go to my Father, my Mother and my family that always encouraged me unconditionally to follow my aspirations because they have always believed in my abilities even when my self-confidence dwindled.

And now my friends...thank you to Cesco and Burri for all the experiences we shared and the stuff we did together (a whole thesis wouldn't be enough to mention them) and for putting up with me since we first met 25 years ago and we started to live like brothers. Thanks to my little "sister" Giulia for the long talks and for giving me always the right answer in the right moment, no matter where I am. Thanks to: Steff for having always his right word (cooosa?), Seppia for being always there even if he's far, Dianans and Leo for the trips and the good time we spent together. Moreover I want to thank my friends and papers pushers Cecchi and Muffone with whom I shared one of the best research

times I have ever had when we were stagiaires at VKI.

In conclusion, I dedicate my last words to my girlfriend Jules, who is always in my mind and in my heart. Thank you, not only for your incredible patience and your inexhaustible lovely support during these years, but also for the time you spent working with me in the night to correct the mistakes I made while I was writing this thesis in English. Thank you for all the times I didn't tell you but I should have, because you deserved it.

---

# Contents

<b>Nomenclature</b>	<b>v</b>
<b>Acronyms</b>	<b>xi</b>
<b>Abstract</b>	<b>xxiii</b>
<b>1 Introduction</b>	<b>1</b>
1.1 Gas Turbine Engines . . . . .	1
1.2 Blade Cooling . . . . .	5
1.2.1 Cooling Techniques . . . . .	5
1.3 Literature Review . . . . .	8
1.3.1 Internal Cooling in Trailing Edge Static Channels . . . . .	9
1.3.2 Internal Cooling in Leading Edge Static Channels . . . . .	10
1.3.3 Internal Cooling in Rotating Channels . . . . .	11
1.3.4 Internal Cooling in Trailing Edge Rotating Channels . . . . .	12
1.3.5 Internal Cooling in Leading Edge Rotating Channels . . . . .	13
1.4 Objectives of Present Study . . . . .	14
<b>2 Mathematical and Numerical Background</b>	<b>17</b>
2.1 Governing Equations . . . . .	17
2.2 Numerical Methods . . . . .	18
2.2.1 Discretization . . . . .	18
2.2.2 Grid . . . . .	18
2.2.3 Calculation of Surface Fluxes . . . . .	19
2.2.4 Solution Algorithm . . . . .	21
2.2.5 Accuracy of the Numerical Solutions . . . . .	21
2.3 Turbulence Modelling . . . . .	22
2.3.1 Reynolds-Averaged Navier-Stokes (RANS) Equations . . . . .	22
2.3.2 Turbulence Models . . . . .	24
2.3.3 Modelling Flow Near the Wall . . . . .	31
<b>3 CFD Assessment of the Aero-Thermal Performance of Trailing Edge Channels</b>	<b>33</b>
3.1 Test Section . . . . .	33
3.1.1 G0 . . . . .	34
3.1.2 G1 . . . . .	35
3.1.3 G2 . . . . .	35
3.2 Data Planes . . . . .	36

3.3	G0 Configuration . . . . .	38
3.3.1	Computational Details . . . . .	38
3.3.2	Quantification of the Numerical Accuracy . . . . .	40
3.3.3	Comparison with the Experimental Results . . . . .	41
3.4	G1 Configuration . . . . .	49
3.4.1	Computational Details . . . . .	49
3.4.2	Quantification of the Numerical Accuracy . . . . .	50
3.4.3	Comparison with Experimental Results . . . . .	50
3.4.4	Evaluation of the Turbulence Models . . . . .	56
3.5	G2 Configuration . . . . .	60
3.5.1	Computational Details . . . . .	60
3.5.2	Quantification of the Numerical Accuracy . . . . .	61
3.5.3	Comparison with Experimental Results . . . . .	61
3.6	Summary and Assessment of the Global Performance . . . . .	67
<b>4</b>	<b>Effects of Rotation and Different Channel Orientations in a Trailing Edge Channel</b> . . . . .	<b>69</b>
4.1	Computational Details . . . . .	69
4.2	G0 Configuration . . . . .	72
4.2.1	Grid Generation and Quantification of Numerical Accuracy . . . . .	72
4.2.2	Comparison with Rotating Experimental Results . . . . .	72
4.2.3	Effects Produced by Ro Increases . . . . .	77
4.2.4	Effects Produced by Varying the Channel Orientation . . . . .	85
4.2.5	Summary . . . . .	91
4.3	G1 Configuration . . . . .	93
4.3.1	Grid Generation and Quantification of the Numerical Accuracy . . . . .	93
4.3.2	Comparison with Rotating Experimental Results . . . . .	94
4.3.3	Effects Produced by Ro Increases . . . . .	99
4.3.4	Effects Produced by Varying the Channel Orientation . . . . .	104
4.3.5	Summary . . . . .	110
<b>5</b>	<b>Effects of Rotation and Different Channel Orientations in a Leading Edge Channel</b> . . . . .	<b>111</b>
5.1	Test Section . . . . .	111
5.2	Data Planes . . . . .	112
5.3	Computational Details . . . . .	114
5.3.1	Quantification of the Numerical Accuracy . . . . .	116
5.4	Results and Discussion . . . . .	116
5.4.1	Comparison of the CFD and Experimental Results at Reference Conditions (Re=20000 Ro=0.2) . . . . .	116
5.4.2	Stream-Wise Velocity Distribution . . . . .	119
5.4.3	Effect of Ro and Re . . . . .	121
5.4.4	Turbulence intensity . . . . .	124
5.4.5	Thermal effects . . . . .	125
5.4.6	Effects of the Channel Orientation . . . . .	127

---

5.5 Summary . . . . .	130
<b>6 Concluding Remarks</b>	<b>133</b>
6.1 Achieved Objectives . . . . .	133
6.1.1 Quantification of the Numerical Accuracy . . . . .	133
6.1.2 Assessment of the Capabilities of the CFD Predictions . . . . .	133
6.1.3 Exploitation of the CFD tool in Engine-Like Conditions . . . . .	134
6.2 Recommendations for Future Research . . . . .	134
6.2.1 Numerical Work . . . . .	134
6.2.2 Physical Effects . . . . .	135
<b>Bibliography</b>	<b>137</b>
<b>A Experimental Uncertainty Analysis</b>	<b>143</b>
A.1 PIV Uncertainty Analysis . . . . .	143
A.2 LCT Uncertainty Analysis . . . . .	143
<b>B High Resolution Scheme</b>	<b>145</b>
<b>C Description of the GCI</b>	<b>147</b>
<b>D Inflow Conditions</b>	<b>149</b>
<b>E Local Distribution of Turbulence Kinetic Energy in the P4 IP Passage</b>	<b>151</b>
<b>Publications</b>	<b>153</b>
<b>Curriculum Vitae</b>	<b>155</b>



# Nomenclature

Notation	Description
$A_{cx}$	$= 2\Omega V$ Coriolis Force per Unit of Mass Along <b>x</b> Component [ $m/s^2$ ].
$C_{xyz}$	$= \sqrt{U^2 + V^2 + W^2}$ Mean Velocity Modulus [ $m/s$ ].
$C_{xy}$	$= \sqrt{U^2 + V^2}$ Mean Velocity Modulus in-Plane <b>xy</b> [ $m/s$ ].
$C_{xz}$	$= \sqrt{U^2 + W^2}$ Mean Velocity Modulus in-Plane <b>xz</b> [ $m/s$ ].
$C_{y'z}$	$= \sqrt{V'^2 + W^2}$ Mean Velocity Modulus in-Plane <b>y'z</b> [ $m/s$ ].
$C_{lim}$	Clip Factor.
$EF_{IP}$	Enhanced Factor on the Suction Side Wall in the Inter Pedestal Passages.
$EF_{SS}$	Enhanced Factor on the Suction Side Wall.
$L_{max}$	Cell Aspect Ratio.
$Nu_0$	$0.023 \cdot Re^{0.8} \cdot Pr^{0.5}$ .
$P_k$	Production Term.
$T_0$	Total Temperature [K].
$T_w$	Wall Temperature [K].
$\Gamma_t$	Eddy Diffusivity.
$\Lambda$	GCI Solution on the Grid.
$\Omega$	Angular Velocity [ $rad/s$ ].
$\Phi_{\Xi}$	Diffusivity of the General Scalar Variable (e.g. if temperature is the general scalar variable thermal diffusivity for the conservation of energy).
$\Xi$	General Scalar Variable.
$\alpha$	Incidence Angle [deg].
$\beta_{21-34}$	Pressure Ratio ( $\frac{p_2}{p_1} = \frac{p_3}{p_4}$ ).
$\beta$	Incidence Angle with Respect to the Rib Normal Direction [deg].
$\delta_{min}$	Minimum Cell Angle.
$\delta_{ij}$	Kronecker Delta.
$\epsilon$	Dissipation Rate [ $\frac{m^2}{s^3}$ ].
$\eta_C$	Compressor Efficiency.
$\eta_{TOT}$	Joule Cycle Efficiency.
$\eta_T$	Turbine Efficiency.

Notation	Description
$\gamma$	Channel Orientation with Respect to the Peripheral Velocity [deg].
$\hbar$	Vorticity.
$\iota$	Blending Function.
$\kappa$	Turbulence Kinetic Energy [ $\frac{m^2}{s^2}$ ].
$\lambda$	Linear Interpolation Factor.
$\mu$	Dinamic Viscosity of the Fluid [ $kg/m \cdot s$ ].
$\nu\kappa$	Von Karman's Constant $\approx 0.41$ .
$\nu$	Kinematic Viscosity of the Fluid [ $m^2/s$ ].
$Nu_{IP}$	<b>Nu</b> on the Inter-Pedestal Passages (i.e. [ $mm$ ] – $240 < y < -120[mm]$ ).
$Nu_{IR}$	<b>Nu</b> on the Inter-Rib Passages (i.e. [ $mm$ ] – $120 < y < 120[mm]$ ).
$Nu_{SS}$	<b>Nu</b> on the Suction Side Wall.
$\omega_{ij}$	Reynolds Stresses Frequency.
$\rho$	Density of the Fluid [ $kg/m^3$ ].
$\sigma_t$	Turbulent Prandtl Number.
$\tau_\omega$	Near-Wall Shear Stress.
$\nu_t$	Eddy Viscosity or Turbulent Viscosity.
$\vartheta$	Heat capacity ratio or adiabatic index or ratio of specific heats, is the ratio of the heat capacity at constant pressure ( $C_P$ ) to heat capacity at constant volume ( $C_V$ ) $\Rightarrow \frac{C_P}{C_V}$ .
$\hat{p}$	Istantaneous Pressure Vector.
$\hat{U}$	Istantaneous Velocity Vector.
$y_{avg}^+$	Average Dimensionless Wall Distance.
$y_{max}^+$	Maximum Dimensionless Wall Distance.
$h^*$	GCI Representative Mesh Size.
$q_\Xi$	Sources or Sinks for the General Scalar $\Xi$ .
$u^+$	Near-Wall Velocity.
$u_\tau$	Friction Velocity.
$xy'_{G2}$	Plane $\parallel$ with Respect to the Suction Side at $z = 1.5[mm]$ , $G2$ Configurations <b>Trailing Edge</b> .
$xy_{G1}$	Plane at $z = 14.05[mm]$ , $G1$ Configurations <b>Trailing Edge</b> .
$xy^i_{G2}$	Plane at $y = 153.5[mm]$ , $G2$ Configurations <b>Trailing Edge</b> .
$xy_{mG2}$	Plane at $y = 322.418[mm]$ , $G2$ Configurations <b>Trailing Edge</b> .
$xz_{G1}$	Plane $\perp$ with Respect to the Rib $y' = 109.186[mm]$ , $G1$ Configurations <b>Trailing Edge</b> .

Notation	Description
$y'z1_{G0}$	Plane $\perp$ with Respect to the Redirecting Wall $x' = 175.331[\text{mm}]$ , $G0$ Configurations <b>Trailing Edge</b> .
$y'z1_{G1}$	Plane $\parallel$ with Respect to the Rib $x' = 284.5[\text{mm}]$ , $G1$ Configurations <b>Trailing Edge</b> .
$y'z2_{G0}$	Plane $\perp$ with Respect to the Redirecting Wall $x' = 248.875[\text{mm}]$ , $G0$ Configurations <b>Trailing Edge</b> .
$y'z2_{G1}$	Plane $\parallel$ with Respect to the Rib $x' = 253.537[\text{mm}]$ , $G1$ Configurations <b>Trailing Edge</b> .
$y'z3_{G0}$	Plane $\perp$ with Respect to the Redirecting Wall $x' = 322.418[\text{mm}]$ , $G0$ Configurations <b>Trailing Edge</b> .
$y'z3_{G1}$	Plane $\parallel$ with Respect to the Rib $x' = 352.08[\text{mm}]$ , $G1$ Configurations <b>Trailing Edge</b> .
$yz_{G2}$	Plane at $x = 262.5[\text{mm}]$ , $G1$ Configurations <b>Trailing Edge</b> .
Bo	$= \frac{T-T_{bulk}}{T} \left( \frac{\Omega Dh}{Ub} \right)^2 \frac{Rm}{Dh}$ Buoyancy Parameter.
e	GCI Error.
I	Turbulence Intensity: $I_{CFD} = \frac{\sqrt{\frac{2}{3}\kappa}}{Ub}$ and $I_{exp} = \frac{\sqrt{\frac{u'^2+v'^2+w'^2}{3}}}{Ub}$ .
IN1	Plane at the Median of the Leading Side Apex <b>Leading Edge</b> .
IN2	Plane at the Median of the Trailing Side Apex <b>Leading Edge</b> .
IN3	Plane at $y = 0$ , <b>Leading Edge</b> .
L	Turbulent Length Scale.
L1	Lower Portion Leading Side Region, <b>Leading Edge</b> .
L2	Upper Portion Leading Side Region, <b>Leading Edge</b> .
N	Number of Cells.
Nu	$= \frac{HTCDh}{K_f}$ Nusselt Number.
p	Pressure [Pa].
pp	GCI Apparent Order.

Notation	Description
r	GCI Refinement Factor.
Re	= $\frac{U_b D h \rho}{\mu}$ Reynolds Number.
Ro	= $\frac{\Omega D h}{U_b}$ Rotation Number.
S1	Plane at $x = 120$ , <b>Leading Edge</b> .
S2	Plane at $x = 220$ , <b>Leading Edge</b> .
S3	Plane at $x = 320$ , <b>Leading Edge</b> .
S4	Plane at $x = 420$ , <b>Leading Edge</b> .
S5	Plane at $x = 520$ , <b>Leading Edge</b> .
T	Temperature [K].
T1	Lower Portion Trailing Side Region, <b>Leading Edge</b> .
T2	Lower Portion Leading Side Region, <b>Leading Edge</b> .
U	Mean Velocity Component Along x Direction [m/s].
U'	Mean Velocity Component Along x' Direction [m/s].
u'	Experimental U Velocity Fluctuation.
U <sub>b</sub>	Bulk Flow Velocity [m/s].
V	Mean Velocity Component Along y Direction [m/s].
v'	Experimental V Velocity Fluctuation.
W	Mean Velocity Component Along z Direction [m/s].
w'	Experimental W Velocity Fluctuation.
x	Test Section Radial Coordinate [mm].
x'	Test Section Relative Coordinate [mm].
x'y	Plane    and at 2 [mm] from the Trailing Side Suction Side, G0 – G1 – G2 Configurations <b>Trailing Edge</b> .
xy	Plane at $z = 0$ [mm], G0 – G1 – G2 Configurations <b>Trailing Edge</b> .
xy1	Plane at $z = -14.55$ [mm], G0 – G1 – G2 Configurations <b>Trailing Edge</b> .
xy2	Plane at $z = 10.55$ [mm], G0 – G1 – G2 Configurations <b>Trailing Edge</b> .

Notation	Description
xy3	Plane at $z = 14.55[\text{mm}]$ , $G0 - G1 - G2$ Configurations <b>Trailing Edge</b> .
xz	Plane at $y = 0[\text{mm}]$ , $G0 - G1 - G2$ Configurations <b>Trailing Edge</b> .
xzi	Plane at $y = -150[\text{mm}]$ , $G0 - G1 - G2$ Configurations <b>Trailing Edge</b> .
xzm	Plane at $y = -180[\text{mm}]$ , $G0 - G1 - G2$ Configurations <b>Trailing Edge</b> .
xzR	Plane at $y = -165[\text{mm}]$ , $G0 - G1 - G2$ Configurations <b>Trailing Edge</b> .
Y	Axial Direction [mm].
y	Test Section Axial Coordinate [mm].
y'	Test Section Relative Coordinate [mm].
y''	Test Section Relative Coordinate [mm].
Z	Direction of the Rotation Axis [mm].
z	Test Section Coordinate [mm].



---

# Acronyms

Notation	Description
<i>AR</i>	Aspect Ratio.
<i>CDS</i>	Central Differencing Scheme.
<i>CFD</i>	Computational Fluid Dynamics.
<i>CV</i>	Small Control Volumes.
<i>C</i>	Vortex Cell.
<i>Dh</i>	Hydraulic Diameter [mm].
<i>FV</i>	Finite Volume Method.
<i>G0</i>	Reference Smooth Configuration, <b>Trailing Edge</b> Cooling Channel.
<i>G1</i>	Rib Configuration on the Radial Central Portion, <b>Trailing Edge</b> Cooling Channel.
<i>G2</i>	Rib Configuration in between Inter-Pedestal Passages), <b>Trailing Edge</b> Cooling Channel.
<i>GCI</i>	Grid Convergence Method.
<i>HTC</i>	Heat Transfer Coefficient.
<i>IP</i>	Inter-Pedestal Passage.
<i>IR</i>	Inter-Rib Passage.
<i>LCT</i>	Liquid Crystal Thermography.
<i>ORS</i>	Omega Reynolds Stress.
<i>P1</i>	1 <sup>st</sup> Pedestal Passage.
<i>P2</i>	2 <sup>nd</sup> Pedestal Passage.
<i>P4</i>	4 <sup>th</sup> Pedestal Passage.
<i>P6</i>	6 <sup>th</sup> Pedestal Passage.
<i>P7</i>	7 <sup>th</sup> Pedestal Passage.
<i>P8</i>	8 <sup>th</sup> Pedestal Passage.
<i>PIV</i>	Particle Image Velocimetry.
<i>PS</i>	Pressure Side Wall, <b>Trailing Edge</b> Cooling Channel.
<i>RANS</i>	Reynolds-Averaged Navier-Stokes Equations.
<i>SST</i>	Shear Stress Transport.
<i>SS</i>	Suction Side Wall, <b>Trailing Edge</b> Cooling Channel.
<i>TIT</i>	Turbine Inlet Temperature.
<i>UDS</i>	Upwind Differencing Scheme.
<i>r.m.s</i>	Root Mean Square.
<i>str</i>	Stream-Traces.



---

# List of Figures

1.1	Rolls-Royce Trent XWB <a href="http://www.rolls-royce.com/news/assets/prg.jsp">http://www.rolls-royce.com/news/assets/prg.jsp</a> , (aircraft engine ) . . . . .	2
1.2	Alstom GT13E2 <a href="http://www.alstom.com/power/gas-power/gas-turbines/gt13e2-/">http://www.alstom.com/power/gas-power/gas-turbines/gt13e2-/</a> , (land-based engine ) . . . . .	2
1.3	Gas turbine thermodynamic cycle . . . . .	3
1.4	Cycle efficiency of a gas turbine engine . . . . .	3
1.5	The time evolution of turbine cooling technology during the last decades [43] . . . . .	4
1.6	Comparison between turbine inlet temperature and blade material temperature limits highlighting the importance of cooling technology [9] . . . . .	4
1.7	Cooling schemes: (a) forced convection, (b) impingement, (c)-(d) film-cooling, (e) transpiration-cooling [52] . . . . .	6
1.8	Cooling design analysis system [20] . . . . .	8
1.9	Cooled high pressure turbine blade [20] . . . . .	9
1.10	Secondary flow model proposed by Liu et al.[50] . . . . .	13
1.11	Secondary flow model suggested by Huang and Liu et al.[39] . . . . .	14
2.1	Illustrative example of a Small Control Volumes ( <i>CV</i> ) in 2-D Cartesian Grid [33] . . . . .	19
2.2	Time averaging for a statistically steady flow . . . . .	23
2.3	Velocity profile in the near-wall region . . . . .	31
3.1	Schematic of the test rig developed for the present experimental campaign [5], [56] and [7], xz-projection with the piping circuit . . . . .	33
3.2	Schematic of the test section ((a),(b)) (Reference Smooth Configuration, <b>Trailing Edge</b> Cooling Channel ( <i>G0</i> ) configuration), channel cross-section (c), inlet cross-section (d), tip cross-section (e) [7] . . . . .	34
3.3	Schematic of the test section, Rib Configuration on the Radial Central Portion, <b>Trailing Edge</b> Cooling Channel ( <i>G1</i> ) configuration . . . . .	35
3.4	Schematic of the test section, Rib Configuration in between Inter-Pedestal Passages), <b>Trailing Edge</b> Cooling Channel ( <i>G2</i> ) configuration . . . . .	36
3.5	Overview of the position of the experimental and Computational Fluid Dynamics ( <i>CFD</i> ) data planes . . . . .	36
3.6	Overview of the position of the experimental and <i>CFD</i> data planes, <i>G1</i> configuration . . . . .	38
3.7	Overview of the position of the experimental and <i>CFD</i> data planes, <i>G2</i> configuration . . . . .	38
3.8	3-D view on the mesh, <i>G0</i> configuration . . . . .	39

3.9	Grid Convergence Method ( <i>GCI</i> ) at the Suction Side Wall, <b>Trailing Edge</b> Cooling Channel ( <i>SS</i> ) surface at $y = -180[mm]$ , <i>G0</i> configuration . . . . .	41
3.10	Experimental [7] and <i>CFD</i> Nu profiles on the <i>SS</i> wall at $y = -96[mm]$ , <i>G0</i> configuration . . . . .	41
3.11	Experimental [7](a) and <i>CFD</i> (b) Nu distribution on the <i>SS</i> , <i>G0</i> configuration . . . . .	42
3.12	Experimental [7] and <i>CFD</i> Nu profiles on the <i>SS</i> wall at $y = -150[mm]$ , <i>G0</i> configuration . . . . .	43
3.13	Experimental [5] (a,b) and <i>CFD</i> (c,d) time-averaged stream-tracers and contours plots of the in-plane velocity modulus $C_{xy}$ in the <i>xy</i> (a,c) and <i>xy2</i> (b,d) planes, <i>G0</i> configuration . . . . .	44
3.14	Experimental [5] and <i>CFD</i> flow angle $\alpha$ extracted in plane <i>xy</i> at $y = -132[mm]$ , <i>G0</i> configuration . . . . .	45
3.15	Experimental [5] and <i>CFD</i> V velocities profiles in plane <i>xy</i> at $y = -150[mm]$ , <i>G0</i> configuration . . . . .	45
3.16	Experimental [5] and <i>CFD</i> Inter–Pedestal Passage ( <i>IP</i> ) mass flow rate distribution, <i>G0</i> configuration . . . . .	46
3.17	Experimental [5] and <i>CFD</i> 3-D <i>IP</i> flow structures, <i>G0</i> configuration . . . . .	47
3.18	Experimental [5] and <i>CFD</i> velocity components inside 4 <sup>th</sup> Pedestal Passage ( <i>P4</i> ) passage in plane <i>xzi</i> at $z = 0[mm]$ , <i>G0</i> configuration . . . . .	48
3.19	Experimental [7] and <i>CFD</i> average Nu value computed over each <i>IP</i> passage, <i>G0</i> configuration . . . . .	48
3.20	3-D view on the mesh, <i>G1</i> configuration . . . . .	49
3.21	<i>GCI</i> error band at <i>SS</i> at $y = -60[mm]$ , <i>G1</i> configuration . . . . .	50
3.22	Experimental [7](a) and <i>CFD</i> (b) Nu distribution on the <i>SS</i> , <i>G1</i> configuration . . . . .	51
3.23	Experimental [56](a,b) and <i>CFD</i> (c,d) time-averaged stream-tracers and contour plots of the in-plane velocity modulus $C_{xy}$ in the <i>xy</i> (a,c) and <i>xy2</i> (b,d) planes, <i>G1</i> configuration . . . . .	52
3.24	Experimental [56](a) and <i>CFD</i> (b) Nu distribution on the <i>SS</i> and time-averaged stream-tracers in planes $xy_{G1}$ and $xz_{G1}$ between the 3 <sup>rd</sup> and 4 <sup>th</sup> rib, <i>G1</i> configuration . . . . .	53
3.25	Experimental [56] and <i>CFD</i> flow angle $\alpha$ extracted in plane <i>xy</i> at $y = -132[mm]$ , <i>G1</i> configuration . . . . .	54
3.26	Experimental [56] and <i>CFD</i> V velocities profiles in plane <i>xy</i> at $y = -150[mm]$ , <i>G1</i> configuration . . . . .	54
3.27	Experimental [56] (a-d) and <i>CFD</i> (e-h) 3-D <i>IP</i> flow structures, <i>G1</i> configuration . . . . .	55
3.28	Experimental [56] and <i>CFD</i> <i>IP</i> mass flow rate distribution, <i>G1</i> configuration . . . . .	55
3.29	Experimental [7] (a) and <i>CFD</i> (b-f) Nu distribution on the <i>SS</i> wall for all the turbulence models tested, <i>G1</i> configuration . . . . .	57
3.30	Experimental [7] (a) and <i>CFD</i> (b-f) Nu maps on the <i>SS</i> and time-averaged stream-tracers path in plane $xy_{G1}$ and $xz_{G1}$ between the 3 <sup>rd</sup> and the 4 <sup>th</sup> rib for all the turbulence models tested, <i>G1</i> configuration . . . . .	58

3.31	Experimental [56](a) and <i>CFD</i> (b-f) stream-tracers and <i>CFD</i> (b-f) distribution of the normalized turbulence kinetic energy $\kappa$ in the Inter-Rib Passage ( <i>IR</i> ) passage in plane $xz_{G1}$ for all the turbulence models, <i>G1</i> configuration	59
3.32	3-D view on the mesh, <i>G2</i> configuration	60
3.33	<i>GCI</i> error band at <i>SS</i> surface $x = -262.5$ , <i>G2</i> configuration	61
3.34	Experimental [7](a) and <i>CFD</i> (b) Nu distribution on the <i>SS</i> , <i>G2</i> configuration	62
3.35	Experimental [7](a) and <i>CFD</i> (b) Nu number distribution on the <i>SS</i> at $y = -169.228[mm]$ , <i>G2</i> configuration	63
3.36	Experimental [7] and <i>CFD</i> flow angle ( $\alpha$ ) extracted in plane $xy$ at $y = -132[mm]$ , <i>G2</i> configuration	63
3.37	Experimental [5] (a,b) and <i>CFD</i> (c,d) time-averaged stream-tracers and contours plots of the in-plane velocity modulus $C_{xy}$ in the $xy$ (a,c) and $xy2$ (b,d) planes, <i>G2</i> configuration	64
3.38	Experimental [7] and <i>CFD</i> V velocity profiles extracted in plane $xy$ at $y = -150[mm]$ , <i>G2</i> configuration	65
3.39	Experimental [7] and <i>CFD</i> time-averaged stream-tracers at the plane $yz_{G2}$ , <i>G2</i> configuration	65
3.40	Experimental [7] and <i>CFD</i> 3-D <i>IP</i> flow structures inside $P4$ , <i>G2</i> configuration	66
3.41	Experimental [7] and <i>CFD</i> averaged-Nu values computed over each <i>IP</i> passage, <i>G2</i> configuration	67
3.42	Experimental [7] and <i>CFD</i> averaged-Nu values computed over each <i>IP</i> passage, <i>G2</i> configuration	68
4.1	3-D view on the domain for <i>G0</i> configuration at $\gamma = 45[^\circ]$	70
4.2	Experimental [5] and <i>CFD</i> U at the channel inlet, $x = -69.8[mm]$	71
4.3	<i>GCI</i> error band at $Ro = 0.46$ and $\gamma = 45[^\circ]$ in plane: $xy$ at $z = 0[mm]$ $y = -132[mm]$ (a) and $xz$ at $y = -132[mm]$ $x = 300[mm]$ , <i>G0</i> rotating configuration	72
4.4	Experimental [3] and <i>CFD</i> Nu number distribution at the Pressure Side Wall, <b>Trailing Edge</b> Cooling Channel ( <i>PS</i> ) at $y = -96[mm]$ at $Ro = 0.26$ , <i>G0</i> rotating configuration	73
4.5	Experimental [3] and <i>CFD</i> Nu distribution at $Ro = 0.26$ at <i>PS</i> (a,b) and at $Ro = 0.23$ at <i>SS</i> (c), <i>G0</i> rotating configuration	74
4.6	Experimental [3] and <i>CFD</i> Nu number distribution at the <i>PS</i> at $y = -150[mm]$ at $Ro = 0.26$ , <i>G0</i> rotating configuration	75
4.7	Experimental [5](a) and <i>CFD</i> (b) time-averaged stream-tracers and contour plots of the in-plane velocity modulus $C_{xy}$ in the $xy$ plane for $Ro = 0.23$ , <i>G0</i> rotating configuration	75
4.8	Experimental [5] and <i>CFD</i> flow angle $\alpha$ extracted in plane $xy$ at $y = -132[mm]$ at $Ro = 0.23$ , <i>G0</i> rotating configuration	76
4.9	Experimental [5] and <i>CFD</i> V profiles extracted in plane $xy$ at $y = -150[mm]$ at $Ro = 0.23$ , <i>G0</i> rotating configuration	76

4.10	Experimental [5] and <i>CFD IP</i> flow structures at $Ro = 0.23$ , $G0$ rotating configuration . . . . .	77
4.11	<i>CFD</i> U velocity profiles at $x = 69.8[mm]$ for $\gamma = 0[^\circ]$ and different $Ro$ . $z = 0[mm]$ (a), $y = 90[mm]$ (b), $y = 0[mm]$ (c), $y = 90[mm]$ (d) . . . . .	78
4.12	<i>CFD</i> contours of U velocity component and stream-tracers path at the channel inlet, $x = -69.8[mm]$ , $Ro = 0$ (a), $Ro = 0.23$ (b), $Ro = 0.46$ (c) . . . . .	79
4.13	<i>CFD</i> contours of the in-plane velocity modulus $C_{xy}$ and stream-tracers in planes $xy3$ (a-c) and $xy$ (d-f) at $Ro = 0$ (a,d), $Ro = 0.23$ (b,e) and $Ro = 0.46$ (c,f), $G0$ rotating configuration . . . . .	80
4.14	<i>CFD</i> velocity vectors distributions at $x = -100, 10, 165, 320$ and $470[mm]$ at $Ro = 0$ (a), $Ro = 0.23$ (b) and $Ro = 0.46$ (c), $G0$ rotating configuration . . . . .	81
4.15	<i>CFD</i> time-averaged stream-tracers and contours plots of in-plane velocity modulus $C_{y'z}$ in planes $y'z1_{G0}$ , $y'z2_{G0}$ and $y'z3_{G0}$ at $Ro = 0$ (a), $Ro = 0.23$ (b) and $Ro = 0.46$ (c), $G0$ rotating configuration . . . . .	82
4.16	<i>CFD</i> flow field inside the $P4$ passage in plane $xz$ at $Ro = 0.46$ , $G0$ rotating configuration . . . . .	83
4.17	<i>CFD</i> Nu distribution on the $SS$ at $Ro = 0.46$ , $G0$ rotating configuration . . . . .	83
4.18	<i>CFD</i> mass flow rate distribution at $Ro = 0$ (red), $Ro = 0.23$ (green) and $Ro = 0.46$ (blue), $G0$ configuration . . . . .	84
4.19	<i>CFD</i> contours of U velocity component and stream-tracers at the channel inlet ( $x = 69.8[mm]$ ) at $Ro = 0.46$ , $\gamma = 22.5[^\circ]$ (a) and $\gamma = 45[^\circ]$ . . . . .	85
4.20	<i>CFD</i> U velocity profiles at $x = 69.8[mm]$ for $Ro = 0.46$ and different channel orientations $\gamma$ . $z = 0[mm]$ (a), $y = -90[mm]$ (b), $y = 0[mm]$ (c), $y = 90[mm]$ (d) . . . . .	86
4.21	<i>CFD</i> contours of the in-plane velocity modulus $C_{xy}$ and stream-tracers in planes $xy3$ (a,d), $xy$ (b,e) and $xy1$ (c,f) at $Ro = 0.46$ (a,d) and $\gamma = 22.5[^\circ]$ (a-c) $\gamma = 45[^\circ]$ , $G0$ rotating configuration . . . . .	87
4.22	<i>CFD</i> profiles of the velocity modulus $C_{xyz}$ at $y = -120[mm]$ and different radial positions at varying $\gamma$ for $Ro = 0.23$ (a-c) and $Ro = 0.46$ (d-f), $G0$ rotating configuration . . . . .	88
4.23	<i>CFD</i> flow field inside the $IP$ passage $2^{nd}$ Pedestal Passage ( $P2$ )(a,b), $P4$ (c,d) and $7^{th}$ Pedestal Passage ( $P7$ )(e,f) in plane $xz$ for $\gamma = 45[^\circ]$ and $Ro = 0.23$ (a,c,e) and $Ro = 0.46$ (b,d,f), $G0$ rotating configuration . . . . .	89
4.24	<i>CFD</i> Nu distribution on the $SS$ wall at $Ro = 0.23$ and $Ro = 0.46$ at $\gamma = 45[^\circ]$ , $G0$ rotating configuration . . . . .	90
4.25	<i>CFD</i> mass flow rate distribution for $\gamma = 0[^\circ]$ , $\gamma = 22.5[^\circ]$ and $\gamma = 45[^\circ]$ at varying rotation numbers, $G0$ rotating configuration . . . . .	91
4.26	<i>GCI</i> error band at $Ro = 0.46$ and $\gamma = 22.5[^\circ]$ in plane: $xy_{G1}$ at $z = 14[mm]$ $y = -60[mm]$ , $G1$ rotating configuration . . . . .	93
4.27	Experimental [14] Heat Transfer Coefficient ( <i>HTC</i> ) at $Ro = 0.26$ on $PS$ , $G1$ rotating configuration . . . . .	94
4.28	<i>CFD</i> <i>HTC</i> (a) and Nu (b) at $Ro = 0.23$ , $G1$ rotating configuration . . . . .	94
4.29	Experimental [56] and <i>CFD</i> time-averaged stream-tracers and contour plots of the in-plane velocity modulus $C_{xy}$ in $xy$ plane at $Ro = 0.23$ , $G1$ rotating configuration . . . . .	95

4.30	Experimental [56](a,b) and <i>CFD</i> (c,d), time-averaged stream-tracers and contour plots of the in-plane velocity modulus $C_{y'z}$ , in planes $y'z1_{G1}$ (b,d) and $y'z2_{G1}$ (a,c), <i>G1</i> rotating configuration . . . . .	96
4.31	Experimental [56] and <i>CFD</i> time-averaged stream-tracers and contour plots of the in-plane ( $xy_{G1}$ ) velocity modulus between the 3 <sup>rd</sup> and the 4 <sup>th</sup> rib, <i>G1</i> rotating configuration . . . . .	97
4.32	Experimental [56] contour plots of the $u'$ (a,c) and $v'$ (b,d) velocity fluctuations in plane $xy_{G1}$ at $Ro = 0$ (a,b) and $Ro = 0.23$ (c,d), <i>G1</i> configuration . . . . .	97
4.33	Experimental [56] and <i>CFD</i> flow angle $\alpha$ extracted in plane $xy$ at $Ro = 0.23$ at $y = -132[mm]$ (a) and $V$ velocity profiles extracted in plane $xy$ at $Ro = 0.23$ at $y = -150[mm]$ (b), <i>G1</i> rotating configuration . . . . .	98
4.34	Experimental [56] and <i>CFD</i> <i>IP</i> flow structures at $Ro = 0.23$ , <i>G1</i> rotating configuration . . . . .	99
4.35	<i>CFD</i> $Nu$ distribution at $Ro = 0.23$ (a) and $Ro = 0.46$ (b), <i>G1</i> rotating configuration . . . . .	100
4.36	<i>CFD</i> time-averaged stream-tracers and velocity modulus $C_{xy}$ contours in plane $xy_{G1}$ at $Ro = 0.23$ (a) and $Ro = 0.46$ (b), <i>G1</i> rotating configuration . . . . .	101
4.37	Experimental [56] and <i>CFD</i> profiles at $Ro = 0$ (a), $Ro = 0.23 - 0.46$ (b) extracted from plane $y'z2_{G1}$ at $y = -15[mm]$ : mean radial velocity $U'$ , <i>G1</i> configuration . . . . .	101
4.38	<i>CFD</i> (c-f) time-averaged stream-tracers and contours plot of the in-plane velocity modulus $C_{y'z}$ , in planes $y'z1_{G1}$ , $y'z2_{G1}$ and $y'z3_{G1}$ at $Ro = 0.23$ (a,b) and $Ro = 0.46$ (c,d), <i>G1</i> rotating configuration . . . . .	102
4.39	<i>CFD</i> flow field inside the <i>IP</i> passage $P4$ in plane $xzR$ at $Ro = 0.46$ , <i>G1</i> rotating configuration . . . . .	103
4.40	<i>CFD</i> mass flow rate distribution at $Ro = 0$ (red) $Ro = 0.23$ (green) and $Ro = 0.46$ (blue), <i>G1</i> rotating configuration . . . . .	104
4.41	<i>CFD</i> $Nu$ distribution for different $Ro$ and $\gamma$ channel orientations, <i>G1</i> rotating configuration . . . . .	105
4.42	<i>CFD</i> time-averaged stream-tracers path and velocity $C_{xy}$ in plane $xy_{G1}$ at $Ro = 0.46$ for different channel orientations, <i>G1</i> rotating configuration . . . . .	106
4.43	<i>CFD</i> profiles of the velocity $U'$ at $Ro = 0.46$ and different $\gamma$ orientations extracted in plane $y'z2_{G1}$ at $y = -15[mm]$ , <i>G1</i> rotating configuration . . . . .	107
4.44	<i>CFD</i> time-averaged stream-tracers and contours plot of the in-plane velocity modulus $C_{y'z}$ , in planes $y'z2_{G1}$ (a,c,e), $y'z1_{G1}$ and $y'z3_{G1}$ (b,d,f) for all $\gamma$ orientations, <i>G1</i> rotating configuration . . . . .	107
4.45	<i>CFD</i> time-averaged stream-tracers and contours plot of the in-plane velocity modulus $C_{y'z}$ , in planes $y'z2_{G1}$ (a,c,e), $y'z1_{G1}$ and $y'z3_{G1}$ (b,d,f) at $Ro = 0.46$ for $\gamma = 0[^\circ]$ (a,b), $\gamma = 22.5[^\circ]$ (c,d) and $\gamma = 45[^\circ]$ (e,f), <i>G1</i> rotating configuration . . . . .	108
4.46	<i>CFD</i> mass flow rate distribution at $\gamma = 0[^\circ]$ , $\gamma = 22.5[^\circ]$ and $\gamma = 45[^\circ]$ at varying rotation numbers, <i>G1</i> rotating configuration . . . . .	109
5.1	Scheme of the test rig development for the present experimental campaign with the piping circuit . . . . .	111

5.2	Overview of the position of the experimental and <i>CFD</i> data planes (S1, S2, S3, S4, S5) Leading edge . . . . .	113
5.3	Overview of the position of the experimental and <i>CFD</i> data planes (IN1 ,IN2 ,IN3) Leading edge . . . . .	113
5.4	3-D view on the mesh for the leading edge geometry . . . . .	114
5.5	Experimental and <i>CFD</i> stream-wise velocity profiles extracted at $x = 120[mm]$ from planes IN3 (a) and IN1-IN2 (b) . . . . .	115
5.6	<i>CFD</i> velocity profiles $V$ for the three meshes tested. Data extracted at $x = 520[mm]$ from plane IN3 . . . . .	116
5.7	<i>CFD</i> (a) and experimental(b)time-averaged stream-tracers in plane S5 for $Re = 20000$ and $Ro = 0.2$ . . . . .	117
5.8	<i>CFD</i> contour map of the pressure distribution on the channel cross-section in S5 plane at $Re = 20000$ and $Ro = 0.2$ . . . . .	117
5.9	<i>CFD</i> (a) and experimental(b) 3-D view of the velocity distribution inside the Ekman layer . . . . .	118
5.10	<i>CFD</i> (a) and experimental(b) time-averaged stream-wise velocity contour map in plane S5 , $Re = 20000$ - $Ro = 0.2$ . . . . .	119
5.11	Contour maps of the stream-wise (a) and span-wise (b) velocities at different channel locations from <i>CFD</i> at $Re = 20000$ , $Ro = 0.2$ . . . . .	120
5.12	<i>CFD</i> contour maps of the stream-wise velocity and stream-tracers at different channel locations (a); evolution along the channel of the stream-wise and span-wise velocities at point $y = 38[mm]$ , $z = 24[mm]$ (b) (see the blue line in Fig. 5.12(a)). The data are at $Re = 20000$ , $Ro = 0.4$ . . . . .	121
5.13	<i>CFD</i> contour maps of the stream-wise velocity and stream-tracers at different channel locations at $Re = 20000$ , $Ro = 0.6$ . . . . .	123
5.14	<i>CFD</i> (a,b) and experimental (c) contour maps of the stream-wise velocity and stream-tracers in plane S5. <i>CFD</i> data at $Ro = 0.4$ and $Re = 40000$ (a) and $Re = 10000$ (b), experimental data at $Ro = 0.4$ and $Re = 10000$ (c) . . . . .	123
5.15	Experimental contour maps of flow turbulence intensity in plane S5 for $Re = 20000$ , $Ro = 0.2$ (a) and $Re = 10000$ , $Ro = 0.4$ (b) . . . . .	124
5.16	<i>CFD</i> contour maps of flow turbulence intensity in plane S5 for $Re = 20000$ , $Ro = 0.2$ (a) and $Re = 10000$ , $Ro = 0.4$ (b) . . . . .	125
5.17	Heat transfer data from Liu et al.[50] . . . . .	126
5.18	<i>CFD</i> contour maps of the stream-tracers velocity in plane S5 for different channel orientation $\gamma = 0[^\circ]$ (a), $\gamma = 22.5[^\circ]$ (b) and $\gamma = 45[^\circ]$ (c), at $Re = 20000$ and $Ro = 0.2$ . . . . .	127
5.19	<i>CFD</i> contour map of the pressure distribution on the channel cross-section in S5 plane at different channel orientation $\gamma = 0[^\circ]$ (a), $\gamma = 22.5[^\circ]$ (b) and $\gamma = 45[^\circ]$ (c), at $Re = 20000$ and $Ro = 0.2$ . . . . .	128
5.20	<i>CFD</i> contour maps of the stream-wise velocity and stream-tracers at different channel locations at $Re = 20000$ $Ro = 0.4$ $\gamma = 22.5[^\circ]$ (a) and $\gamma = 45[^\circ]$ (b) . . . . .	129
5.21	<i>CFD</i> contour maps of the stream-wise velocity and stream-tracers at different channel locations at $Re = 20000$ $Ro = 0.6$ $\gamma = 22.5[^\circ]$ (a) and $\gamma = 45[^\circ]$ (b) . . . . .	129

---

B.1	Automatic blanding functionality of the high-resolution scheme . . . . .	145
D.1	Experimental [5] [56] U velocity profiles in-planes xy(a) and xz(b) at $x = -69.8[mm]$ . . . . .	149
E.1	Experimental(a,c) [56] and <i>CFD</i> (b,d) time-averaged stream-tracers and contour plots of the velocity $C_{xz}$ (a,b) and turbulence intensity I (c,d) inside the 4 <sup>th</sup> <i>IP</i> passage ( $P_4$ ) in-plane xzi, <i>G1</i> configuration . . . . .	151



---

# List of Tables

3.1	xy planes see Fig. 3.5, $G0$ $G1$ $G2$ configurations . . . . .	37
3.2	yz and xz inlet planes and xz $IP$ planes see Fig. 3.5, $G0$ $G1$ $G2$ configurations . . . . .	37
3.3	yz planes see Fig. 3.5(d), $G0$ configuration . . . . .	37
3.4	yz, xz and $y'z$ planes see Fig. 3.6, $G1$ configuration . . . . .	37
3.5	yz, xz and $y'z$ planes see Fig. 3.7, $G2$ configuration . . . . .	37
3.6	Grid details, $G0$ configuration . . . . .	40
3.7	$GCI$ study, $G0$ configuration . . . . .	40
3.8	Grid details, $G1$ configuration . . . . .	49
3.9	$GCI$ study, $G1$ configuration . . . . .	50
3.10	Grid details, $G2$ configuration . . . . .	60
3.11	$GCI$ study, $G2$ configuration . . . . .	61
3.12	Experimental [7] and $CFD$ total average Nu number for configuration $G1$ , $G2$ with respect to $G0$ configuration . . . . .	68
4.1	$GCI$ study, $G0$ rotating configuration . . . . .	72
4.2	$CFD$ comparison of total Nu numbers at different Ro numbers, $G0$ rotat- ing configuration . . . . .	84
4.3	$CFD$ comparison of total Nu numbers at different Ro numbers and channel orientations, $G0$ rotating configuration . . . . .	91
4.4	$GCI$ study, $G1$ configuration . . . . .	93
4.5	$CFD$ comparison of total Nu numbers at different Ro numbers, $G1$ rotat- ing configuration . . . . .	104
4.6	$CFD$ comparison of total Nu numbers at different Ro numbers and channel orientations $\gamma$ , $G1$ rotating configuration . . . . .	109
5.1	S1, S2, S3, S4 and S5 planes see Fig. 5.2, leading edge . . . . .	113
5.2	IN1 ,IN2 and IN3 planes see Fig. 5.3, leading edge . . . . .	114
5.3	Grid details for the Leading Edge geometry . . . . .	114
5.4	Grid parameters for grid independency study for the Leading Edge geometry	116



---

# Abstract

State-of-art gas turbine are designed to operate at turbine inlet temperatures higher than 2000[K]. Such temperature levels are sustainable only by means of aggressive and efficient cooling of the components exposed to the hot gas path. It should be pointed out that not only must the maximum metal temperature be kept below safety limits, but the thermal field must be reasonably uniform too, in order to limit thermal stresses. Moreover, modern blade cooling systems consist of a combination of internal cavities with cross-sections specifically developed for each different blade portion; therefore, specific studies are essential to describe their performances in detail in order to provide designers with the most accurate knowledge.

The need for such detailed information is in conflict with some common practices in cooling system design: most of the studies deal with square or rectangular channels cross-section (hence resembling ducts in the central body of the blade), the link between coolant flow field and heat transfer rates is seldom analyzed; finally, the coupling of rotation and different channel orientations is rarely taken into account.

Over the last few years *CFD* (Computational Fluid Dynamic) has been exploited to provide valuable information on complex flow fields and heat transfer in internal cooling passages; indeed, it is already used as an engineering tool in design and optimization processes of gas turbine cooling. On the other hand, the reliability of the numerical tools available at present is not sufficiently high and, hence, detailed experimental analyses are still required for numerical validation purposes.

The present thesis focuses on the aspects pertaining to the suitability of *CFD* for the prediction of the aero-thermal performances inside cooling channels designed for two essential portions of the blade, namely **trailing edge** and **leading edge**, whose sizes and shapes are quite different from those resembling cooling channel in the central portion of the blade.

The **trailing edge** cooling model is characterized by a trapezoidal cross-section of high aspect-ratio and coolant discharge at the blade tip and along the wedge-shaped trailing side, where seven lengthened pedestals are also installed. Three different configurations are taken into account, namely the smooth channel and two others characterized by the use of ribs in different portions of the duct. Firstly, an extensive comparison with detailed experimental data including local flow velocities, turbulence proprieties and local heat transfer coefficient in static ( $Ro = 0$ ) and orthogonal rotating conditions ( $Ro = 0.23$ ) is carried out using the *Shear Stress Transport (SST)* turbulence model. Moreover, for one rib-roughened configuration in static condition ( $Ro = 0$ ) different turbulence models are tested in order to enhance all computational results. Finally, the *CFD* code is exploited to analyzed more engine-like conditions, namely  $Ro = 0.46$  and  $\gamma = 22.5 - 45[^\circ]$ . The results show that rotation and channel orientation produce contrasting effects which are more significant in the rib-roughened configuration. In fact, on the radial central portion

rotation/orientation generates an increase/decrease in the heat transfer; conversely, on the trailing side region, rotation/orientation has a negative/positive effect on the thermal field.

The **leading edge** cooling model consists of a straight, smooth channel with an equilateral triangle cross-section. Geometry and test conditions resemble those pertaining to the passages used for the internal cooling of gas turbine blades leading edge. On the same geometry and at comparable working conditions, heat transfer data are also available from literature. Experimental data are used for *CFD* validation purposes at  $Re = 20000$   $Ro = 0.2$  and  $Re = 10000$   $Ro = 0.4$ . Consequently, a wide range of working conditions, namely  $Re = 10000 - 40000$   $Ro = 0.2 - 0.6$  are numerically explored by the *SST* turbulence model. The results show that the rotation-induced flow structure is rather complicated showing relevant differences compared to the flow models that have been supposed by the research community so far. Indeed, the secondary flow turned out to be characterized by the presence of two or more vortex cells depending on channel location and  $Ro$  number. No separation or reattachment of these structures is found on the channel walls but they are observed at the channel apices. The stream-wise velocity distribution shows a velocity peak close to the lower apex and the overall flow structure does not reach a steady configuration along the channel length. This evolution is hasten (in space) if the rotation number is increased while changes of the  $Re$  number have no effects. Moreover, thanks to the understanding of the flow mechanisms associated to rotation, it was possible to provide a precise justification for the channel thermal behavior. Finally, different channel orientations (namely  $\gamma = 22.5 - 45[^\circ]$ ) are numerically investigated. The results further demonstrate that the variation of the channel orientation to more engine-like conditions significantly affects the flow field and, hence, the aero-thermal behavior.

---

# 1

## Introduction

The gas turbine, is one of the most challenging and complex engineering artifacts conceived for the production of mechanical power and aero propulsion, and operates at the very limits of aerodynamics and materials technologies. The continuous demand for enhanced overall efficiency and higher specific power output together with a reduction of CO<sub>2</sub>-emissions result in higher turbine inlet temperatures and increasing compressor pressure ratios. However, nowadays hot gas temperatures are already significantly above the allowed material temperatures. Therefore, optimized internal cooling schemes are essential to reach higher thermal efficiencies and safe operation during life cycle. The technology of cooling gas turbine components has developed over the years from simple smooth cooling passages to very complex internal and external geometries. The fundamental aim of this technology area is to obtain the highest overall cooling effectiveness with the lowest possible penalty on the thermodynamic cycle performance. It should be pointed out that because of the enormous range of applications where gas turbines are used any small gain in thermal efficiency and performance results in a major economic impact worldwide.

### 1.1 Gas Turbine Engines

A simple gas turbines consists of three main sections:

- a compressor where the pressure of the evolving fluid, generally air, is increased;
- a combustor where the temperature of the fluid is raised by igniting fuel in dedicated burners;
- a power turbine which drives the compressor and expands the highly energetic gas from the combustor.

Behind the turbine, the gas still contains a significant amount of energy which can be transformed in various forms: in air-crafts it is converted into a high-velocity jet (see Fig. 1.1 which presents an example of an aircraft engine). Conversely, in land-based it is transformed into shaft power for a generator which converts the mechanical energy into electrical power (see Fig. 1.2 in which a land-based engine is illustrated).

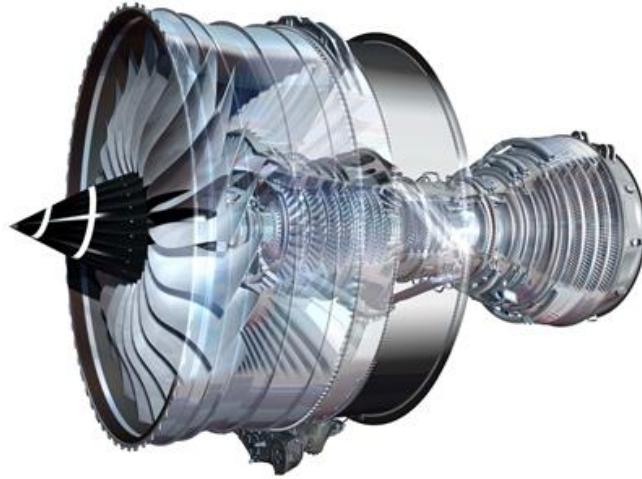


FIGURE 1.1 – Rolls-Royce Trent XWB <http://www.rolls-royce.com/news/assets/prg.jsp>, (aircraft engine) .

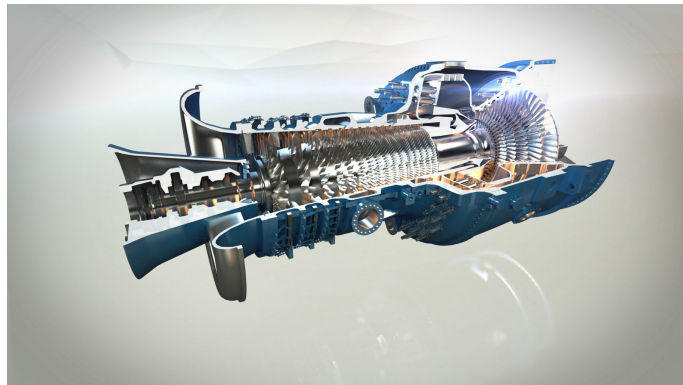


FIGURE 1.2 – Alstom GT13E2 <http://www.alstom.com/power/gas-power/gas-turbines/gt13e2-/>, (land-based engine) .

A thermodynamic description of gas turbine is provided by the Joule cycle (also known as Brayton cycle) shown in Fig. 1.3. In the ideal cycle, compression (1-2) and expansion (3-4) of a gas are adiabatic ( $q=0$ ) and isentropic ( $S=\text{constant}$ ). Moreover, there are no pressure losses in the combustion chamber and exhausting ducts and the working fluid is a perfect gas with constant properties.

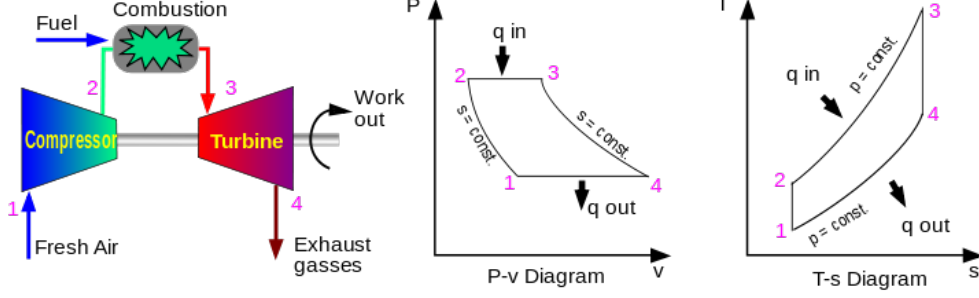


FIGURE 1.3 – Gas turbine thermodynamic cycle.

If we consider a real cycle, i.e. taking into account the turbine ( $\eta_T$ ) and compressor efficiency ( $\eta_C$ ), the cycle efficiency ( $\eta_{TOT}$ ) is equal to:

$$\eta_{TOT} = \frac{\eta_T \frac{T_3}{T_1} \left(1 - \frac{1}{\beta_{21-34}^m}\right) - \frac{1}{\eta_C} (\beta_{21-34}^m - 1)}{\left(\frac{T_3}{T_1} - 1\right) - \frac{1}{\eta_C} (\beta_{21-34}^m - 1)} \quad (1.1)$$

where:

$$m = \frac{\vartheta - 1}{\vartheta} \quad (1.2)$$

The equation 1.1 demonstrates how the efficiency of such cycle depends on the pressure ratio ( $\beta_{21-34}$ ), the overall temperature ratio ( $\frac{T_3}{T_1}$ ) and evidently the efficiency of compressor ( $\eta_C$ ) and turbine ( $\eta_T$ ) (see Fig. 1.4). From this simple cycle analysis it should be clear that one of the most direct ways to enhance the efficiency is to increase the maximum operating temperature of the cycle, i.e. **Turbine Firing Temperature ( $T_f$ )**(exit of combustor/inlet of high pressure turbine, point 3 in Fig. 1.3) and, hence, the extracted work. Consequently, remarkable efforts have been made in many countries, in many engines companies and governmental and academic laboratories, to understand the fluid mechanics of turbines and compressors, to produce higher-temperature materials and to improve cooling of surfaces scrubbed by hot gases. In advanced gas turbines, these temperatures are far higher than the melting point of the blade material: therefore, turbine blades need to be considerably

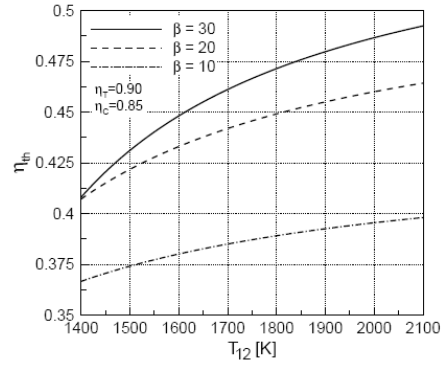


FIGURE 1.4 – Cycle efficiency of a gas turbine engine.

therefore, turbine blades need to be considerably

cooled. The technology of cooling gas turbine components via internal flows of single-phase gasses has developed over the years from simple smooth cooling passages to very complex geometries involving many different surfaces, architectures and fluid-surface interactions; the time evolution of turbine cooling technology during the last few decades is illustrated in Fig. 1.5.

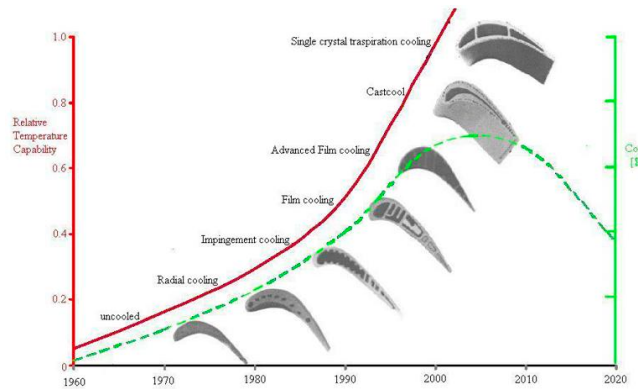


FIGURE 1.5 – The time evolution of turbine cooling technology during the last decades [43].

Figure 1.6 shows the historical development of  $T_f$ , highlighting the separate impact of materials improvement and cooling technologies.

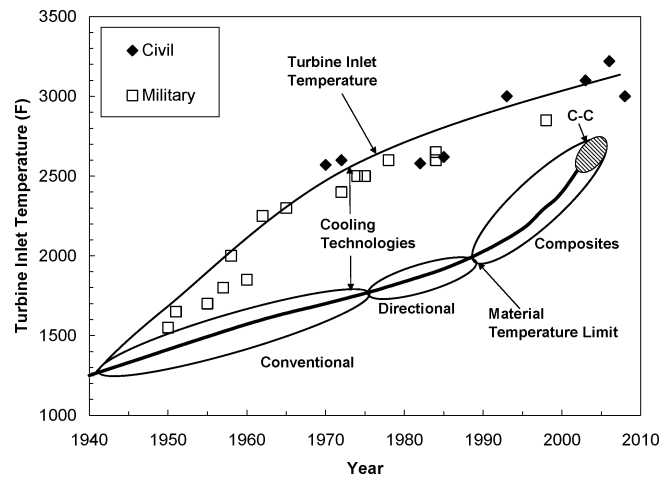


FIGURE 1.6 – Comparison between turbine inlet temperature and blade material temperature limits highlighting the importance of cooling technology [9].

## 1.2 Blade Cooling

As (Fig. 1.6) shows, in the last 3 decades, this temperature raised up from about 1600 [K] ( $\approx 2550[F]$ ) to about 2100 [K] ( $\approx 3200[F]$ ) in the most recent demonstrator engines. The progress made in increasing the temperature is first brought by the innovation in the metallurgical domain. There are very few materials that can withstand high temperatures and combined stresses, which are mainly caused by the non-uniform temperature distribution, high aerodynamic load and centrifugal forces. Nowadays, the use of oxide-dispersion strengthened alloys and ceramic thermal barrier coatings allow metal temperatures as high as 1300 [K]. In order to reach much higher temperatures than the ones withstood by the blade materials, it is important to have the best possible cooling system making it possible to work with  $Tf$  equal to 2000 [K]. It should be pointed out that normally cooling is required only in the first or in the first two stages, after which the gas temperatures drop below tolerable levels in terms of metal surviving. Indeed, the first stator vanes are exposed to the highest  $Tf$  (including the hot spot from the burner). The first rotating blade row is exposed to lower temperatures because of circumferential averaging, dilution of turbine gases with first stator vane cooling air and relative velocity effects. The second stator vane is exposed to a lower temperature because of cooling air dilution, work extraction from the turbine gases and mixing that dilutes the hot spots. The turbine temperature decreases in a similar manner through each later stage. Throughout the years, different kinds of cooling techniques have been developed which can essentially be divided into two big families, depending on the media used as coolant:

- steam cooling techniques which are exploited for example in industrial, land-based applications (e.g. combined cycle);
- air cooling techniques (considered in the present thesis) which are more suitable for aircraft applications, because of the availability and the lower weight of the medium used.

In the latter techniques the air cooling of turbine blades the air is bled from the last stages of the compressor. The use of 20 to 30% [52] of this compressed air to cool high-pressure turbines is characterized by severe penalty on the thermodynamic efficiency unless the  $Tf$  is sufficiently high for the gains to outweigh the losses. Indeed, in all properly operating cooled turbine systems, the efficiency gain is significant enough to justify the added complexity and cost of the cooling technologies employed.

### 1.2.1 Cooling Techniques

The previous considerations show that it is necessary to develop an excellent design of these cooling systems that requires the maximum heat transfer capability with the minimum coolant mass flow and cooling system pressure drop. In order to obtain the best possible design the following conditions must be satisfied:

- the level and distribution of blade metal temperature should be such as to assure a satisfactory blade life;

- the reduction in turbine efficiency and overall cycle efficiency compared to a non-cooled turbine with the same turbine inlet temperature should be kept as small as possible;
- the performance level of the cooling system should not deteriorate during operation;
- the system should be mechanically simple and relatively easy to manufacture and service;
- the application of the cooling system should be justified on the basis of the overall economics of the installation.

Throughout the years various cooling techniques have been developed to keep the vane and the blade metal temperatures below allowable limits while maintaining  $Tf$  high. Air cooling can act internally (e.g. convection and impingement cooling (Figs. 1.7 (a,b)) or externally (e.g. film-cooling and transpiration-cooling (Figs. 1.7(c,d,e)) with respect to the blade.

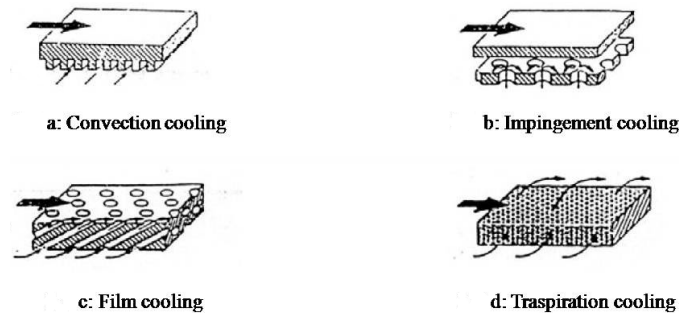


FIGURE 1.7 – Cooling schemes: (a) forced convection, (b) impingement, (c)-(d) film-cooling, (e) transpiration-cooling [52].

### Internal forced convection cooling

The older technique is the *internal forced convection cooling* (Fig. 1.7 (a)) for which compressor air circulates inside intricate serpentine or rectilinear passages inside the blade, extracts heat by convection and is discharged into the main gas stream. Moreover, heat transfer can be enhanced by roughening the cooling passages walls with repeated geometrical elements, (e.g.: pins, ribs, dimples). The main effects of these artificial roughness elements are basically:

- increasing the heat transfer surface area;
- creating high turbulence level in the core flow.

### Impingement cooling

Forced convection is coupled with *impingement cooling* in order to enhance performance: the coolant bleeds via rows of holes through a perforated wall, consequently jet arrays are produced and impinge onto the inner wall of the blade, lowering its temperature. The *impingement cooling* is used in the most critical sections of the airfoil (e.g leading edge), where high heat transfer coefficients are requested.

### Film cooling

*Film cooling* is by far the most effective but at the same time the most complicated cooling technique that is used in high pressure turbine stages. It is a process whereby a thin buffer layer of cooling air covers the airfoil surface in order to protect it from high-temperature gasses. This buffer layer is maintained by a continuous discharge of coolant, which exits from the internal blade passages through a series of slots or holes (Figs. 1.7 (c,d)). In mixing with the hot stream gasses, the film gradually dissipated and this dissipation results in deterioration of cooling effectiveness in the main flow direction. For this reason, series of rows are used to support the film layer in areas where high external heat transfer rates are encountered. If there are multiple rows, the boundary layer is perturbed consecutively and never attains an equilibrium state. The resulting flow structure leads to a very complex flow and thermal field downstream the holes.

### Transpiration cooling

The *transpiration cooling*, although still under development, is considered to be the new frontier in blade cooling, replacing the consolidated techniques describe above. In transpiration cooling the blade is surrounded by porous media, through which the coolant comes out into the hot gas (Fig. 1.7(e)). The pore size is particularly small (typical dimensions are around 10 to 50 [ $\mu m$ ]), consequently it causes the main problems in the application of the technique. It is a matter of fact that the porous media can be easily contaminated by dust and the carbon residuals of the combustion process. The residuals have the tendency to get blocked in the pores and thus progressively reducing the effectiveness of the cooling process during the operational life of the engine. Another problem is the increased roughness of the blade surface, because of the porous skin surrounding the airfoil. Currently the resulting aerodynamic performance is in general lower than a standard steel blade. Nevertheless, this futuristic cooling technique is able to maintain the same cooling effectiveness by using 50% less cooling air than film cooling. An extensive review of mechanisms and performance of heat transfer cooling techniques was presented by Han et al.[36]. The design of the cooling system for turbine airfoils is a complex process, which requires a multi-disciplinary approach. An overview of the method is presented in the generic summary diagram in Fig. 1.8 from [20]. For the present purpose, the design analysis is shown as a four level system:

- **Level 0** is the preliminary design (not shown in Fig. 1.8) and it mainly deals with the mission requirements, such as efficiency, cost of electricity, power sizing and

number of starts. Hence this level sets the target goals on the cooling system, including the coolant consumption, turbine airfoil life, and inspection intervals.

- **Level 1** concerns the conceptual design of the components largely based on the nominal target conditions and divorced from the surrounding system constraints and competing requirements or trade-offs. Analysis can be performed based on 1D,2D or 3D complexities and details, and is primarily used to compare various options in design.
- **Level 2** cooling analysis is the much more detailed inclusion of surrounding effects and constraints from aerodynamics, material properties, mechanical loads, lifting limitations, clearances etc. The analyses performed in this level often should be combined thermal-mechanical predictions using very detailed finite element models and are performed at one steady-state operating condition, e.g. 100% load. The result obtained in this level is the basic system design with balanced choices that satisfy the engine design goals.
- **Level 3** brings in the operational transient aspects to determine if requirements or constraints are violated under conditions such as a normal start-up, fast start-up, trips and hot restarts. If the results in this level require additional changes be made with new analysis at Levels 1 and 2.

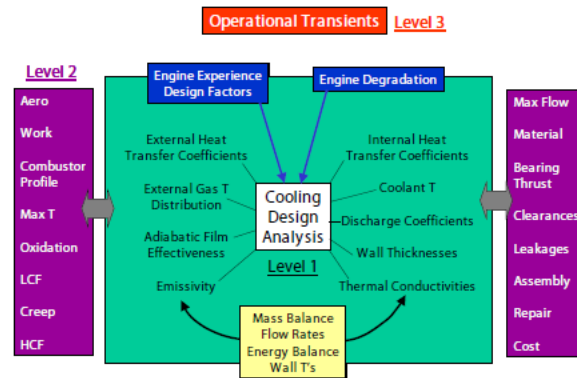


FIGURE 1.8 – Cooling design analysis system [20].

### 1.3 Literature Review

A modern blade cooling systems can be very complex as shown in Fig. 1.9. In this example, the main portion of the blade is cooled using a turbulated-five-pass serpentine circuit. Moreover, the blade has three different cooling circuits isolated in the shank cooling supply and with a combination of cavities with cross-sections specifically developed for the different blade portions, in particular:

- *triangular* for the blade *leading edge*;
- *rectangular* for the *central body*;
- and *trapezoidal* for the *trailing edge*.

Therefore, specific studies are required for a detailed description of their performance ([19] [35]).

Nevertheless, this section deals only with selected aspects relevant to those features which are significant for the present study, namely *trailing edge* and *leading edge* without the attempt to summarize the large corpus of literature concerning internal cooling techniques for gas turbine blades. By way of example this topic was reviewed by Weigand et al.[69], Han et al.[36] and Ligrani et al.[47].

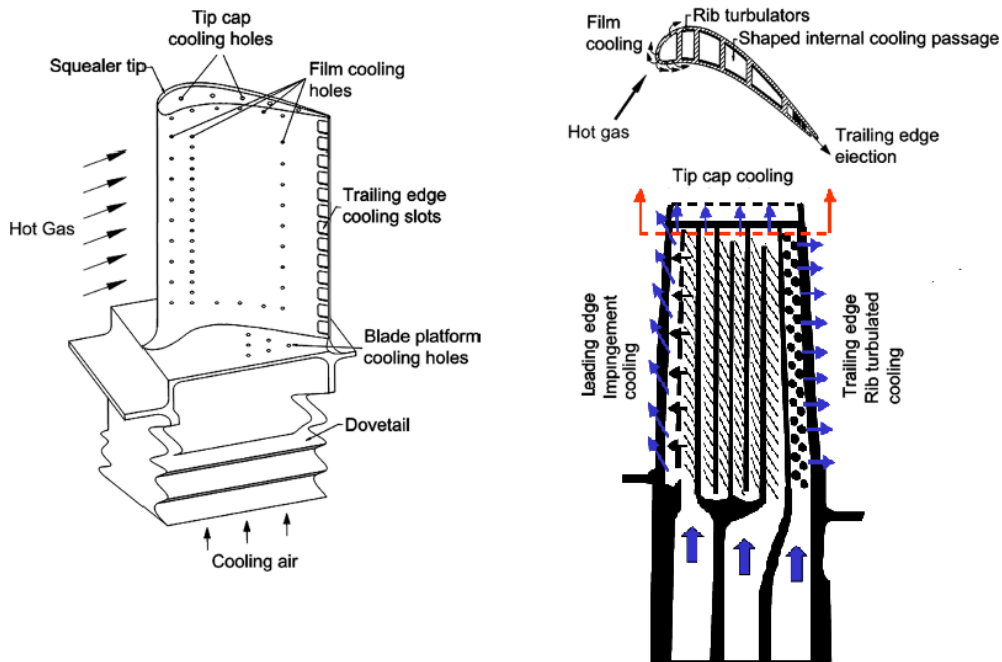


FIGURE 1.9 – Cooled high pressure turbine blade [20] .

### 1.3.1 Internal Cooling in Trailing Edge Static Channels

The trailing edge cooling channel is often a life-limiting part of the blade. The efficient cooling of this area represents a particularly challenging task: since the aerodynamic requirements of high slenderness is in conflict with the need of integrating internal cooling passage. In this respect Cunha et al.[27] presented analytical models for representative trailing edge configurations and provided fundamental insight into the relevant characteristics affecting the design of trailing edge configurations for high-pressure turbine airfoils.

However, looking at the open literature and focusing on the present thesis, a good starting point is the work by Taslim et al. [65] where the effects of cross-over jets for the cooling of the blade trailing edge cavity were studied using **Liquid Crystal Thermography (LCT)** in six different channel geometries varying the **Re** number. Recently complete numerical and experimental analyses were performed by Armellini et al. [6] and Coletti et al. [25] for a ribbed cooling channel with internal impinging jets and slots along the blade trailing edge. The detailed aero-thermal analyses pointed out the limits of the numerical solver in predicting the very complex flow field which develops inside the channel. However, a recent contribution provided by Taslim and Nongsaeng [66] found a reasonable agreement between numerical and experimental heat transfer data for a channel with axial outflow and cross over jets. Experimental aero-thermal investigations coupled with numerical analyses of a cooling channel similar to the one that will be analyzed in the present work can be found in Bianchini et al. [13]. The effects of different internal pin fins were analyzed showing that numerical computations predict reasonably well the air distribution in the channel and the global heat transfer level if compared to the experimental data. Finally, more recently, Armellini et al. [7] performed a complete experimental aero-thermal analysis in static condition comparing two rib-roughened configurations characterized by turbulence promoters installed respectively inside the channel central portion (*G1*) and in between the inter-pedestal passages at the trailing side (*G2*). Compared to the smooth case (*G0*), the first configuration (*G1*) achieved the better performances with significant overall *HTC* enhancement and affordable pressure loss penalties.

### 1.3.2 Internal Cooling in Leading Edge Static Channels

The Leading Edge of high pressure turbine blades is one of the most challenging issue which should be tackled in order to guarantee an adequate thermal protection at the front part of an airfoil because of the presence of a stagnation point. Here the highest temperature, as well as the largest temperature gradients appear, therefore, efficient cooling techniques must be adopted in order to prevent engine failure.

A number of experimental and numerical works concerning the thermal performances of triangular-shaped channels resembling the leading edge ducts can be found in the open literature. It should be pointed out that the heat transfer and pressure drop measurements inside the triangular channel were in good agreement with the correlations developed for turbulent tube flow using the hydraulic diameter of the triangular duct as the tube diameter [51].

Metzger and Vedula [55] performed experimental measurements of the heat transfer enhancement in a ribbed triangular duct studying the effects of rib angle, rib orientation and rib pitch-to-diameter ratio on heat transfer performance. For all the tested configurations, 60[°] angled ribs produce higher heat transfer. More recently Haasenritter and Weigand [34] numerically predicted the heat transfer enhancement in a ribbed triangular duct using a  $k-\epsilon$  turbulence model founding a good agreement with the aforementioned experimental data [55]. Zhang et al. [72] experimentally investigated heat transfer and friction factors in a fully and partially ribbed right angle triangular duct with small radii corners and different Reynolds numbers. They found that the heat transfer coefficient and friction factors in triangular ducts with partial ribbed walls (90[°] or 45[°]) were 10%

higher than those with fully ribbed walls. Amro et al.[1] provided an experimental investigation of heat transfer inside a ribbed triangular channel with rounded apex corner and double-sided fully overlapping ribs in the arc area. Considering the local as well as overall heat transfer enhancement and friction factor, they concluded that 45[°] inclined ribs with double-sided orthogonal arc ribs were the best solution. All these studies used straight side walls representing the pressure and suction side of a blade leading edge. Finally an experimental and numerical investigation of the influence of more engine-similar cross-sections of smooth and 45[°] angled rib leading edge channel was carried out by Domaschke et al.[30] at different  $Re$  numbers taking into account the side wall curvature and hence the associated curved ribs geometry.

### 1.3.3 Internal Cooling in Rotating Channels

In order to explain the flow field behavior and, therefore, the heat transfer level into rotor blade cooling channels, the centrifugal forces and the rotational effects (known as Coriolis) must be considered. In this situation the three components of the Navier-Stokes can be written as follows:

- $x$  component

$$U \frac{\partial U}{\partial x} + V \frac{\partial U}{\partial y} + W \frac{\partial U}{\partial z} = \nu \nabla^2 U - \frac{1}{\rho} \frac{\partial p}{\partial x} - 2\Omega V \quad (1.3)$$

- $y$  component

$$U \frac{\partial V}{\partial x} + V \frac{\partial V}{\partial y} + W \frac{\partial V}{\partial z} = \nu \nabla^2 V - \frac{1}{\rho} \frac{\partial p}{\partial y} + 2\Omega U \quad (1.4)$$

- $z$  component

$$U \frac{\partial W}{\partial x} + V \frac{\partial W}{\partial y} + W \frac{\partial W}{\partial z} = \nu \nabla^2 W - \frac{1}{\rho} \frac{\partial p}{\partial z} \quad (1.5)$$

It is clear that the Coriolis forces have two effects:

- one in the  $x$ -component (see 1.3);
- one in the  $y$ -component (see 1.4).

The main contributions that analyze the fundamental configuration of a radial channel of rectangular cross-section in orthogonal rotation (i.e. with the rotation axis parallel to the channel height) with outward flow are the ones studied by Hart [37], Lezius and Johnston [46], Speziale [64] and Speziale and Thangam [63]. The stream-wise velocity distribution on the channel cross-section should present two characteristic features:

- a local maxima located at about the mid channel height and displaced towards the channel trailing side;
- the highest velocity peaks should be found in the flow layers near the top and the bottom walls (with respect to the rotation axis ( $z$ )).

Respectively, there are two causes of this behavior:

- the mass flow displacement towards the trailing side that takes place in the bulk flow because of the combined effect of a pressure gradient and Coriolis forces. Indeed, a pressure gradient aligned along  $y$  direction and pointing towards the channel trailing side is induced by the  $y$  component (see 1.4) of the Coriolis forces that acts on the bulk flow, namely force per unit mass ([37], [46], [64] and [63]). This pressure gradient is not balanced by the Coriolis forces inside the slower boundary layers and, consequently, the near wall flow is forced to move towards the lower pressure region, i.e. towards the channel leading side generating the extensively explained in literature Coriolis double vortex.
- the effect of the  $x$  component of the Coriolis forces  $A_{cx} = 2\Omega V$  (see 1.3) providing the acceleration of the flow layers because of the positive  $V$  velocity, which is way the boundary layer flows on the upper and lower walls are displaced towards the leading side by the rotation-induced secondary structures.

Moreover, Bons and Kerrebrock [15] performed the first experimental aero-thermal analysis inside a rotating squared channel which simulate turbine blade cooling passage. Velocity measurements were taken using Particle Image Velocimetry (*PIV*) for both heated and non-heated cases. Under the same conditions, high resolution heat transfer measurements showed a first correlation between flow and heat transfer phenomena. Unlike the static case the results reveal that the rotational effects led to a decrease in the *HTC* levels at the leading side with respect to the stationary case. Conversely, the heat transfer mechanism is enhanced on the trailing side. These effects are produced by Coriolis double vortex previously described. More recently, Coletti et al.[26] showed how the stabilizing/destabilizing effect can have a great impact on the flow field inside a rib-roughened channel, more precisely on the boundary layer tripping and re-attachment induced by the ribs and on the release of coherent structures at the ribs lip. The *PIV* measurements performed in the facility developed by Di Sante et al.[29] demonstrated that for a geometrical configuration in which the rotation has a stabilizing effect on the rib-roughened wall, the reattachment point moves closer to the rib lip than in the static case, otherwise it is further in the destabilizing case.

### 1.3.4 Internal Cooling in Trailing Edge Rotating Channels

Chang et al.[23], Rallabandi et al.[57] and Liu et al.[48] carried out experimental thermal analyses concerning rotating cooling schemes with axial flow discharge, which are thus comparable to modern trailing edge cavities. In the aforementioned works, the thermal field investigations were conducted inside rotating channels of trapezoidal cross-section with flow ejection at the trailing side through holes [23] or slots [57] [48]. Even if these works provide ready-to-use correlations applicable even to models with complex geometries under rotation, it should be noted that the flow patterns hypothesized by the researches to justify heat transfer performances derived from the previous studies ([37], [46], [64], [63] and [15]) about simpler geometries such as rectangular or squared channels. Indeed, no experimental or numerical results were available/used in order to

have a thorough understanding of the flow structures which explains the features of the heat transfer distribution. The main geometrical features of the cooling schemes studied in the present thesis have a trapezoidal cross-section single radial passage with flow exit at both blade tip and trailing side (for further details see Sec. 3.1). A first flow field analysis of the smooth geometry ( $G0$ ) in static and rotating conditions was performed by Armellini et al.[5] by means of *PIV* and *STEREO-PIV* measurements. On the same smooth geometry Andrei et al.[3] carried out an analysis of the thermal field in static and orthogonally rotating conditions. Finally, Mucignat et al.[56] and Bonanni et al.[14] performed experimental investigation of the combined effect of ribs and rotation inside a rib-roughened trailing edge channel ( $G1$ ), respectively for the flow and thermal field.

### 1.3.5 Internal Cooling in Leading Edge Rotating Channels

With specific regard to leading edge internal cooling, i.e. ducts with triangular shaped cross-section, a number of works are already available in the open literature about the experimental investigations of the effects of rotation on the thermal field. The most recent and noteworthy results are represented by the works by Liu et al.[50], Liu et al.[49] and Huang and Liu [39], who analyzed the heat transfer inside the same equilateral triangular channel with smooth and rib-roughened walls at both static and rotating conditions. The authors tested several channel configurations by changing the ribs's angle of attack, by comparing the performances obtained with continuous and V-shaped ribs and, finally, by changing the duct orientation with respect to the rotation axis. Experimental thermal data were provided over a wide range of  $Re$  and  $Ro$  and by considering also the effect of varying the buoyancy parameter  $Bo$  ( $Re = 10000 - 40000$ ,  $Ro = 0 - 0.65$ ,  $Bo = 0 - 2.3$ ). The results were used to provide useful and ready-to-use correlations applicable to this kind of channel under rotation. On the other hand, the flow models that were used to justify the thermal fields analysis were unfortunately rather simplified and were not supported by dedicated experiments. A picture of the flow model suggested at first by Liu et al.[50] is illustrated in Fig. 1.10. Rotational effects were assumed to sustain a secondary flow structure composed of two counter-rotating vortices of different dimensions, a big one close to the top side, and a smaller one close to the lower apex. The rotation-induced vortices drive flow from the leading side to the trailing one at about mid-channel height, the opposite flow deflection is found close to the top wall and the lower apex. The sketch reported in Fig. 1.10, suggest the existence of a sort of symmetrical behavior with respect to the plane of rotation, namely the main direction of the secondary flows is perpendicular to the rotation axis and flow separation/reattachment points should be found on leading/trailing sides, respectively. Moreover, if the duct orientation changes the model suggested by Huang and Liu [39] is illustrated in Fig. 1.11 which is a direct transposition of the Liu et al.[50] simplified model (see 1.10).

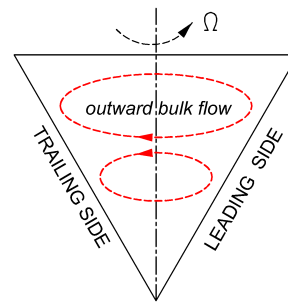


FIGURE 1.10 – Secondary flow model proposed by Liu et al.[50].

This kind of flow model is basically a direct transposition of the experimental and numerical results obtained by Hart [37], Lezius and Johnston [46], Speziale [64], Speziale and Thangam [63] and Bons and Kerrebrock [15] (explained in Subsec. 1.3.3)

Unfortunately, when the channel geometries or the duct orientations are different from the basic ones (e.g. rectangular or square channels in orthogonal rotation), few studies are available. The work by Dutta et al. [31] is, to the author's knowledge, the only examples available in literature referring to cooling schemes resembling modern leading edge cavities where the  $k-\epsilon$  high  $Re$  turbulence model were used in order to support their experimental heat transfer analysis. The *CFD* predictions show secondary flow structures induced by rotation whose main features are similar to the ones illustrated in Fig. 1.10. Unfortunately, no experimental validation were provided and only small rotation numbers were considered. Moreover, the exploited numerical tool could have been affected by from computational limitations experienced at that time.

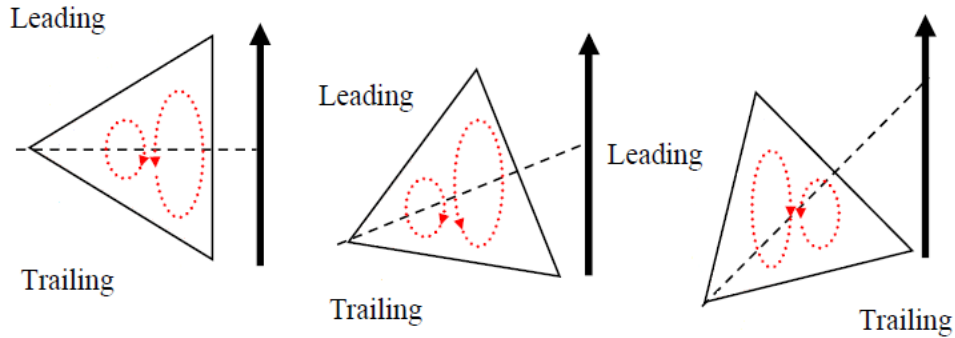


FIGURE 1.11 – Secondary flow model suggested by Huang and Liu et al. [39].

## 1.4 Objectives of Present Study

The present work addresses aspects on the suitability of *CFD* for the prediction of the aero-thermal performance inside cooling channel designed for two portions of the blade (namely *trailing edge* and *leading edge*) in static and rotating conditions and varying the channel orientation. The thesis is structured according to the following outline. After a first introduction on the mathematical and numerical background of the *CFD* code (Ch.2), an assessment of the capabilities of *SST* turbulence model developed on ANSYS CFX®v14.0 was carried out in a cooling channel for the trailing edge of high-lift stator blades (Ch.3). This was performed comparing the aero-thermal experimental results available in literature ([7], [5], [56]) to the numerical prediction for three different configurations, i.e *G0* (see Sec. 3.3), *G1* (see Sec. 3.4) and *G2* (see Sec. 3.5). Moreover, for one

configuration, namely *G1*, in order to fix all the computational failed predictions in the rib-roughened surface of the trailing edge cooling channel, four more turbulence models were tested (see Subsec. 3.4.4). Chapter 4, extends the evaluation of the capabilities of the *SST* turbulence model in rotating condition for configurations *G0* (see Subsec. 4.2.2) and *G1* (see Sec. 4.3.2) thanks to the experimental data set ([5], [3], [56] and [14]). Subsequently, the *CFD* code were exploited to investigate engine-like conditions, i.e increasing the rotation number to  $Ro = 0.46$  (see Subsec. 4.2.3 for *G0* configuration and 4.3.3 for *G1* configuration) and different channel orientations with respect to the rotation axis ( $\gamma = 22.5, 45[^\circ]$  see Subsec. 4.2.4 for *G0* configuration and 4.3.4 for *G1* configuration). Chapter 5 sets out a detailed analysis of the flow features found in a triangular cross-section duct resembling cooling channel for the leading edge of high lift rotor blade. The task is pursued by closely combining numerical and experimental analyses. Experimental measurements are used to validate numerical *Reynolds-Averaged Navier-Stokes Equations (RANS)* simulations which are useful to get an easier and faster analysis of the 3-D flow structure and extend the study to a wider range of test conditions (i.e. varying  $Ro$   $Re$  and  $\gamma$  channel orientation).

However, each chapter contain an overview of each configuration, information on computational details, assessments on the numerical accuracy and comparisons of experimental and numerical results as previously explained. The conclusion provides a summary of the main findings and recommendations for future research.



---

# 2

## Mathematical and Numerical Background

In the present chapter a short description of the Computational Fluid Dynamic (*CFD*) theory will be provided. In particular: Sec. 2.1 explains the governing equation for fluid flow and heat transfer, Sec. 2.2 pinpoints the numerical methods used to solve these equations and finally Sec. 2.3 gets an insight into the theoretical background of turbulence models used in this work.

### 2.1 Governing Equations

The motion of a fluid is governed by a set of fundamental mathematical principles: mass, momentum and energy conservation. In this section the conservation equations are summarized in steady-state form for an incompressible fluid with constant properties. It should be noted that the tensor notation used is:

$$U_i \equiv U, U_j \equiv V, U_k \equiv W \Rightarrow i \equiv x, j \equiv y, k \equiv z. \quad (2.1)$$

The mass conservation or continuity equation is:

$$\nabla(\hat{U}) = 0, \quad (2.2)$$

where  $\hat{U}$  is the instantaneous velocity vector. The momentum conservation, also known as Navier-Stokes equations, is:

$$\rho \nabla(\hat{U}) = -\nabla \hat{p} + \mu \nabla^2 \hat{U} \quad (2.3)$$

Finally the conservation energy can be described using a generic conservation equation:

$$\hat{U} \nabla(\Xi) = \nabla(\Phi_{\Xi} \nabla(\Xi)) + q_{\Xi} \quad (2.4)$$

where  $\Xi$  is the general variable (e.g. temperature),  $\Phi_{\Xi}$  is the diffusivity of  $\Xi$  (thermal diffusivity for the conservation of energy) and  $q_{\Xi}$  represents sources or sinks for the scalar.

## 2.2 Numerical Methods

Numerical methods are used to approximate the set of strongly coupled non-linear partial differential equations by a system of algebraic equations.

### 2.2.1 Discretization

The first step is the application of a discretization method. In fluid dynamics, this is done in a number of cases by employing the method in which an integral form of the conservation equations is used as starting point (**Finite Volume Method (FV)**). The discretization subdivides the computational domain into a finite number of small control volumes (**CV**). The conservation equations are then integrated over each **CV**. The resulting algebraic equations typically contain surface fluxes that require approximations. All variable values are to be calculated at a computational node located in the centroid of each **CV**. As a consequence, values at the **CV** surfaces need to be expressed in terms of nodal values as well. Therefore, the **FV** method includes the application of interpolation, integration and differentiation methods. The result is an algebraic equation for each **CV**, which correlates the values at its center with the values of several neighboring **CVs**. The overall solution thus consists of a number of discrete solutions at discrete locations. One significant advantage of the **FV** method is that it is conservative by definition, which means that the solution satisfies the quantity conservation (mass, momentum, energy, etc.) for each individual cell as well as for the whole solution domain. The main disadvantage of the **CV** method is that the methods of higher order than second are difficult and complex to develop. More itemized descriptions can be found in [33], [24] and [2].

The **CFD** code used in the present thesis, namely ANSYS CFX  $\text{\textcircled{R}}$ v14.0, used node-centered discretization, which means that the nodals location is defined by the **CV** constructed around them. Hence, at the boundaries domain, there are half of the **CVs** whose nodes are located directly on the boundaries.

### 2.2.2 Grid

The discrete locations at which the variables are to be calculated are defined by the numerical grid which is a discrete representation of the geometric domain on which the problem is to be solved. It divides the solution domain into a finite number of sub-domains. In the present investigation, the types of grids used for the fluid domains are block-structured grids with hexahedral elements. In a block structured grid, there is a two (or more)-levels subdivision of the solution domain. On the coarse level, there are blocks which are relatively large segments of the domain: their structure may be irregular and they may or may not overlap. On the fine level (within each block) a structured grid is defined. This kind of grid is very flexible, which is why it allows finer grids to be used in the regions where higher resolution is required.

The assessment of the quality of a grid is a substantial part in controlling the overall error introduced by the discretization process. In order to evaluate the grids quality, the following parameters were used: orthogonality  $\delta_{min}$ , cell expansion rate and cell

aspect ratio  $L_{max}$ . The orthogonality describes the degree to which the angles between adjacent elements faces depart from an ideal value, which would be  $90^\circ$  in the case of hexahedral elements. This error can be expressed by the minimum face angle  $\delta_{min}$  of the grid. The cell expansion rate describes the rate of change in the magnitude of adjacent elements and in the present work it always refers to the direction normal to the wall. The parameter can be considered a measure for discontinuities in the grid. The cell aspect ratio  $L_{max}$  represents a measure for the degree to which the grid elements are stretched. It is defined as the ratio of maximum to minimum element surface area. Empirical values for the quality measures are minimum face angles  $\delta_{min} > 10^\circ$ , expansion rate smaller than 2.5 and aspect ratio  $L_{max} < 10^3$  [4].

### 2.2.3 Calculation of Surface Fluxes

The system of algebraic equations resulting from the discretization process for a particular  $CV$  involves fluxes of the conserved variables through the  $CV$  boundaries. Thus, on the  $CV$  surfaces, the variable value and its gradient are needed. In order to express the latter in terms of nodal ( $CV$  center) values, where the data are stored, an interpolation is used. The interpolation schemes employed in the present investigation are briefly explained for an arbitrary variable  $\Xi$ . An illustration of a 2-D  $CV$  with its boundaries is shown in Fig. 2.1.

#### Upwind Differencing

The idea behind the first-order *upwind scheme* (**Upwind Differencing Scheme (UDS)**) is to have physical reliability for convective flows simply by keeping the face value between two cells be equal to the value for the nearest upstream cell:

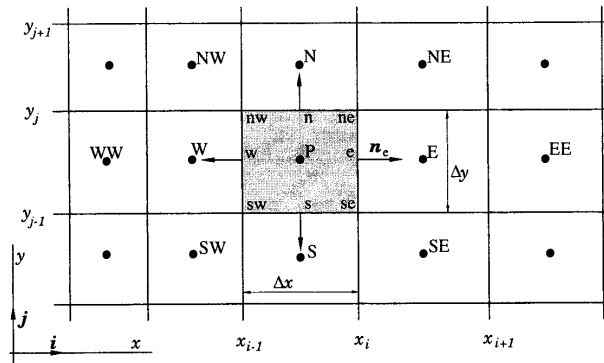


FIGURE 2.1 – Illustrative example of a  $CV$  in 2-D Cartesian Grid [33].

$$\Xi_e \begin{cases} \Xi_P, & \text{for flow from } P \text{ to } E \\ \Xi_E, & \text{for flow from } E \text{ to } P \end{cases} \quad (2.5)$$

This scheme is considered very robust and numerically stable, in fact peaks and fluctuations in the variables are typically smoothed out. However, the scheme is known to be susceptible to numerical diffusion [33] and, therefore, it overestimates the transport of entities in the flow direction. Since the rate of error reduction is only a first order as well, very fine grids are required to obtain accurate solutions. In order to improve accuracy the second-order *UDS* scheme was developed, which predicts the face values using information from two *UDS* cells.

In order to provide an estimation of the eastern-face value, the scheme assumes that the gradient between the considered cell and the eastern face is the same as the one between the western cell and the considered cell. In mathematical terms:

$$\frac{\Xi_e - \Xi_P}{x_e - x_p} = \frac{\Xi_P - \Xi_W}{x_P - x_W} \rightarrow \Xi_e = \frac{(\Xi_P - \Xi_W)(x_e - x_P)}{x_P - x_W} + \Xi_P \quad (2.6)$$

For equidistant grid, 2.6 gives that:

$$\Xi_e = 1.5\Xi_P - 0.5\Xi_W \quad (2.7)$$

### Central Differencing or Linear Interpolation

The *central difference scheme* (**Central Differencing Scheme (CDS)**) is based on the assumption of a linear variation of the dependent variable in the *FV*. Hence, the variable value at the eastern cell face,  $\Xi_e$  can be obtained by a linear interpolation between the two neighboring nodes, P and E. This yields for the approximation of the convective fluxes.

$$\Xi_e = \Xi_E \lambda + \Xi_P (1 - \lambda) \quad (2.8)$$

where the linear interpolation factor  $\lambda$  is defined as:

$$\lambda = \frac{x_e - x_P}{x_E - x_P} \quad (2.9)$$

The assumption of a linear profile between the P and the E nodes also offers the simplest approximation of the gradient, which is needed for the evaluation of diffusive fluxes:

$$\left( \frac{\partial \Xi}{\partial x} \right)_e \approx \frac{\Xi_E - \Xi_P}{x_E - x_P} \quad (2.10)$$

The *CDS* is a second-order scheme because of the linear interpolation. The advantages of second-order schemes are increased accuracy and faster convergence on sufficiently fine grids. However, second-order schemes may tend to produce oscillations in regions of steep gradients.

### Blended Differencing

The combination of the interpolation schemes previously described is possible by using a blending function  $\iota$ , which usually has the form:

$$\Xi_{blend} = \Xi_{FO} + \iota(\Xi_{SO} - \Xi_{FO}) \quad (2.11)$$

where:

- $\Xi_{FO}$  is the variable  $\Xi$  obtained by a first-order scheme;
- $\Xi_{SO}$  is approximated value of the variable  $\Xi$  resulting by a second-order method.

The blending function allows the combination of first- and second-order difference schemes and, hence, the choice between the robustness of the first-order and the increased accuracy of the second-order scheme. As can be seen from Eq.2.11, a value of  $\iota = 0$  leads to a first-order approximation, while a value of  $\iota = 1$  results in a second-order method.

In Ansys CFX  $\text{\textcircled{R}}$ v14.0, the so-called *high resolution scheme* automatically computes the value of  $\iota$  locally in an attempt to achieve boundedness of the solution. Therefore,  $\iota$  is reduced to a value lower than one obtained in presence of steep gradients. In the present work, all results are computed with the high resolution scheme. An example of the behavior of this scheme can be found in Apx.B.

### 2.2.4 Solution Algorithm

Discretization yields a large system of non-linear algebraic equations which were solved. The method of solution depends on the problem. Regarding the solution strategy used in this investigation a steady-state flow assumption was employed solving flow problems by means of a pseudo-time marching or an equivalent iteration scheme. Since the equations were non-linear, an iteration scheme was used to solve them. These methods use successive linearization of the equations and the resulting linear systems were almost always solved by iteration techniques. In particular ANSYS CFX  $\text{\textcircled{R}}$ v14.0 uses a fully implicit coupled solver that computes the equations for velocity and pressure as a single system. Moreover, the code applies an automatic (or manual) under-relaxation to the equations in the form of a pseudo time-step. Knowing these characteristics is important since it can significantly affect convergence.

### 2.2.5 Accuracy of the Numerical Solutions

Numerical solutions of fluid flow and heat transfer problems are only approximate solutions and should never be considered exact. Indeed they are always subject to systematic errors which can be classified into three different categories:

1. Iteration errors: they are defined as the difference between the iterative and exact solutions of the algebraic equations system and they are often referred as to *convergence errors*. Such errors can be controlled by ensuring sufficient convergence criteria, i.e. a tiny error reduction in the iterative solution method. In the present study, low iteration errors were obtained by a drop in the equation residuals of between 3 and 4 orders of magnitude for each equation solved.

2. Discretization errors: they are defined as the difference between the exact solution of the conservation equations and the exact solution of the discretized equation system. Theoretically, the discretization converges towards the analytical solution if the grid spacing tends to zero. Thus, the grid resolution mainly determines the error magnitude, which implies that small discretization errors can only be obtained using very high grid resolutions. It should be pointed out that very tiny elements can not usually be obtained because of the limited computer resources, hence the discretization errors have to be accepted with a reasonable grid resolution. In the present work, for the trailing edge geometries (see Subsections 3.3.1 3.4.1 3.5.1 and Sec. 4.1) a systematic method is adopted to estimate the local distribution of the discretization error, i.e the *GCI* analysis (see Apx.C for more details). Conversely, for the leading edge geometry, only a mere comparison of the results of three different grids with different spatial resolutions is carried out.
3. Modelling errors: they are defined as the difference between the actual flow and the exact solution of the mathematical model. They depend on the assumptions made in deriving the transport equations for the variables. In turbulent flows the modelling errors may be major and, hence, the exact solution of the model equations may be qualitatively wrong as a result of the wrong choice of the turbulence model. Moreover, modelling errors are also introduced by simplifying the geometry of the solution domain or by simplifying boundary conditions. These errors are not known a priori but they can be evaluated only by comparing the numerical solutions with accurate data in which the modelling, discretization and convergence errors are negligible. In fact, in this thesis, the detailed experimental data available in literature ([5], [56] for the flow field and [3], [14] and [7] for the heat transfer) will be used as a benchmark to assess the *CFD* results. The uncertainty of the experiments is presented in Apx.A

## 2.3 Turbulence Modelling

The set of conservation equations introduced above is a valid theoretical description of most types of flows including their turbulent characteristics. However, very fine meshes are necessary to solve correctly these equations even by solving the tiny eddies and, therefore, their energy dissipation. It should be recalled that the number of grid nodes  $N$  required to achieve this purpose is a function of the mean flow *Re* number, i.e.  $N = Re^{\frac{1}{4}}$ . Since engineering problems are typically associated with high *Re* number flows, approximations were developed in order to model the effects of turbulence without completely solving them.

### 2.3.1 Reynolds-Averaged Navier-Stokes (RANS) Equations

In a statistically steady flow, a general instantaneous variable  $\widehat{\phi}(X, t)$  can be written as the sum of a time-averaged value ( $\overline{\phi(X)}$ ) and a fluctuation ( $\phi(X, t)'$ ) of that value:

$$\widehat{\phi}(X, t) = \overline{\phi(X)} + \phi(X, t)' \quad (2.12)$$

This variable decomposition was first introduced by Osborne Reynolds and, therefore, is known as *Reynolds averaging*. The average value in Eq.2.12 is defined as:

$$\overline{\phi(X)} = \lim_{\tau \rightarrow \infty} \frac{1}{\tau} \int_0^\tau \widehat{\phi}(X, t) dt \quad (2.13)$$

where the time interval  $\tau$  must be larger than the time scale of the fluctuations. If  $\tau$  is large enough,  $\overline{\phi(X)}$  does not depend on the time at which the averaging is started. It should be observed that for an unsteady flow, Eq.2.13 is not valid and it must be replaced by ensemble averaging. Since the flows in the present work are statistically steady, this concept will not be discussed. Figure 2.2 shows the *Re* averaging for the velocity distribution in a statistically steady turbulent flow.

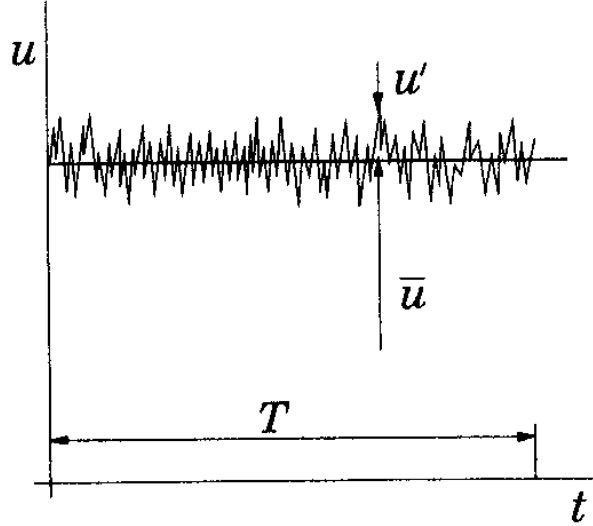


FIGURE 2.2 – Time averaging for a statistically steady flow.

Application of the *Re* averaging, i.e. decomposition and time-averaging, to the instantaneous Navier-Stokes equations (Eq.2.3) yields:

$$U_j \frac{\partial U_i}{\partial x_j} = \frac{\partial}{\partial x_j} (\nu \frac{\partial U_i}{\partial x_j} - \overline{u_i u_j}) - \frac{1}{\rho} \frac{\partial p}{\partial x_i} \quad (2.14)$$

The resulting equations are known as *RANS*. The time-averaged equation for a conserved scalar  $\Xi$  therefore becomes:

$$U_j \frac{\partial \Xi}{\partial x_j} = \frac{\partial}{\partial x_j} (\Phi_\Xi \frac{\partial \Xi}{\partial x_j} - \overline{u_j \psi}) \quad (2.15)$$

The averaging process introduces some new unknown variables as a results of the non-linearity of the convective terms in the non-averaged equations, i.e:

- $u_i u_j$  (*Reynolds stresses*) in the *RANS* equations;
- $u_j \psi$  (*Turbulent scalar flux*) in the equation for the scalar transport.

From the physical viewpoint, they represent the rate at which momentum and the scalar quantities are transported through the flow by the action of the turbulent fluctuations. Finally, the presence of the *Reynolds stresses* and *Turbulent scalar fluxes* in the conservation equations means that the latter are not closed, in fact they contain more variables than the number of equations. Closure requires the use of some approximations, which usually take the form of prescribing the *Reynolds stress tensor* and *turbulent scalar fluxes* in terms of mean quantities. It is possible to derive equations for the higher order correlations e.g., for the *Reynolds stress tensor*, but these contain even more (and higher-order) unknown correlations requiring modelling approximations. These equations will be introduced in the next subsection (see Subsec. 2.3.2) but the important point is that it is impossible to derive a close set of exact equations. The approximations introduced are called *turbulence models* in engineering or parametrization in the Geo-sciences.

### 2.3.2 Turbulence Models

In order to close the equations mentioned above, a turbulence model - for example in the form of a set of differential equations or algebraic formulas - must be introduced for the unknown *Reynolds stresses*. One possible approach is to assume that the effects of turbulence can be represented as an increased viscosity. This assumption is derived from an analogy with laminar flows in which energy dissipation and transport of mass, momentum and energy normal to the streamlines are mediated by viscosity, which leads to the *eddy-viscosity models* used for the *Reynolds stresses*. Another approach is the construction of differential transport equations for the Reynolds stress tensor which can be solved in the same way as the Navier-Stokes equations. Such models are known as *Reynolds stress models*(RMS) or *second order closures*. A brief description of the turbulence model used in this thesis is given hereinafter. It should be pointed out that it is not clear which model is best for which kind of flow (none is expected to be good for all flows), partly because in many attempts to answer this question, numerical errors were too significant to allow a clear conclusion to be drawn [18].

#### The Eddy Hypothesis

The eddy-viscosity concept is based on Boussinesq postulate [16] [61] in which the momentum transfer caused by turbulent eddies can be modelled with an eddy viscosity. This is in analogy with how the momentum transfer caused by the molecular motion in a gas can be described by a molecular viscosity. Boussinesq assumption states that the *Reynolds stresses*,  $u_i u_j$ , is proportional to the traceless mean strain rate tensor  $S_{ij}$  and can be written in the following way:

$$-\overline{u_i u_j} = 2\nu_t S_{ij} - \frac{2}{3} \delta_{ij} \kappa \quad (2.16)$$

The mean strain rate tensor ( $S_{ij}$ ) is defined below:

$$S_{ij} = \frac{1}{2} \left( \frac{\partial U_i}{\partial x_j} + \frac{\partial U_j}{\partial x_i} \right) \quad (2.17)$$

hence the *Reynolds stresses*:

$$-\overline{u_i u_j} = \nu_t \left( \frac{\partial U_i}{\partial x_j} + \frac{\partial U_j}{\partial x_i} \right) - \frac{2}{3} \delta_{ij} \kappa \quad (2.18)$$

Equation 2.18 provides a definition of the eddy-viscosity ( $\nu_t$ ), which is the ratio of the *Reynolds stresses* and the mean strain rate tensor. It should be observed that  $\nu_t$  is not a function of the fluid but a function of the flow. It therefore depends on the local level of the turbulence activity and, hence, it varies from point to point. The dimensional analysis shows that the turbulent viscosity is proportional to the velocity and length scales of the large scale turbulent motions.

$$\nu_t = C_\mu \times (\text{velocity scale}) \times (\text{length scale}) \quad (2.19)$$

where  $C_\mu$  is a dimensionless constant.

Similarly to the eddy-viscosity hypothesis, the eddy-diffusivity hypothesis states that the Reynolds fluxes of a scalar are linearly related to the mean scalar gradient:

$$-\overline{u_i \psi} = \Gamma_t \frac{\partial \Xi}{\partial x_i} \quad (2.20)$$

The eddy-diffusivity  $\Gamma_t$  is related to the eddy-viscosity  $\nu_t$  by  $\sigma_t$ :

$$\Gamma_t = \frac{\nu_t}{\sigma_t} \quad (2.21)$$

The equation above can be solved only if the turbulent viscosity ( $\nu_t$ ) is known by Eq.2.19. Hence, its evaluation is essential to compute the *Reynolds stresses* and the *turbulent scalar fluxes*, respectively.

### Two-Equation Turbulence Models

Two-equation turbulence models are very widely used since they offer a good compromise between numerical effort and computational accuracy. Both velocity and length scale are solved using two different transport equations (whence the term *two-equations turbulence models*.) in order to determine the eddy-viscosity according to Eq.2.19. In almost all *two-equation turbulence models* the velocity scale is computed from the turbulence kinetic energy  $\kappa$  as follows:

$$\kappa = \frac{1}{2} \overline{u_i u_i} \quad (2.22)$$

Conversely, the turbulence length scale is estimated from two properties of the turbulence field, namely the turbulence kinetic energy and its dissipation rate. The turbulence

kinetic energy  $\kappa$  can be derived from the Navier-Stokes equations by using an exact equation:

$$\underbrace{U_j \frac{\partial \kappa}{\partial x_j}}_I = \underbrace{\frac{\partial}{\partial x_j} \left( \nu \frac{\partial \kappa}{\partial x_j} \right)}_{II} - \underbrace{\frac{\partial}{\partial x_j} \left( \frac{1}{2} \overline{u_j u_i u_i} + \overline{p u_j} \right)}_{III} - \underbrace{\overline{u_i u_j} \frac{\partial U_i}{\partial x_j}}_{P_k} - \underbrace{\nu \frac{\partial \overline{u_i \partial u_i}}{\partial x_j \partial x_j}}_{\epsilon} \quad (2.23)$$

For further details about the derivation of this equation see [71]. Terms I in Eq.2.23 need no modelling because they contain no additional unknowns.

The first and second term on the right-hand side (II-III) of Eq.2.23 represent *turbulent diffusion* of kinetic energy, which is actually transport of velocity fluctuations by the fluctuations themselves. This term is modelled using a gradient-diffusion assumption, which relates the diffusion of  $\kappa$  to its spatial gradient:

$$\nu \frac{\partial \kappa}{\partial x_i} - \left( \frac{1}{2} \overline{u_j u_i u_i} + \overline{p u_j} \right) \approx \frac{v_t}{\sigma_t} \frac{\partial \kappa}{\partial x_j} \quad (2.24)$$

where  $v_t$  is the eddy viscosity defined above and  $\sigma_t$  is a *turbulent Prandtl number* whose value is approximately one.

The third term in Eq.2.23 ( $P_k$ ) represents the *production term*. It describes the rate of production of turbulence kinetic energy by the mean flow and therefore represents the transfer of kinetic energy into the turbulent motions. This term can be modelled by using the eddy-viscosity assumption to describe the Reynolds stresses (see Eq.2.18) hence:

$$\overline{u_i u_j} \frac{\partial U_i}{\partial x_j} \approx v_t \left( \frac{\partial U_i}{\partial x_j} \frac{\partial U_j}{\partial x_i} \right) \frac{\partial U_i}{\partial x_j} \quad (2.25)$$

Finally, the last term on the right hand side of Eq.2.23 is the *dissipation term* representing the rate of  $\epsilon$  at which turbulence kinetic energy is irreversibly converted into internal energy. The choice to evaluate this term is not obvious and a number of equations have been developed for this purpose. The most popular one is based on the observation that the dissipation is needed in the energy equation and in so-called equilibrium turbulent flows, i.e., the ones in which the rates of production and destruction of turbulence are in near-balance. Therefore, the dissipation ( $\epsilon$ ),  $\kappa$  and the length scale  $L$  are related by:

$$\epsilon \approx \frac{\kappa^{\frac{3}{2}}}{L} \quad (2.26)$$

This idea is based on the fact, that at high Reynolds numbers, there is a cascade of energy from the largest scales to the smallest ones and that the energy transferred to the small scales is dissipated.

### k- $\epsilon$ Turbulence Model

One of the most prominent turbulence models, the  $k - \epsilon$  model developed by Jones and Launder [41], has been implemented in most general purpose *CFD* codes and is considered the industry standard model. Two separate transports equations for the

turbulence kinetic energy  $\kappa$  and the dissipation rate  $\epsilon$  are needed respectively, in order to evaluate the eddy-viscosity. Therefore, Eq. 2.19 becomes:

$$v_t = C_\mu \frac{\kappa^2}{\epsilon} \quad (2.27)$$

The exact Eq.2.19 is modelled according to the procedure described above. Hence, Eq.2.23 can be summarized as:

$$U_j \frac{\partial \kappa}{\partial x_j} = \frac{\partial}{\partial x_j} \left( \frac{v_t}{\sigma_\epsilon} \frac{\partial \kappa}{\partial x_j} \right) + P_k - \epsilon \quad (2.28)$$

$$U_j \frac{\partial \epsilon}{\partial x_j} = \frac{\partial}{\partial x_j} \left( \frac{v_t}{\sigma_\epsilon} \frac{\partial \epsilon}{\partial x_j} \right) + C_{\epsilon 1} \frac{\epsilon}{\kappa} - C_{\epsilon 2} \frac{\epsilon^2}{\kappa} \quad (2.29)$$

It should be pointed out that the production rate  $P_k$  in the equations above is given by:

$$P_k = v_t \frac{\partial U_i}{\partial x_j} \left( \frac{\partial U_i}{\partial x_j} + \frac{\partial U_j}{\partial x_i} \right). \quad (2.30)$$

$C_\mu$  in Eq.2.27 and  $C_{\epsilon 1}$ ,  $C_{\epsilon 2}$  and  $\sigma_\epsilon$  in Eqs. 2.28, 2.29 are empirical constant:

$$C_\mu = 0.09; C_{\epsilon 1} = 1.44; C_{\epsilon 2} = 1.92; \sigma_\kappa = 1; \sigma_\epsilon = 1.3. \quad (2.31)$$

As mentioned above, the  $k - \epsilon$  model is the most widely used model in engineering computations on account of its rather simple structure which allows an easy implementation. Moreover, it provides good predictions for many flows of engineering interest but there are applications for which the  $k - \epsilon$  model may not be suitable:

- flows with boundary layer separation;
- flows with sudden changes in the mean strain rate;
- flows in rotating fluids;
- flows over curved surfaces.

Moreover, it would typically require a near-wall resolution of  $y_{max}^+ < 0.2$  because it does not involve the complex nonlinear damping functions, while the other *RANS* model would require at least  $y_{max}^+ < 2$  [4].

### k- $\omega$ Turbulence Model

The k- $\omega$  model developed by Wilcox[70] solves two transport equations, one for the turbulence kinetic energy ( $\kappa$ ) and one for the turbulent frequency  $\omega$ .

$$\omega = \frac{\epsilon}{\beta \kappa} \quad (2.32)$$

Hence, the turbulence viscosity is related to the turbulence kinetic energy and turbulent frequency via the relation:

$$v_t = \frac{\kappa}{\omega} \quad (2.33)$$

The complete set of equations for the k- $\omega$  model can be given as follow:  
k-equation:

$$U_j \frac{\partial \kappa}{\partial x_j} = -\overline{u_i u_j} \frac{\partial U_i}{\partial x_j} - \beta^* \kappa \omega + \frac{\partial}{\partial x_j} \left[ (\nu + \sigma^* v_t) \frac{\partial \kappa}{\partial x_j} \right] \quad (2.34)$$

$\omega$ -equation:

$$U_j \frac{\partial \omega}{\partial x_j} = \alpha \frac{\omega}{\kappa} \left( -\overline{u_i u_j} \frac{\partial U_i}{\partial x_j} \right) - \beta \omega^2 + \frac{\partial}{\partial x_j} \left[ (\nu + \sigma v_t) \frac{\partial \omega}{\partial x_j} \right] \quad (2.35)$$

The model constants are given by:

$$\alpha = \frac{5}{9}; \beta = 0.075; \beta^* = 0.09; \sigma = 2; \sigma^* = 2. \quad (2.36)$$

A disadvantage of k- $\epsilon$  turbulence model is the excessive generation of turbulence energy,  $P_k$ , in proximity to stagnation points. In order to avoid the build-up of turbulence kinetic energy in stagnation regions, limiters are placed in the computation of the  $\widetilde{P}_k$  in the k- $\omega$  model developed in ANSYS CFX  $\text{\textcircled{R}}$ v14.0. The formulation follows Menter [54] and reads:

$$\widetilde{P}_k = \min(P_k, C_{lim}, \omega, \beta^*, \kappa) \quad (2.37)$$

where  $P_k$  is calculated in the same way as in the k- $\epsilon$  model (see Eq.2.30). The coefficient  $C_{lim}$  is called Clip Factor and has a value of 10 for  $\omega$  based models. This limiter does not affect the shear layer performance of the model but consistently prevented the stagnation point build-up in aerodynamic simulations. Another advantage of the k- $\omega$  model is that it allows more accurate near-wall treatment with an automatic switch from a wall function to a low Reynolds number formulation. The main problem with the Wilcox model is its well-known great sensitivity to free-stream conditions ([54]).

### SST Turbulence Model

*SST* turbulence model developed by Menter [54] uses a blending between the k- $\omega$  model near the surface and the k- $\epsilon$  model in the outer region. It consists of a transformation of the k- $\epsilon$  model into a k- $\omega$  formulation and a subsequent addition of the corresponding equations. The k- $\omega$  model is therefore multiplied by a blending function  $F_1$  and the transformed k- $\epsilon$  by a function  $(1 - F_1)$ . This yields the modified transport equations:

$$U_j \frac{\partial \kappa}{\partial x_j} = -\overline{u_i u_j} \frac{\partial U_i}{\partial x_j} - \beta^* \omega \kappa + \frac{\partial}{\partial x_j} \left[ (\nu + \sigma_t v_t) \frac{\partial \kappa}{\partial x_j} \right] \quad (2.38)$$

$$U_j \frac{\partial \omega}{\partial x_j} = \alpha \frac{\omega}{\kappa} \left( -\overline{u_i u_j} \frac{\partial U_i}{\partial x_j} \right) - \beta \omega^2 + \frac{\partial}{\partial x_j} \left[ (\nu + \sigma v_t) \frac{\partial \omega}{\partial x_j} \right] + 2(1 - F_1) \sigma \frac{1}{\omega} \frac{\partial \kappa}{\partial x_j} \frac{\partial \omega}{\partial x_j} \quad (2.39)$$

the blending functions  $F_1$  are critical to the success of the method. Their formulation is based on the distance from the nearest surface and from the flow variables.

$$F_1 = \tanh(\text{arg}_1^4) \quad (2.40)$$

with:

$$\text{arg}_1 = \min \left[ \max \left( \frac{\sqrt{\kappa}}{\beta^* \omega Y}, \frac{500\nu}{Y^2 \omega} \right), \frac{4\kappa}{CD_{k\omega} Y^2 \sigma_{\omega 2}} \right] \quad (2.41)$$

where  $Y$  is the distance from the nearest wall and:

$$CD_{k\omega} = \max \left( \frac{2\sigma_{\omega 2}}{\omega} \frac{\partial \kappa}{\partial x_j} \frac{\partial \omega}{\partial x_j}, 1.0 \times 10^{-10} \right) \quad (2.42)$$

where:

$$\sigma_{\omega 2} = 0.856 \quad (2.43)$$

$F_1$  is equal to zero far from the surface ( $k$ - $\epsilon$  model) and switches over to one inside the boundary layer ( $k$ - $\omega$  model). The turbulent eddy viscosity is defined as follows:

$$\nu_t = \frac{a_1 \kappa}{\max(a_1 \omega; \Omega F_2)} \quad (2.44)$$

Where  $\Omega$  is the invariant measure of the strain rate and  $F_2$  is a second blending function defined by:

$$F_2 = \tanh(\text{arg}_2^2) \quad (2.45)$$

$$\text{arg}_2 = \max \left( \frac{2\sqrt{\kappa}}{\beta^* \omega Y}, \frac{500\nu}{Y^2 \omega} \right). \quad (2.46)$$

### SST-RM (Reattachment Modification) Turbulence Model

The *SST*-RM model is an innovative version of the *SST* model (beta feature on Ansys CFX  $\text{\textcircled{R}}$ v14.0) w developed by Menter et al.[53] in order to improve the prediction of the reattachment location. In particular, an additional source term in the turbulence kinetic energy transport equation is included:

$$P_{RM} = P_k \cdot \min \left[ 4 \cdot \max \left( 0, \frac{\min(\Omega^2, \hbar^2)}{0.09\omega^2} - 1.6 \right), 1.5 \right] \quad (2.47)$$

### Reynolds Stress Turbulence Models

Eddy-viscosity models have significant deficiencies; some of which are the result of the eddy-viscosity assumption (Eq. 2.18) which may not be valid. A more complex kind of turbulence model is provided by *Reynolds stress turbulence models*, which are not based on Boussinesq's eddy-viscosity hypothesis (i.e.[16]). Indeed, the unknown Reynolds stresses ( $\overline{u_i u_j}$ ) are obtained directly from the solution of differential transport equations for all Reynolds stress tensors and the dissipation rate. By way of example, in 3-D flows,

six equations for the Reynolds stresses and one equation for the dissipation have to be solved. The exact production term and the inherent modelling of stress anisotropies theoretically make Reynolds Stress models more suited to complex flows; however, practice shows that they are often not superior to two-equation models [4]. The Reynolds averaged momentum equations can be derived from the Navier-Stokes equations and for a steady state flow they are:

$$\begin{aligned}
 \underbrace{U_k \frac{\partial}{\partial x_k} (\overline{u_i u_j})}_I &= - \underbrace{\left( \overline{u_i u_k} \frac{\partial U_j}{\partial x_k} + \overline{u_j u_k} \frac{\partial U_i}{\partial x_k} \right)}_{II} - \underbrace{2\nu \overline{\left( \frac{\partial u_i \partial u_j}{\partial x_k \partial x_k} \right)}}_{III} + \underbrace{\frac{p'}{p} \left( \frac{\partial u_i}{\partial x_j} + \frac{\partial u_j}{\partial x_i} \right)}_{IV} - \\
 - \underbrace{\frac{\partial}{\partial x_k} \left[ \overline{u_i u_j u_k} + \frac{\left( p' \overline{u_i \delta_{ij}} + p' \overline{u_i \delta_{ij}} \right) - \nu \frac{\partial}{\partial x_k} (\overline{u_i u_j})}{\rho} \right]}_V &
 \end{aligned} \tag{2.48}$$

- **Term I** is the *convection term* which stands for the rate of change of  $\overline{u_i u_j}$  along a path-line.
- **Term II** is the production rate of Reynolds stresses by means of velocity gradients;
- **Term III** is the *dissipation tensor*. It represents the irreversible conversion of turbulence kinetic energy into internal heat. This term can be modelled under the isotropic assumption, i.e. the turbulent fluctuations are considered to have the same order of magnitude in every direction; hence:

$$\omega_{ij} = \frac{2}{3} \omega \kappa \beta \delta_{ij} \tag{2.49}$$

where  $\omega_{ij}$  is the Reynolds stresses frequency and  $\omega$  is obtained in the same way as in the k- $\omega$  model. This assumption is valid only for high Reynolds numbers.

- **Term IV** is often called the *pressure-strain* and is the production rate of Reynolds stresses because of velocity gradients. From continuity assumption this term is traceless, so it does not contribute directly to the production/dissipation of the kinetic energy. Its effect is redistribution of the energy between the stress components and, therefore, it plays a very important role in determining the degree of anisotropy of the stresses. The modelling process of this term is complex and shall not be discussed here. The interested reader is referred to the methods proposed in [62][44] for comprehensive exposition on the topic.
- **Term V** is the *turbulent diffusion* which stands for the rate of spatial redistribution of the Reynolds stresses by means of turbulent fluctuations, pressure fluctuations and molecular diffusion. Actually only the turbulent fluctuations are considered and modelled using a gradient-transport hypothesis which assumes the diffusion of a quantity is proportional to its spatial gradient as:

$$\overline{u_i u_j u_k} \approx C_s \frac{1}{\beta \omega} \overline{u_k u_l} \frac{\partial \overline{u_i u_j}}{\partial x_l} \tag{2.50}$$

where  $C_s$  is an empirical constant and viscous and pressure diffusion are neglected.

### 2.3.3 Modelling Flow Near the Wall

The *wall-function approach* in Ansys CFX  $\text{\textcircled{R}}$ v14.0 is an extension of the method devised by Launder and Spalding[45]. Figure 2.3 shows the velocity distribution of a viscous flow near the wall.

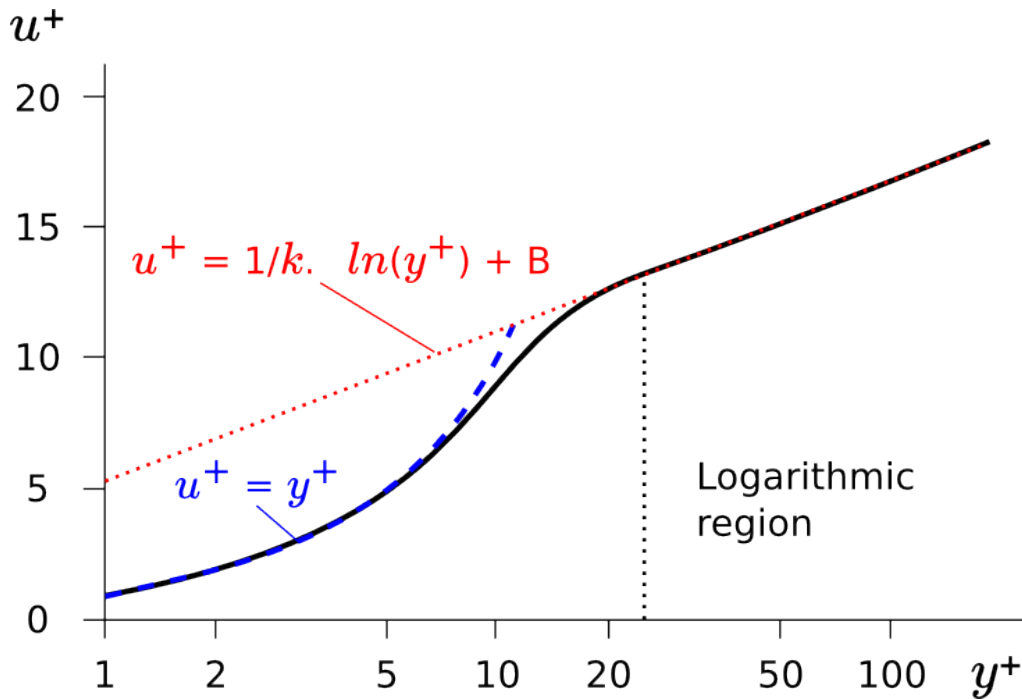


FIGURE 2.3 – Velocity profile in the near-wall region.

In the near-wall region, the tangential velocity is related to the wall-shear-stress ( $\tau_w$ ) by means of a logarithmic relation. In the wall-function approach, the viscosity affecting the sublayer region is bridged employing empirical formulas in order to provide near-wall boundary conditions for the mean flow and turbulence transport equations. These formulas connect the wall conditions (for example, the wall-shear-stress) to the dependent variables at the near-wall mesh node which is assumed to be lying in the fully-turbulent region of the boundary layer. The logarithmic relation for the near-wall velocity is given by:

$$u^+ = \frac{U_t}{u_\tau} = \frac{1}{\nu\kappa} \ln(y^+) + C \quad (2.51)$$

where:

$$u^+ = \frac{\rho \Delta y u_\tau}{\mu} \quad (2.52)$$

$$u_\tau = \sqrt{\frac{\tau_\omega}{\rho}} \quad (2.53)$$

$u^+$  is the near-wall velocity,  $u_\tau$  is the friction velocity,  $U_t$  is the known velocity tangent to the wall at a distance of  $\Delta y$  from the wall,  $y^+$  is the dimensionless distance from the wall,  $\tau_\omega$  is the wall shear stress,  $\nu\kappa$  is the von Karman constant and C is a log-layer constant depending on wall roughness (natural logarithms are used  $\approx 5.1$ ).

The most general approach is the *low-Reynolds-number-method* which considers the effects in the boundary layer, where the turbulent Reynolds number is low near the wall. In this method a very fine resolution grid is required in order to fully resolve the viscous sub-layer. Very small mesh sizes in the direction normal to the wall with approximately 15 nodes located inside the viscous sub-layer and typical size of  $y_{max}^+ < 2$  for the first node must be used. Although this method is associated with higher computational effort, the results are usually of higher quality in particular for complex 3-d flow problems where heat transfer should be accounted for as well. In the present investigation, all computations use the *low-Reynolds* number method for all the walls.

---

# 3

## CFD Assessment of the Aero-Thermal Performance of Trailing Edge Channels

### 3.1 Test Section

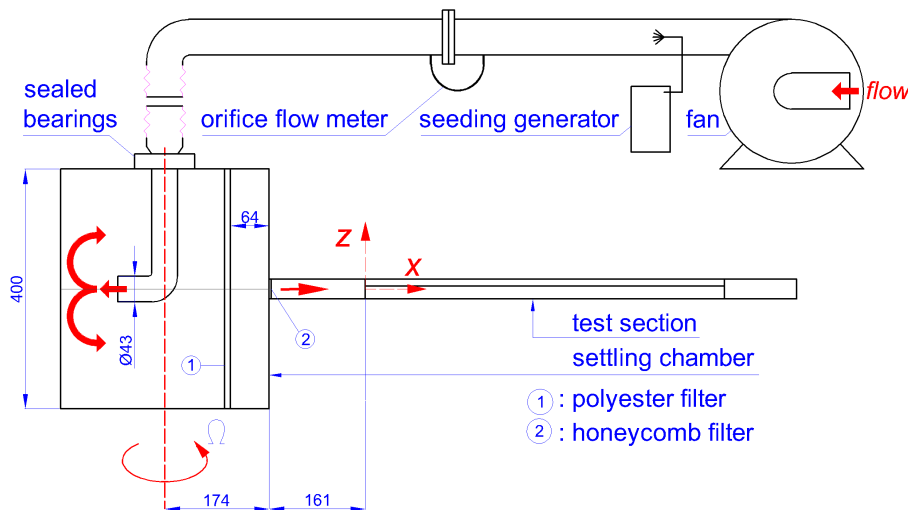


FIGURE 3.1 – Schematic of the test rig developed for the present experimental campaign [5], [56] and [7], xz-projection with the piping circuit.

In order to give a brief explanation of the experimental circuit, the test facility is sketched

in Fig. 3.1. The flow is fed using a 4[kW] centrifugal fan, which allows the required mass flow ratio to be obtained in order to achieve the selected  $Re$  number at the channel inlet (about 0.05 [Kg/s]). The flow is seeded by the Laskin seeding generator just downstream of the fan outlet. Flexible aluminum tubes link the fan to a 3[m] long with a steel pipe with a diameter of 97[mm]. In the middle of the latter, an orifice flow meter is installed which follows the UNI specifications [67]. After-wards by means of a 4[m] long piping circuit of the same internal diameter the top of settling chamber is reached. Sealed bearings connect the rotating settling chamber to the aluminum tube (Fig. 3.1). The sealed bearings on the top face of the settling chamber are connected to a 45[mm] internal diameter pipe. At the settling chamber middle height, a 90[°] bend turns the flow towards the settling chamber’s wall opposite to the test section. Furthermore, at 65[mm] upstream of the test section inlet, a polyester Fiber Filter was installed (Fig. 3.1 1). The latter produces the pressure losses necessary to ensure uniform flow conditions at the test section entry. Any effect of flow separation produced a sudden contraction of the flow was avoided by placing a 3[mm] honey-comb filter at the channel inlet (Fig. 3.1 2). The total pressure drop of the circuit is equal to 4356[Pa] and varies slightly according to the tests conditions. The distance between the axis of rotation and the origin of the channel coordinate system (see Fig. 3.1) is equal to 5.75  $Dh$  and is computed on the model inlet cross-section.

In the following subsections a description of the dimension and characteristics of:  $G0$  Subsec. 3.1.1,  $G1$  Subsec. 3.1.2 and  $G2$  Subsec. 3.1.3 configurations will be given.

### 3.1.1 G0

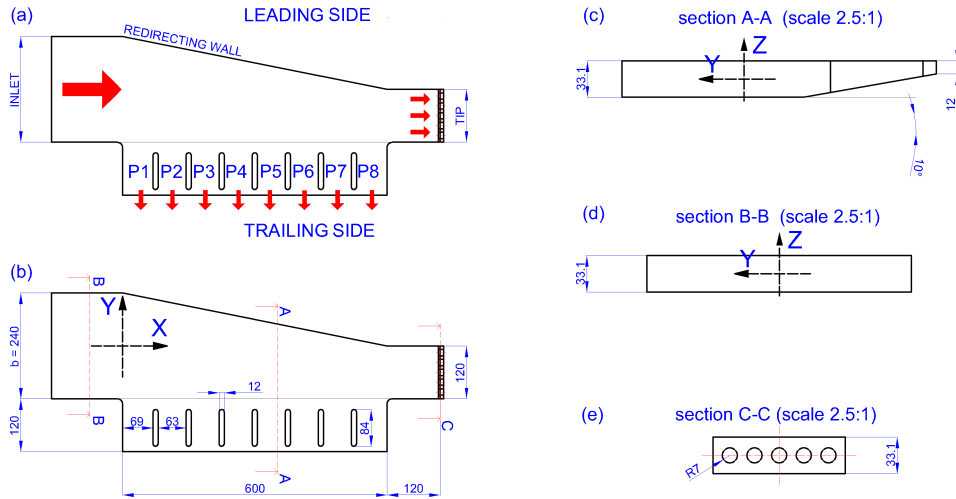


FIGURE 3.2 – Schematic of the test section ((a),(b)) ( $G0$  configuration), channel cross-section (c), inlet cross-section (d), tip cross-section (e) [7].

The basic configuration *G0* is shown in Fig. 3.2. The flow enters the channel along the radial direction and it is exhausted at both the tip and trailing side. The inlet section is rectangular with a *HydraulicDiameter*[*mm*](*Dh*) equal to 58.18[*mm*] and a high *Aspect Ratio* (*AR*) (equal to 7.25), while the trailing side exit portion has a wedge-shaped cross-section. In order to provide an almost uniform flow at the entrance of the trailing side exit section, the channel width was progressively reduced from hub to tip by means of a redirecting wall. At the model tip, a short channel with rectangular cross-section (having the same height as the main channel but with an  $AR = 3.625$ ) guides the flow towards the tip exit made of five equally spaced holes of 7[*mm*] radius. Inside the trailing side section, seven lengthened pedestals were installed to ensure structural rigidity and to promote flow turbulence. Finally, the channel wall at  $z = 16.55$ [*mm*] is intended to be the *PS*, whereas the opposite is the *SS*.

### 3.1.2 G1

Configuration *G1* (see Fig. 3.3) differs from *G0* for the use of seven ribs (one for each pedestal) at the *SS* wall (the channel wall at  $z < 0$ [*mm*]) that go from the redirecting wall up to the inclined wall's top at the trailing side. The ribs have a squared cross-section ( $5 \times 5$ [*mm*]) and are inclined at  $60^\circ$  to the radial direction (the direction of the *x* axis). The blockage ratio, referred to the local channel height is equal to 15[%] and the *IR* distance is equal to 60[*mm*]. It should be pointed out that in order to preserve the aerodynamically thin trailing edge and the required minimal thickness of the wall, the channel height must be very small. As a consequence, any increase in heat transfer such as the use of turbulators results in very high blockage ratios compared to other passages in the airfoil; therefore, it is not uncommon to find blockages of 25[%] or greater inside a trailing edge cooling channel [19].

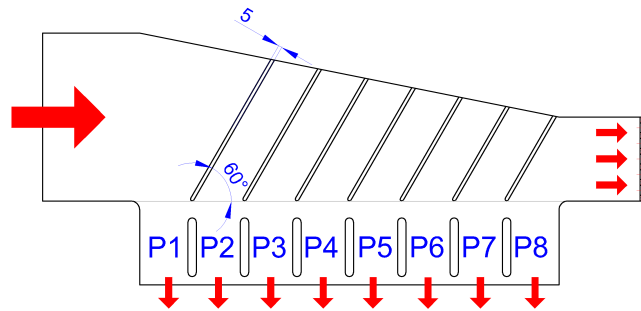


FIGURE 3.3 – Schematic of the test section, *G1* configuration.

### 3.1.3 G2

Finally, *G2* configuration (see Fig. 3.4) is characterised by  $3 \times 3$ [*mm*] cross-section ribs installed between the pedestals on the *SS* wall of the exhaust section at the trailing side.

Three ribs are installed in each inter-pedestal passage and the one in the middle is placed at half pedestal length. The blockage ratio, referred to the local channel height, ranges from 11[%] to 19[%] and the  $IR$  distance is equal to 30[mm]. With the aim to keep the mass flow rate fraction discharged at the model tip constant for all the considered geometries, the diameter of the tip discharging holes was reduced to 12.5[mm] in  $G2$ .

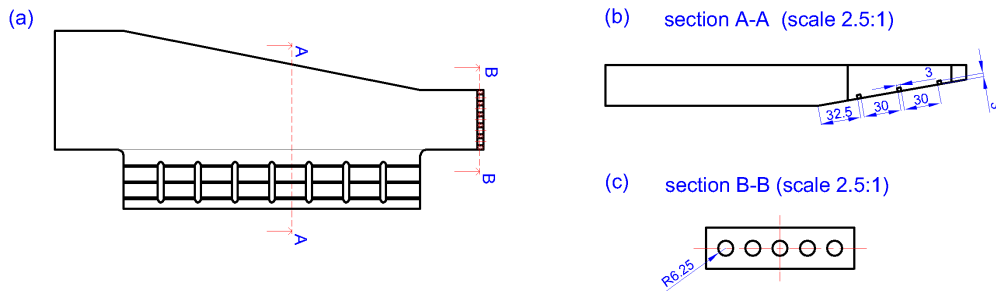


FIGURE 3.4 – Schematic of the test section,  $G2$  configuration.

### 3.2 Data Planes

The nomenclature and the positions of the planes used for the analysis of the  $G0$ ,  $G1$  and  $G2$  configurations in static ( $Ro = 0$  Ch.3) and rotating ( $Ro > 0$  Ch.4) conditions are shown in Figs. 3.5, 3.6 and 3.7 while the Tabs. 3.1, 3.2, 3.3, 3.4 and 3.5 report the plane positions taking as reference the dimensions illustrated for the basic  $G0$  configuration in Fig. 3.2.

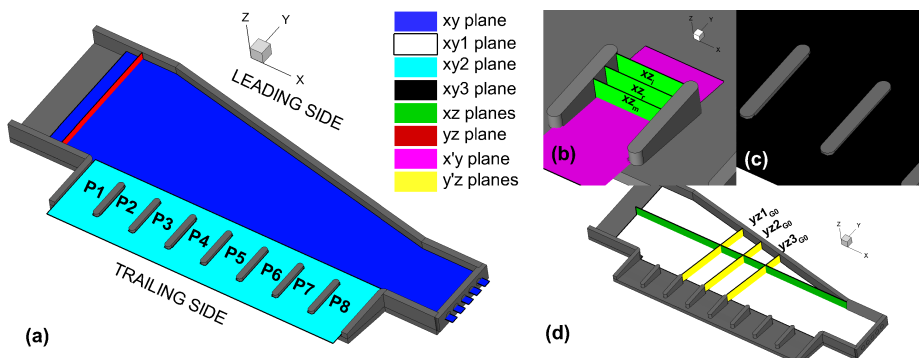


FIGURE 3.5 – Overview of the position of the experimental and  $CFD$  data planes.

Planes	$z$ position [mm]
xy	0
xy1	-14.55
xy2	10.55
xy3	14.55
$x'y$	and at 2 [mm] from the <i>SS</i>

TABLE 3.1 – xy planes see Fig. 3.5, *G0 G1 G2* configurations.

Planes	position [mm]
xz	$y = 0$
yz	$x = -69.8$
xzi	$y = -150$
xzR	$y = -165$
xzm	$y = -180$

TABLE 3.2 – yz and xz inlet planes and xz *IP* planes see Fig. 3.5, *G0 G1 G2* configurations.

Planes <i>G0</i>	position $\perp$ to redirecting wall $x'$ [mm]
$y'z1_{G0}$	175.331
$y'z2_{G0}$	248.875
$y'z3_{G0}$	322.418

TABLE 3.3 – yz planes see Fig. 3.5(d), *G0* configuration.

Planes <i>G1</i>	position [mm]
$xy_{G1}$	$z = -14.05$
$xz_{G1}$	$\perp$ with respect to the rib $y' = 109.186$
$y'z1_{G1}$	with respect to the rib $x' = 284.5$
$y'z2_{G1}$	with respect to the rib $x' = 253.537$
$y'z3_{G1}$	with respect to the rib $x' = 352.08$

TABLE 3.4 – yz, xz and  $y'z$  planes see Fig. 3.6, *G1* configuration.

Planes <i>G2</i>	position [mm]
$yz_{G2}$	$x = 262.5$
$xy'_{G2}$	with respect to the <i>SS</i> at $z = 1.5$
$xy^i_{G2}$	$y = 153.5$
$xym_{G2}$	$y = 322.418$

TABLE 3.5 – yz, xz and  $y'z$  planes see Fig. 3.7, *G2* configuration.

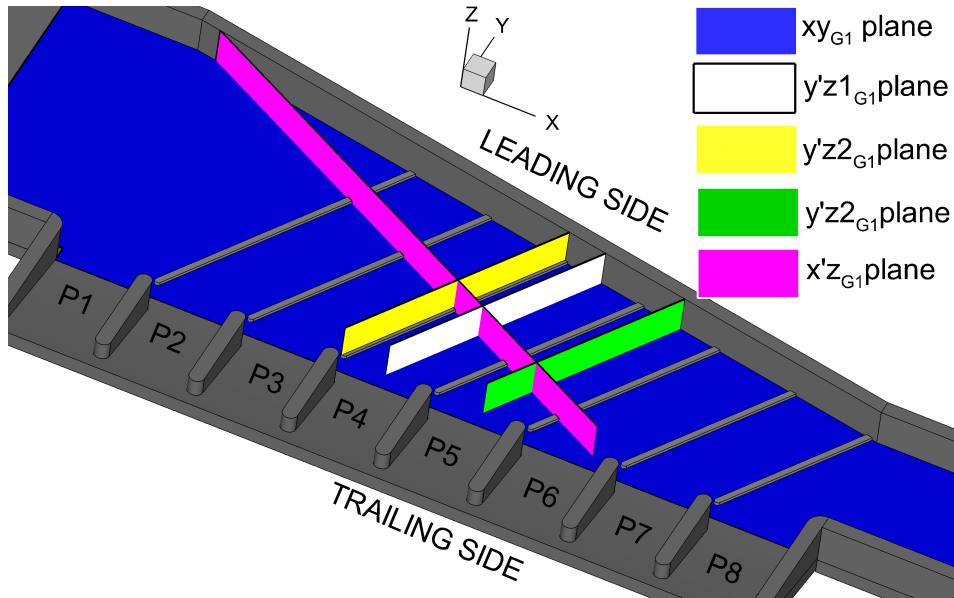


FIGURE 3.6 – Overview of the position of the experimental and *CFD* data planes, *G1* configuration.

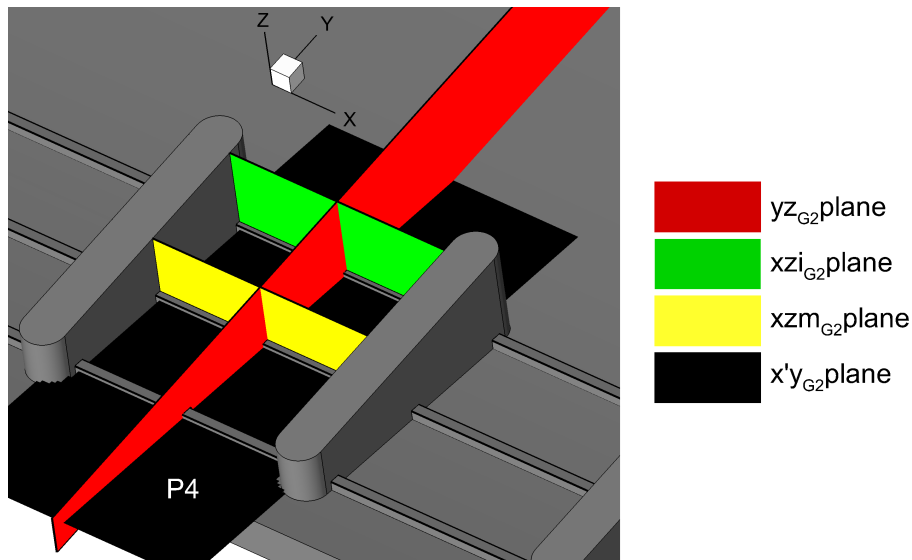
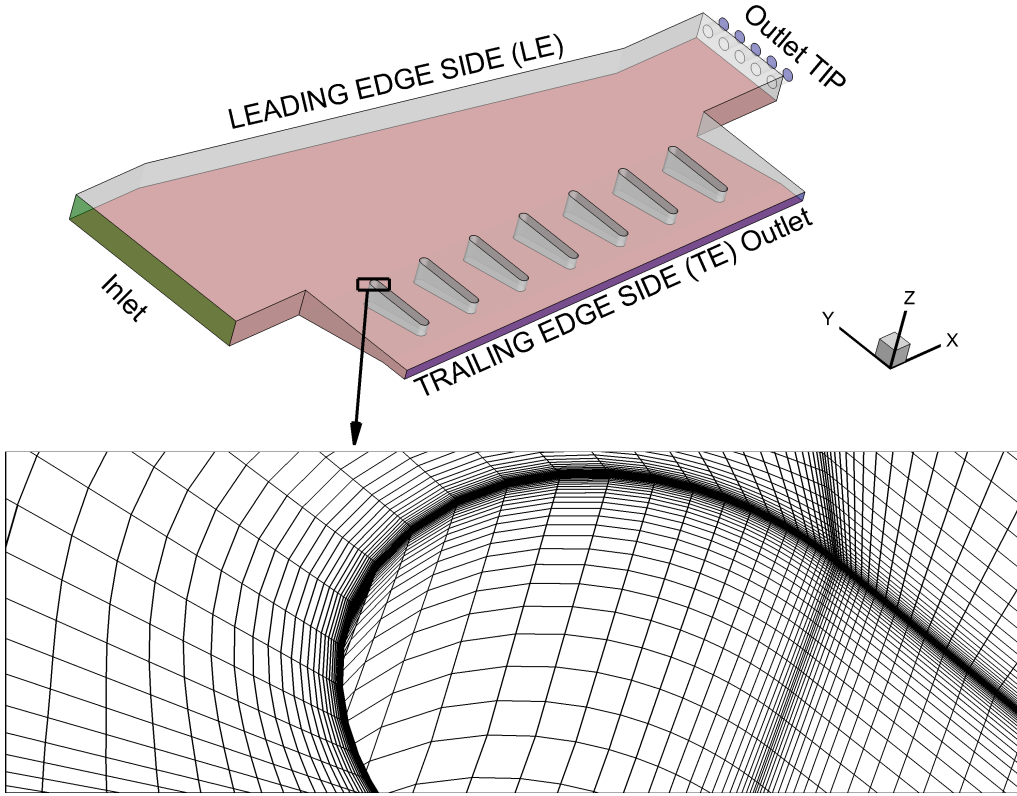


FIGURE 3.7 – Overview of the position of the experimental and *CFD* data planes, *G2* configuration.

### 3.3 *G0* Configuration

#### 3.3.1 Computational Details

The computational domain was discretized by a multi-block structured mesh with hexahedral elements. A 3-D view of the grid for *G0* configuration is shown in Fig. 3.8 where

FIGURE 3.8 – 3-D view on the mesh,  $G_0$  configuration.

7299794 cells were used. Such a considerable number of cells results mainly from the need to use very tiny elements in the regions in proximity to the pedestal surfaces, as highlighted in Fig. 3.8, where 3-D flow separation takes place. In these regions, O-grids [4] were applied in order to obtain high cell's orthogonality. Furthermore, very fine mesh scales in the direction normal to wall were applied in all regions in order to ensure the proper performance of the low  $Re$  number turbulence model which requires the dimensionless wall distance of the first grid point to be smaller than 2 [4]. In fact, small cell growth rates (not greater than 1.2) were used for all the surfaces. A summary of the grid details and the mesh quality parameters is given in Tab.3.6 where:  $N$  is the Grid cells number,  $y_{max}^+$  and  $y_{avg}^+$  represent respectively the maximum and the average of the dimensionless distance between the wall and the first cell outside the wall,  $\delta_{min}$  is the smallest cell angle and  $L_{max}$  is the highest aspect ratio defined as the size of the smallest element edge divided by the size of the largest element edge.

The boundary conditions applied follow a classic scheme for incompressible air with constant fluid properties taken at  $T = 293.15[K]$ . A constant velocity at the total tempera-

$N$	$y_{max}^+$	$y_{avg}^+$	$\delta_{min}$	$L_{max}$
7299794	1.33	0.36	30.15	586

TABLE 3.6 – Grid details,  $G0$  configuration.

ture  $T_0 = 293.15[K]$  was set at the channel inlet surface (marked in green Fig. 3.8) using an interpolation (see Apx.D) of the experimental data obtained by Armellini et al.[5], while the ambient static pressure ( $p=101325[Pa]$ ) was forced in the outlet (indicated in blue in Fig. 3.8). No slip and adiabatic conditions were applied to the walls except for the heated surface ( $SS$  marked in red in Fig. 3.8) where a constant wall temperature  $T_w = 323.15[K]$  was imposed.

### 3.3.2 Quantification of the Numerical Accuracy

Discretization errors were estimated using the local  $Nu$  by means of the  $GCI$  method (explained in Apx.C). In order to fulfill its requirements, three similar meshes characterized by different spatial resolutions were employed. The parameters of the grids used in the refinement study are summarized in Tab.3.7 where: the fine grid corresponds to the one introduced above,  $N$  is the grid cells number and  $y_{avg}^+$  represents the average of the dimensionless distance between the wall and the first cell outside the wall. The results obtained with the refinement study are shown in Fig. 3.9, where the  $GCI$  (see Apx.C) is plotted by way of error bars for the  $Nu$  number extracts at the  $SS$  surface along a line at  $y = -180[mm]$ . The results of the mesh sensitivity have sufficiently low  $GCI$  values (see Fig. 3.9). It should be noted that the heat transfer and, therefore, the  $GCI$  values in the  $IP$  are not included. The analysis, indeed, shows an average error below than 3[%] with the exception of limited regions downstream of each pedestal, with a maximum absolute value of about 10[%]. Therefore, the finer mesh results to be a good compromise between spatial resolution and computational effort associated with the overall number of elements.

Grid	$N$	$y_{avg}^+$
Fine	7299794	0.36
Intermediate	3064025	0.46
Coarse	1323880	0.69

TABLE 3.7 –  $GCI$  study,  $G0$  configuration.

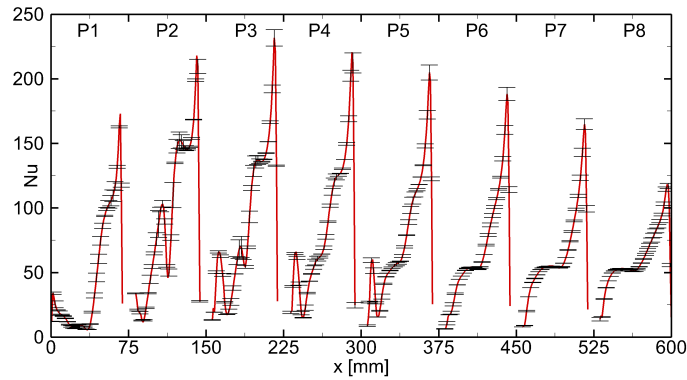


FIGURE 3.9 –  $GCI$  at the  $SS$  surface at  $y = -180[mm]$ ,  $G0$  configuration.

### 3.3.3 Comparison with the Experimental Results

In order to draw a first comparison between experimental [7] results and numerical predictions, Fig. 3.11 shows the local  $Nu$  distributions on the  $SS$  wall. As can be seen, from a qualitative viewpoint, the  $CFD$  reproduces quite well the trends illustrated in the  $Nu$  maps. Indeed, in the central part of the channel the agreement is very good, as showed in more detail in Fig. 3.10, in which the  $Nu$  profiles are extracted along a line at  $y = -96[mm]$ , where a slightly decreasing of the  $Nu$  value from hub to tip can be seen. A further confirmation of the good computations of the  $CFD$  code is shown in Fig. 3.11 where a region of low heat transfer is found near the tip in proximity to the inclined wall (also known as redirect wall). This region fills a large portion of the tip exhaust channel.

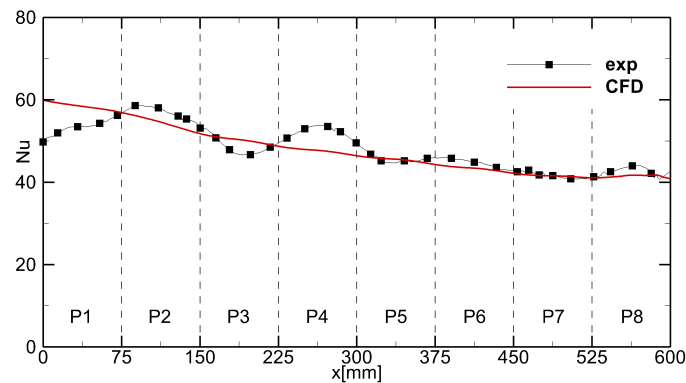


FIGURE 3.10 – Experimental [7] and  $CFD$   $Nu$  profiles on the  $SS$  wall at  $y = -96[mm]$ ,  $G0$  configuration.

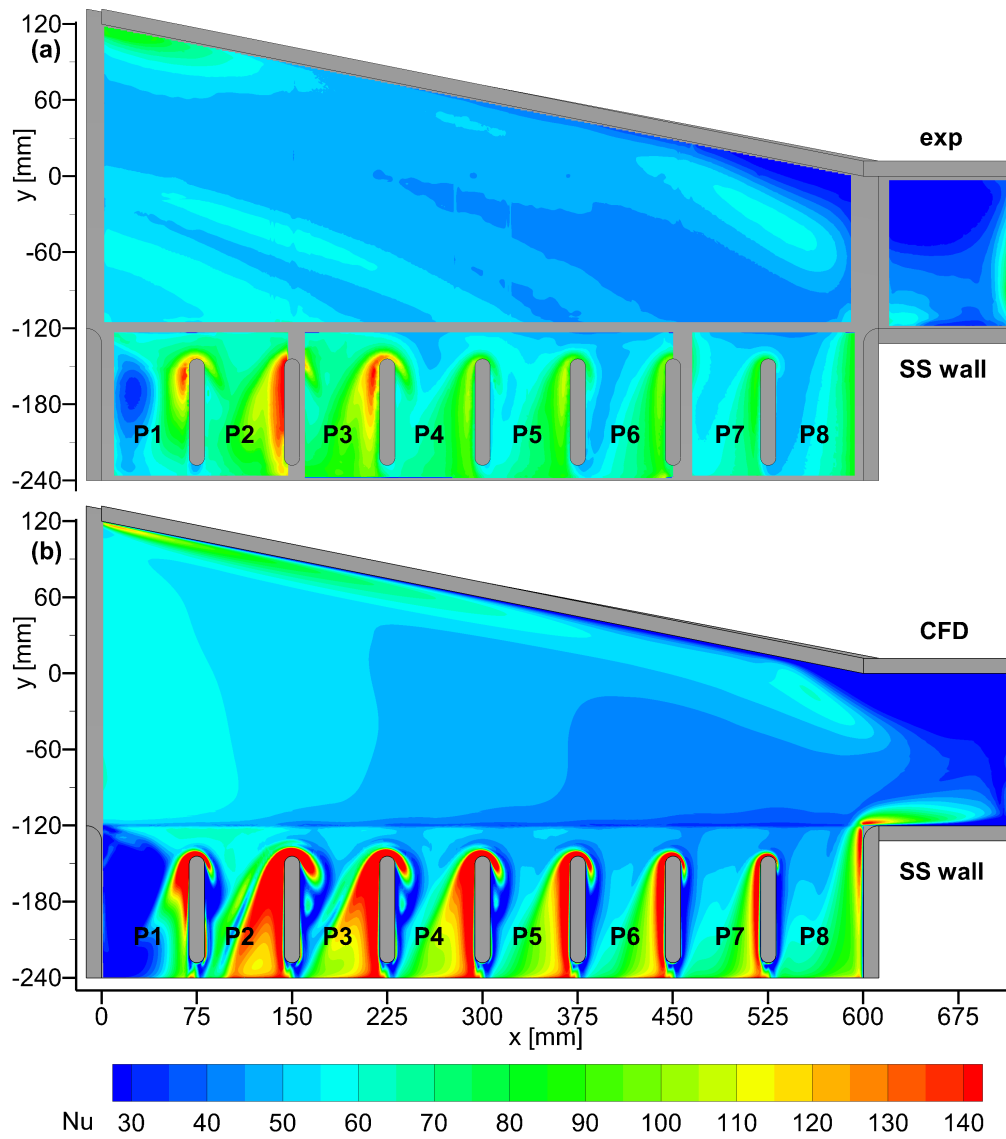


FIGURE 3.11 – Experimental [7](a) and *CFD* (b) *Nu* distribution on the *SS*, *G0* configuration.

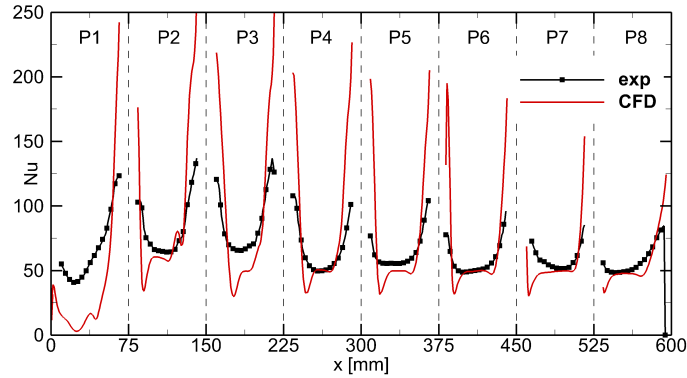


FIGURE 3.12 – Experimental [7] and *CFD* *Nu* profiles on the *SS* wall at  $y = -150[\text{mm}]$ , *G0* configuration.

By contrast, in the trailing side exhaust region, where there is a complex thermal field, greater discrepancies between the experimental [7] and numerical values are found. The first one is the over-prediction of the size of the low heat transfer region inside 1<sup>st</sup> Pedestal Passage (*P1*). The second one is the over-prediction of the peak values on the upstream side (i.e. towards  $y < 0[\text{mm}]$ ) of each pedestal. However, in both experimental [7] and numerical results, these high heat transfer regions have peak values and extensions which decrease while moving towards the channel tip, as displayed in Fig. 3.11 and more in detail in Fig. 3.12. The latter shows the *Nu* values extracted from the *SS* surface at  $y = -150[\text{mm}]$ .

The *Nu* distribution and the discrepancies between experimental [7] and numerical values commented in the previous paragraph, can be fully described if the time-averaged flow field is considered. As displayed in Fig. 3.13, which represents the velocity maps and stream-tracers in planes *xy* (Figs. 3.13 (a,c)) and *xy2* (Figs. 3.13 (b,d)), all the main characteristics of the flow field are very well simulated by the *CFD* computations. It must be pointed out that the seeding generating the experimental [5] and the numerical stream-tracers is clearly not equivalent and these lines should therefore be used solely as a support in the visualization.

In the central portion of the channel, where the heat transfer process is obtained by simple force convection, the flow velocity decreases along the radial direction ( $x$ ), as a result of the gradual coolant discharge at the trailing side which accounts for the slight *Nu* decreases commented in the previous paragraph. At the blade tip, the big recirculation bubble is accurately predicted by the *CFD* code and accounts for the low heat transfer values commented above. The flow recirculation is produced by the geometrical discontinuity between the tip and the redirecting wall, coupled with the diffusion process that takes place while the coolant is redirected towards the trailing side, as highlighted by the diverging path of the stream-tracers in both the experimental and numerical results (Figs. 3.13(a,c)).

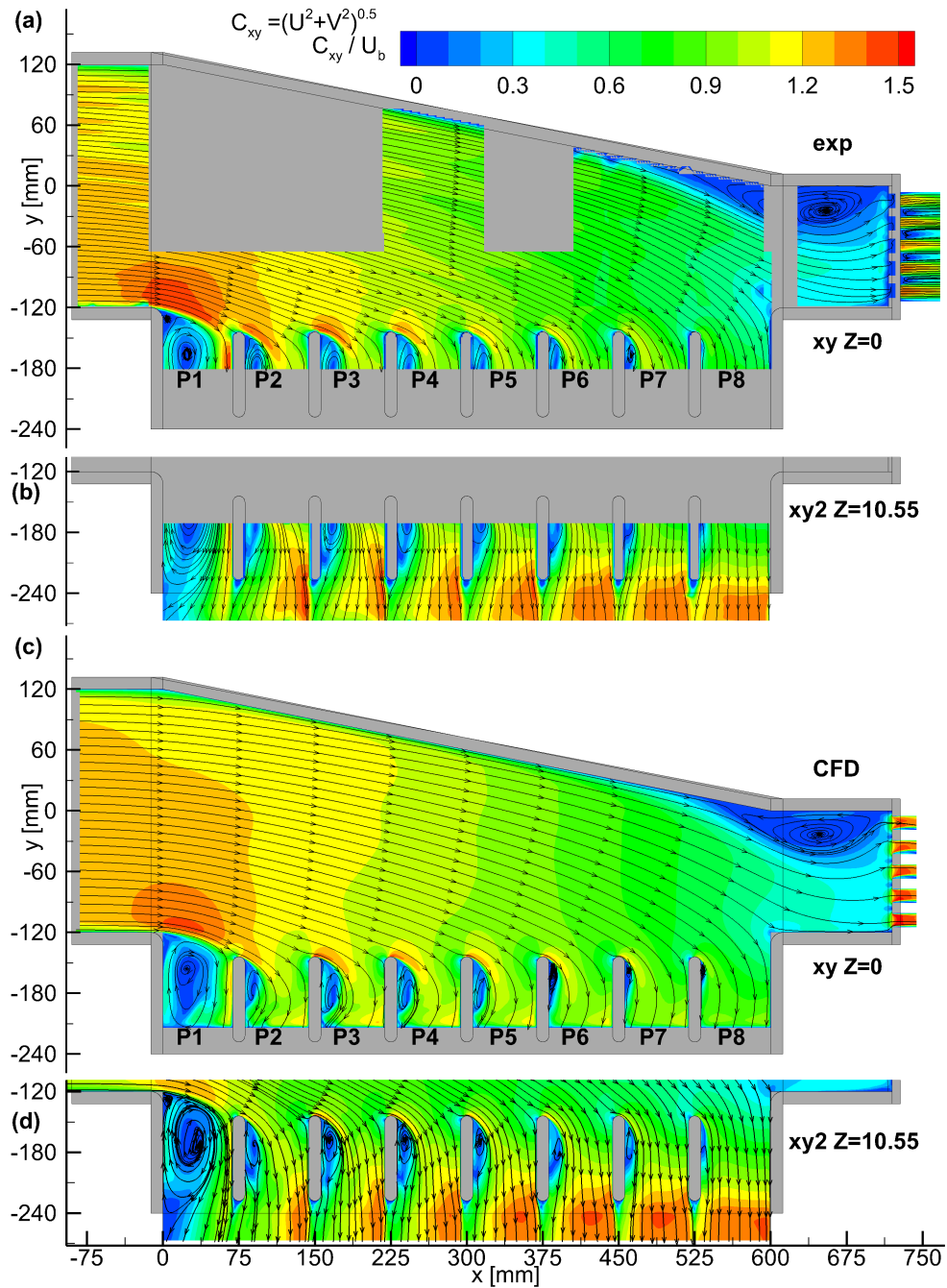


FIGURE 3.13 – Experimental [5] (a,b) and *CFD* (c,d) time-averaged stream-tracers and contours plots of the in-plane velocity modulus  $C_{xy}$  in the  $xy$  (a,c) and  $xy2$  (b,d) planes,  $G0$  configuration.

At the trailing side, which shows more discrepancies in the prediction of the heat transfer by the *CFD* code, the agreement between the experimental [5] and the numerical time-averaged flow field data is good as shown by the decreasing size of the recirculation bubbles from hub to tip, in the downstream area of each pedestal (Fig. 3.13).

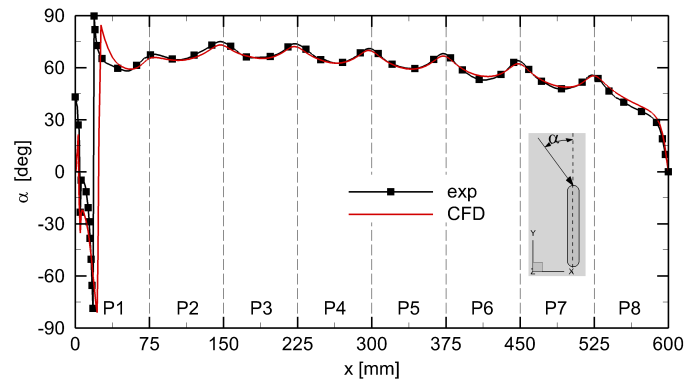


FIGURE 3.14 – Experimental [5] and *CFD* flow angle  $\alpha$  extracted in plane  $xy$  at  $y = -132[mm]$ , *G0* configuration.

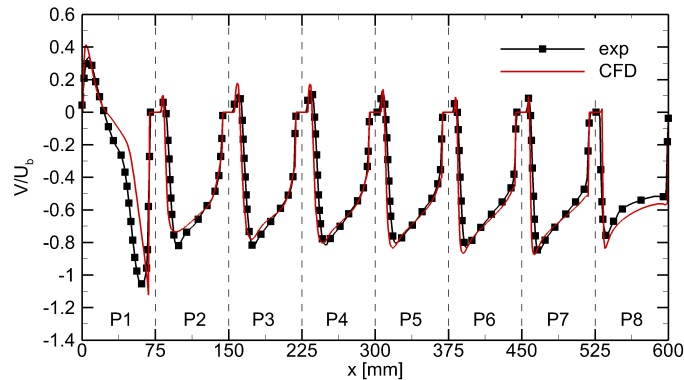


FIGURE 3.15 – Experimental [5] and *CFD*  $V$  velocities profiles in plane  $xy$  at  $y = -150[mm]$ , *G0* configuration.

In order to better demonstrate the match between the *CFD* predictions and the experimental [5] results another comparison concerning the flow approaching the pedestals is made : Fig. 3.14 plots the incidence angle  $\alpha$  between the  $y$  axis and the flow, extracted from plane  $xy$  along a line at  $y = -132[mm]$ . The flow angle  $\alpha$  to the pedestal chord decreases moving from hub to tip, according to the reduction of the recirculation bubble, as illustrated in the velocity maps in Fig. 3.13. It can be seen that in the 1<sup>st</sup> *IP* passage (*P1*) a marked change in sign of  $\alpha$  is highlighted, which is the result of the inversion of the

axial velocity generated by the large recirculation bubble commented above (Fig. 3.13). Its extension is slightly over-predicted by the *CFD* simulation, which accounts for the differences in the size of the low heat transfer regions previously observed (Fig. 3.11). From *P2* to *8<sup>th</sup> Pedestal Passage (P8)* *IP* passage, the match between experimental [5] and *CFD* data is full. Similar conclusions can be drawn for Fig. 3.15 which reports the profiles of the mean velocity component  $\bar{V}$  extracted from plane *xy* along a line at  $y = -150[mm]$ .

As pointed out above, the *CFD* simulation predicts a larger flow separation and a lower peak velocity only in the first *IP* passage while in the other *IP* passages, the numerical results reproduce very accurately the flow near the pedestal and the size of the separated flow regions, as fully confirmed by the air split analysis shown below. Figure 3.16 displays the mass flow rate discharged at the tip and in each *IP* channel compared to the total mass flow entering the channel. Both experimental [5] and numerical results agree and show an almost uniform flow along the trailing side. Only in the *P1* passage, as a consequence of the blockage effect imposed by the large recirculation bubble previously commented, less than half of the coolant flow rate is discharged, if compared to the others *IP* passages.

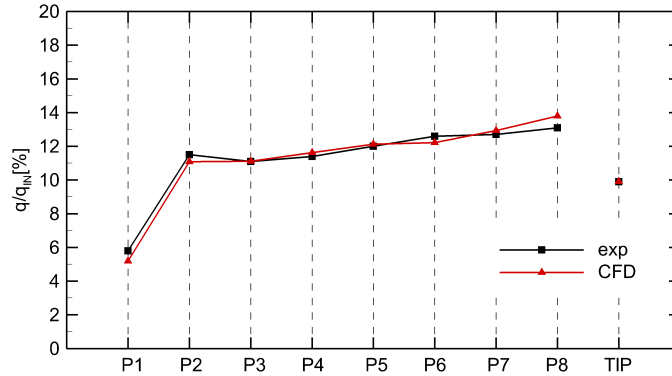


FIGURE 3.16 – Experimental [5] and *CFD* *IP* mass flow rate distribution, *G0* configuration.

In order to complete the heat transfer analysis and check the capabilities of the *CFD* code, an analysis of the 3-D flow structures produced inside the *IP* passage was carried out. The comparison between the experimental [5] and numerical data is conducted in *P4* passage on planes  $x'y$  (Figs. 3.17(a,e)),  $xy3$  (Figs. 3.17(b,f)),  $xzi$  (Figs. 3.17(c,g)) and  $xzm$  (3.17(d,h)).

Experimental [5] and numerical time-averaged stream-tracers paths situated on the plane  $xy3$  (Fig. 3.17 (b,f)), near the upstream face of the pedestal at  $x = 300[mm]$ , suggest the existence of a horseshoe vortex branch generated by the deviation of the approaching boundary layer. A detailed description of these 3-D flow structures can be found in Devenport and Simpson [28]. The time-averaged stream-tracers path in plane  $xzi$  (Figs. 3.17(c,g)) and  $xzm$  (Figs. 3.17) confirm the existence of these horseshoe vor-

tices on *PS* ( $z > 0[mm]$ ) and *SS* ( $z < 0[mm]$ ) and show that the prediction made by the *CFD* simulations is accurate.

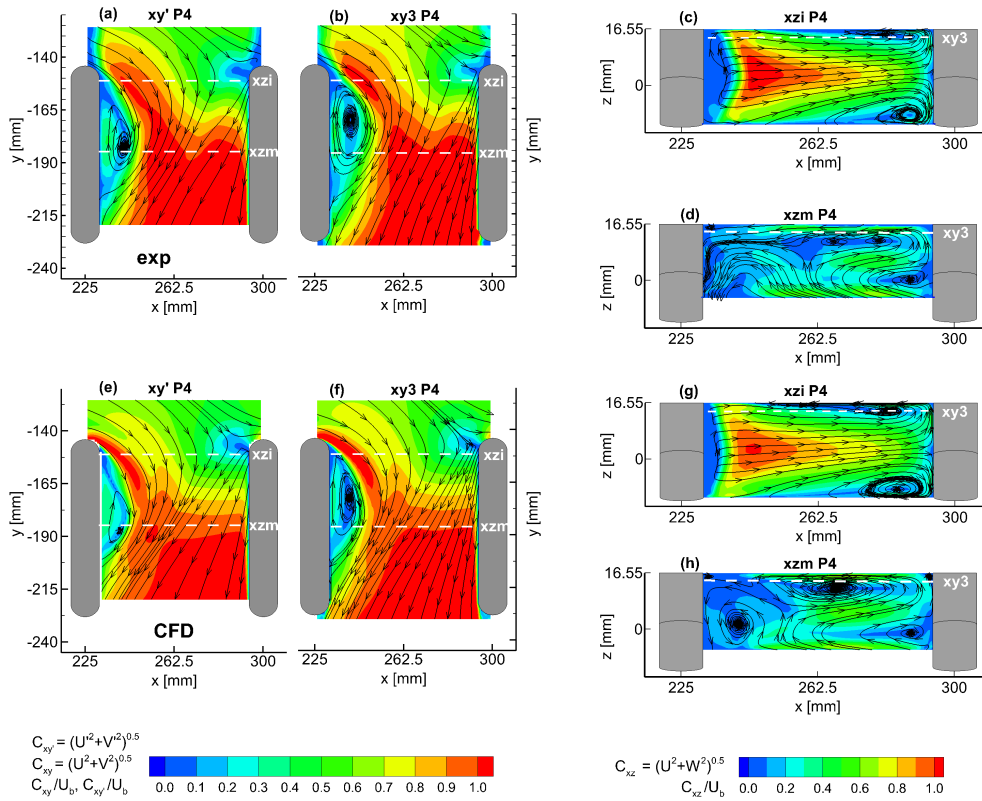


FIGURE 3.17 – Experimental [5] and *CFD* 3-D *IP* flow structures, *G0* configuration.

Indeed, both size and position of the main vertical structures are correctly predicted, the only significant discrepancy can be observed in the different size of the horseshoe vortices produced on the *PS* of the channel ( $z > 0[mm]$ ). This is probably due to the unsteady nature of such flow structures, as commented in Armellini et al.[5]. Moreover, minor differences are highlighted in the stream-tracers path in the recirculation bubbles ( $x < 245[mm]$ ), that can be observed also by means of the velocity components profiles in Fig. 3.18 extracted in plane *xzi* of the 4<sup>th</sup> *IP* passage (*P*<sub>4</sub>) at  $z = 0[mm]$ . A justification of this behavior is found by considering the reduced measurement accuracy in that region, which is due to the extremely low in-plane velocities and the lower spatial resolution if compared with the numerical one. Finally, Fig. 3.19 plots the area-averaged *Nu* values computed across each *IP* discharge channel at the trailing side. The averaging area extends inside each passage between  $y = -235[mm]$  and  $y = -130[mm]$  for both the experimental [7] and numerical *Nu* numbers. As can be seen, these averaged data confirm all the previous comments: indeed in the *P*<sub>1</sub> passage the *CFD* code under-predicts the average heat transfer because of the aforementioned over-prediction of the size of the recirculation bubble, while, in the other *IP* passages there is an over-prediction of the averaged *Nu* values. This effect can result from the over-prediction computed by the *CFD* code on the effect of the horseshoe vortex and, hence, of the heat transfer: this behavior might have originated from an over-prediction of the turbulence kinetic energy ( $\kappa$ ) as explained in Apx.E.

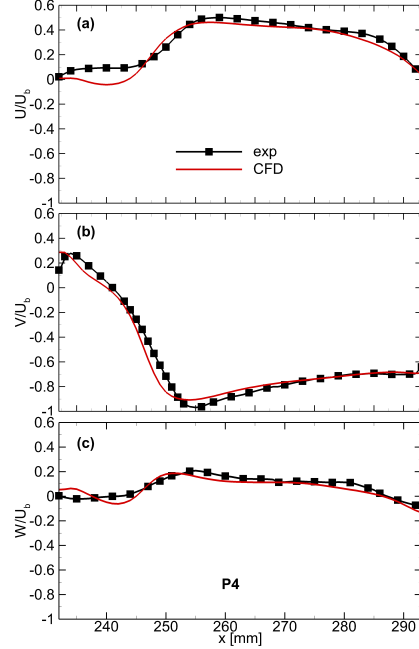


FIGURE 3.18 – Experimental [5] and *CFD* velocity components inside *P*<sub>4</sub> passage in plane *xzi* at  $z = 0[mm]$ , *G0* configuration.

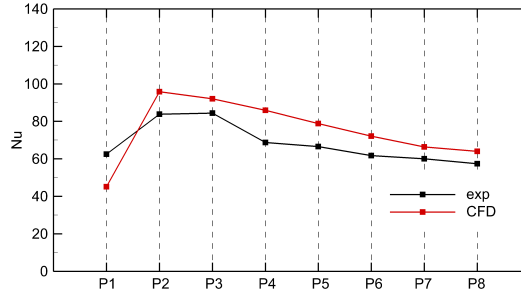


FIGURE 3.19 – Experimental [7] and *CFD* average *Nu* value computed over each *IP* passage, *G0* configuration.

## 3.4 G1 Configuration

### 3.4.1 Computational Details

The computational domain was discretized by a multi-block structured mesh with hexahedral elements. A 3-D view of the grid for *G1* configuration is illustrated in Fig. 3.20.

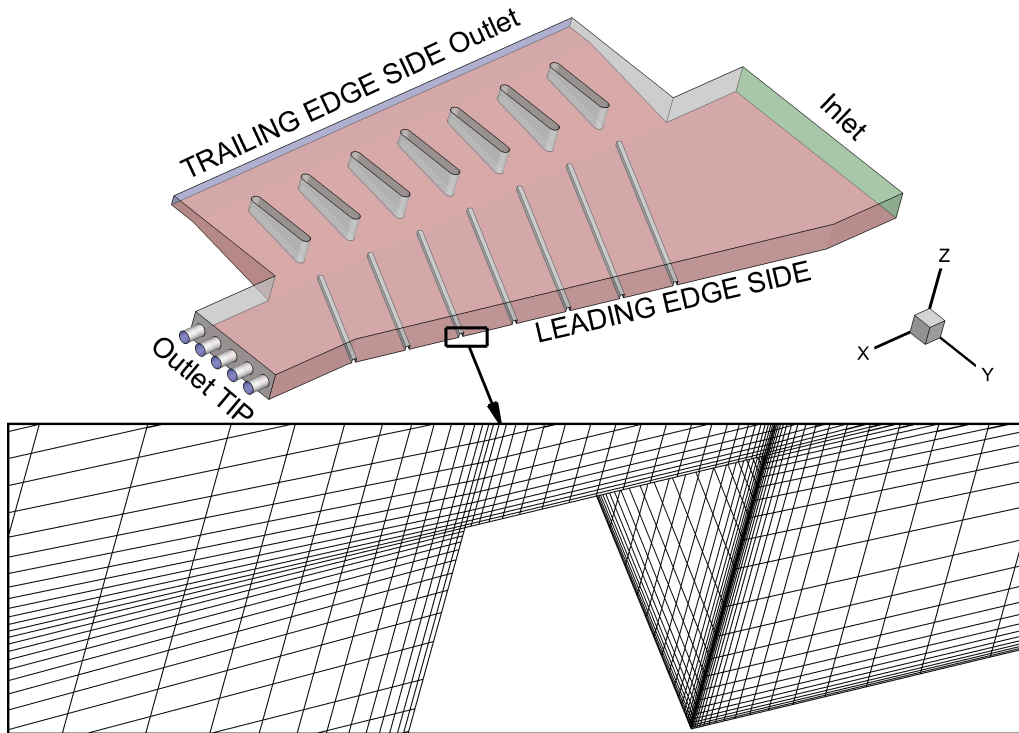


FIGURE 3.20 – 3-D view on the mesh, *G1* configuration.

$N$	$y_{max}^+$	$y_{avg}^+$	$\delta_{min}^+$	$L_{max}$
8872752	1.98	0.38	28.8	374

TABLE 3.8 – Grid details, *G1* configuration.

The only differences, compared with *G0* mesh characteristics (see Subsec. 3.3.1), are found in the rib-roughened region at the *SS* wall, as demonstrated in Fig. 3.20. A summary of the grid and the mesh quality parameters is given in Tab.3.8 which displays an increase in the number of cells, compared with the *G0* configuration, which assures the proper functionality of the turbulence model on the rib-roughened *SS* wall.

The boundary conditions were the same applied in the *G0* configuration. As can be observed in Fig. 3.20, the ribs walls were not heated (indeed they are not marked in red) and, therefore, they were simulated as an adiabatic no slip walls in order to match the experimental conditions [7] as accurately as possible.

### 3.4.2 Quantification of the Numerical Accuracy

For an estimation of the discretization errors, the *GCI* procedure is used again (see Apx. C). The parameters of the grids computed are summarized in Tab.3.9. It must be pointed out that all the requirements for the calculation of the *GCI* are fully achieved. Figure 3.21 plots the resulting distribution of the *GCI* calculated by way of the three different grids shown as *Nu* numbers extracted in the *SS* wall at the  $y = -60[mm]$  and displays the very low discretization errors bars estimated by the refinement study. It should be noted that the heat transfer and, therefore, the *GCI* values on the rib surfaces are not included. The results of the analysis are satisfactory and characterized by an average error value computed below 3[%], with the exception of a limited region near to the last rib in the stagnation zone with an absolute value which is, however, lower than 10[%].

Grid	N	$y_{avg}^+$
Fine	8872752	0.38
Intermediate	4000198	0.50
Coarse	1794969	0.69

TABLE 3.9 – *GCI* study, *G1* configuration.

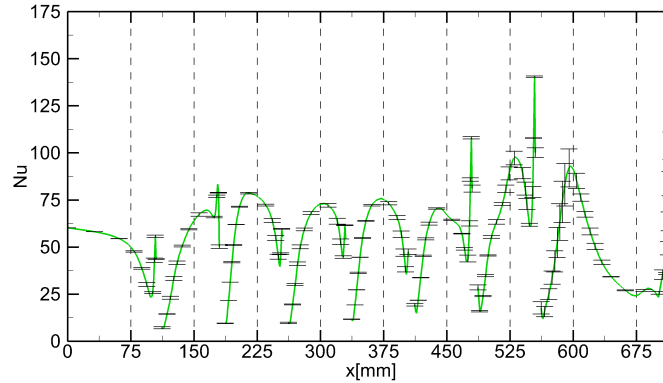


FIGURE 3.21 – *GCI* error band at *SS* at  $y = -60[mm]$ , *G1* configuration.

### 3.4.3 Comparison with Experimental Results

Figure 3.22 shows the comparison between the experimental [7] and numerical *Nu* maps in *G1* configuration: comparing the results with the basic *G0* configuration, both *Nu* maps show an increase in the heat transfer in the rib region as well as in the trailing side outlet. However, the *CFD* code displays a different distribution of the *Nu* values with high peaks of heat transfer from the 3<sup>rd</sup> to the 7<sup>th</sup> rib and, once more, in the *IP* region.

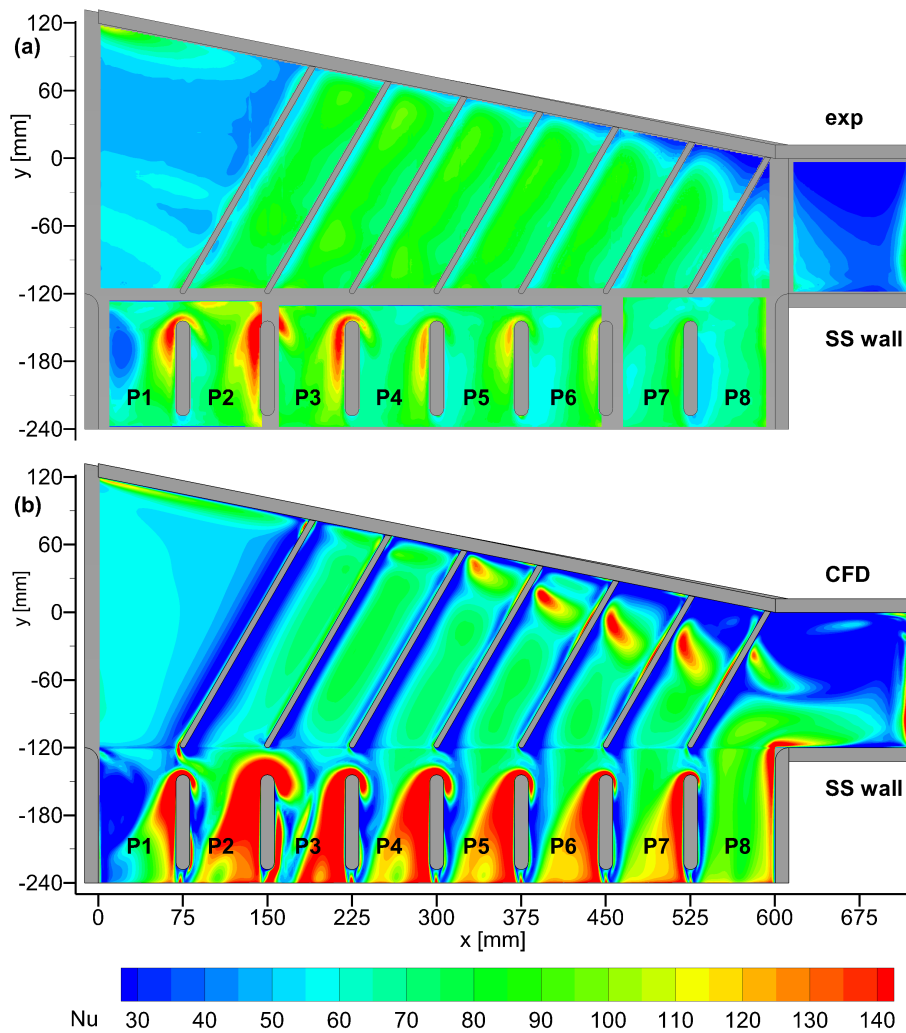


FIGURE 3.22 – Experimental [7](a) and *CFD* (b)  $Nu$  distribution on the *SS*, *G1* configuration.

The  $Nu$  distribution and the discrepancies between the experimental [7] and numerical values can be fully described if the time-averaged flow field is considered. Figure 3.23 illustrates the experimental [56] and numerical velocity maps and stream-tracers in planes  $xy$  and  $xy2$ . From a qualitative viewpoint, in the central part of the channel the *CFD* contours show an over-prediction of the velocity  $C_{xy}$  and an over-estimation of the recirculation bubble's size at the blade tip.

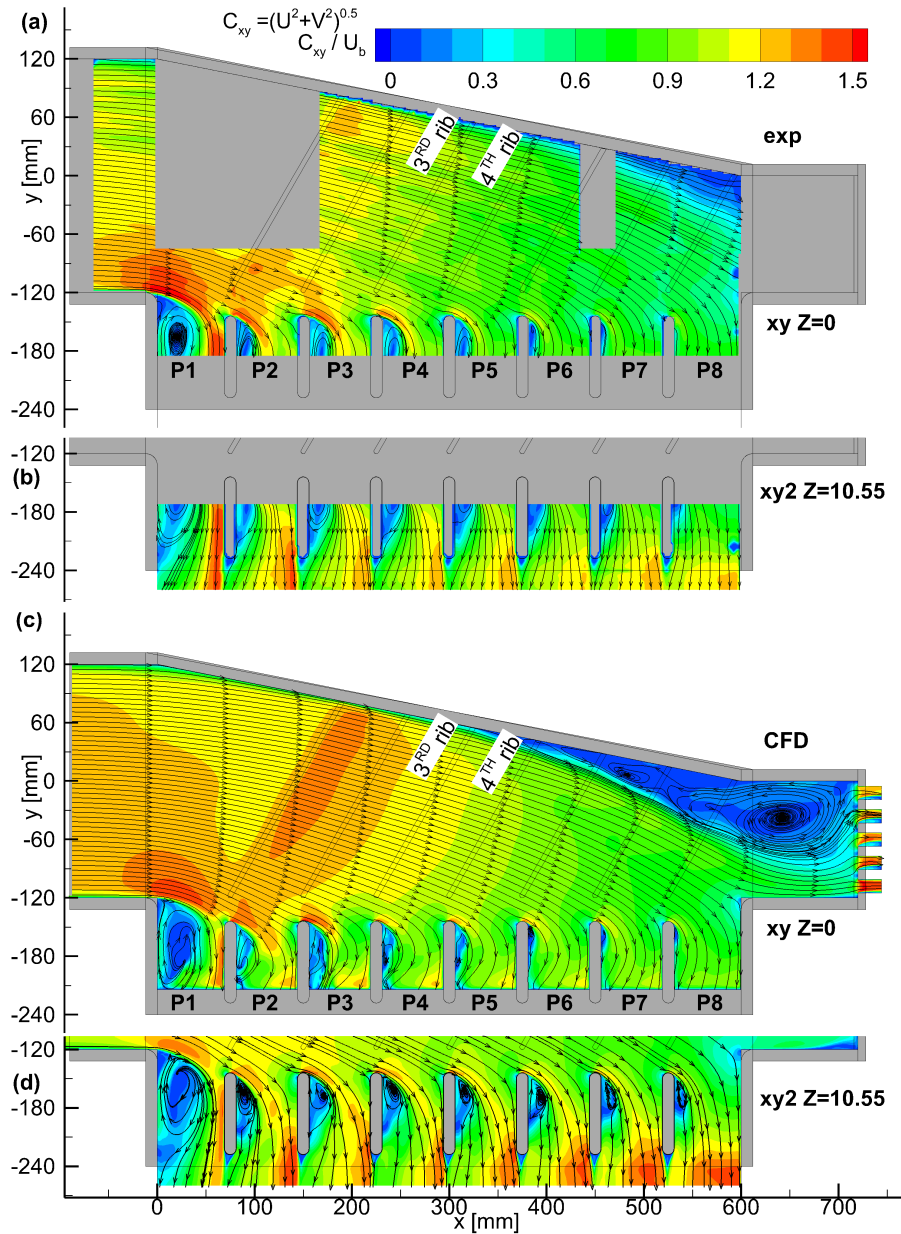


FIGURE 3.23 – Experimental [56](a,b) and *CFD* (c,d) time-averaged stream-tracers and contour plots of the in-plane velocity modulus  $C_{xy}$  in the  $xy$  (a,c) and  $xy2$ (b,d) planes,  $G1$  configuration.

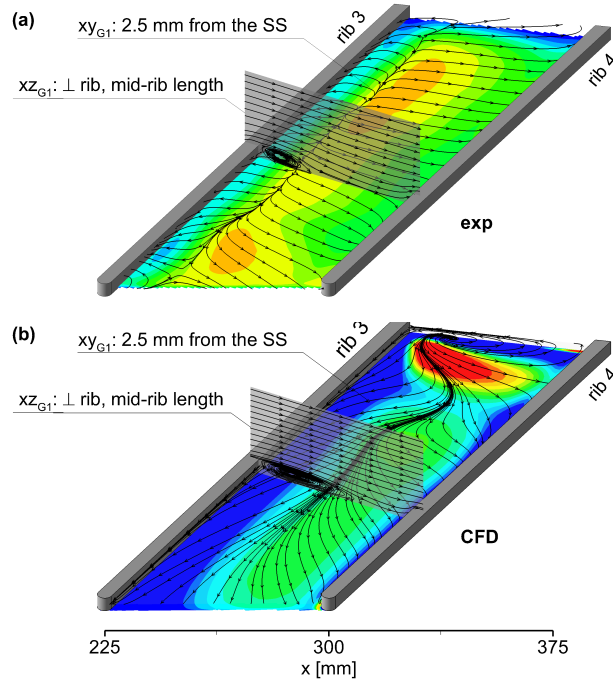


FIGURE 3.24 – Experimental [56](a) and *CFD* (b)  $Nu$  distribution on the *SS* and time-averaged stream-tracers in planes  $xy_{G1}$  and  $xz_{G1}$  between the 3<sup>rd</sup> and 4<sup>th</sup> rib, *G1* configuration.

Going more into detail, Figs. 3.24(a,b) show the comparison between the  $Nu$  number distribution on the *SS* of the channel between the 3<sup>rd</sup> and the 4<sup>th</sup> rib and the time-averaged stream-tracers at the plane  $xy_{G1}$  and  $xz_{G1}$ . As for the flow fields comparison, the *CFD* code predicts a larger extension of the separated flow downstream the rib (see stream tracers in plane  $xz_{G1}$  at rib mid-length). The reattachment location greatly depends on the amount of the eddy introduced into the domain. As a part of the standard *SST* formulation, limiters are placed on the eddy-viscosity ( $\nu_t$ ) (as commented in Subsec. 2.3.2). For these types of flow regime, the limiters yielded a large suppression of the eddy-viscosity ( $\nu_t$ ) which produce excessive large scale separation. Moreover, the recirculating flow region in the *IR* plane  $xy_{G1}$  is further characterized by a considerable 3-D structure close to the redirecting wall of the channel and by a global flow deviation towards the trailing side exit between the 3<sup>rd</sup> rib and the reattachment line. Consequently, a different  $Nu$  distribution is found, i.e. the *CFD* thermal data are characterized by a larger extension of the low  $Nu$  region downstream of the rib, a strong  $Nu$  peak in the proximity to the flow impingement close to the redirecting channel wall, and a lower heat transfer in between the reattachment line and the next rib.

Conversely, at the trailing side, where *CFD* code over-predicts again the  $Nu$  values, the flow field appears to be simulated quite well as confirmed by Figs. 3.25 and 3.26, which respectively plot the very good agreement between the experimental [56] and numeri-

cal results concerning the incidence angle ( $\alpha$ ) extracted from plane  $xy$  along a line at  $y = -132[mm]$  and the mean velocity component  $V$  extracted from plane  $xy$  along a line at  $y = -150[mm]$ .

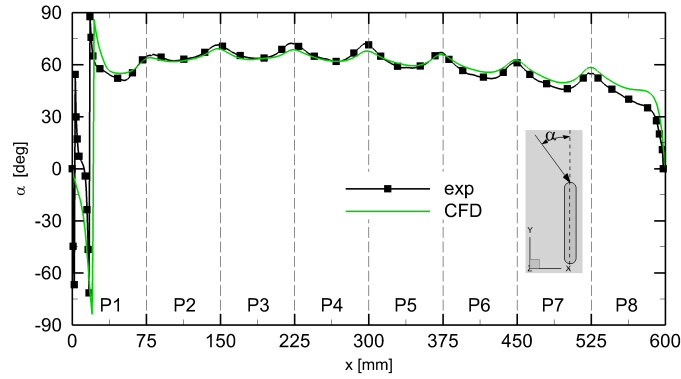


FIGURE 3.25 – Experimental [56] and *CFD* flow angle  $\alpha$  extracted in plane  $xy$  at  $y = -132[mm]$ , *G1* configuration.

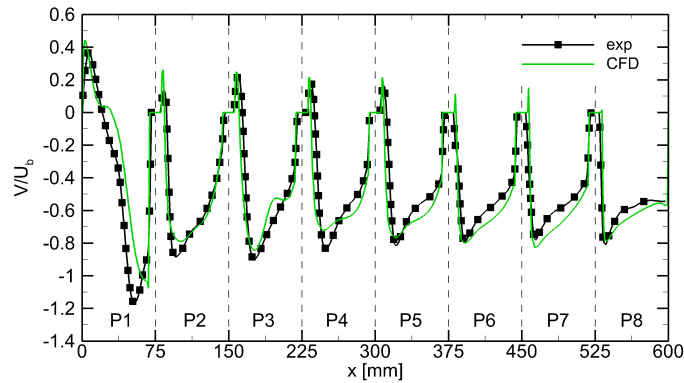


FIGURE 3.26 – Experimental [56] and *CFD*  $V$  velocities profiles in plane  $xy$  at  $y = -150[mm]$ , *G1* configuration.

Furthermore, since the horseshoe vortex is closely related to the thickness of the boundary layer's deviation [10], the agreement described above (3.25 and 3.26) is fully confirmed in Fig. 3.27 which shows a comparison of the stream-tracers in planes  $x'y$  (Figs. 3.27 (a,e)),  $xy3$  (Figs. 3.27(b,f)),  $xzi$  (Figs. 3.27(c,g)) and  $xzm$  (Figs. 3.27(d,h)). The bigger size of the horseshoe vortex close to the *SS* wall accounts for the increase in the heat transfer in the trailing side exhaust region. Once again the discrepancies found in the  $Nu$  values computed by the *CFD* code in the *IP* region might have been produced by an over-prediction in the turbulence kinetic energy  $\kappa$  (for more details see Apx. E)

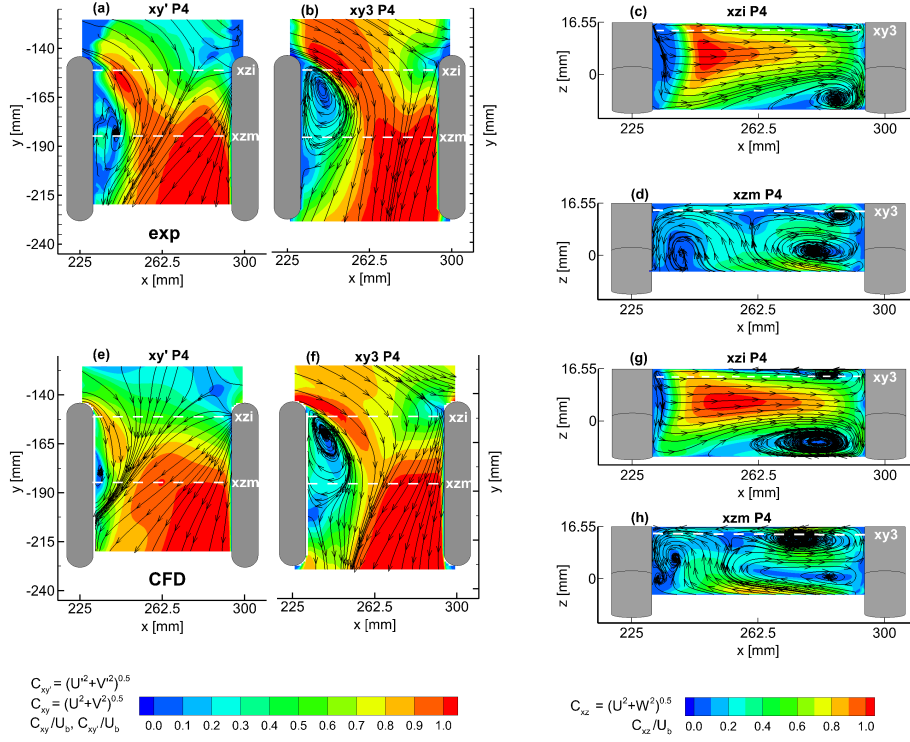


FIGURE 3.27 – Experimental [56] (a-d) and *CFD* (e-h) 3-D *IP* flow structures, *G1* configuration.

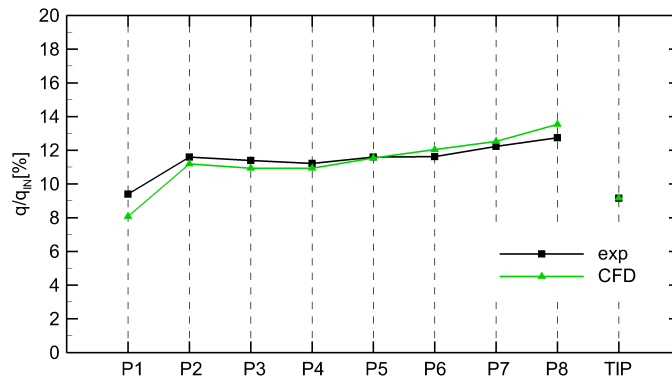


FIGURE 3.28 – Experimental [56] and *CFD* *IP* mass flow rate distribution, *G1* configuration.

Finally, a comparison between experimental [56] and numerical rates of mass-flow discharged at the tip and in each *IP* passage compared to the total one entering the channel will be carried out (Fig. 3.28). As can be seen, the match is satisfactory and both exper-

imental [56] and *CFD* values show that the mass flow discharge in *P1* passage is higher than in *G0* configuration Fig. 3.16. This increase is to be ascribed to the blockage caused by the 1<sup>st</sup> rib that redirects the flow towards  $y < 0$  [mm] in the *P1* passage.

### 3.4.4 Evaluation of the Turbulence Models

It should be noted that in this trailing edge configuration, the turbulence promoters are placed at  $30^\circ$  to the  $y$  axial direction. In this respect, several works, as Casado et al. [21] describe the significant guidance effect and the thermal performance obtained using inclined ribs in straight channels. By contrast, in the present case, the flow redirection imposed by the inclined wall at the leading side and the open trailing side, drastically reduces the flow angle of attack to the obstacles. Indeed, the experimental stream-tracers in Fig. 3.24(a) show the flow approaching the obstacle with an angle of attack of about  $0^\circ$ , measured along the direction normal to the rib, like in  $90^\circ$  turbulators configurations which represent one of the greatest challenges for the *RANS* formulation [68].

In order to fix all the computational failed predictions in the rib-roughened surface of the trailing edge cooling channel in *G1* configuration, four more turbulence models were tested:

- $k-\epsilon$ ;
- $k-\omega$ ;
- *SST*-RM (which is a beta feature on ANSYS CFX  $\text{\textcircled{R}}$ v14.0 [4] see Subsec. 2.3.2);
- *Omega Reynolds Stress (ORS)* which gives the best results for the 90 degree turbulators as demonstrated in [68].

In order to facilitate visualization and comparison, both experimental [7] and *SST* results are presented again hereinafter.

The results of the different simulations are reported in Fig. 3.29 in terms of *Nu* distribution over all the channel's surfaces and in Fig. 3.30 for the detail of the *IR* region. In the rib-roughened wall (Fig. 3.30) the only model that computes reasonably well is the *ORS* which does not predict the impingement towards the leading-side but overestimates the size of the separate structure downstream the ribs. However, in this region, the average heat transfer level is under-predicted by approximately 10 % by this model unlike all the other turbulence models according to which the average *Nu* more than 16% is lower than the one found in the experimental results [7]. The only turbulence model able to make a correct prediction of the extension of the separated structure downstream of the ribs (compare the stream-tracers path in plane  $xz_{G1}$  in Fig. 3.30) is the  $k-\epsilon$  model.

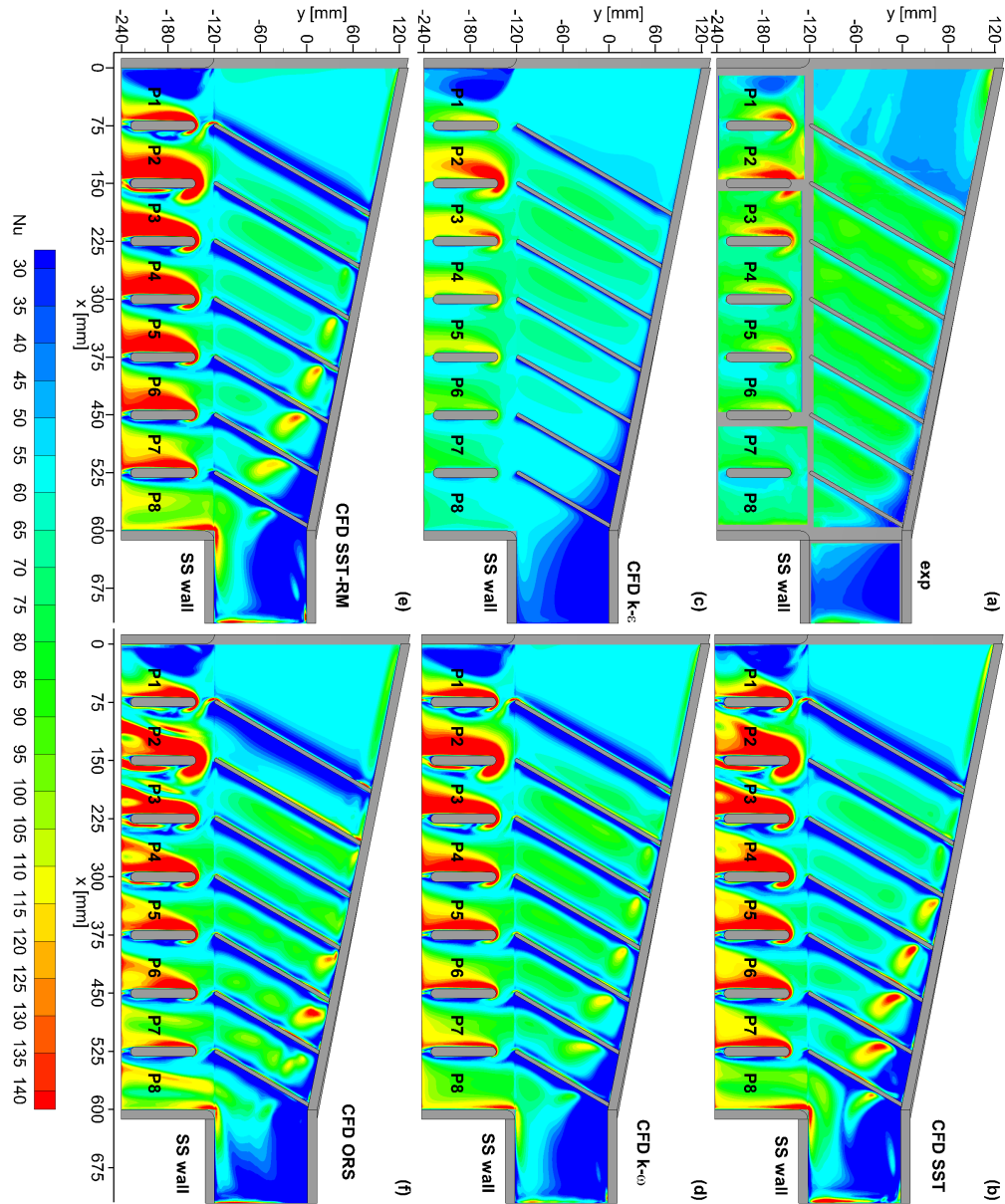


FIGURE 3.29 – Experimental [7] (a) and *CFD* (b-f) *Nu* distribution on the *SS* wall for all the turbulence models tested, *G1* configuration.

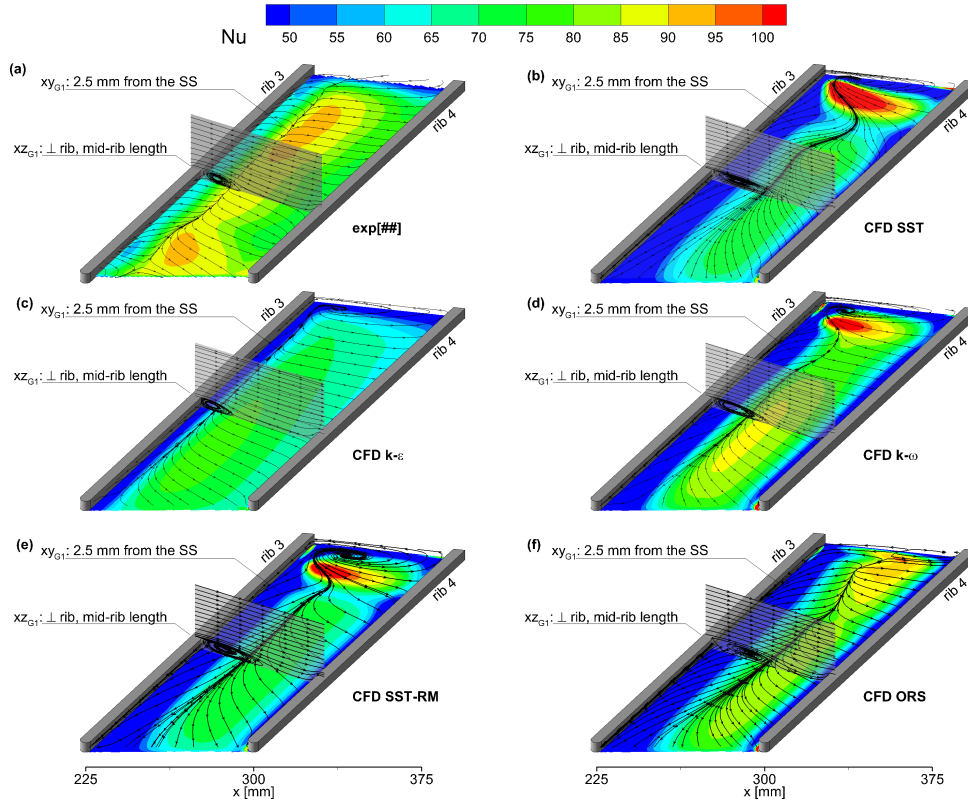


FIGURE 3.30 – Experimental [7] (a) and *CFD* (b-f)  $Nu$  maps on the *SS* and time-averaged stream-tracers path in plane  $xy_{G1}$  and  $xz_{G1}$  between the 3<sup>rd</sup> and the 4<sup>th</sup> rib for all the turbulence models tested,  $G1$  configuration.

Figure 3.31 illustrates the comparison of the predicted turbulence kinetic energy ( $\kappa$ ) by all the turbulence models between the 3<sup>rd</sup> and the 4<sup>th</sup> rib in plane  $xz_{G1}$ . It should be borne in mind that the  $k-\epsilon$  implemented in ANSYS CFX  $\text{\textcircled{R}}$ v14.0 is the only turbulence model with no limitations in the transfer of the turbulence kinetic energy between the mean flow and the turbulence motions [4] (for more details see Subsec. 2.3.2). Indeed Fig. 3.31 shows that the  $k-\epsilon$  turbulence model achieved the higher values of  $\kappa$ . In addition the experimental results [56] (Fig. 3.31) are presented only to make a comparison between the different sizes of the recirculation bubble. It should be pointed out that the reattachment point after the rib was evaluated in the position where  $U'$  is equal to zero ( $U'$  is the velocity along axis  $x'$  which is perpendicular to the direction of the rib).

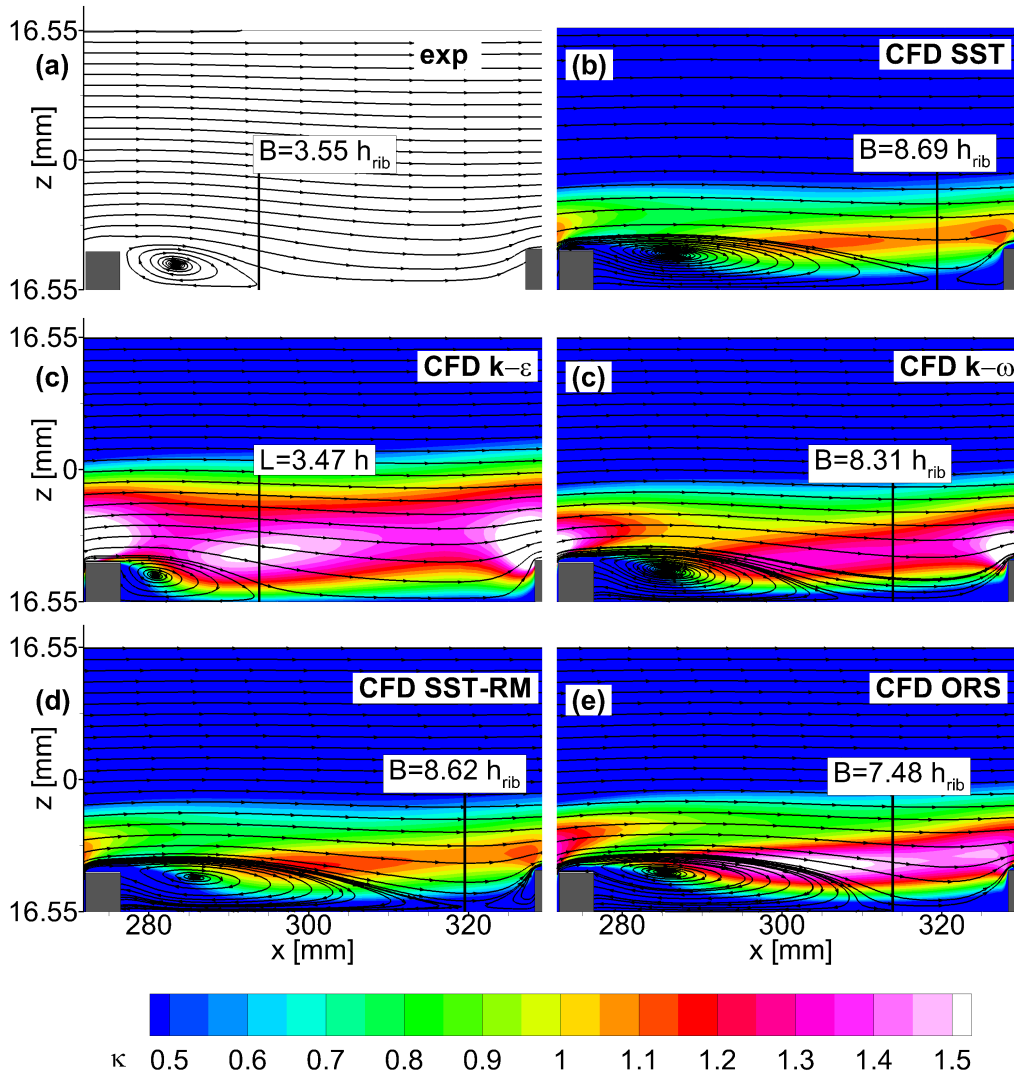


FIGURE 3.31 – Experimental [56](a) and *CFD* (b-f) stream-tracers and *CFD* (b-f) distribution of the normalized turbulence kinetic energy  $\kappa$  in the  $IR$  passage in plane  $xz_{G1}$  for all the turbulence models,  $G1$  configuration.

However, all these results demonstrate that  $90^\circ$  turbulator configurations continue to be a challenge for the RANS formulations even inside of ANSYS CFX  $\text{\textcircled{R}}$ v14.0. Slight improvements can be obtained by *ORS* turbulence model which, however, requires four times the convergence time necessary in two equation models and, therefore, there is no reason to use this turbulence model.

## 3.5 G2 Configuration

### 3.5.1 Computational Details

The computational domain was discretized using a multi-block structured mesh with hexahedral elements. A 3-D view of the grid for *G2* configuration is displayed in Fig. 3.32.

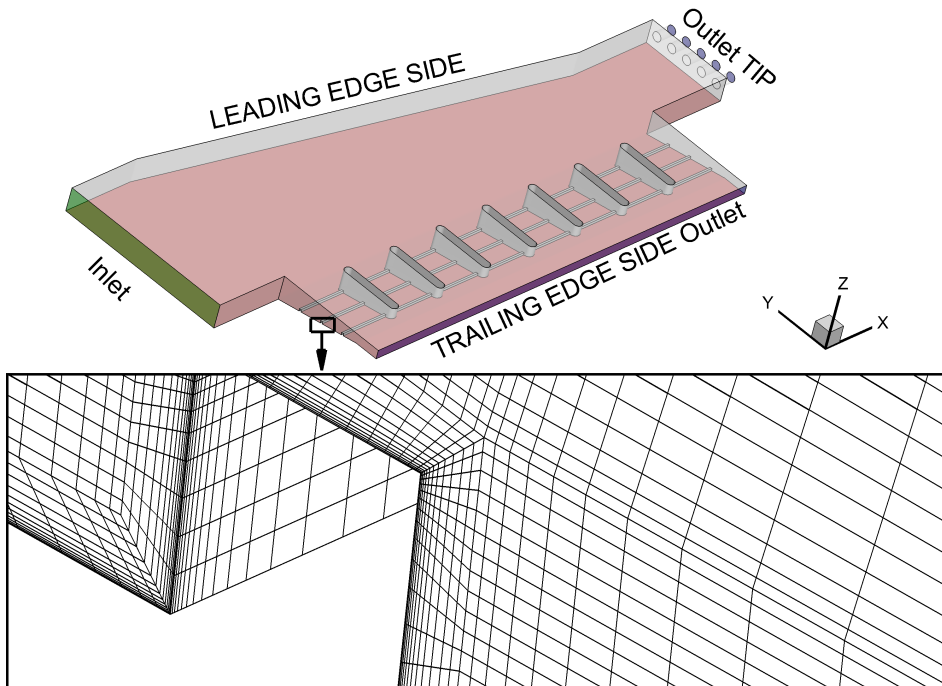


FIGURE 3.32 – 3-D view on the mesh, *G2* configuration.

The only differences from the basic *G0* mesh characteristics (see Subsec. 3.3.1), are to be found in the *IP* passages as a result of the presence of the ribs, as highlighted in Fig. 3.32. A summary of the grid and the mesh quality parameters is given in Tab.3.10 where, in order to assure the proper function of the *SST* turbulence model, the mesh has the highest number of cells if compared with the other configurations *G1* (see Subsec. 3.4.1) and *G0* (see Subsec. 3.3.1).

$N$	$y_{max}^+$	$y_{avg}^+$	$\delta_{min}$	$L_{max}$
9314430	1.83	0.35	27.9	310

TABLE 3.10 – Grid details, *G2* configuration.

The boundary conditions are the same applied for the *G0* configuration (see Subsec. 3.4.1).

As demonstrated in Fig. 3.32, the ribs walls are not heated (indeed, they are not marked in red in Fig. 3.32) and, therefore, they are simulated as an adiabatic no-slip walls in order to match the experimental conditions [7] as accurately as possible.

### 3.5.2 Quantification of the Numerical Accuracy

Discretization errors are again estimated by means of the  $GCI$  method (refer to Apx. C) and, according to the method requirements, all the grids parameters are summarized in Tab.3.11. The resulting distribution of the  $GCI$  calculated by way of three different grids is shown in Fig. 3.33 as a  $Nu$  extracted in the  $SS$  wall at  $x = -262.5[mm]$ . The analysis of the mesh sensitivity shows quite low  $GCI$  values, yet reveals areas of clear mesh-dependency inside the  $IP$  region where the ribs increase the turbulence and the 3-D flow effects. Therefore, it can be assumed that even small changes in the mesh resolution in these areas determine changes in the resulting heat transfer distribution, but consequently an increase in computational cost. Moreover, the maximum absolute value is always lower than 15[%] with an average of about 2[%], hence the results of this mesh sensitivity are sufficient for this simulation.

Grid	N	$y_{avg}^+$
Fine	9314430	0.35
Intermediate	4136918	0.48
Coarse	1888926	0.65

TABLE 3.11 –  $GCI$  study,  $G2$  configuration.

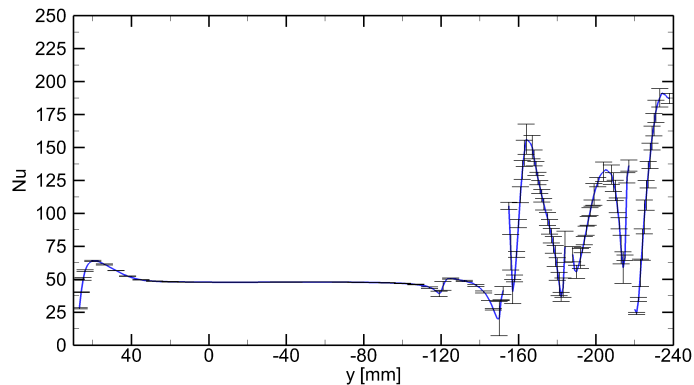


FIGURE 3.33 –  $GCI$  error band at  $SS$  surface  $x = -262.5$ ,  $G2$  configuration.

### 3.5.3 Comparison with Experimental Results

Figure 3.34 represents the comparison between experimental [7] (Fig. 3.34 (a)) and  $CFD$  (Fig. 3.34 (b))  $Nu$  maps on the  $SS$  for  $G2$  configuration. As might be expected by comparing the results with the basic  $G0$  configuration, both experimental [7] and numerical data show: a noteworthy increase in the heat transfer that is limited to the trailing side exhaust region (where the turbulators were placed), yet in the central part and in the tip region of the channel no significant differences are found.

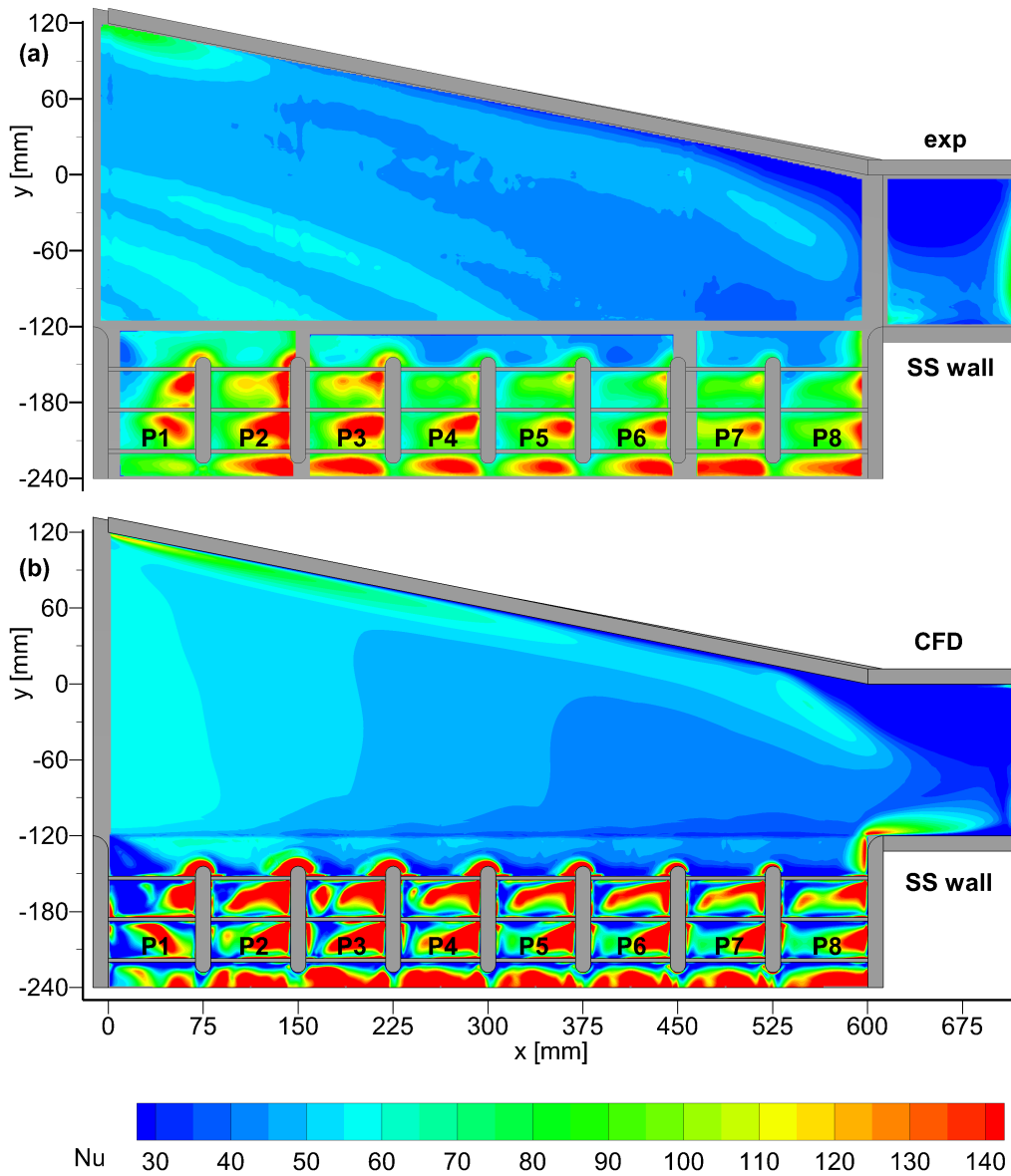


FIGURE 3.34 – Experimental [7](a) and *CFD* (b) *Nu* distribution on the *SS*, *G2* configuration.

As can be noted in Fig. 3.34 and more in detail in Fig. 3.35, which shows the *Nu* values extracted on the *SS* wall at  $y = -169.23[\text{mm}]$  (half between 1<sup>st</sup> and 2<sup>nd</sup> *IR* passage), the *CFD* code reproduces quite well the trends in the *Nu* maps but over-predicts the peaks of the *Nu* number.

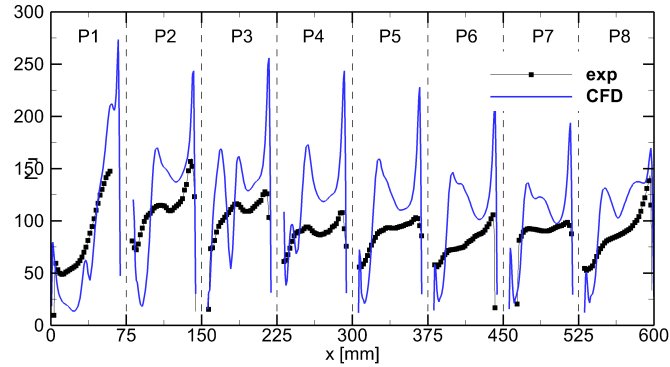


FIGURE 3.35 – Experimental [7](a) and *CFD* (b) *Nu* number distribution on the *SS* at  $y = -169.228[\text{mm}]$ , *G2* configuration.

In order to better understand the heat transfer process and the discrepancies between experimental [7] and *CFD* results, the flow field inside the channel is considered. Figure 3.37 shows the comparison between experimental [7] and numerical time-averaged velocity maps and stream-tracers in planes *xy* and *xy2*. In the dead water area at the model tip and on the downstream side of each pedestal, the *CFD* simulations predict correctly the shrinking of the recirculation bubbles which are smaller than the bubbles obtained for the basic *G0* configuration. Indeed, going more into detail, Fig. 3.36 (which plots the incidence angle ( $\alpha$ ) of the flow respect to the *y* axis extracted from plane *xy* along a line at  $y = -132[\text{mm}]$ ) and Fig. 3.38 (which reports the profiles of the mean velocity component  $V$  extracted from plane *xy* along a line at  $y = -150[\text{mm}]$ ) give evidence of the agreement between experimental [7] and numerical results and further confirm the comments earlier provided.

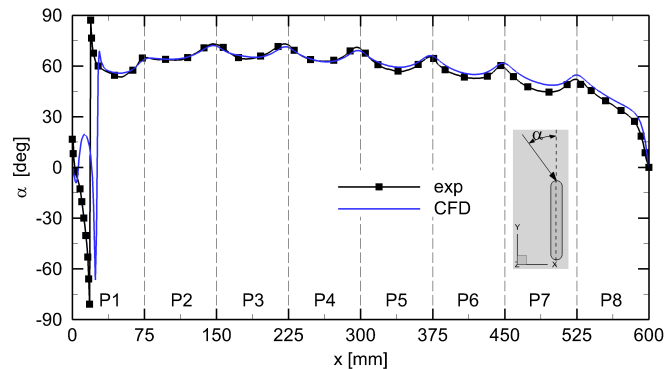


FIGURE 3.36 – Experimental [7] and *CFD* flow angle ( $\alpha$ ) extracted in plane *xy* at  $y = -132[\text{mm}]$ , *G2* configuration.



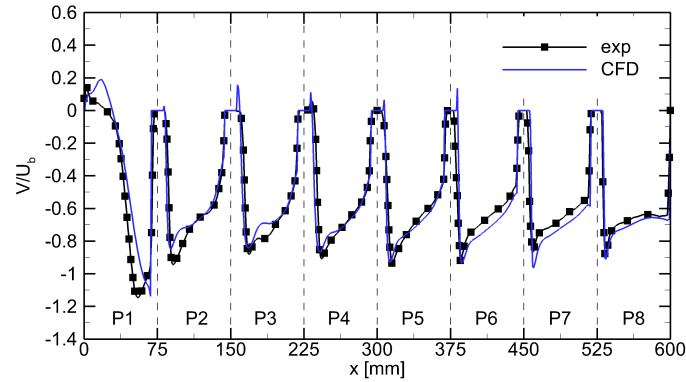


FIGURE 3.38 – Experimental [7] and *CFD*  $V$  velocity profiles extracted in plane  $xy$  at  $y = -150[mm]$ , *G2* configuration.

In order to complete the  $Nu$  analysis and to ascertain the reasons for the discrepancies between experimental [7] and numerical results, a study of the 3-D flow structures which are produced inside the *IP* passages must be carried out. First of all, in the  $P_4$  passage the comparison between the time-averaged stream-tracers paths in plane  $yz_{G2}$  (Fig. 3.39) shows the very good prediction performed by *CFD* code, which simulates very well the successive flow separations and reattachments at the *SS* produced by ribs.

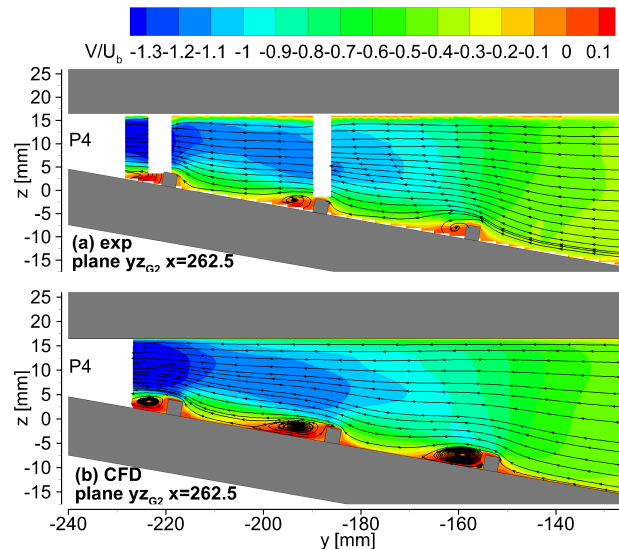


FIGURE 3.39 – Experimental [7] and *CFD* time-averaged stream-tracers at the plane  $yz_{G2}$ , *G2* configuration.

Moreover, Fig. 3.40 shows a comparison between time-averaged stream-tracers paths in planes  $xy'_{G2}$  (Figs. 3.40(a,e)),  $xy3$  (Figs. 3.40(b,f)),  $xyi_{G2}$  (Figs. 3.40(c,g)) and  $xym_{G2}$  (Figs. 3.40(d,h)). As can be seen, the match between experimental [7] and *CFD* results is fully achieved and gives evidence of the developing of an horseshoe vortex because of the deviation of the stream-tracers towards the hub that takes place on the flow layers near the *SS* in plane  $xy'_{G2}$  (Figs. 3.40 (a,e)) and near the *PS* wall in plane  $xy3$  (Figs. 3.40 (b,f)). The time-averaged stream-tracers paths in plane  $xyi_{G2}$  (Figs. 3.40(c,g)) and in  $xym_{G2}$  (Figs. 3.40(d,h)) confirm the existence of these horseshoe vortices on the *PS* ( $z > 0$ [mm]) and *SS* ( $z < 0$ [mm]) and show the accurate prediction computed by *CFD* simulations.

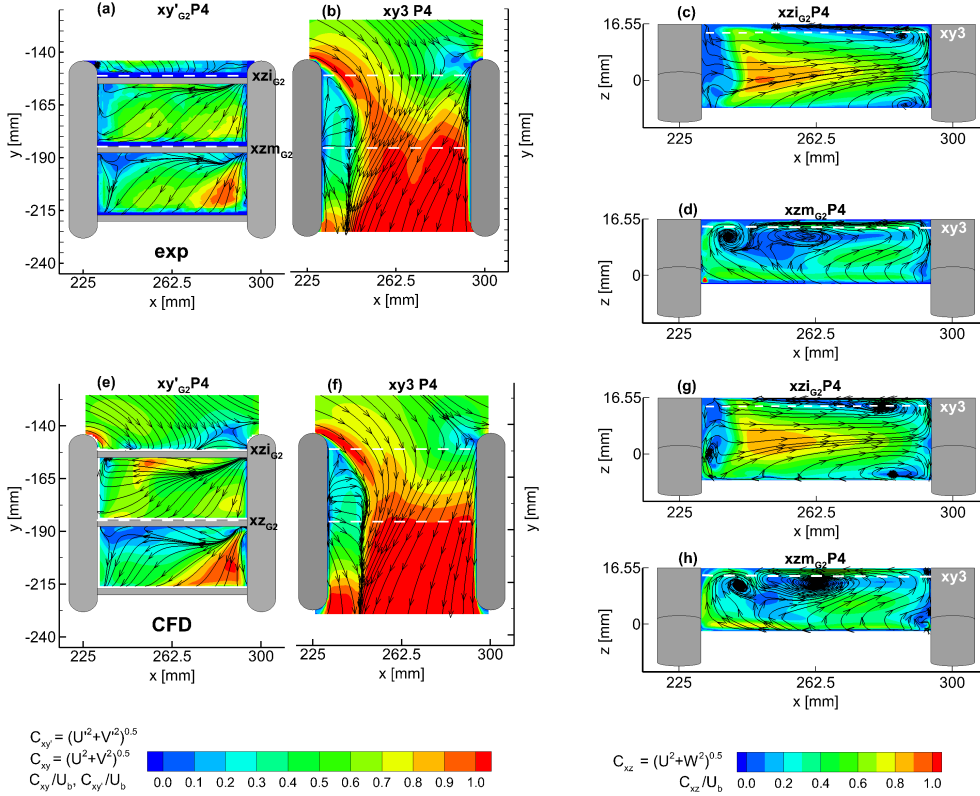


FIGURE 3.40 – Experimental [7] and *CFD* 3-D *IP* flow structures inside *P4*, *G2* configuration.

Finally in Fig. 3.41 a comparison between the experimental [7] and *CFD* average *Nu* values inside each *IP* passage is made. As can be seen, the numerical average values are over-predicted from the *P2* to *P8* passages as a result of the over-prediction of the effects of mixing induced by the horseshoe vortex branch and the ribs, and hence of the heat transfer inside the *IP* exhaust passages. An over-prediction of the turbulence kinetic energy might have produced again the increase mentioned above (see Apx.E).

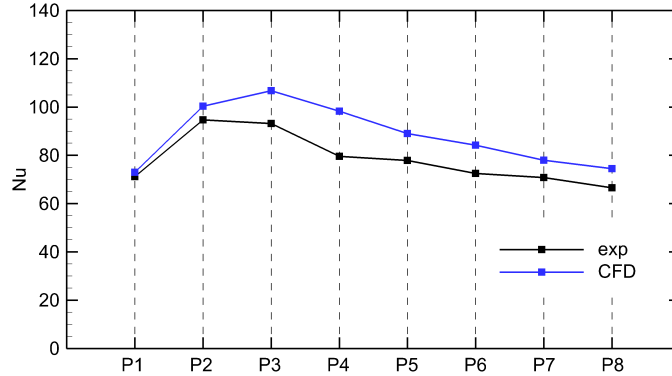


FIGURE 3.41 – Experimental [7] and *CFD* averaged-*Nu* values computed over each *IP* passage, *G2* configuration.

### 3.6 Summary and Assessment of the Global Performance

In this chapter an assessment of the *SST* turbulence model developed in the commercial software ANSYS CFX  $\text{\textcircled{R}}$ v14.0 in static ( $Ro = 0$ ) condition for three different configurations, namely *G0*, *G1* and *G2*, was carried out thanks to the experimental database available in literature: [7], [5] and [56]. Moreover, because of the computational failed predictions made by this turbulence model for *G1* configuration, four more turbulence models were tested: *k- $\epsilon$* , *k- $\omega$* , *SST-RM* and *ORS*. Only *k- $\epsilon$*  model seems to predict correctly the recirculation region after the rib and, hence, the heat transfer distribution in the inter-rib passage. However some problems, in particular related to convergence, were ascertained. This effect might be ascribed to the near wall resolution of  $y_{max}^+ < 0.2$  only required by this turbulence model [4] which was impossible to achieve because of the CPU limitations (i.e. maximum number of cells). Conversely, the other *RANS* models would require at least  $y_{max}^+ < 2$  [4].

Table 3.12 shows an analysis concerning the enhancement of the heat transfer allowed by configuration *G1* and *G2* obtained comparing experimental and *CFD* *Nu* value averaged on the whole *SS* wall and then normalized according to the one obtained for the basic *G0* configuration. As can be seen, both results show an increase of more than 20[%] for configuration *G1*, whereas *G2* achieves an increase of about only 5[%]. The small differences in  $\bar{Nu}$  are within the measurements uncertainty, therefore, this averaged behavior, predicted by the *CFD* simulations, can be considered completely equivalent to the experimental data [7].

Finally, Fig. 3.42 shows an evaluation of a comparison between the different mass flow rates discharged at the tip and by each *IP* passage compared to the total mass flow entering for the three configurations.

	$G1$	$G2$
$EF_{EXP} = Nu/Nu_{G0} - exp$	1.25	1.05
$EF_{CFD} = Nu/Nu_{G0} - CFD$	1.21	1.06
$1 - EF_{CFD}/EF_{exp}$	3.2	0.9

TABLE 3.12 – Experimental [7] and  $CFD$  total average  $Nu$  number for configuration  $G1$ ,  $G2$  with respect to  $G0$  configuration.

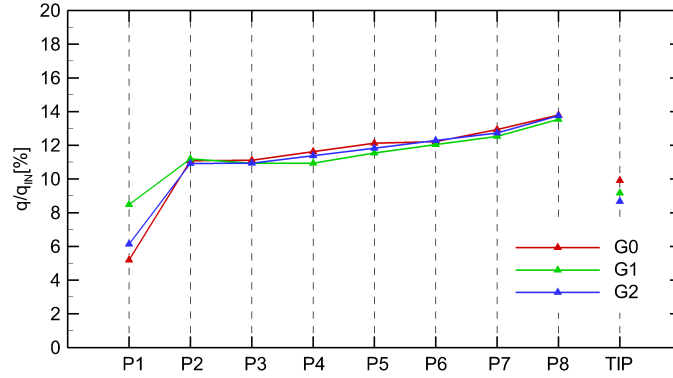


FIGURE 3.42 – Experimental [7] and  $CFD$  averaged- $Nu$  values computed over each  $IP$  passage,  $G2$  configuration.

It should be noted that only the numerical results are plotted because the correspondence with the experimental data [5] and [56] available (no experimental data are available for  $G2$  configuration) was already verified in the previous subsections (Subsec. 3.3.3 and Subsec. 3.4.3). These results further confirm that  $G1$  configuration provides a better performance than  $G0$  and  $G2$  configurations since it gives evidence of almost uniform mass flow rates equal to 11[%] of  $q_{in}$  discharged in the  $IP$  passages. In  $G0$  and  $G2$  configurations less than half flow coolant rate is discharged in the  $P1$  passage as a result of the blockage effect imposed by the large recirculation bubble. Obtaining a uniform mass flow rate along the trailing side region and even inside each  $IP$  passage is crucial to ensuring uniform flow conditions at the trailing side exits, which is mandatory if the blade is provided with cut-back cooling [12], [11].

---

# 4

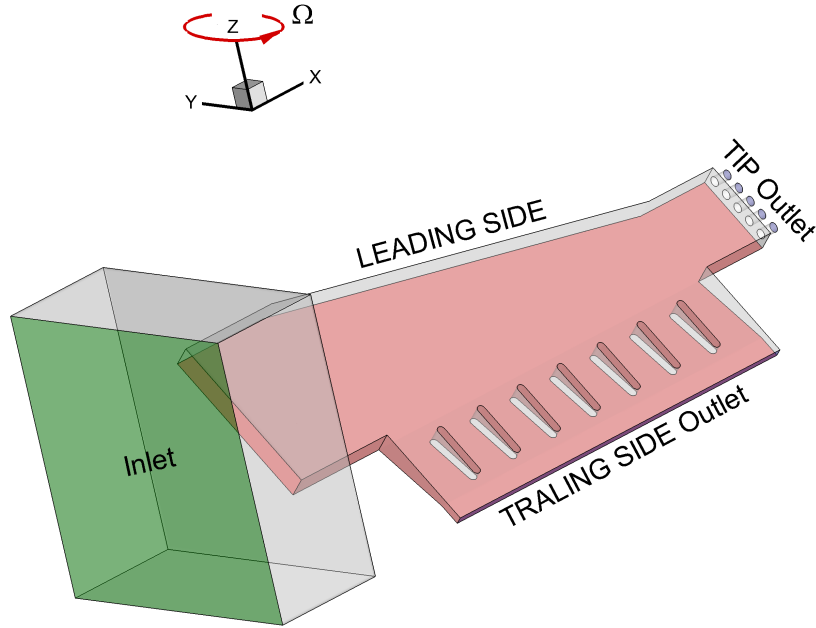
## Effects of Rotation and Different Channel Orientations in a Trailing Edge Channel

In the previous chapter (Ch. 3) a validation by using the experimental data available in Armellini et al.[5], Armellini et al.[7] and Mucignat et al.[56] was carried out merely in static condition for configuration *G0*, *G1* and *G2*. In the present chapter an upgrade of the validation for *G0*'s mesh and *G1*'s mesh is to be done in the same rotating conditions (i.e.  $Ro = 0.23 - 0.26$ ) as those in the data available respectively in Armellini et al.[5] and Andrei et al.[3] for configuration *G0*, and in Mucignat et al.[56] and in Bonanni et al.[14] for *G1* configuration. Subsequently, the numerical results will be extended to engine-like rotation number, namely  $Ro = 0.46$ , and different channel orientations with respect to the rotation axis *Z* (i.e.  $\gamma = 22.5^\circ$  and  $\gamma = 45^\circ$ ).

### 4.1 Computational Details

Experimental data are not available for channel orientations and *Ro* numbers other than the ones studied in Armellini et al.[5] and Andrei et al.[3] for *G0* configuration and in Mucignat et al.[56] and in Bonanni et al.[14] for *G1* configuration (i.e.  $Ro = 0.23 - 0.26$  and  $\gamma = 0^\circ$ ). The lack of measurements of inlet velocity profiles which can be used as numerical boundary conditions for  $\gamma \neq 0^\circ$  and  $Ro > 0.23$  compelled the authors to simulate the entire channel inlet by using a large domain mesh including, part of the settling chamber, as shown in Fig. 4.1 (which illustrates the domain for *G0* configuration at  $\gamma = 45^\circ$ ).

The boundary conditions are the same as the ones applied in the previous chapter (see Subsec. 3.3.1 and Subsec. 3.4.1). As can be seen in Fig. 4.1, only the inlet boundary condition was shifted to the inlet of the settling chamber where a mass flow equal to  $0.0487 [Kg/s]$  was imposed in order to obtain the same experimental *Re* number (equal to 20000) in the channel.

FIGURE 4.1 – 3-D view on the domain for  $G0$  configuration at  $\gamma = 45^\circ$ .

In the experiments, which provide the validation data for the present simulations (Armellini et al.[5], Andrei et al.[3], Mucignat et al.[56] and Bonanni et al.[14]), a polyester fiber filter was placed at the channel exit in order to pressurize the test section and made the effects of the centrifugal pressure gradients negligible compared to the ones originated from the Coriolis forces. The filter was modelled as an isotropic porous region by introducing an additional source term in the momentum equation [4]. The kinetic pressure loss coefficient required by the solver was set at a value that the computed pressure loss across the filter was equal to the measured one for  $\gamma = 0^\circ$  and  $Ro = 0$  (Armellini et al.[5], Andrei et al.[3], Mucignat et al.[56] and Bonanni et al.[14]). The honey-comb filter(number 2 in Fig. 3.1) used in the experiments at the junction between the channel and the settling chamber was modelled using the same approach. In this case a directional loss model was implemented, which required a kinetic pressure loss coefficient to be specified along both stream-wise and transverse directions. In particular, much higher losses in the transverse directions,  $y$  and  $z$ , than in the stream-wise direction,  $x$ , were applied. This results in the suppression of the transverse velocity components  $V$  and  $W$ , as it is expected for a flow going through a fine honey-comb . The parameter setting was verified by comparing the velocity profiles computed at the channel inlet with the experimental data Armellini et al.[5] and Mucignat et al.[56], for  $\gamma = 0^\circ$  and  $Ro = 0, 0.23$ .

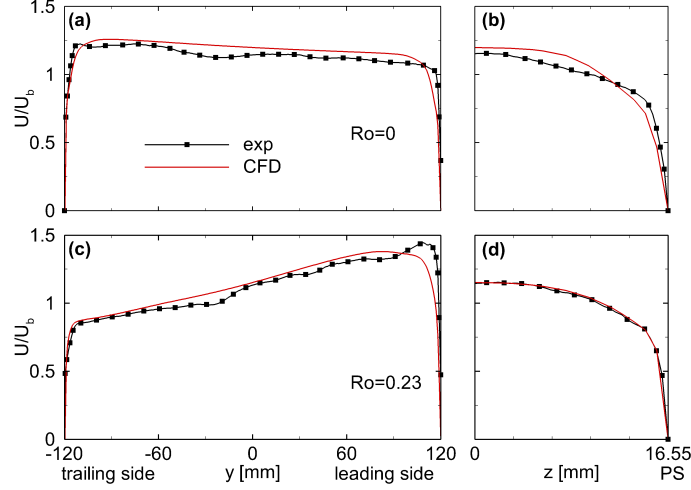


FIGURE 4.2 – Experimental [5] and *CFD*  $U$  at the channel inlet,  $x = -69.8[mm]$ .

Figure 4.2 shows the profiles of the mean velocity component  $U$  (non-dimensionalized by the bulk flow velocity in the inlet channel,  $U_b$ ) in the symmetry planes of the inlet channel  $xy$  and  $xz$ , at the position  $x = -69.8[mm]$ , for  $Re = 20000$ ,  $Ro = 0, 0.23$  and  $\gamma = 0^\circ$ . The numerical results match the experimental ones, despite the limited channel length available for the flow development downstream the honey-comb filter placed at the channel inlet ( $x = -161[mm]$ ). The slight flow imbalance towards the trailing side of the channel ( $y < 0[mm]$ ) is due to the blockage effect caused by the redirecting wall at the leading side. This effect is well simulated by the *CFD* computations for  $Ro = 0$  (Fig. 4.2 (a)), as well as the strong flow imbalance towards the leading side ( $y > 0[mm]$ ) for  $Ro = 0.23$  (Fig. 4.2 (c)). As commented in Armellini et al.[5], the opposite flow imbalance observed in the case of rotating channel is due to potential flow effects. Indeed, the slightly viscous flow entering the channel from the settling chamber tends to conserve its angular momentum giving rise to relative eddies whose angular velocity is opposite to the rotating channel's one. The superposition of these counter-rotating eddies and the through-flow results in higher relative velocities in the channel leading side and lower ones in the trailing side region. It should be pointed out that this inviscid flow effect generates a flow imbalance that is opposite to the one expected as a result of the Coriolis forces. In addition to the mean velocity profiles, also the predicted turbulence intensity  $I$  between the experimental and numerical values was evaluated in plane  $xy$  at  $y = 0[mm]$ . The experimental data must be computed by means of the velocities fluctuations measured along the three spatial directions  $I = \sqrt{(u'^2 + v'^2 + w'^2)/3}/U_b = 3.28[\%]$ [5], while the numerical turbulence intensity was computed using the turbulence kinetic energy  $\kappa$   $I = \sqrt{2/3 \cdot \kappa}/U_b = 3.9[\%]$ .

## 4.2 G0 Configuration

### 4.2.1 Grid Generation and Quantification of Numerical Accuracy

The computational domain was discretized by using multi-block structured mesh with hexahedral elements. As commented in the previous section (see Sec. 4.1), unlike to the mesh developed for the static condition ( $Ro = 0$  see Subsec. 3.3.1) for  $G0$  configuration, only a large domain mesh for half of the settling

Grid	N	$y_{avg}^+$
Fine	8684084	0.51
Intermediate	3645059	0.69
Coarse	1529978	0.95

TABLE 4.1 –  $GCI$  study,  $G0$  rotating configuration.

chamber was added. Figure 4.1 illustrates a 3-D view of the domain for the configuration  $G0$  at  $\gamma = 45^\circ$  where 8684084 cells were used. Discretization errors were estimated using the local velocity modulus ( $C_{xyz}$ ) by means of the  $GCI$  method (see Apx.C): in order to fulfill its requirements, three similar meshes characterized by different spatial resolutions were employed for the maximum rotation number  $Ro = 0.46$  and  $\gamma = 45^\circ$ . The parameters of the grids used in the refinement study are summarized in Tab.4.1. Figures 4.3 (a, b) show two profiles of the velocity modulus,  $C_{xyz}$ , extracted at  $y = -132[mm]$  respectively along the  $x$  and  $z$  directions. Each error bar is representative of the local value of the  $GCI$  computed for the finest mesh. The analysis provides satisfactory results along all the channel height Fig. 4.3(b) and width Fig. 4.3(a), with an average error lower than 2[%] with the exception of limited regions inside the boundary layer, where small changes in the mesh resolution determine changes in the resulting flow field. Therefore, the finer mesh is a good compromise between spatial resolution and computational effort.

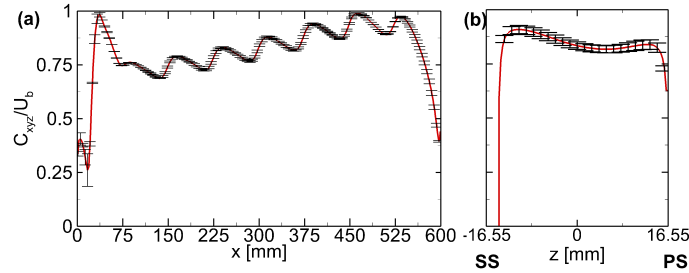


FIGURE 4.3 –  $GCI$  error band at  $Ro = 0.46$  and  $\gamma = 45^\circ$  in plane:  $xy$  at  $z = 0[mm]$   $y = -132[mm]$  (a) and  $xz$  at  $y = -132[mm]$   $x = 300[mm]$ ,  $G0$  rotating configuration.

### 4.2.2 Comparison with Rotating Experimental Results

Figure 4.5 represents the  $Nu$  maps for  $G0$  configuration. It should be noted that the thermal measurements ([3]) were obtained at  $Ro = 0.26$  (slightly higher than the rotation number of the flow field data[5]). Moreover, in contrast with the data presented in the previous chapter (ch.3), the heat transfer measurements were performed

at the *PS* (Fig. 4.5(a)). Hence, two different simulation were carried out: one with the *PS* heated at  $Ro = 0.26$  (Fig. 4.5 (b)) in order to have the same conditions as in the heat transfer experiments conducted in Andrei et al.[3]; the other with the *SS* heated at  $Ro = 0.23$  (Fig. 4.5 (c)) in order to compare the heat transfer results with the static ones (see Subsec. 3.3.3) and the flow field with the experiments [5].

As can be seen (Figs. 4.5(a,b)), from a qualitative viewpoint, the *CFD* predictions reproduce quite well the trends in the *Nu* maps; the comparison between static and rotating numerical results (Fig. 3.11 vs Fig. 4.5(c)) shows an increase in the size of the region of low heat transfer near the tip close to the redirecting wall, and a decrease in the size of the low heat transfer area in the *P1* passage. Moreover, an overall decrease and more uniform *Nu* values inside all the other *IP* passages are found when the rotation takes place.

The comparison between the results in rotating conditions at the *PS* (Figs. 4.5 (a,b)) displays an over-prediction of the size of the low heat transfer region near the tip close to the redirecting wall computed by the *CFD*. However, the agreement in the central part of the channel is good, as can be seen more in detail in Fig. 4.4, in which the *Nu* profiles are extracted along a line at  $y = -96[mm]$  at the *PS*. Only in the last two *IP* passages, the numerical results show a more evident decrease in the *Nu* values, resulting from the aforementioned over-prediction in the size of the region with the low heat transfer. By contrast, in the trailing side exhaust region greater discrepancies between the experimental and numerical values are found. Figure 4.6 shows the *Nu* values extracted from the *PS* surface at  $y = -150[mm]$  where the *CFD* code overpredicts the heat transfer distribution close to the *IP* walls. However, in both experimental and numerical results, these high heat exchange regions show peaks values and extensions which are quite constant moving towards the channel tip, as displayed in Fig. 4.5 and more in detail in Fig. 4.6.

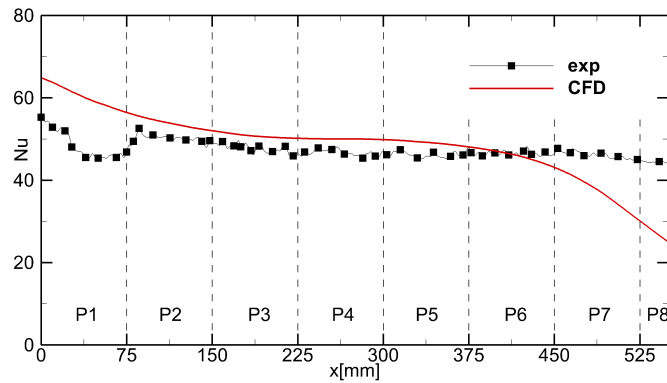


FIGURE 4.4 – Experimental [3] and *CFD* *Nu* number distribution at the *PS* at  $y = -96[mm]$  at  $Ro = 0.26$ , *G0* rotating configuration.

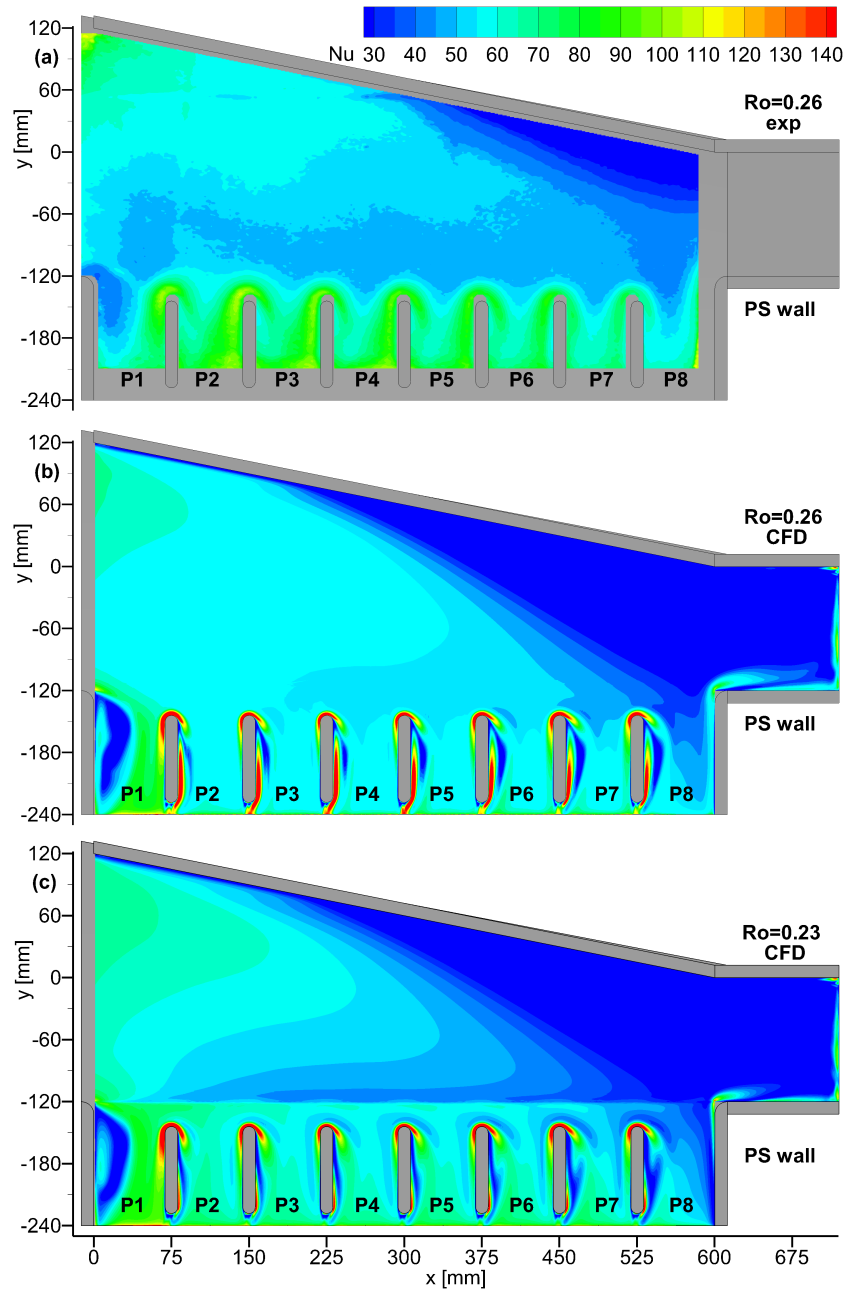


FIGURE 4.5 – Experimental [3] and *CFD* Nu distribution at  $Ro = 0.26$  at *PS* (a,b) and at  $Ro = 0.23$  at *SS* (c), *GO* rotating configuration.

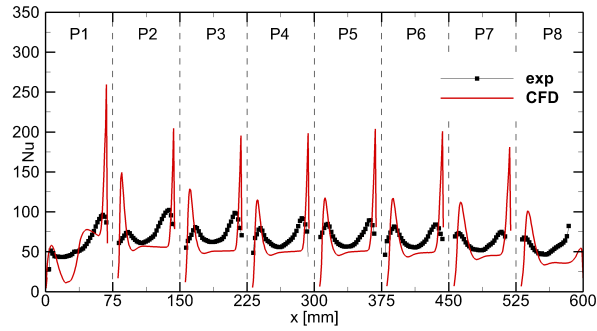


FIGURE 4.6 – Experimental [3] and *CFD* *Nu* number distribution at the *PS* at  $y = -150$  [mm] at  $Ro = 0.26$ , *G0* rotating configuration.

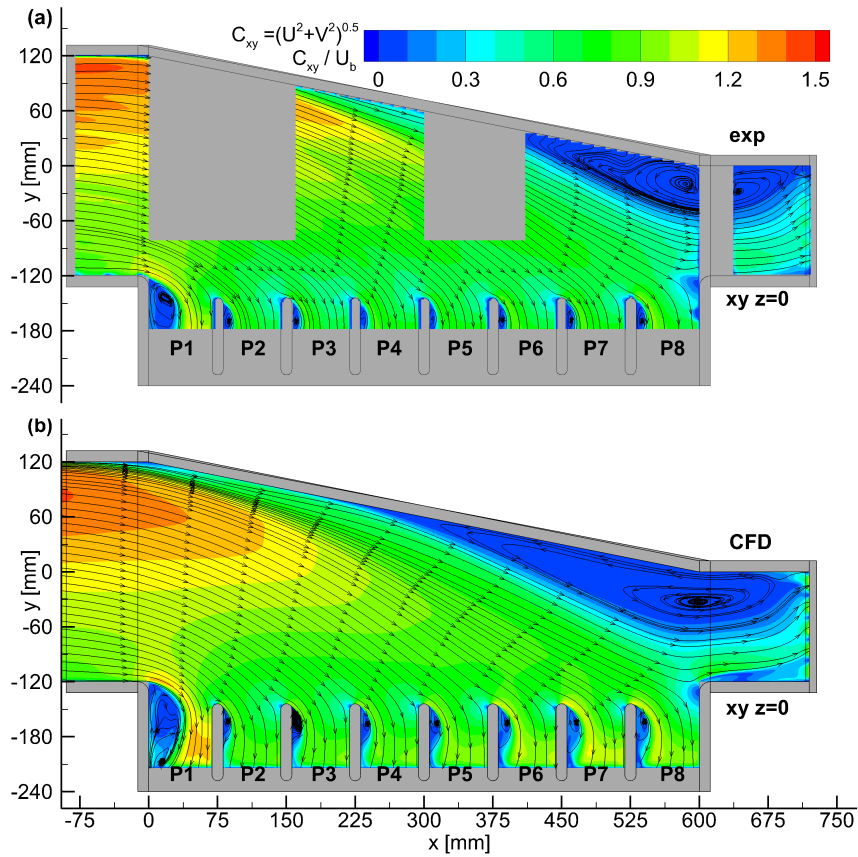


FIGURE 4.7 – Experimental [5](a) and *CFD* (b) time-averaged stream-tracers and contour plots of the in-plane velocity modulus  $C_{xy}$  in the  $xy$  plane for  $Ro = 0.23$ , *G0* rotating configuration.

In order to have a better understanding of the heat transfer mechanism and the discrepancies between experimental and numerical results, the flow field inside the channel is considered. Figure 4.7 illustrates the comparison between the experimental and numerical time-averaged velocity maps and the stream-tracers in plane  $xy$ . It should be noted that all the main characteristics of the flow field are very accurately simulated by the *CFD* computations, and the comparison with the results obtained in static condition (Fig. 3.13) demonstrates a different behavior of the flow: wider flow separation at the blade tip (which accounts for the larger size of the region with low heat transfer commented above) and more uniform flow velocity at the trailing side.

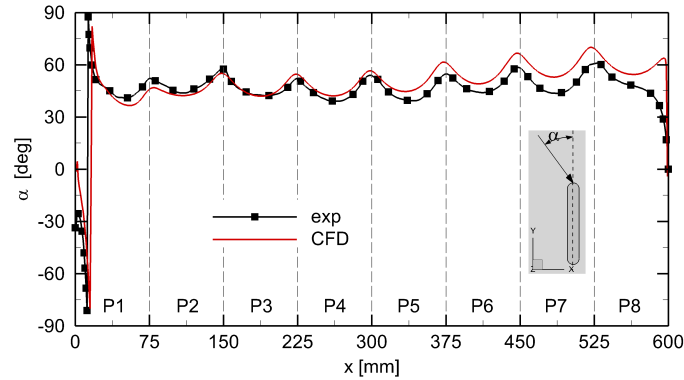


FIGURE 4.8 – Experimental [5] and *CFD* flow angle  $\alpha$  extracted in plane  $xy$  at  $y = -132[mm]$  at  $Ro = 0.23$ ,  $G0$  rotating configuration.

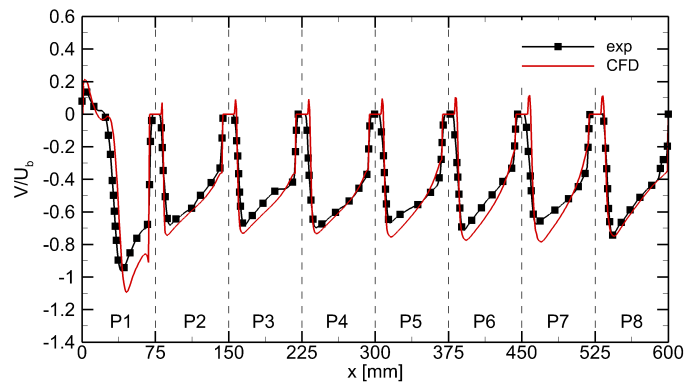


FIGURE 4.9 – Experimental [5] and *CFD*  $V$  profiles extracted in plane  $xy$  at  $y = -150[mm]$  at  $Ro = 0.23$ ,  $G0$  rotating configuration.

Going more into detail, the incidence angle  $\alpha$  extracted from plane  $xy$  along a line at  $y = -132[mm]$  which is plotted in Fig. 4.8 demonstrates the good match between experimental and numerical values; only in the last three *IP* passages ( $6^{th}$  Pedestal Passage

(P6)–P8) slight differences are found again as a result of the over-prediction of the recirculation bubble’s size computed by the *CFD* code. Similar conclusions can be drawn for Fig. 4.9 which plots the comparison between the experimental and numerical mean velocity profiles  $\mathbf{V}$  extracted from plane *xy* along a line at  $y = -150[\text{mm}]$ .

At this point it might be inferred that the agreement between experimental and *CFD* results is less satisfactory than in the static case (Subsec. 3.3.3 Fig. 3.15). However, the general flow structure is well captured and the complex *IP* flow topology is correctly simulated for  $Ro = 0.23$ , as shown in Fig. 4.10 which illustrates a comparison between experimental and *CFD* time-averaged stream-tracers in planes *xy* (Figs. 4.10 (a,d)), *xy3* (Figs. 4.10 (b,e)), *xzR* (Figs. 4.10 (c,f)) inside the  $P_4$  *IP* passage. As can be seen, if these results are compared with the ones obtained in static condition (Fig. 3.17), the disappearance of the horseshoe vortices is observed in both experimental and numerical data. This flow behavior can be ascribed to the rotational effects (described more in detail in the subsection below (Subsec. 4.2.3) that produce a noteworthy acceleration of the near-wall flow leading to the thinning of the boundary layers and, therefore, resulting in the disappearance of the horseshoe vortices.

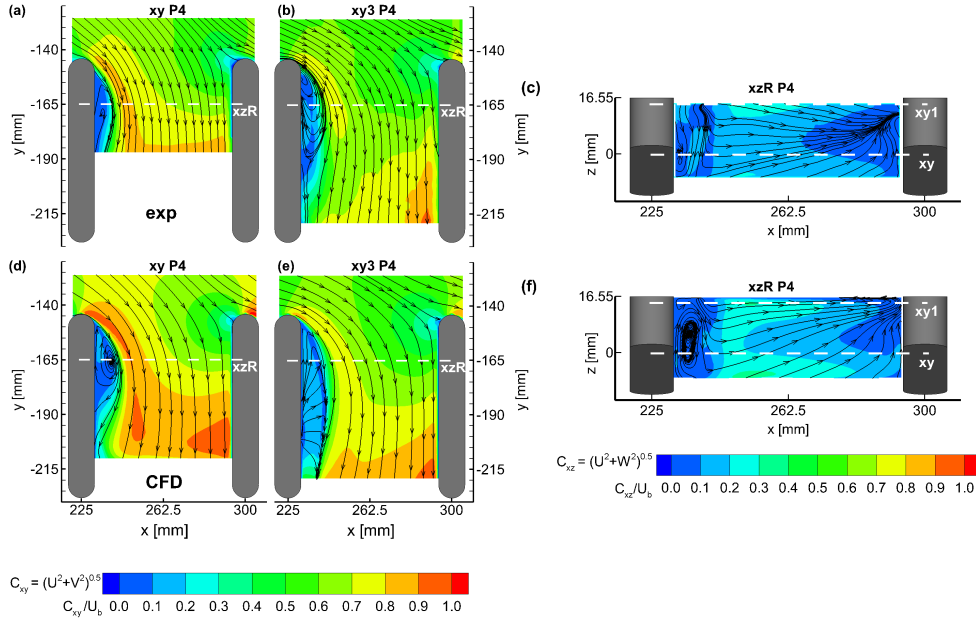


FIGURE 4.10 – Experimental [5] and *CFD* *IP* flow structures at  $Ro = 0.23$ , *G0* rotating configuration.

### 4.2.3 Effects Produced by $Ro$ Increases

In this subsection, the rotational effects will be analyzed on the basis of the numerical results obtained for channel configurations  $\gamma = 0[^\circ]$  and  $Ro = 0, 0.23$  and  $0.46$ . For a

clear reading of this subsection, it is useful to bear in mind that for  $\gamma = 0[^\circ]$  the  $y$  axis is aligned with the peripheral velocity. For each of the three rotation numbers, Fig. 4.11 shows the velocity component  $U$  at the channel inlet.

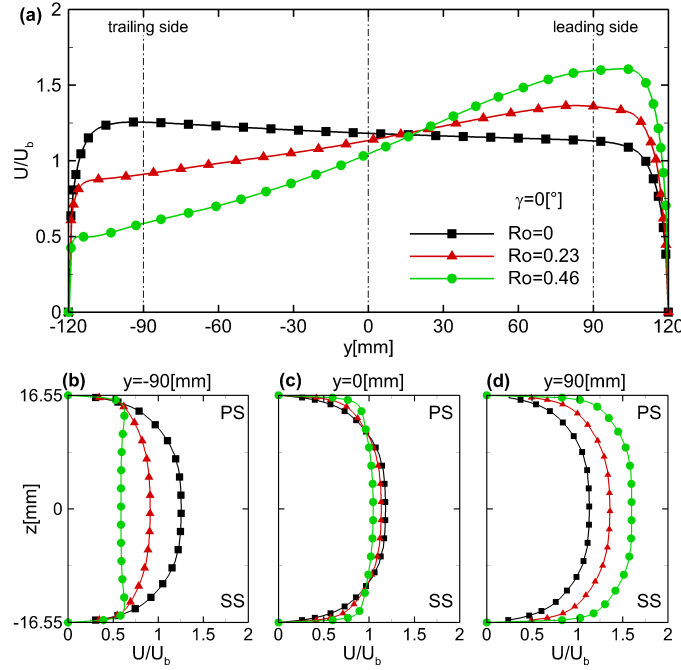


FIGURE 4.11 – *CFD*  $U$  velocity profiles at  $x = 69.8[mm]$  for  $\gamma = 0[^\circ]$  and different  $Ro$ .  $z = 0[mm]$ (a),  $y = 90[mm]$ (b),  $y = 0[mm]$ (c),  $y = 90[mm]$ (d).

As  $Ro$  increases (Fig. 4.11(a)) the flow imbalance towards to the channel leading side ( $y > 0[mm]$ ) becomes stronger, as expected in view of the dependence of the potential flow effects on the channel angular velocity, as commented at the beginning of this chapter. In the vertical planes (Figs. 4.11(b-d)) the velocity distributions at the channel leading side (Fig. 4.11 (d)) are similar to each other, while, moving towards the trailing side, the differences become more significant (Figs. 4.11(a,b)). In particular, for  $Ro = 0.46$ , at the mid channel width (Fig. 4.11(c)) the  $U$  velocity profile becomes flatter and characterized by thinner boundary layers, while at the trailing side (Fig. 4.11(b)) an over-speed near the confining walls is found. This behavior is consistent with the increasing intensity of the Coriolis forces which results in wider and more intense secondary structures in the channel cross-section, as evidenced in Fig. 4.12, which illustrates the velocity contour plots and the time-averaged stream-tracers in the channel cross-section at  $x = -69.8[mm]$ . It should be pointed out that when the channel starts rotating, the Coriolis forces produce a negative pressure gradient along the  $y$  direction, i.e., higher pres-

ures occur at the trailing side ( $y < 0[mm]$ ). Since Coriolis forces are proportional to the velocity magnitude, inside the boundary layers the pressure gradient is not balanced by the local Coriolis forces, which leads to the establishment of the widely known secondary structures shown by the stream-tracers in Figs. 4.12(b,c). While the core flow is deviated towards the trailing side ( $y < 0[mm]$ ), the Coriolis-induced pressure gradient generates also a stream-wise component, which accounts for the acceleration of the boundary layer flow along the  $x$  direction. This effect is particularly evident for  $Ro = 0.46$  at position  $y = -90[mm]$ . Moreover, as can be seen in Figs. 4.12 (b,c), the vortices induced by rotation are confined to the channel leading side, i.e. where the velocities are higher as a result of the potential flow effect (discussed when Fig. 4.2 was introduced).

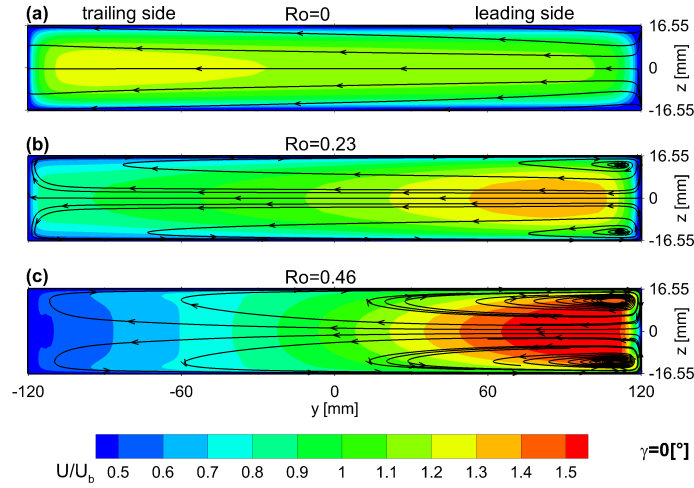


FIGURE 4.12 – CFD contours of  $U$  velocity component and stream-tracers path at the channel inlet,  $x = -69.8[mm]$ ,  $Ro = 0$ (a),  $Ro = 0.23$ (b),  $Ro = 0.46$ (c).

Figure 4.13 illustrates the overall flow behavior inside the channel with the time-averaged velocity maps and stream-tracers in plane  $xy$  ( $z = 0[mm]$ ) (Figs. 4.13(d-f)) and  $xy3$  ( $z = 14.55[mm]$ ) (Figs. 4.13(a-c)). As  $Ro$  increases, a flow accumulation is found near the leading side at the channel inlet and the separation bubble at the blade tip increases in size. Moreover, when looking at the mean-flow path on near-wall plane  $xy3$  (Figs. 4.13 (a-c)), the flow deviation towards  $y > 0[mm]$ , imposed at channel inlet by the Coriolis effects, grows as  $Ro$  increases. Conversely, the flow in the channel's central plane  $xy$ , displays a deviation towards the trailing side which is stronger for  $Ro = 0.23$  than for  $Ro = 0$  and  $Ro = 0.46$  (comparing Figs. 4.13 (d-f)). This trend can be explained if the following characteristics are considered: very different velocities distributions at the channel inlet (Figs. 4.11 and 4.12) and the Coriolis forces effects in the central part of the channel where the flow is deviated towards the exit slots.

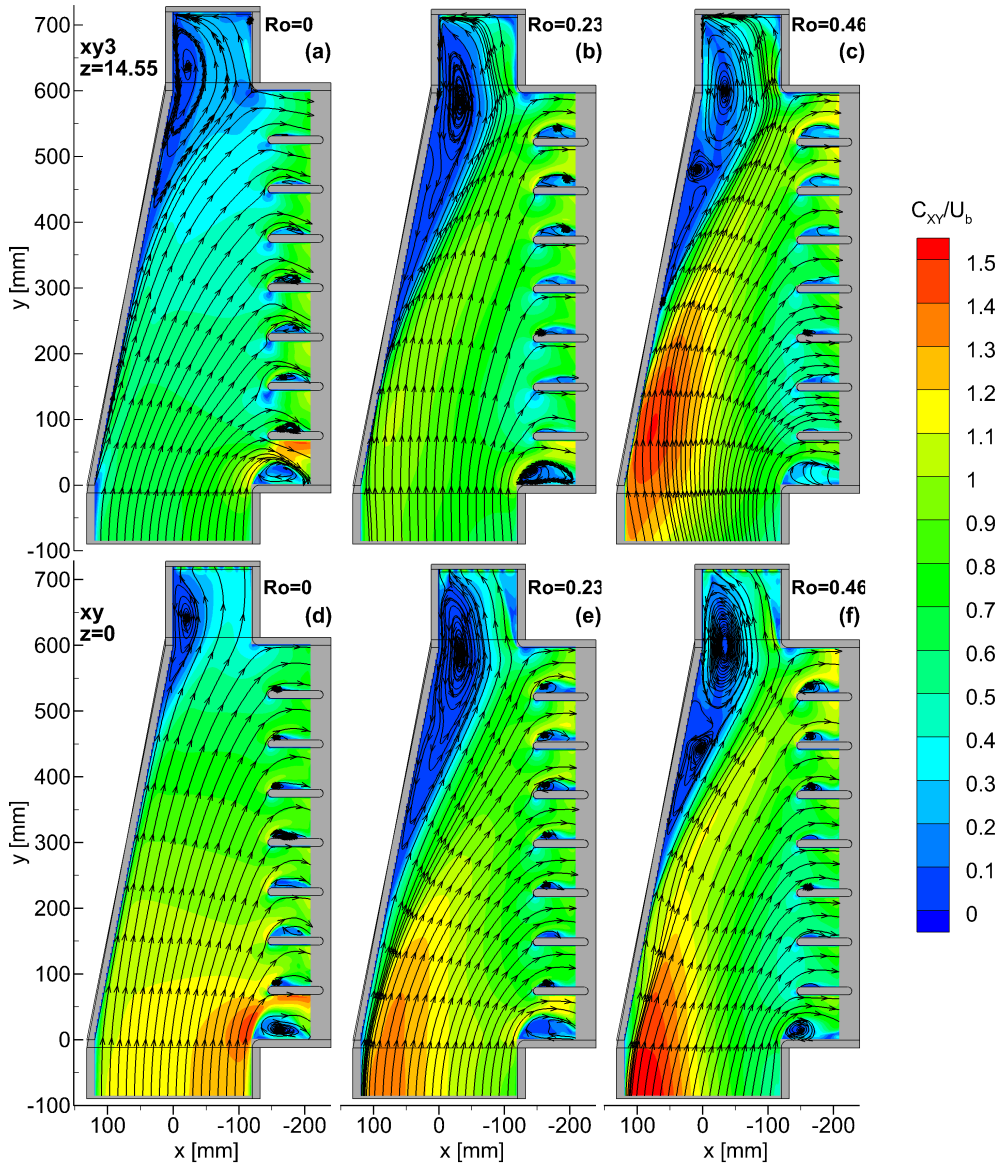


FIGURE 4.13 – *CFD* contours of the in-plane velocity modulus  $C_{xy}$  and stream-tracers in planes  $xy3$ (a-c) and  $xy$ (d-f) at  $Ro = 0$ (a,d),  $Ro = 0.23$ (b,e) and  $Ro = 0.46$ (c,f), *GO* rotating configuration.

In order to support this explanation, distributions of velocity vectors are presented in Fig. 4.14 as  $Ro$  varies along the  $z$  axis at different  $(x,y)$  channel positions. It should be pointed out that in static condition (Fig. 4.14 (a)) the core flow is characterized by higher inertia and it will therefore tend to maintain its radial direction, while the slower flow at the boundary layers (characterized by lower inertia) will be easily deviated towards the trailing side exhaust. The single concavity shape of the vector plot in Fig. 4.14 (a) is a demonstration of the previous description. A similar trend, but with an opposite concavity, is found at  $Ro = 0.23$  (Fig. 4.14 (b)) and is more significant at  $Ro = 0.46$  (Fig. 4.14(c)). As commented above, the  $x$  component of the pressure gradient induced by the Coriolis forces acting on the faster core flow, causes an increase in the velocity boundary layer's flow along the radial direction. It can be seen that, if  $Ro$  increases further on (Fig. 4.14 (c)), the inlet flow distribution is completely different from those at  $Ro = 0$  and  $Ro = 0.23$ , and it generates a much stronger Coriolis effect. Indeed, for the maximum rotation ( $Ro = 0.46$ ), the highest flow velocities are found in proximity to the upper ( $PS$ ) and lower ( $SS$ ) walls inside the boundary layers. For these reasons, the Coriolis forces will be stronger in these flow layers than in the core flow, therefore causing an acceleration of the latter along the radial direction and, as a result, the velocity vectors assume the wavy shape distribution observed in Fig. 4.14(c). Similar velocity distributions can be found for  $Ro = 0.23$  as well, but at radial positions close to the channel tip, i.e., after the space necessary for the Coriolis effect to develop.

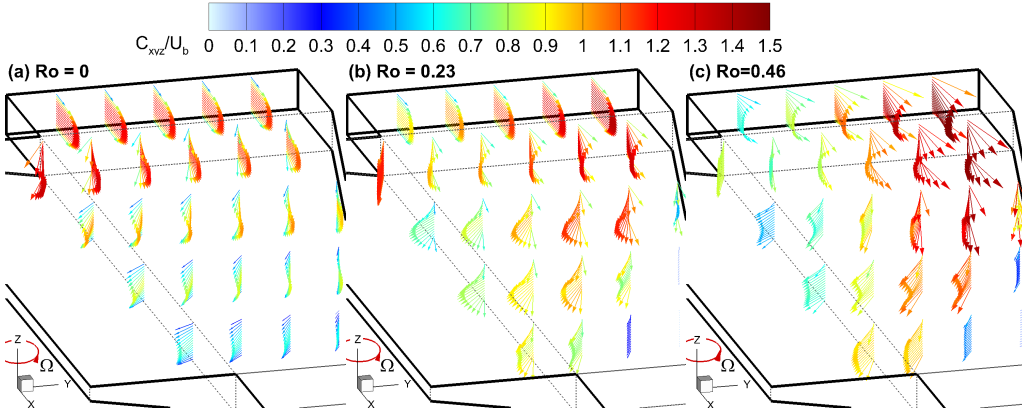


FIGURE 4.14 – CFD velocity vectors distributions at  $x = -100, 10, 165, 320$  and  $470[mm]$  at  $Ro = 0$  (a),  $Ro = 0.23$ (b) and  $Ro = 0.46$  (c), G0 rotating configuration.

Going more into detail, Fig. 4.15 illustrates the time-averaged stream-tracers and the velocity maps  $C_{y'z}$  in planes  $y'z1_{G0}$ ,  $y'z2_{G0}$ ,  $y'z3_{G0}$  for all the  $Ro$  numbers ( $Ro = 0$  (a),  $Ro = 0.23$  (b) and  $Ro = 0.46$  (c)) (for more details see Fig. 3.5). As can be seen, in spite of the flow discharge along the trailing side, the mass flow redistribution resulting from the rotation generates the widely known secondary structures shown by the stream-tracers path in Figure 4.15 (b,c).

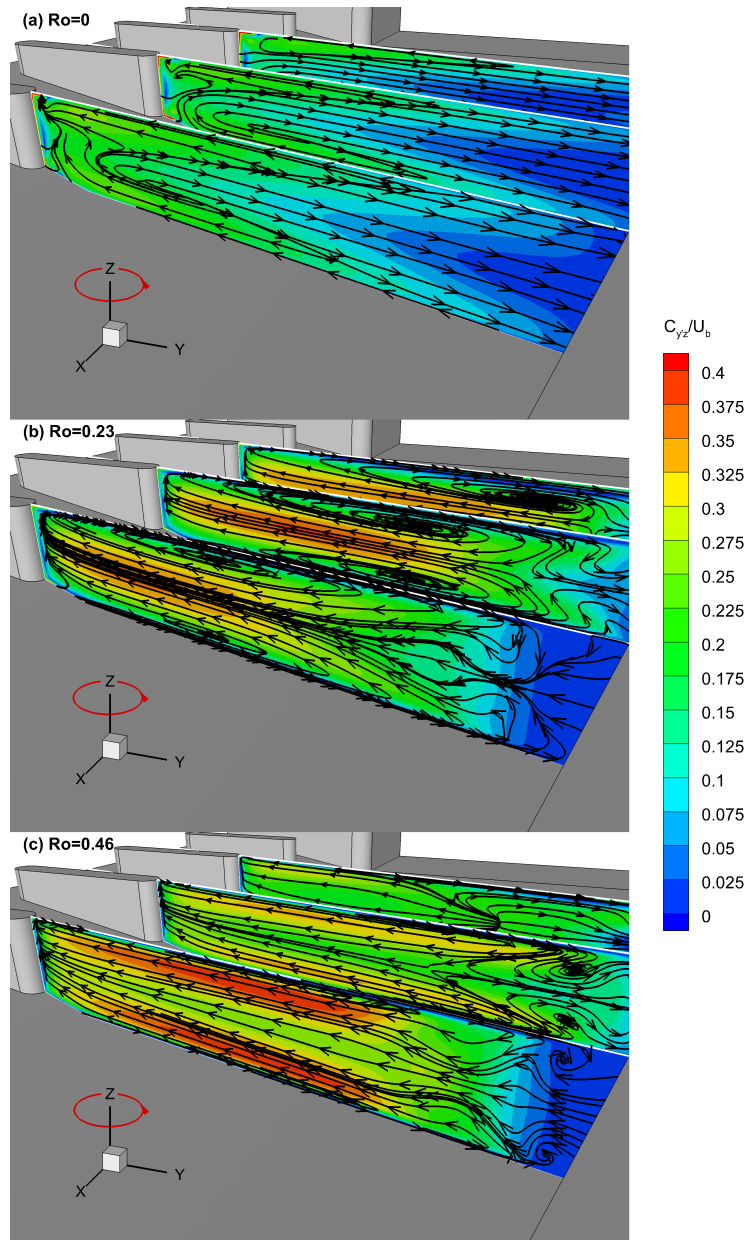


FIGURE 4.15 – *CFD* time-averaged stream-tracers and contours plots of in-plane velocity modulus  $C_{y'z}$  in planes  $y'z1_{G0}$ ,  $y'z2_{G0}$  and  $y'z3_{G0}$  at  $Ro = 0$  (a),  $Ro = 0.23$  (b) and  $Ro = 0.46$  (c),  $G0$  rotating configuration.

Moreover, as  $Ro$  increases (compare Figs. 4.15 (b,c)) these secondary structures are much thinner and confined at the  $SS$  and  $PS$  walls; the highest velocities (as commented above) are found inside the boundary layers and two counter rotating structures appear at the leading side wall (Fig. 4.15 (c)). Unlike the two main secondary flow Coriolis vortices, the latter display an opposite vorticity and can be ascribed to the increase in size of the low momentum region. Indeed, as a result of the Coriolis effects, a considerable mass displacement from the leading side to the trailing side occurs and, hence, a decrease in the stream-wise velocity takes place in proximity to the leading wall which is no longer able to balance the pressure gradient generated by the Coriolis forces in  $y$  direction. The develop of these counter rotating rolls has been observed also by Speziale and Thangam [63] in a rectangular channel at intermediate rotation rates.

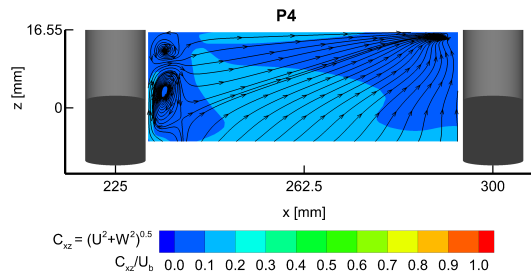


FIGURE 4.16 – CFD flow field inside the  $P_4$  passage in plane  $xz$  at  $Ro = 0.46$ ,  $G_0$  rotating configuration.

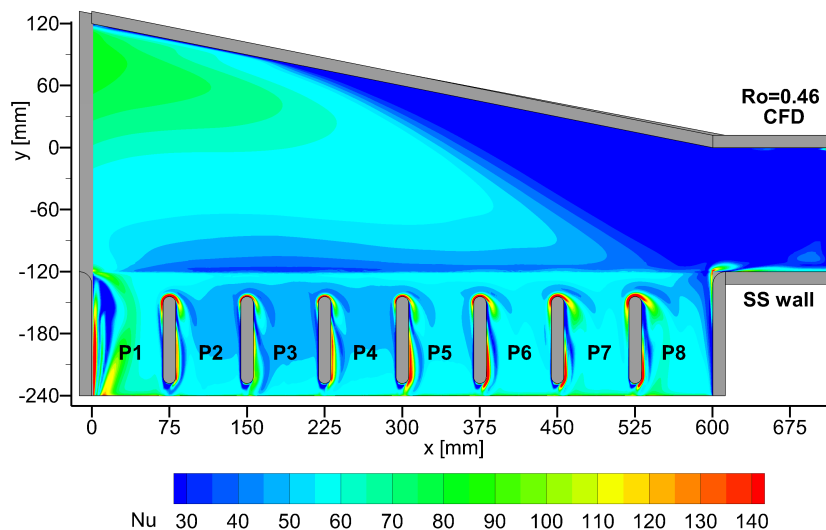


FIGURE 4.17 – CFD  $Nu$  distribution on the  $SS$  at  $Ro = 0.46$ ,  $G_0$  rotating configuration.

Considering these local effects on the flow direction, the overall consequences of the channel rotation are a flattening velocity distribution and a reduction in the boundary layer thickness on the lower (*SS*) upper (*PS*) walls. Consequently, no horseshoe vortices develop inside the *IP* passages, as already commented in the previous subsection (see Subsec. 4.2.2) for  $Ro = 0.23$  (Fig. 4.10) and in this section for  $Ro = 0.46$  (Fig. 4.16). Therefore, in the *IP* region the rotational effects produce a more uniform flow characterized by a strong reduction in the size of both separated flow regions and by the absence of visible horseshoe vortices. Hence, a more uniform distribution of the heat transfer field over the entire *IP SS* side surface is found, as previously

	$EF_{IP}$	$EF_{SS}$
$Ro = 0.23$	0.84	0.88
$Ro = 0.46$	0.74	0.89

TABLE 4.2 – *CFD* comparison of total  $Nu$  numbers at different  $Ro$  numbers, *G0* rotating configuration.

shown in Fig. 4.5 (if these results are compared with the static ones Fig. 3.11) for  $Ro = 0.23$  and more significantly in this section in Fig. 4.17 for  $Ro = 0.46$ . Indeed, the enhancement factor generated by the turbulent mixing associated with the horseshoe vortices is lost when rotation takes place. Table 4.2 shows an analysis of the  $Nu$  values for different rotation numbers, averaged respectively on the whole *IP* and *SS* walls and normalized with respect to the ones obtained in static conditions. As the previous comments suggest, as  $Ro$  increases a progressive reduction in the values of the heat transfer occurs in the *IP* region. On the contrary, in the rotation numbers' range analyzed no significant differences are found in the overall heat transfer.

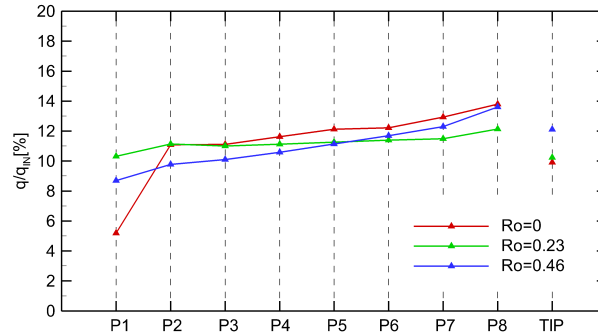


FIGURE 4.18 – *CFD* mass flow rate distribution at  $Ro = 0$  (red),  $Ro = 0.23$  (green) and  $Ro = 0.46$  (blue), *G0* configuration.

In conclusion, as for the mass flow splitting between the two exhaust sections of the channel, both experimental [5] and numerical investigations show that for  $Ro = 0$  and  $Ro = 0.23$  about 90[%] of the inlet mass flow is discharged at the trailing side, while the remaining 10[%] of the flows is discharged through the tip's holes. As shown in Fig. 4.18, minor differences are found for  $Ro = 0.46$  only, where the numerical simulations show that about 87.5[%] of the inlet mass flow is discharged at the trailing side with an almost linear distribution slightly increasing from 8[%] to 13[%], from hub (*P1*) to tip (*P8*).

These results are due to the choice of pressurizing the channel by means of a filter placed at the outlet section. In this way the effect of the centrifugal pressure field on the overall flow structure is minimized and therefore marks the rotational effects [5].

#### 4.2.4 Effects Produced by Varying the Channel Orientation

In this subsection the numerical results obtained for different channel orientations, namely  $\gamma = 22.5[^\circ]$  and  $\gamma = 45[^\circ]$ , are presented.

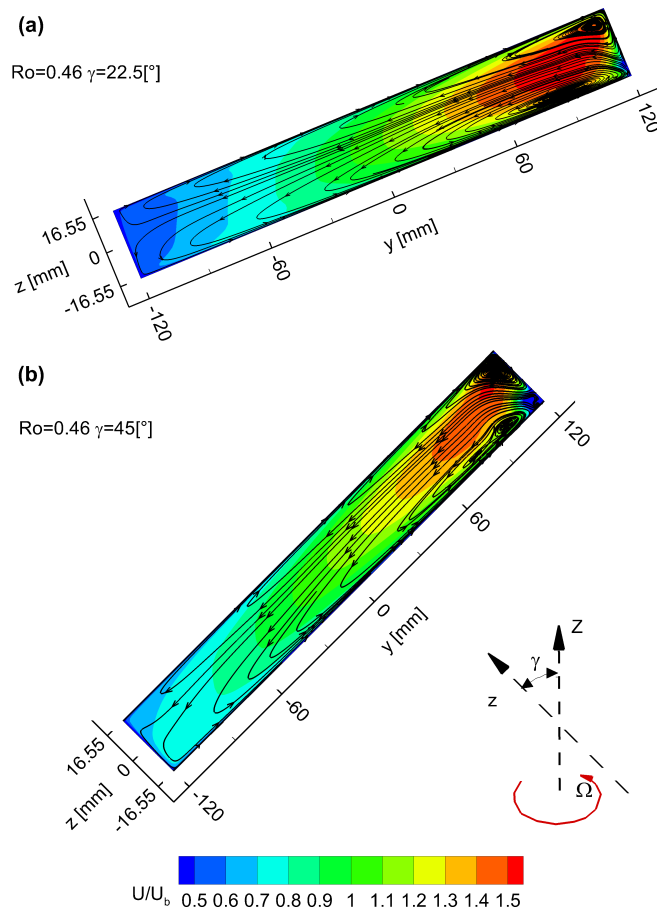


FIGURE 4.19 – *CFD* contours of  $\mathbf{U}$  velocity component and stream-tracers at the channel inlet ( $x = 69.8[mm]$ ) at  $Ro = 0.46$ ,  $\gamma = 22.5[^\circ]$  (a) and  $\gamma = 45[^\circ]$ .

Figure 4.19 shows the contour plots of the velocity component  $\mathbf{U}$  and stream-tracers in the inlet duct cross-section at  $x = -69.8[mm]$  and for channel orientation  $\gamma = 22.5[^\circ]$  (Fig. 4.19(a)) and  $\gamma = 45[^\circ]$  (Fig. 4.19(b)) at  $Ro = 0.46$ . These data should be com-

pared with those displayed in Fig. 4.12(c) for  $\gamma = 0^\circ$  at the same rotation number. The potential flow effect is still remarkable, but the velocity distribution is no longer symmetric with respect to the channel  $y$  axis. These results are due to the misalignment of the direction wherein the potential flow effect operates (the direction of the peripheral velocity,  $Y$  axis) and the channel width's direction ( $y$  axis). For the same reason, the Coriolis-induced vortices are not symmetric and characterized by a larger structure detected on the lower side of the channel ( $SS$ ). The velocity deficit located at the channel corner at  $z = -16.55[\text{mm}]$  and  $y = -120[\text{mm}]$  is produced by the interaction between the two vortices cells and is particularly evident for the channel orientation  $\gamma = 45^\circ$ , as shown in Fig. 4.19(b).

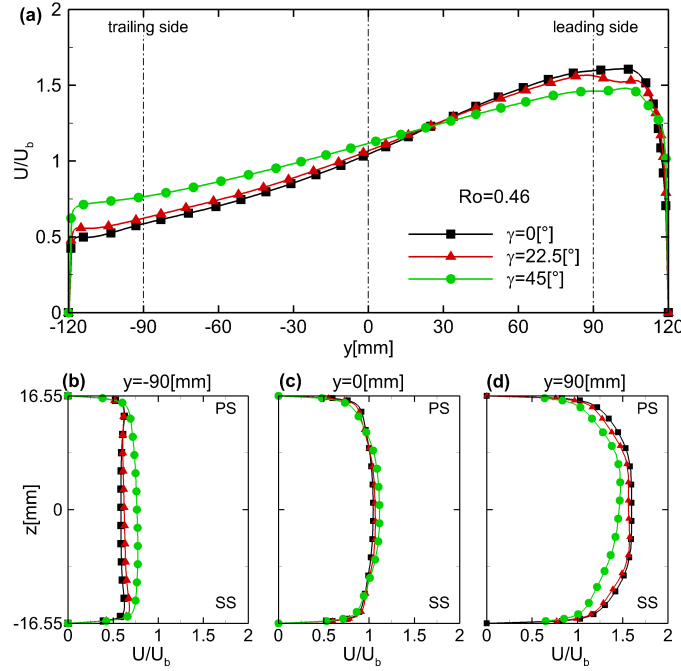


FIGURE 4.20 – *CFD*  $U$  velocity profiles at  $x = 69.8[\text{mm}]$  for  $Ro = 0.46$  and different channel orientations  $\gamma$ .  $z = 0[\text{mm}]$  (a),  $y = -90[\text{mm}]$  (b),  $y = 0[\text{mm}]$  (c),  $y = 90[\text{mm}]$  (d).

Figure 4.20 plots the comparison between the inlet velocity profiles for  $Ro = 0.46$  at different channel orientations. For  $\gamma = 22.5^\circ$ , the profiles are quite similar to those extracted for  $\gamma = 0^\circ$ . On the contrary, as  $\gamma$  increases to  $45^\circ$ , a significant reduction in flow imbalance occurs as a result of the potential flow effect along the channel width (Fig. 4.20 (a)). In comparison to  $\gamma = 0^\circ$  and  $\gamma = 22.5^\circ$  channel orientations the different sizes and positions of the Coriolis-induced vortices detected in Fig. 4.19(b) account for the change in the velocity profile along the  $z$  direction at the leading side (Fig. 4.20 (d)) and generate a flow accumulation at  $z > 0[\text{mm}]$ . Finally, a lessening of the Coriolis

effects on the trailing side observed for  $\gamma = 0[^\circ]$  and  $\gamma = 22.5[^\circ]$  (Fig. 4.20(b)) account for the disappearance of the near-wall flow accelerations.

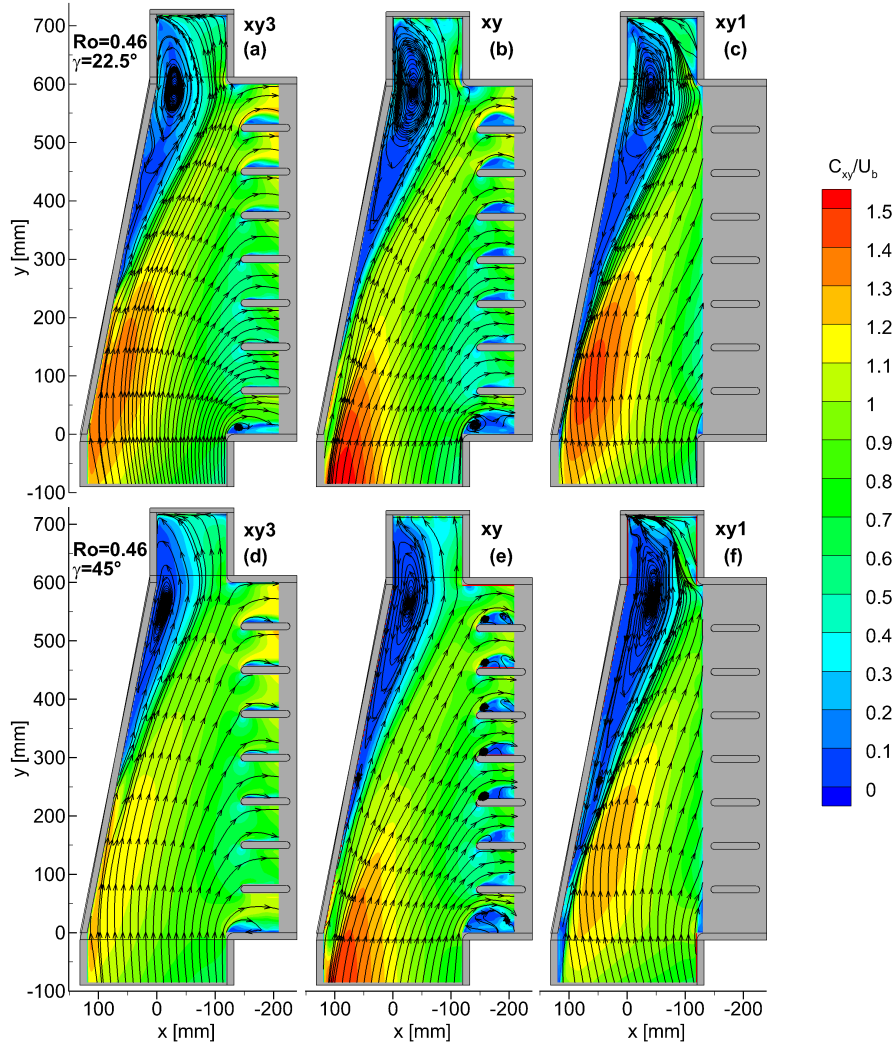


FIGURE 4.21 – *CFD* contours of the in-plane velocity modulus  $C_{xy}$  and stream-tracers in planes *xy3* (a,d), *xy* (b,e) and *xy1* (c,f) at  $Ro = 0.46$ (a,d) and  $\gamma = 22.5[^\circ]$ (a-c)  $\gamma = 45[^\circ]$ , *G0* rotating configuration.

Consistently with the rotational effects on the inlet flow previously commented, the velocity distribution inside the main channel is not symmetric along the channel height, as shown by the time-averaged stream-tracers and velocity maps in Fig. 4.21 and, as expected, it is more evident for  $\gamma = 45^\circ$  (Figs. 4.21(d-f)). Therefore, the flow deviation towards the leading side turns out to be stronger in proximity to the lower wall of the channel (*SS*) than near the upper one (*PS*) (compare Figs. 4.21 (f) vs (d)). Moreover, as can be seen (Figs. 4.21 (d-f)), the separation bubble at the channel tip is wider for  $z < 0$  [mm], because the flow separation from the redirecting wall at the channel leading side occurs further upstream at lower elevations, as a consequence of the velocity deficit observed in Fig. 4.19 (b) at the corner of the inlet channel. For the intermediate orientation  $\gamma = 22.5^\circ$ , the effect of the channel orientation is less evident and the flow field appears to be more similar to the one obtained for  $\gamma = 0^\circ$  (compare Figs. 4.13 (c,f) vs Figs. 4.21 (a,b))

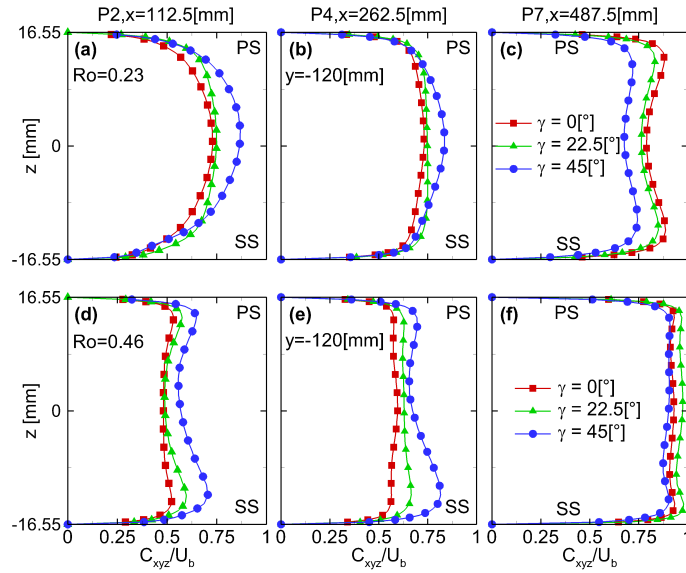


FIGURE 4.22 – *CFD* profiles of the velocity modulus  $C_{xyz}$  at  $y = -120$  [mm] and different radial positions at varying  $\gamma$  for  $Ro = 0.23$  (a-c) and  $Ro = 0.46$  (d-f), *GO* rotating configuration.

A more quantitative comparison is performed in the plots of Fig. 4.22, where the profiles of the velocity modulus  $C_{xyz}$  are compared at different positions, for given values of  $Ro$  and varying the channel orientation. As can be seen, when  $Ro = 0.46$  is considered (Figs. 4.22 (d-f)) and as  $\gamma$  increases, an asymmetric velocity distribution along the channel height is found which is much more significant for  $\gamma = 45^\circ$  as commented when Fig. 4.21 was introduced. However, considering that the velocity distributions are mainly affected by the rotational effects, the highest peaks are found near the upper (*PS*) and lower (*SS*) confining walls. It should be pointed out that when  $Ro$  is lower (Figs. 4.22 (a-c)), the change in the channel orientations produces major differences in the flow fields. Indeed,

for  $\gamma = 45^\circ$ , the velocity profiles at lower radial positions (Figs. 4.22 (a,b)) show an almost parabolic shape associated with higher velocity peaks and thicker boundary layers, while at larger radii (Fig. 4.22(c)), the velocity profiles for different values of  $\gamma$  are more similar to each other. The differences observed in the flow evolution along the channel radius are generated by the effect produced by the channel orientation on the inlet flow.

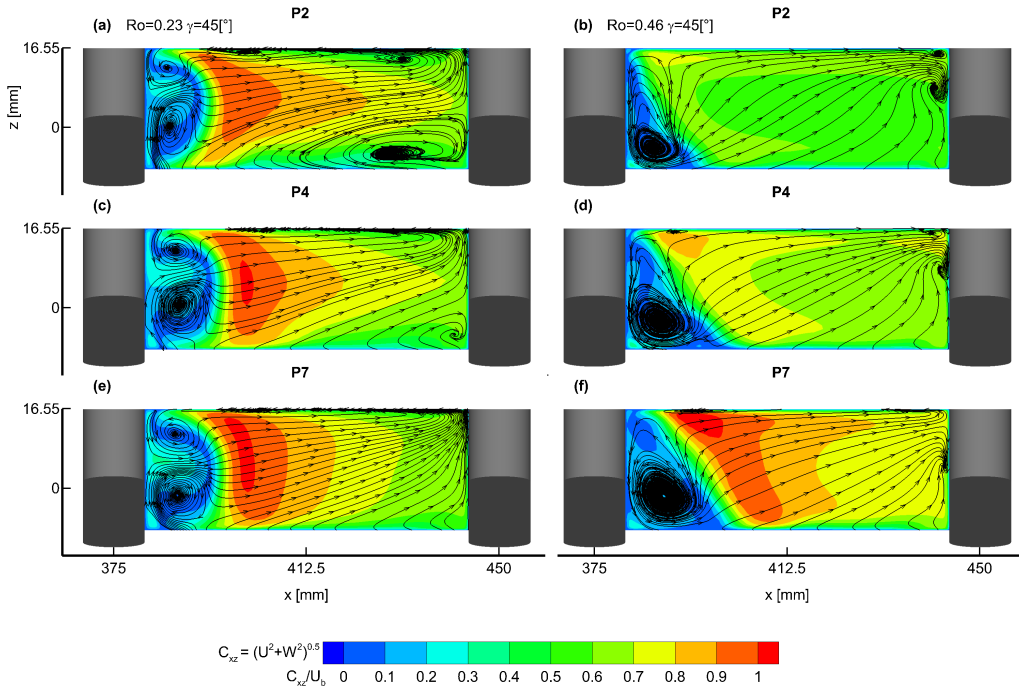


FIGURE 4.23 – CFD flow field inside the *IP* passage *P2*(a,b), *P4*(c,d) and *P7*(e,f) in plane  $xz$  for  $\gamma = 45^\circ$  and  $Ro = 0.23$ (a,c,e) and  $Ro = 0.46$ (b,d,f), *G0* rotating configuration.

Indeed, as  $\gamma$  increases (Fig. 4.23), the rotational effects occur in proximity to the channel leading side ( $y > 0$  [mm]) and if the main flow path (see Figs. 4.13 4.15 4.21) is considered, they have a considerable influence on the flow discharged at larger radii of the trailing side. Conversely, the flow discharged through the *IP* passages closer to the hub (*P1*–*P4*) is affected by the inlet flow for  $y < 0$  [mm]. Evidence of this effect is provided by the recurrence of the horseshoe vortices from the 1<sup>st</sup> (*P1*) to the 4<sup>th</sup> (*P4*) *IP* passage for  $Ro = 0.23$  and  $\gamma = 45^\circ$ , as illustrated in Figs. 4.23(a,c). For  $Ro = 0.46$  the rotational effects are more significant and prevail over the effect of the channel orientation, indeed very small horseshoe structures are found only on the upstream side of each pedestal (close to the *PS* side), as shown in Figs. 4.23 (b,d,f).

The effects mentioned above are fully confirmed when the *Nu* distribution at the *SS* is considered for  $\gamma = 45^\circ$  at  $Ro = 0.23$  and  $Ro = 0.46$ , as demonstrated in Fig. 4.24. Indeed, from a qualitative viewpoint, the effect of the turbulent mixing associated with

the horseshoe vortices is evident in Fig. 4.24 (a) from the 1<sup>st</sup> *IP* passage (*P1*) to the 4<sup>th</sup> *IP* passage (*P4*) and is lost, as expected, in Fig. 4.24(b) if the rotation is increased, which confirms the results commented in the previous paragraph.

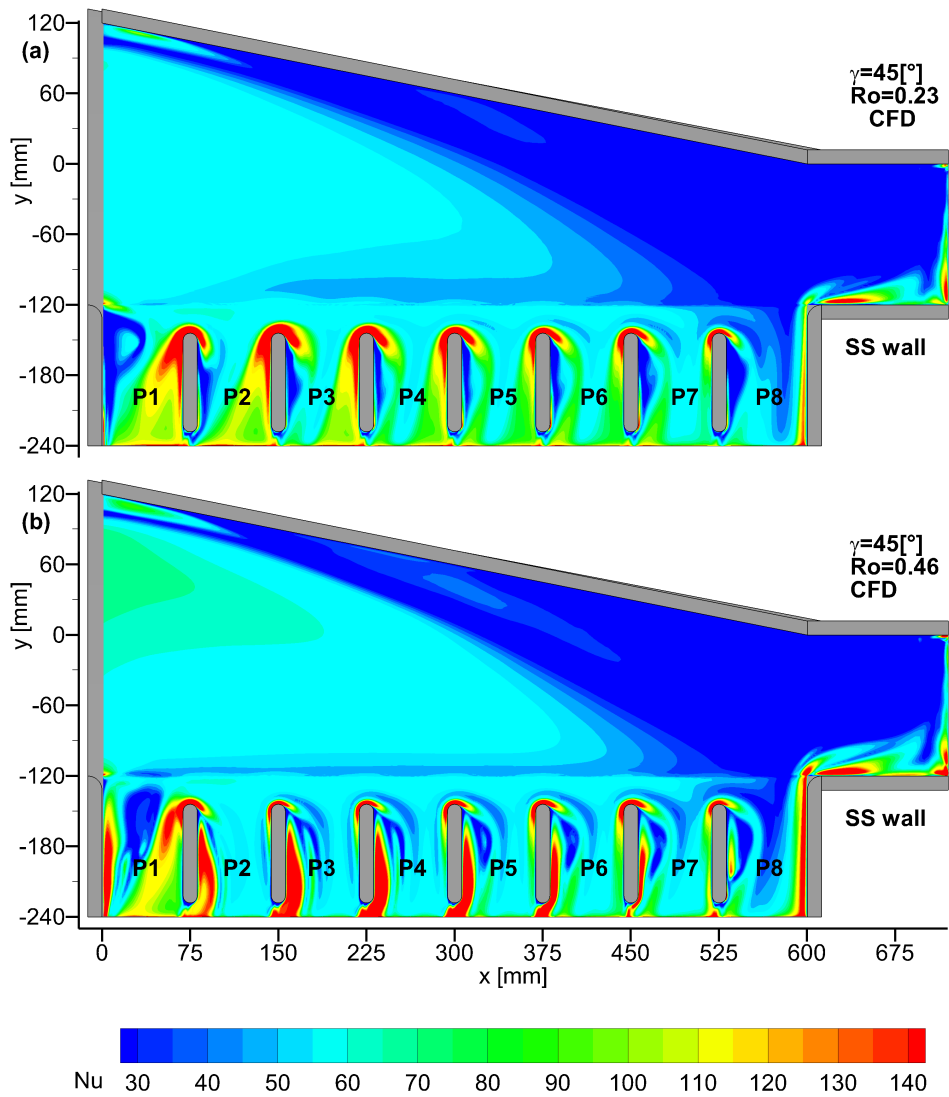


FIGURE 4.24 – *CFD* *Nu* distribution on the *SS* wall at  $Ro = 0.23$  and  $Ro = 0.46$  at  $\gamma = 45^\circ$ , *G0* rotating configuration.

Table 4.3 provides a demonstration of all the comments presented above by showing an analysis of the  $Nu$  values for different  $Ro$  numbers and channel orientations, averaged respectively on the whole  $IP$  and  $SS$  walls and normalized according to the ones obtained in static condition at  $\gamma = 0[^\circ]$ . Indeed, as  $\gamma$  and  $Ro$  increase, an increase in the heat transfer values in the whole  $SS$  occurs as well and is always lower than the one obtained in static condition; in addition, solely when  $\gamma$  orientation is equal to  $45[^\circ]$  and the rotation number  $Ro$  is equal to 0.23, the turbulent mixing associated with the horseshoe branch reappears and, hence, the  $Nu$  values in the  $IP$  wall become quite similar to the highest one, i.e.,  $Ro = 0$  and  $\gamma = 0[^\circ]$ . Finally, the mass flow is plotted in Fig. 4.25 for all the  $\gamma$  orientations and  $Ro$  numbers and does not present any significant differences when the channel orientation is changed. Indeed, this depends solely on the pressure distribution inside the channel which is slightly affected only by the different flow distributions produced by a change in the channel orientation.

	$EF_{IP}$	$EF_{SS}$
$Ro = 0.23 \gamma = 22.5[^\circ]$	0.87	0.90
$Ro = 0.23 \gamma = 45[^\circ]$	0.97	0.91
$Ro = 0.46 \gamma = 22.5[^\circ]$	0.83	0.94
$Ro = 0.46 \gamma = 45[^\circ]$	0.92	0.97

TABLE 4.3 – *CFD* comparison of total  $Nu$  numbers at different  $Ro$  numbers and channel orientations,  $G0$  rotating configuration.

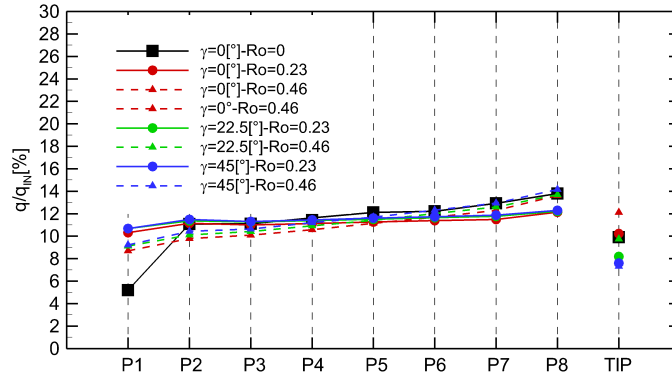


FIGURE 4.25 – *CFD* mass flow rate distribution for  $\gamma = 0[^\circ]$ ,  $\gamma = 22.5[^\circ]$  and  $\gamma = 45[^\circ]$  at varying rotation numbers,  $G0$  rotating configuration.

#### 4.2.5 Summary

In the present sub-section an assessment of the capabilities of the  $SST$  turbulence model developed inside the commercial software ANSYS CFX  $\text{\textcircled{R}}$ v14.0 in rotating ( $Ro = 0.23$ ) condition for the configuration  $G0$  was made. Moreover, on the blade trailing edge, the combined effects of rotation and channel orientation on the aero-thermal performances were analysed through a numerical investigation. The experimental data ([3],[5]) were used in order to provide a database for the numerical validation. Coriolis forces act on

the flow field under rotation altering the pressure field inside the passage. As regards the main path of the flow, the gradient of the Coriolis-induced pressure field points towards the hub region of the trailing side exhaust section. This pressure gradient is not balanced by the Coriolis forces inside the layers with the slowest flow, which are therefore accelerated in the radial direction and deflected towards the channel leading side. The outcomes of this phenomenology on the flow field for  $\gamma = 0[^\circ]$  can be summarized as follows:

- Coriolis-induced whirling structures arise inside the inlet portion of the channel. These vortices are weak for  $Ro = 0.23$ , while they are stronger for  $Ro = 0.46$ . Moreover, as a result of the mass flow imbalance caused by the potential flow effects that act on the flow at the channel inlet, their cores are found in proximity of the leading side of the passage;
- for  $Ro = 0.23$  a highest velocity flow is found at about the channel mid-height, while for  $Ro = 0.46$  the acceleration of the near-wall flow is so strong that already in the duct region close to the hub, the highest velocities are found just outside the boundary layers and not at the channel mid-height. The increases in  $Ro$  values result in a more uniform velocity distribution along the channel's height, with a considerable reduction of the boundary layers thickness at both upper and bottom walls and a different swirl of the velocity vectors. The outcome of this phenomenon on the flow field inside the exhaust region at the trailing side is the disappearance of the horseshoe vortices on the pedestals upstream face with a resulting reduction in the values of the heat transfer in this region.
- as  $Ro$  increases the separation bubble found at the channel tip increases progressively.

All these effects are fully confirmed by the spatial-average  $Nu$  in Tab.4.2.

Conversely, if the channel orientation is different from  $\gamma = 0[^\circ]$ , a misalignment of the planes on which the Coriolis forces act and the one that contains the width of the duct ( $y$  direction) is found. Consequently:

- Coriolis-induced whirling structures inside the inlet duct are no longer symmetric with respect to the  $y$  axis of the channel, the higher velocities are found close to the channel bottom wall. Moreover, the rotational effects are lessened on the trailing side, having a direct influence on the flow discharged close to the hub. In particular, for  $Ro = 0.23$  and  $\gamma = 22.5[^\circ]$ , the horseshoe vortices reappear on the upstream face of the first four pedestals. In this situation, as a result of the reappearance of the horseshoe vortices, the heat transfer value in the trailing side region become quite similar to highest one, i.e.  $\gamma = 0[^\circ]Ro = 0$ ;
- the interaction between the asymmetric Coriolis vortices produces a flow separation all along the corner between the channel bottom and leading walls. This causes the separation bubble at the tip to have different extensions along the channel height, the larger size being found at the lowest elevations.

## 4.3 G1 Configuration

### 4.3.1 Grid Generation and Quantification of the Numerical Accuracy

The computational domain was discretized by using a multi-block structured mesh with hexahedral elements. As commented in Sec. 4.1, in comparison to the mesh developed for the static condition (Subsec. 3.4.1) for the *G1* configuration, only a large domain mesh for half of the settling chamber was added. For an estimation of the discretization error, the *GCI* procedure was employed again ( see Apx.C). The parameters of the grids computed are summarized in Tab.4.4. It should be pointed out that all the requirements for the calculation of the *GCI* were fully achieved for the maximum rotation number ( $Ro = 0.46$ ) and  $\gamma = 22.5[^\circ]$  in *G1* configuration.

Grid	N	$y_{avg}^+$
Fine	10257042	0.56
Intermediate	4359806	0.76
Coarse	1939336	1.03

TABLE 4.4 – *GCI* study, *G1* configuration.

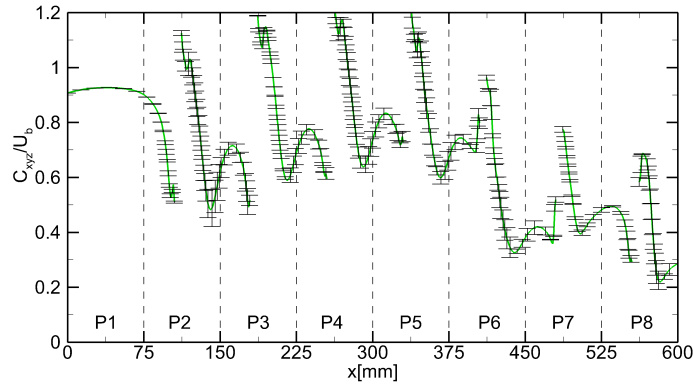


FIGURE 4.26 – *GCI* error band at  $Ro = 0.46$  and  $\gamma = 22.5[^\circ]$  in plane:  $xy_{G1}$  at  $z = 14[mm]$   $y = -60[mm]$ , *G1* rotating configuration.

Figure 4.26 plots the resulting distribution of the *GCI* calculated by using of the three different grids shown as  $C_{xyz}$  velocity modulus extracted in plane  $xy_{G1}$  at  $y = -60[mm]$  and displays the very low discretization errors bars estimated by the refinement study. It should be noted that the velocity modulus and, therefore, the *GCI* values in the ribs are not included. The results of the analysis are satisfactory and characterized by an average error value computed below 2[%], with the exception of a limited region in proximity to the ribs where, however, the discretization error is lower than 7[%]. In these regions, because of the very complex 3-D flows, small changes in the mesh resolution determine changes in the resulting flow field.

### 4.3.2 Comparison with Rotating Experimental Results

In order to provide a first comparison between experimental results and numerical predictions, Fig. 4.27 and Fig. 4.28 show the local  $HTC$  and  $Nu$  number distribution. It should be pointed out that as for experimental data only Fig. 4.27 in Bonanni et al.[14] is available, and these results were obtained on the  $PS$  at  $Ro = 0.26$ , which is slightly higher than the rotation number of the flow field data.

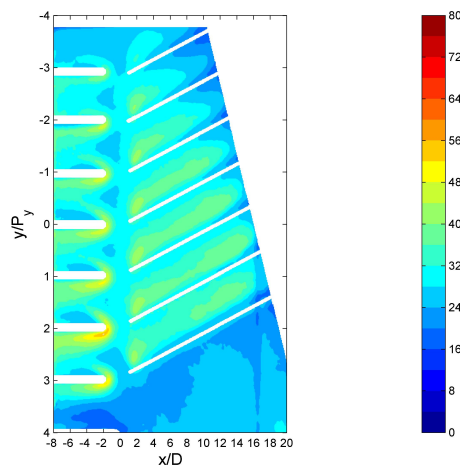


FIGURE 4.27 – Experimental [14]  $HTC$  at  $Ro = 0.26$  on  $PS$ ,  $G1$  rotating configuration.

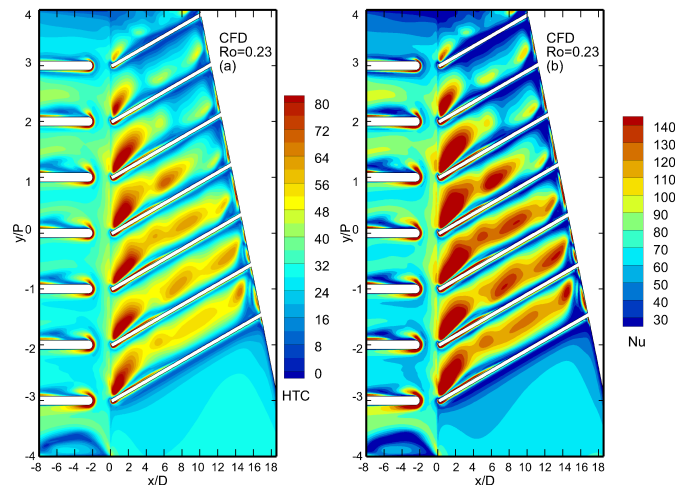


FIGURE 4.28 –  $CFD$   $HTC$  (a) and  $Nu$  (b) at  $Ro = 0.23$ ,  $G1$  rotating configuration.

The comparison between Fig. 4.27 and Fig. 4.28 (a) shows the good prediction in the trends performed by the *CFD* code but, again, it overestimates the peaks of the heat transfer. From a qualitative viewpoint, the over-prediction in these areas is about 25[%] but comparing these results with the ones obtained in static condition (Figs. 4.28 (b) vs 3.22), it is possible to observe a less uniform and higher heat transfer downstream the ribs and a more uniform *Nu* distribution inside the *IP* passages.

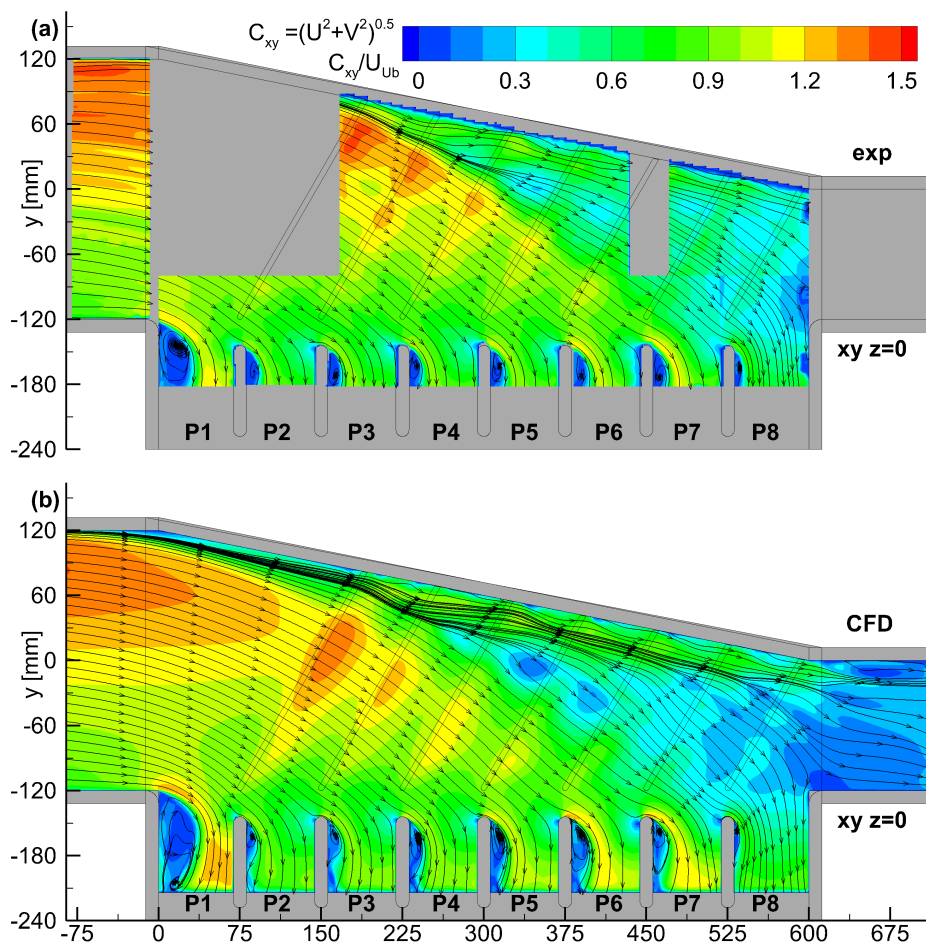


FIGURE 4.29 – Experimental [56] and *CFD* time-averaged stream-tracers and contour plots of the in-plane velocity modulus  $C_{xy}$  in *xy* plane at  $Ro = 0.23$ , *G1* rotating configuration.

A complete description of the heat transfer process and the discrepancies between experimental and numerical values commented above can be provided if the flow field is considered. Figure 4.29 displays the comparison between experimental [56] and numerical time-averaged stream-tracers and  $C_{xy}$  velocity modulus in the *xy* plane for  $Ro = 0.23$ .

The agreement is full and both the experimental and numerical data show more significant changes in the flow field than the static situation (see Fig. 3.23). Indeed Fig. 4.29 shows a flow region close to the leading side where a mass flow deficit can be observed. This region begins approximately at the 1<sup>st</sup> rib ( $x = 170[mm]$ ), and its extension increases as the coolant flows downstream. At the same time, the experimental [56] and *CFD* stream-tracers in Fig. 4.29 suggest the presence of a helicoidally secondary structure generating the separation line that can be noticed between the core flow and the low velocity region. Moreover, taking into account the development of this structure close to the leading side wall, the velocity deficit observed at the model tip for  $Ro = 0$  (Figs. 3.23 (a,c)) completely disappears when rotation takes place. Indeed, unlike *G0* configuration (as discussed in Subsec. 4.2.3 when Fig. 4.13 was introduced) a growth of the recirculation bubble does not occur when rotation takes place.

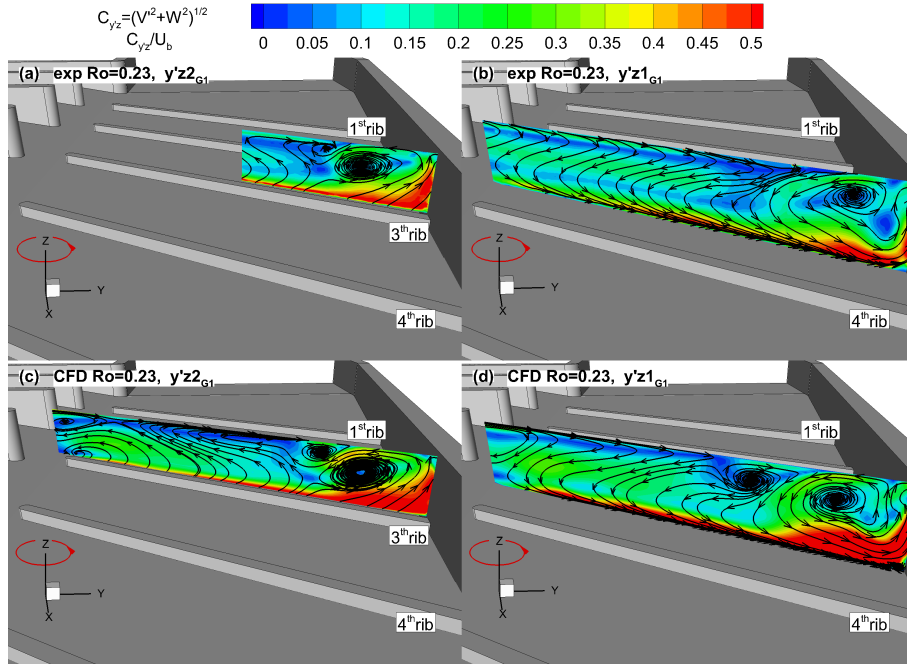


FIGURE 4.30 – Experimental [56](a,b) and *CFD* (c,d), time-averaged stream-tracers and contour plots of the in-plane velocity modulus  $C_{y'z'}$ , in planes  $y'z1_{G1}$  (b,d) and  $y'z2_{G1}$  (a,c), *G1* rotating configuration.

A clear view of this structure is provided in Fig. 4.30 which displays the comparison between experimental [56] and numerical results at  $Ro = 0.23$  in  $y'z1_{G1}$  and  $y'z2_{G1}$  planes (parallels to the ribs), where  $y'$  indicates the direction along the rib's length. These data are illustrated by means of the time-averaged stream-tracers and contour plots of the in-plane velocity modulus  $C_{y'z'}$ . The clear match between the experimental [56] and

the numerical stream-tracers accounts for the existence of a recirculating structure close to the channel leading side, whose presence has to be ascribed to the flow migration towards the leading side induced by both ribs and rotational effects (see Figs. 4.30 (a,b) vs Figs. 4.30 (c,d)).

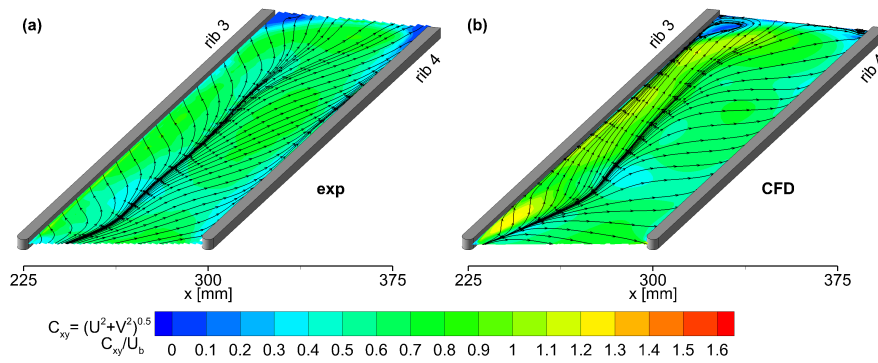


FIGURE 4.31 – Experimental [56] and *CFD* time-averaged stream-tracers and contour plots of the in-plane ( $xy_{G1}$ ) velocity modulus between the 3<sup>rd</sup> and the 4<sup>th</sup> rib, *G1* rotating configuration.

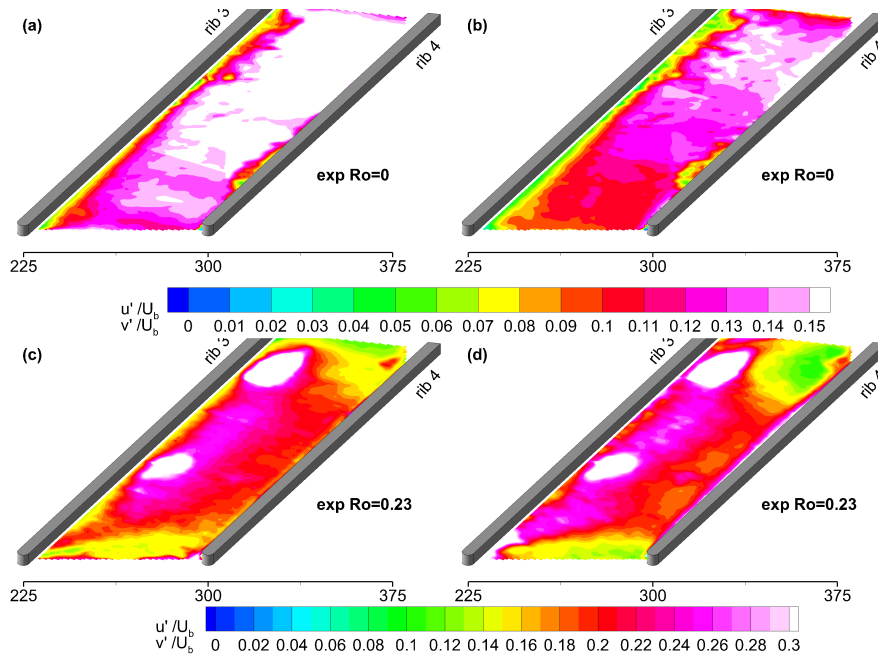


FIGURE 4.32 – Experimental [56] contour plots of the  $u'$  (a,c) and  $v'$  (b,d) velocity fluctuations in plane  $xy_{G1}$  at  $Ro = 0$  (a,b) and  $Ro = 0.23$  (c,d), *G1* configuration.

Moreover, going more into detail, Fig. 4.31 illustrates experimental [56] and *CFD* time averaged stream-tracers and contour plots of the of the in-plane velocity modulus  $C_{xy}$  in plane  $xy_{G1}$  in the same *IR* region analyzed previously in static ( $Ro = 0$ ) condition (see Subsec. 3.4.3 Fig. 3.24). Unlike the static case ( $Ro = 0$ ), in rotating condition the match of both reattachment line positions, mean flow distribution and velocity modulus is fully achieved. In order to explain such different results from those obtained in static case ( $Ro = 0$ ), Fig. 4.32 reports the experimental [56] contour plots of the *RootMeanSquare(r.m.s)* values of the in-plane components of the velocity fluctuations, namely  $u'$  (Figs. 4.32 (a,c)) and  $v'$  (Figs. 4.32(b,d)). The comparison between static (Figs. 4.32 (a,b)) and rotating (Figs. 4.32(c,d)) cases demonstrates that for the latter condition a rather more isotropic turbulence activity is found in this area, consequently the rotating flow field is accurately predicted by the *CFD* code. Indeed, isotropic turbulence assumption is made in all the two-equation turbulence models (see Subsec. 2.3.2).

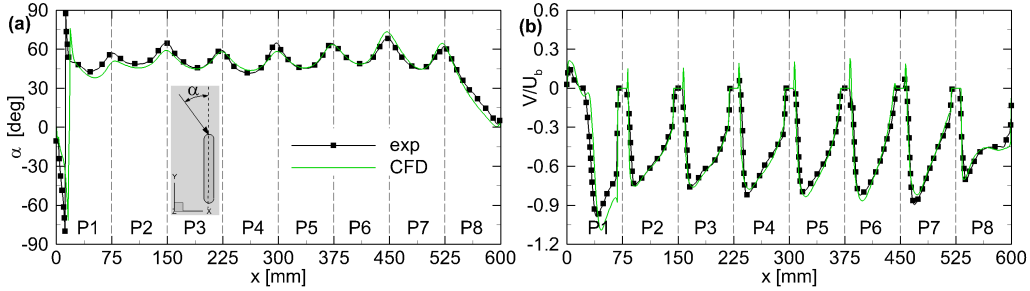


FIGURE 4.33 – Experimental [56] and *CFD* flow angle  $\alpha$  extracted in plane  $xy$  at  $Ro = 0.23$  at  $y = -132[mm]$  (a) and  $V$  velocity profiles extracted in plane  $xy$  at  $Ro = 0.23$  at  $y = -150[mm]$  (b), *G1* rotating configuration.

A further confirmation of the good match between the experimental [56] and the *CFD* results at  $Ro = 0.23$  is provided by Fig. 4.33 (a) which plots the incidence angle  $\alpha$  extracted from  $xy$  plane along a line at  $y = -132[mm]$  and Fig. 4.33 (b) which reports the profiles of the mean velocity component  $V$  extracted from  $xy$  plane along a line at  $y = -150[mm]$ . Finally, both experimental [56] and numerical results reveal the disappearance of the horseshoe vortex branch inside *P4 IP* passage. As in *G0* configuration (see Subsec. 4.10), this flow behavior can be imputed to the rotational effects which produce a noteworthy acceleration of the near-wall flow resultin in the thinning of the boundary layers and, therefore in the horseshoe vortices disappearance. The only differences between experimental and numerical stream-tracers paths are found inside the separated flow region (i.e. downstream the pedestal at  $x = 225[mm]$ ) and can be considered less important. Indeed, in this flow region the in-plane velocity modulus  $C_{xy}$  is close to zero, which means that the stream-tracers are less important because they are affected by the experimental accuracy.

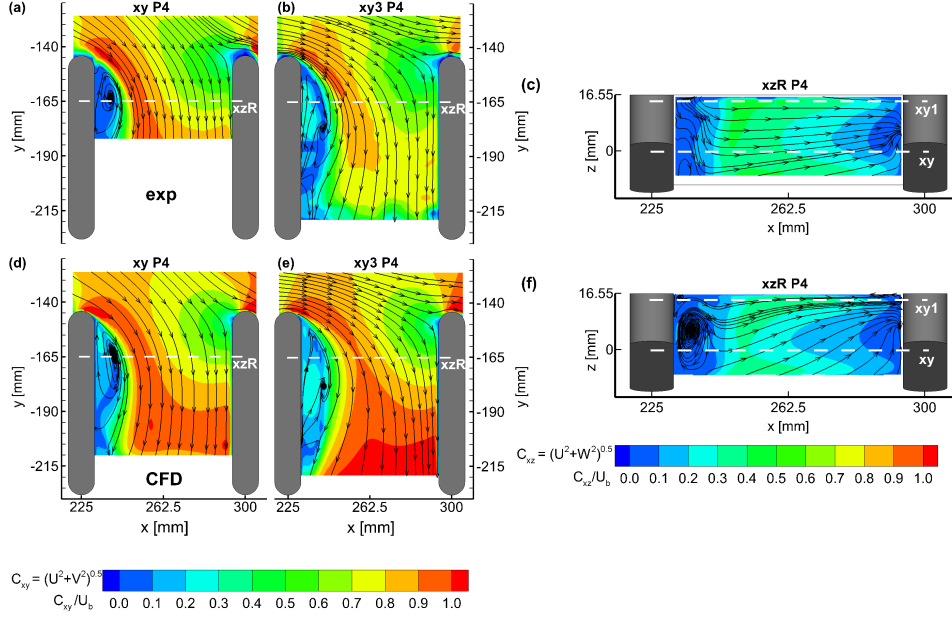


FIGURE 4.34 – Experimental [56] and *CFD IP* flow structures at  $Ro = 0.23$ , *G1* rotating configuration.

### 4.3.3 Effects Produced by $Ro$ Increases

This subsection will provide an analysis of the rotational effects on the basis of the numerical results obtained for channel configurations  $\gamma = 0[^\circ]$  and  $Ro = 0.23$   $0.46$ . For a clearer understanding of this subsection (as for *G0* configuration see Subsec. 4.2.3), it is also useful to bear in mind that for  $\gamma = 0[^\circ]$  the  $y$  axis is aligned with the peripheral velocity. Moreover, it should be pointed out that all the considerations given in Subsec. 4.2.3 for the *G0* configuration at the inlet can be extended to *G1* configuration as well.

Figure 4.35 illustrates a comparison between the *CFD* predictions of the  $Nu$  distribution at  $Ro = 0.23$  Fig. 4.35 (a) and at  $Ro = 0.46$  Fig. 4.35(b). As  $Ro$  increases, the heat transfer between the *IR* passages is clearly enhanced. Conversely, in the *IP* passages, slightly lower  $Nu$  values are found. This effect can be explained by considering Fig. 4.36, which shows the numerical time-averaged stream-tracers paths and velocity  $C_{xy}$  in plane  $xy_{G1}$  at  $Ro = 0.23$  (a,b) and  $0.46$  (c). Indeed, as  $Ro$  increases, the combined effect of the Coriolis-induced pressure gradient in the slow flow layers and the ribs guidance effect generate:

- a noteworthy increase in the velocity modulus  $C_{xy}$ ;
- an intense migration towards the leading edge side.

Both these effects account for the noteworthy increase in the heat transfer in the *IR* passage, as commented when Fig. 4.35 (b) was introduced.

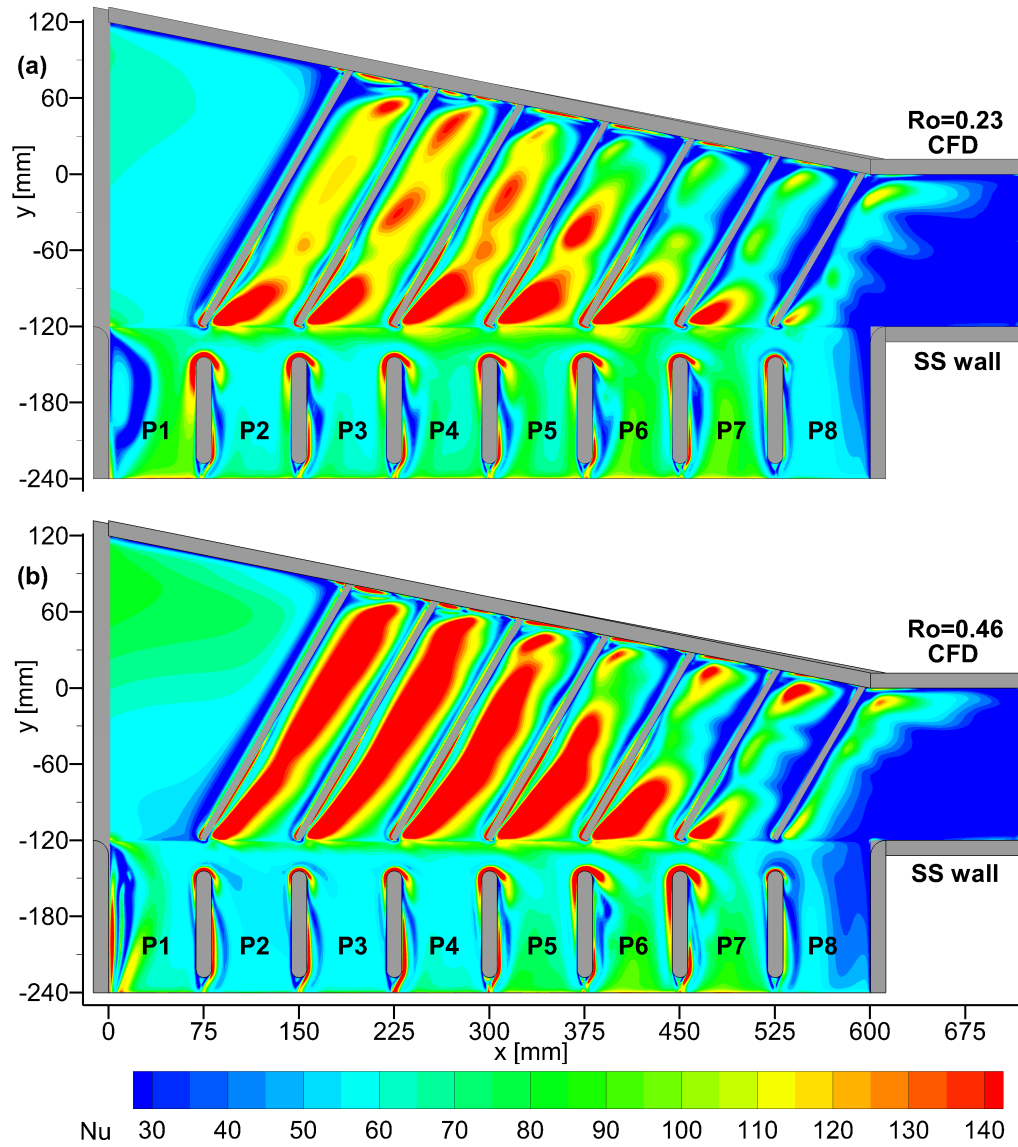


FIGURE 4.35 – CFD Nu distribution at  $Ro = 0.23$  (a) and  $Ro = 0.46$  (b),  $G1$  rotating configuration.

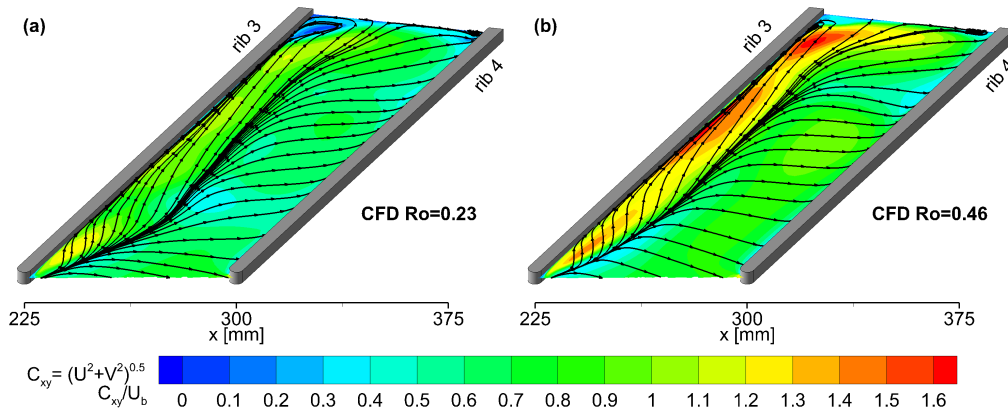


FIGURE 4.36 – *CFD* time-averaged stream-tracers and velocity modulus  $C_{xy}$  contours in plane  $xy_{G1}$  at  $Ro = 0.23$  (a) and  $Ro = 0.46$  (b),  $G1$  rotating configuration.

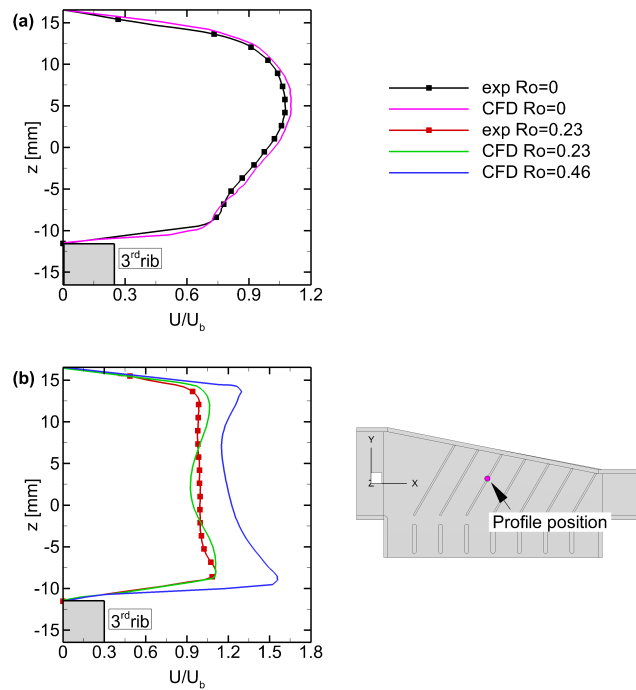


FIGURE 4.37 – Experimental [56] and *CFD* profiles at  $Ro = 0$  (a),  $Ro = 0.23 - 0.46$  (b) extracted from plane  $y'z_{G1}$  at  $y = -15$  [mm]: mean radial velocity  $U'$ ,  $G1$  configuration.

A further confirmation is provided by the profiles in Fig. 4.37 which plots the comparison between the experimental data [56] at  $Ro = 0 - 0.23$  and the numerical predictions at

$Ro = 0 - 0.23 - 0.46$  of the velocity modulus  $U'$  (which is the velocity along axis  $x'$  that is perpendicular to the direction of the rib Figs. 4.37 (a,b)) extracted from the plane  $y'z2_{G1}$  at  $y = -15[mm]$ . Firstly, a good match between experimental and numerical profiles can be observed (Figs. 4.37 (a-d)) and it should be also pointed out that under rotation Coriolis forces act in plane  $xy$  along the direction normal to the stream-tracers and, hence, generate a pressure gradient pointing towards  $x$  and  $y > 0$ . The latter is no longer balanced by Coriolis forces in the slow flow layers closer to the channel's walls. Therefore, in comparison to static profiles results, it produces a substantial flow acceleration along the radial direction and higher flow angles (respectively Figs. 4.37 (a,c) vs Figs. 4.37 (b,d)).

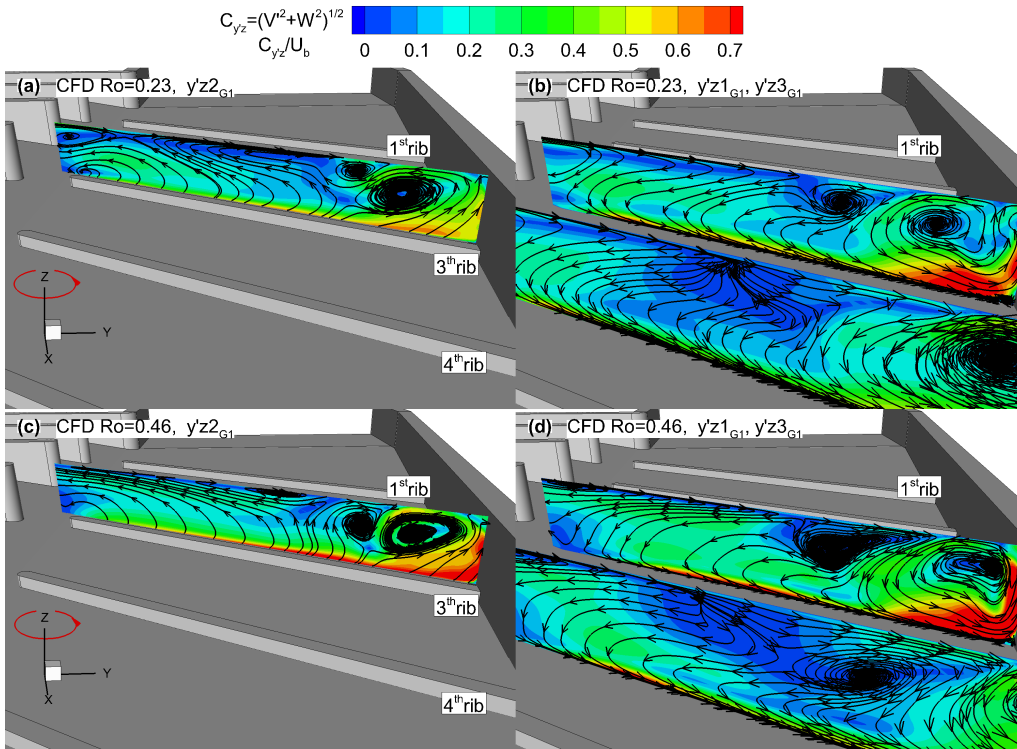


FIGURE 4.38 – CFD (c-f) time-averaged stream-tracers and contours plot of the in-plane velocity modulus  $C_{y,z}$ , in planes  $y'z1_{G1}, y'z2_{G1}$  and  $y'z3_{G1}$  at  $Ro = 0.23$ (a,b) and  $Ro = 0.46$  (c,d),  $G1$  rotating configuration.

These considerations explain the increasing velocities observed when  $Ro$  increases in plane  $xy_{G1}$  in Fig. 4.36. Therefore, they also justify the more intense flow migration towards the leading side resulting from the ribs guidance effect which is further enhanced by the Coriolis-induced pressure gradient which pushing the flow towards  $y > 0[mm]$  in the separation bubble downstream each obstacle. Indeed the flow migration towards the leading side induced by ribs generates a recirculating structure close to channel's leading

side which is strengthened at corners between the rib-roughened surface and the leading side wall as  $Ro$  increases. In this region the guided flow has to be redirected towards the channel's upper surface ( $PS$ ), impinging on this latter at the channel upper-right corner, and hence, determining an enlargement of these structures. This behavior has important outcomes on the heat transfer field which could be significantly enhanced by this local impinging flow whose intensity increases note-worthily as the rotation number increases, as commented above. Finally, at the maximum  $Ro$  (i.e.  $Ro = 0.46$ ), in spite of the ribs guidance effects, one of the secondary structures appears close to the  $PS$  wall, as a result of the Coriolis effects (Figs. 4.38 (c,d)).

Considering both rotational and rib guidance effects on the flow direction, the horseshoe vortex branch cannot be detected when rotation takes place, as commented in the previous subsection (Subsec. 4.3.2) when Fig. 4.34 was introduced for  $Ro = 0.23$  and in this subsection for  $Ro = 0.46$  in Fig. 4.39 where the effects are clearly more evident. Indeed, a more uniform distribution of the heat transfer over the entire  $IP$  passage is found as previously shown in Fig. 4.35. Indeed, the enhancement factor generated by the turbulent mixing associated with the horseshoe vortices is lost when rotation takes place, as for  $G0$  configuration (see Subsec. 4.2.3).

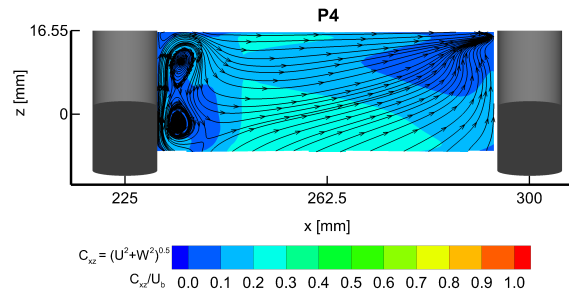


FIGURE 4.39 – CFD flow field inside the  $IP$  passage  $P4$  in plane  $xzR$  at  $Ro = 0.46$ ,  $G1$  rotating configuration.

A more quantitative view of the averaged  $Nu$  variation as  $Ro$  increases is reported in Tab.4.5. Three different values were computed:  $Nu_{SS}$  (which results from the spatial average over all the  $SS$ ),  $Nu_{IR}$  (where the area was restricted to  $IR$  region) and  $Nu_{IP}$  (which takes into account the remaining region).

In comparison to  $Ro = 0.23$ , at  $Ro = 0.46$  an increase of about 7% is found on the  $SS$  wall because of an augmentation of 15% in the  $IR$  region penalized by a 7% decrease in the  $IP$  area.

In conclusion, the mass flow splitting between the two exhaust sections of the channel is plotted in Fig. 4.3.4 for all  $Ro$  numbers for  $G0$  configuration (dashed line) and  $G1$  configuration (solid line). In this respect the following considerations are worth mentioning: in static condition, as just commented in Subsec. 3.4.3, the blockage effect produced by the 1<sup>st</sup> rib increases the mass exhausted in the  $P1$  passage (compare the red lines in Fig. 4.40); conversely, when rotation takes place no significant differences between configurations  $G0$  and  $G1$  are found, as demonstrate in Fig. 4.40 (green and blue lines).

	$Nu_{SS}$	$Nu_{IR}$	$Nu_{IP}$
$Ro = 0.23$	70.8	71	70.0
$Ro = 0.46$	75.7	81.7	65.2

TABLE 4.5 – *CFD* comparison of total  $Nu$  numbers at different  $Ro$  numbers,  $G1$  rotating configuration.

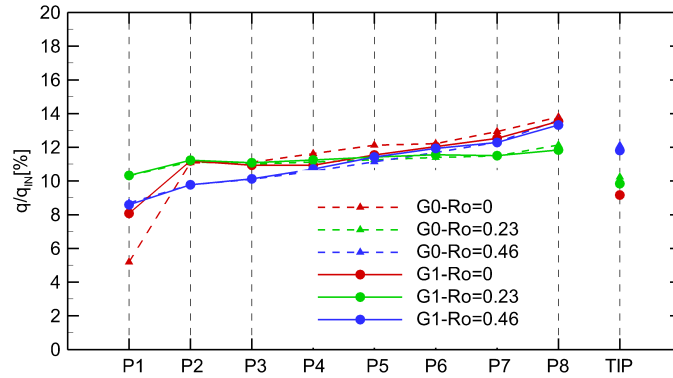


FIGURE 4.40 – *CFD* mass flow rate distribution at  $Ro = 0$  (red)  $Ro = 0.23$  (green) and  $Ro = 0.46$  (blue),  $G1$  rotating configuration.

#### 4.3.4 Effects Produced by Varying the Channel Orientation

In this subsection the numerical results obtained for different channel orientations, namely  $\gamma = 22.5[^\circ]$  and  $\gamma = 45[^\circ]$  will be presented. All considerations stated in Subsec. 4.2.4 for  $G0$  configuration at the inlet can be extended also to  $G1$  configuration. Figure 4.41 provides an overall view of the effect of  $\gamma$  and  $Ro$  on  $Nu$  distribution. As can be seen, two opposite trends can be observed:

- an almost uniform reduction in the  $Nu$  values between the  $IR$  passages;
- slight increases of the  $Nu$  in the  $IP$  passages.

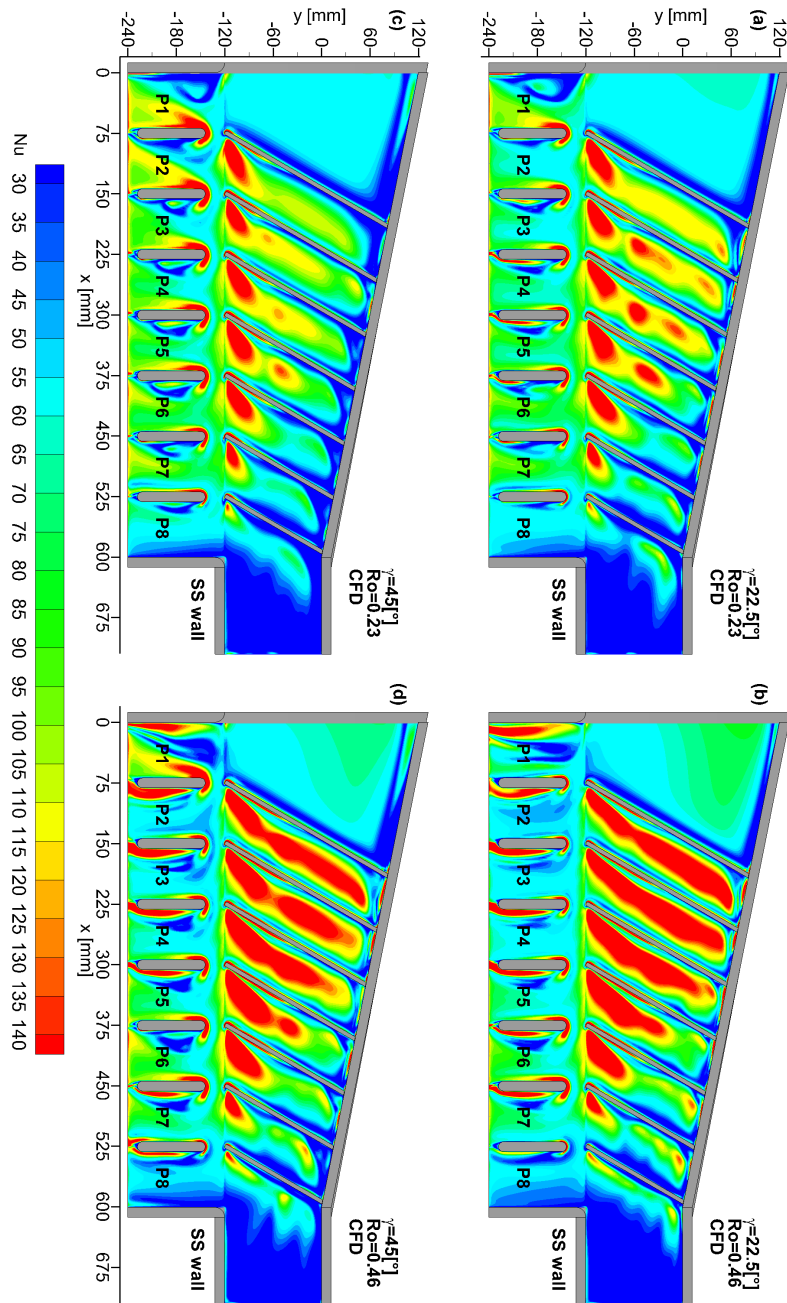


FIGURE 4.41 – CFD Nu distribution for different  $Ro$  and  $\gamma$  channel orientations, G1 rotating configuration.

With regard to the slight decreases in heat transfer augmentation promoted by ribs, Fig. 4.42 shows the comparison between the numerical time-averaged stream traces path and velocity  $C_{xy}$  in plane  $xy_{G1}$  at  $Ro = 0.46$  for different channel orientations (namely  $\gamma = 0^\circ$  (a),  $\gamma = 22.5^\circ$  (b) and  $\gamma = 45^\circ$  (c)). As  $\gamma$  increases, the combined effects of the Coriolis-induced pressure gradient in the slow flow layers and the ribs guidance effect decrease, consequently leading to a reduction in the velocity modulus  $C_{xy}$  and, hence, in the migration towards the leading side.

The profiles of the velocity modulus  $U'$  extracted from plane  $y'z2_{G1}$  at  $y = -15[mm]$  in Fig. 4.43 support all the previous comments. Indeed, the velocity profiles are characterized by two relative maxima close to the walls (i.e.  $SS$ ,  $PS$ ), because of the rotational effects, but, as  $\gamma$  increases, their peak values are reduced and consequently turbulence and heat transfer augmentation are lessened. The lower mean value of the velocity profiles over the channel height as  $\gamma$  increases is a consequence of the different distributions of the flow inside the inlet channel (see Figs. 4.19, 4.20). In fact, the flow imbalance resulting from rotation is reduced as  $\gamma$  increases (Fig. 4.20).

The helicoidally secondary structure (described in Subsec. 4.3.2 when Fig. 4.30 was introduced) is shown in Figure 4.45 by the time-averaged stream-tracers and contour plots of the in-plane velocity modulus  $C_{y'z}$  at  $Ro = 0.46$  for different channel orientations in the  $y'z1_{G1}$ ,  $y'z2_{G1}$  and  $y'z3_{G1}$  planes (parallels to the ribs). This figure provides a further demonstration of all the previous comments: as  $\gamma$  increases a less intense migration towards the leading side in proximity of the rib roughened wall ( $SS$ ) is found. This effect should be ascribed again to the different distributions of the flow inside the inlet channel (see Figs. 4.19, 4.20) as  $\gamma$  increases.

The modest increases of the  $Nu$  observed in Fig. 4.41 for different channel orientations ( $\gamma$ ) in the  $IP$  regions close to the hub, are due to the reappearance of the horseshoevor-

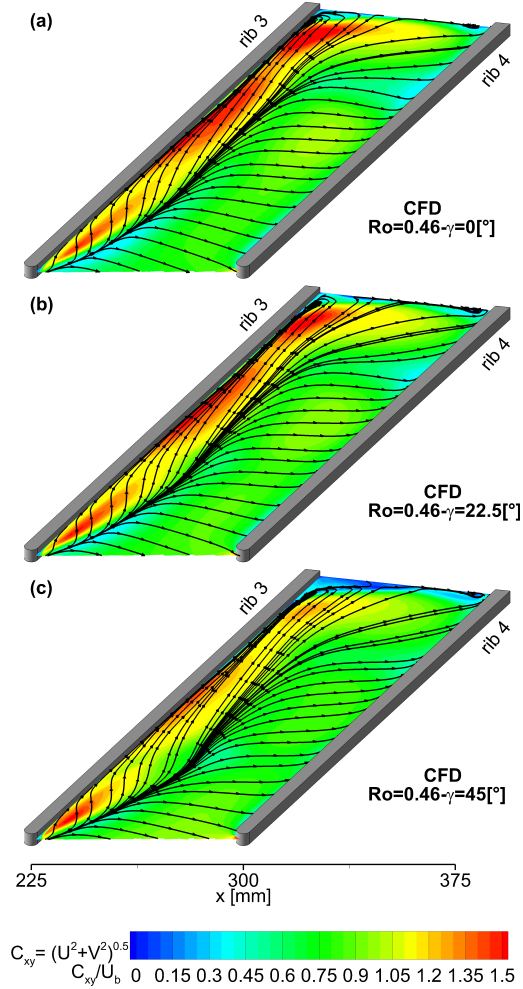


FIGURE 4.42 - *CFD* time-averaged stream-tracers path and velocity  $C_{xy}$  in plane  $xy_{G1}$  at  $Ro = 0.46$  for different channel orientations,  $G1$  rotating configuration.

tices (whose dimension is generally reduced when  $Ro > 0$ ) in particular in one situation:  $Ro = 0.23 - \gamma = 45[^\circ]$ , as shown in Fig. 4.44. This effect was also observed for configuration  $G0$  (see Subsec. 4.2.4 Fig. 4.23) and is not altered by the ribs in the  $SS$  wall.

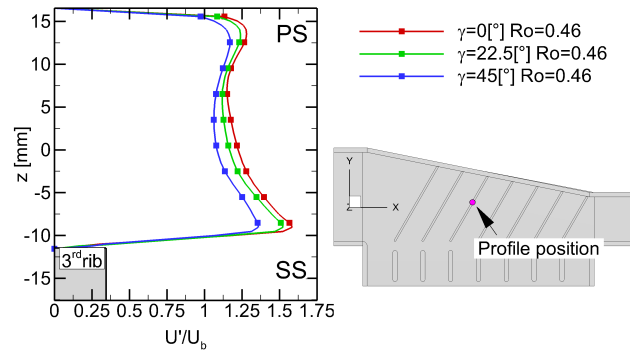


FIGURE 4.43 – *CFD* profiles of the velocity  $U'$  at  $Ro = 0.46$  and different  $\gamma$  orientations extracted in plane  $y'z'_{G1}$  at  $y = -15$  [mm],  $G1$  rotating configuration.

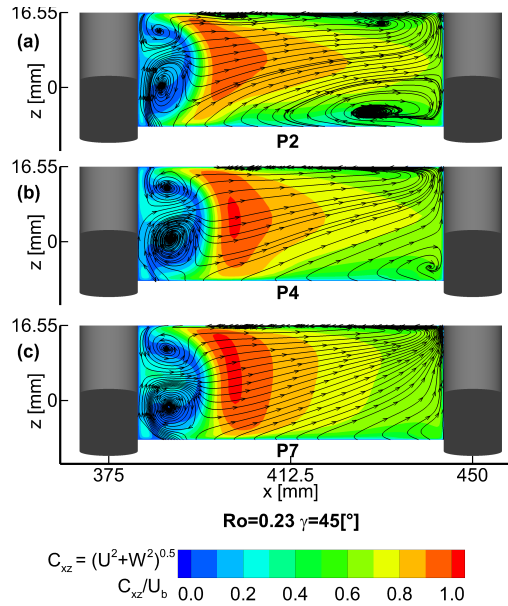


FIGURE 4.44 – *CFD* time-averaged stream-tracers and contours plot of the in-plane velocity modulus  $C_{y'z'}$ , in planes  $y'z'_{G1}$  (a,c,e),  $y'z'_{G1}$  and  $y'z'_{G1}$  (b,d,f) for all  $\gamma$  orientations,  $G1$  rotating configuration.

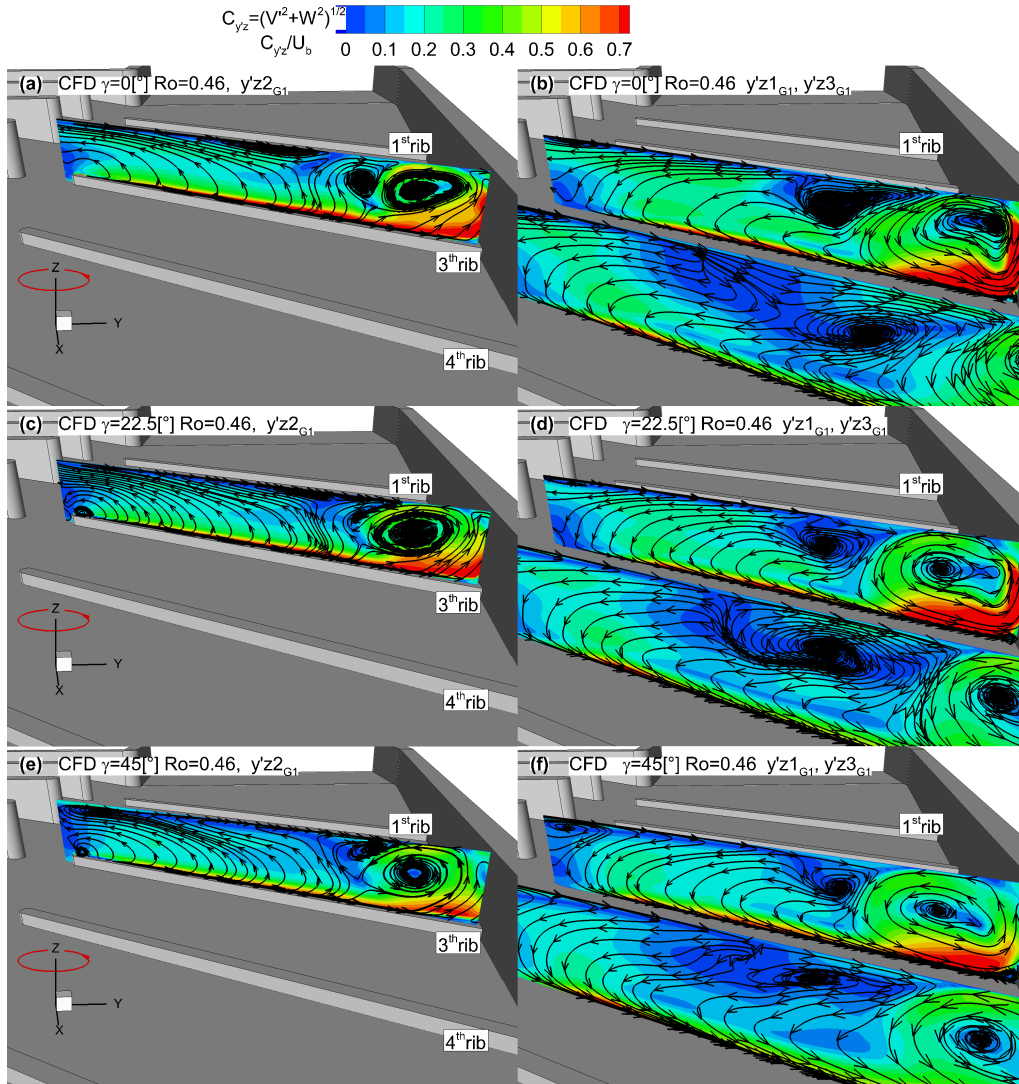


FIGURE 4.45 – CFD time-averaged stream-tracers and contours plot of the in-plane velocity modulus  $C_{y,z}$ , in planes  $y'z_{G1}$  (a,c,e),  $y'z_{G1}$  and  $y'z_{G3}$  (b,d,f) at  $Ro = 0.46$  for  $\gamma = 0^\circ$  (a,b),  $\gamma = 22.5^\circ$  (c,d) and  $\gamma = 45^\circ$  (e,f),  $G1$  rotating configuration.

In order to provide a quantitative evaluation of the effects mentioned above, Tab.4.6 extends the data previously reported in Tab.4.5 also to different channel orientations ( $\gamma$ ). As can be better appreciated by the  $Nu$  area-averaged values, the overall effect of a change in  $\gamma$  at fixed  $Ro$  is almost negligible if the overall  $SS$  area is considered. Conversely, this is the result of two opposite trends that are equally important for this specific configuration, and hence counterbalance each other: a negative effect in the ribbed portion and a positive one in the  $IP$  regions. As regards  $Nu$  increase with  $\gamma$  in the trailing edge portion, it can be pointed out that, the flow behavior is not uniformly distributed between the 8  $IP$  passages, as demonstrated by previous observations on this subject. In particular a decreasing trend is found from hub to tip. As an example, if cases  $Ro = 0.46 - \gamma = 0^\circ$  and  $Ro = 0.46 - \gamma = 45^\circ$  are compared, an overall increase of about 12[%] in  $Nu_{IP}$  is computed, while an increase in 25[%] or 3[%] is computed if the area is restricted only to  $P2$  and  $P7$ , respectively.

Finally, the mass flow is plotted in Fig. 4.46 for all the  $\gamma$  orientations and  $Ro$  numbers and does not present any significant differences when the channel orientation is changed. Indeed, this depends exclusively on the pressure distribution inside the channel which is slightly affected only by the different flow distributions resultin from a change in the channel orientation.

	$Nu_{SS}$	$Nu_{IR}$	$Nu_{IP}$
$Ro = 0.23 \gamma = 0^\circ$	70.8	71.0	70.0
$Ro = 0.23 \gamma = 22.5^\circ$	70.1	69.1	71.8
$Ro = 0.23 \gamma = 45^\circ$	68.5	63.9	76.6
$Ro = 0.46 \gamma = 0^\circ$	75.7	81.7	65.2
$Ro = 0.46 \gamma = 22.5^\circ$	76.9	81.3	69.3
$Ro = 0.46 \gamma = 45^\circ$	76.6	78.7	72.8

TABLE 4.6 – *CFD* comparison of total  $Nu$  numbers at different  $Ro$  numbers and channel orientations  $\gamma$ ,  $G1$  rotating configuration.

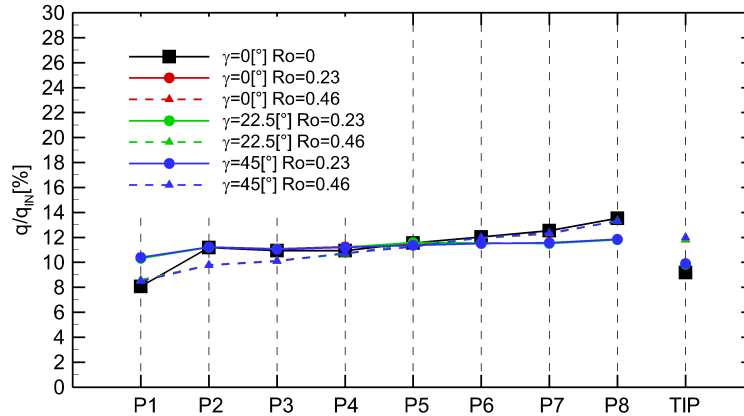


FIGURE 4.46 – *CFD* mass flow rate distribution at  $\gamma = 0^\circ$ ,  $\gamma = 22.5^\circ$  and  $\gamma = 45^\circ$  at varying rotation numbers,  $G1$  rotating configuration.

### 4.3.5 Summary

This sub-section presented an assessment of the capabilities of the *SST* turbulence model developed inside the commercial software ANSYS CFX  $\text{\textcircled{R}}$ v14.0 in rotating ( $Ro = 0.23$ ) condition for configuration *G1*. It was found that the turbulence model predicts all the main flow features in the inter-rib passage. This accurate prediction, if compared to the static case ( $Ro = 0$  see Subsec. 3.4.3), might be explained with the isotropic turbulence which assumed in all the two-equation models [4]. Indeed, when rotation takes place, this assumption is closer to the real physical phenomena as shown by the experimental turbulence distribution along  $x$  and  $y$  direction (see Fig. 4.32).

The experimental data available in literature ([7], [14] and [56]) were limited for the heat transfer and for the flow field to a single value of rotation number (i.e.  $Ro = 0.26$  for heat transfer and  $Ro = 0.23$  for the flow field, respectively) and channel orientation ( $\gamma = 0^\circ$ ). The author was compelled to extend these results to engine-like rotation number ( $Ro = 0.46$ ) and channel orientations ( $\gamma = 22.5^\circ - 45^\circ$ ) in order to study the combined effects of ribs, rotation and different channel orientations on the aero-thermal performances in a rib-roughened trailing edge cooling channel. Indeed, as shown by the average  $Nu$  in Tabs.4.5 4.6, these effects can become important:

- as  $Ro$  increases, the heat transfer in the roughened wall increases as well because of the enhancement of combined Coriolis and rib's guidance effects. Conversely, in the *IP* region, a progressive decrease in the  $Nu$  values is found as a result of the disappearance of the turbulent mixing generated by the horse-shoe vortex branch. The latter confirms the results obtained for the smooth configuration (*G0*) on the same geometry but without ribs (see Subsec. 4.2.3);
- as  $\gamma$  increases (to engine-like channel orientation) keeping  $Ro$  constant, a progressive decrease in the heat transfer in the rib-roughened wall is found because of the reduction in the combined Coriolis and rib's guidance effects. Only when  $Ro = 0.23$  and  $\gamma = 45^\circ$ , the turbulent mixing associated with the horse-vortex branch reappears and hence, the  $Nu$  in the *IP* wall reaches the maximum averaged value in rotating condition.

# 5

## Effects of Rotation and Different Channel Orientations in a Leading Edge Channel

### 5.1 Test Section

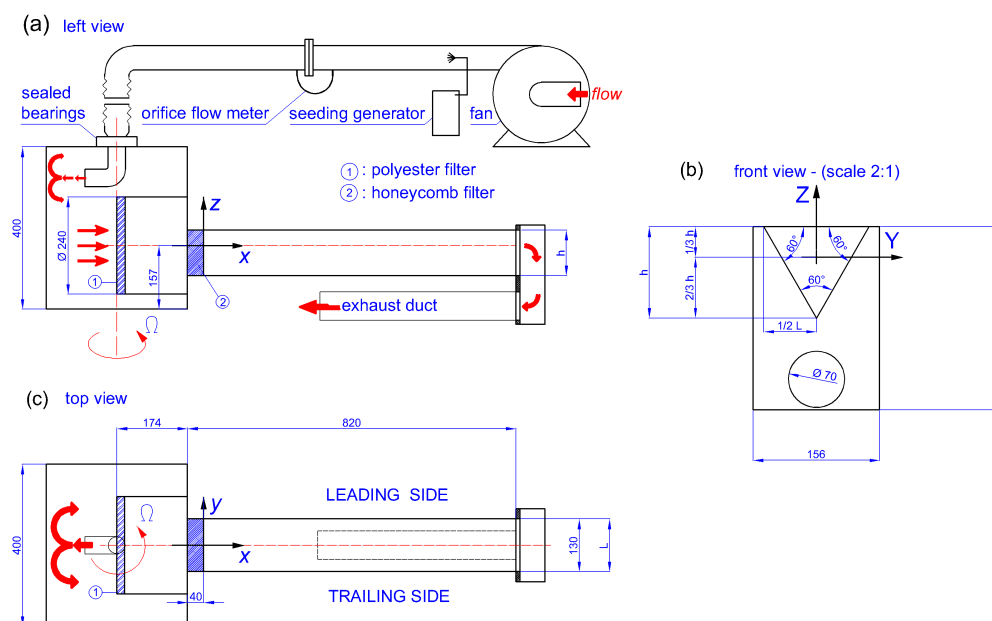


FIGURE 5.1 – Scheme of the test rig development for the present experimental campaign with the piping circuit.

The present channel geometry is sketched in Fig. 5.1 and resembles the one tested by Liu et al.[50], Liu et al.[49] and Huang and Liu [39]. The reason behind this choice is the wide availability of thermal data found in the author's work.

The cooling model basically consists of a straight, smooth channel with an equilateral triangle cross-section of side  $L = 130[mm]$ , and with a length of  $820[mm]$ . The test section is connected to a rotating settling chamber which is composed by a main plenum and a secondary cylindrical cavity with a diameter equal to  $240[mm]$  and coaxial with the channel axis (Figs. 5.1 (a,b)). Upstream the second cavity, a uniform flow inside the secondary plenum is obtained as a result of the pressure drop imposed by a polyester fiber filter. After the second cavity and at the channel inlet a  $40[mm]$  long honey-comb filter is placed to prevent flow separation, while at the channel outlet a second small settling chamber allows the control of the exit boundary conditions by confining the outlet flow in a return channel made of a circular tube of a  $70[mm]$  internal diameter. As in Liu et al.[50], Liu et al.[49] and Huang and Liu [39], the return channel allows avoiding any perturbation to the channel flow near the tip region that could conversely occur under rotation if the channel were set with free radial outlet.

The reference test conditions are  $Re = 20000$  and  $Ro = 0.2$  (defined on: bulk velocity  $Ub = 4.15[\frac{m}{s}]$ , hydraulic diameter  $Dh = 75.05[mm]$  and test section angular velocity  $\Omega = 11.06$ ) which can be considered to be representative of current engine conditions. Experimental measurements at  $Re = 20000$   $Ro = 0$  and  $Re = 10000$   $Ro = 0.4$  were also performed for the *CFD* validation purpose and, finally, a wider range of working conditions ( $Re = 10000, 20000$  and  $40000$  and  $Ro = 0.2, 0.4$  and  $0.6$ ) were numerically explored.

The selected geometry (a smooth radial channel) is rather simplified compared to modern leading edge cooling cavities, which are characterized by jet impingement cooling and film cooling holes (see Elbiary and Taslim [32]). Nevertheless, the study of this geometry has two considerable advantages:

- the availability of the thermal data obtained by Liu et al.[50];
- providing a thorough analysis of the rotational effects inside triangular channels in order to set the basis for the understanding of even more complex and realistic geometries for blade leading edge cooling.

## 5.2 Data Planes

The nomenclature and the positions of the planes used in this chapter for the analysis are shown in Figs. 5.2 and 5.3.

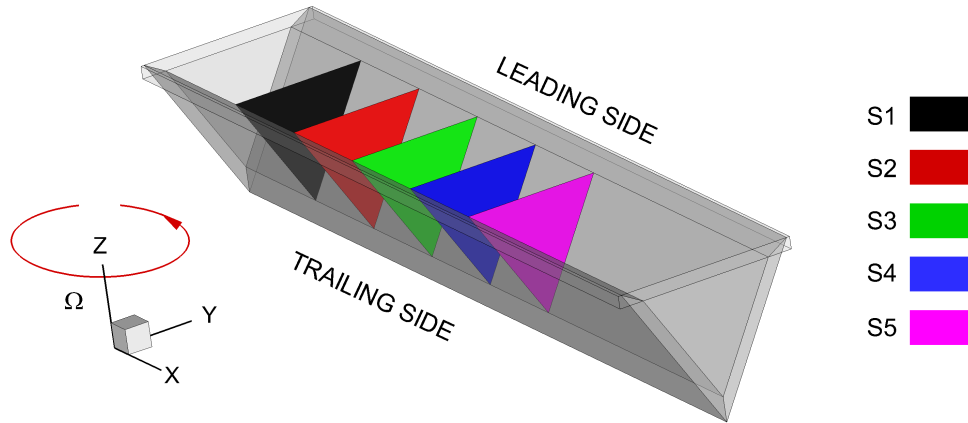


FIGURE 5.2 – Overview of the position of the experimental and *CFD* data planes (S1, S2, S3, S4, S5) Leading edge.

Planes S	position [mm]
S1	$x = 120$
S2	$x = 220$
S3	$x = 320$
S4	$x = 420$
S5	$x = 520$

TABLE 5.1 – S1, S2, S3, S4 and S5 planes see Fig. 5.2, leading edge.

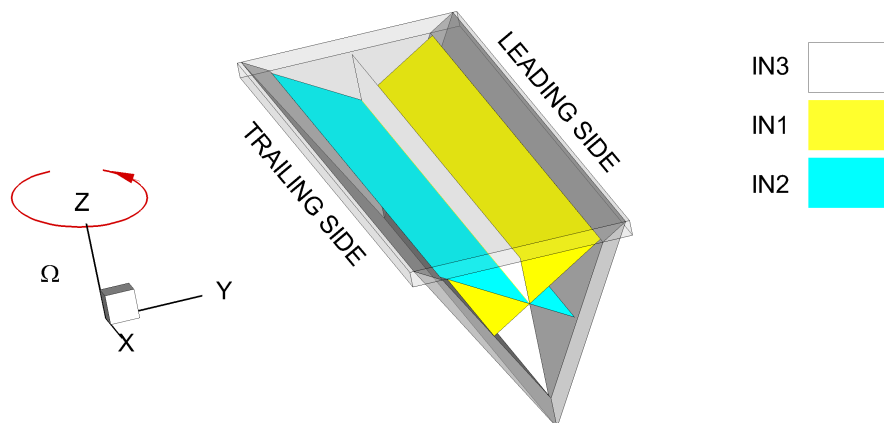


FIGURE 5.3 – Overview of the position of the experimental and *CFD* data planes (IN1, IN2, IN3) Leading edge.

Planes	position [mm]
IN1	$y' = 0$ median of the leading side apex
IN2	$y'' = 0$ median of the trailing side apex
IN3	$y = 0$

TABLE 5.2 – IN1 ,IN2 and IN3 planes see Fig. 5.3, leading edge.

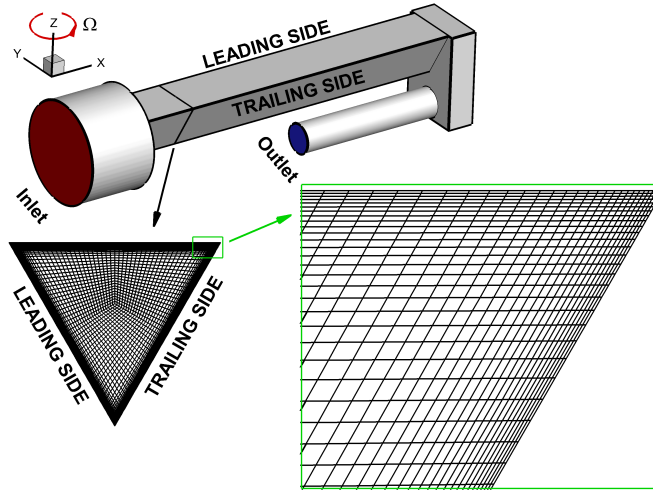


FIGURE 5.4 – 3-D view on the mesh for the leading edge geometry.

### 5.3 Computational Details

The computational domain Fig. 5.4 was discretized by a multi-block structured mesh with 4584121 hexahedral elements. Such a considerable number of cells results mainly from the need of using very tiny elements in the regions close to the apexes, as highlighted in Fig. 5.4. In these regions, quarter of O-grids [4] were applied in order to obtain higher cell's orthogonality. Furthermore, very fine mesh scales in the direction normal to the wall were used to all regions in order to allow a proper performance of the low- $Re$  model, which requires the dimensionless wall distance of the first grid point to be smaller than 2 [4]. Consequently, small cell growth rates (not greater than 1.2) were used for all the surfaces. A summary of the grid details and the mesh quality parameters is given in Tab.5.3.

N	$y_{max}^+$	$y_{avg}^+$	$\delta_{min}$	$L_{max}$
4584121	0.97	0.24	35.25	129

TABLE 5.3 – Grid details for the Leading Edge geometry.

The boundary conditions applied follow a classic scheme for incompressible air with

constant fluid properties taken at  $T = 293.15[K]$ . It should be pointed out that as a result of the optical constraints found in the rotating rig, it was impossible to obtain an experimental velocity map at the inlet to be used as a boundary conditions for *CFD*. These experimental limitations compelled the author to simulate the whole channel inlet by using a large domain mesh which includes part of the settling chamber (Fig. 5.4). Hence, a constant mass flow value equal to  $0.0176 [Kg/s]$  was imposed at the inlet (red surface in Fig. 5.4), in order to reach the same experimental *Re* number (equal to 20000) in the channel, while the ambient pressure ( $101325 [Pa]$ ) was forced at the outlet (blue surface in Fig. 5.4). In the experiments, which provide the validation data for the present simulations, a honeycomb filter (number(2) in Fig. 5.1) was used at the junction between the channel and the settling chamber. This filter was modelled as a directional loss porous region, which required a kinetic pressure loss coefficient to be specified along both stream-wise and transverse directions. In particular, much higher losses in the transverse directions, *y* and *z*, than in the stream-wise direction, *x*, were applied in order to suppress the transverse velocity components, *V* and *W*, as it is expected for a flow that goes through a fine honey-comb. The parameters setting was verified by comparing the velocity profiles computed at the channel inlet with the experimental data for  $Re = 20000$  and  $Ro = 0$  as shown in Figure 5.5, which reports the comparison between experimental and numerical stream-wise velocity profiles extracted at position  $x = 120[mm]$  from planes IN3 in Fig. 5.5 (a), and from planes IN1 and IN2 in Fig. 5.5 (b) (see Fig. 5.3 for planes position). An overall good agreement is found between experimental and numerical data. The only discrepancies are observed near the apexes.

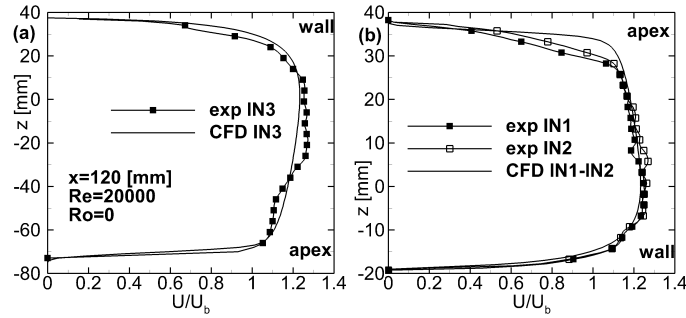


FIGURE 5.5 – Experimental and CFD stream-wise velocity profiles extracted at  $x = 120[mm]$  from planes IN3 (a) and IN1-IN2 (b).

This behavior is surely due to the difficulties in modelling correctly the behavior of the honey-comb filter in the corner regions. However, these differences do not affect significantly the features of the simulated flow field on which the following analysis is based, as demonstrated by the comparison in the next sub-sections between experimental and *CFD* data downstream the inlet section.

### 5.3.1 Quantification of the Numerical Accuracy

In order to ensure the consistency of the *CFD* simulations, a grid independence study was performed. This was accomplished by employing three similar meshes characterized by different spatial resolutions. The parameters of the grids used in the refinement study are summarized in Tab.5.4 where: the medium grid corresponds to the one described above. Figure 5.6 reports also a comparison of the solutions obtained by the three different meshes at  $Re = 20000$  and  $Ro = 0.2$  with the velocity profiles  $V$  extracted from plane IN3 at  $x = 520[mm]$ . It can be seen that no significant differences are found between the fine and medium meshes results. Therefore, the medium mesh was considered as a good compromise between spatial resolution and computational effort associated with the overall number of elements.

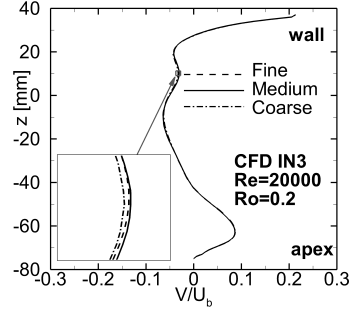


FIGURE 5.6 – *CFD* velocity profiles  $V$  for the three meshes tested. Data extracted at  $x = 520[mm]$  from plane IN3.

Grid	$N$	$y_{avg}^+$
Fine	9772752	0.19
Medium	4584121	0.24
Coarse	2085576	0.31

TABLE 5.4 – Grid parameters for grid independency study for the Leading Edge geometry.

## 5.4 Results and Discussion

In this section the Coriolis effects on the flow field inside the rotating channel will be discussed. In particular the analysis will focus on : secondary flows (Subsec. 5.4.1), stream-wise velocity distribution (Subsec. 5.4.2), effect of  $Ro$  and  $Re$ (Subsec. 5.4.3), turbulence intensity  $I$ (Subsec. 5.4.4), effects on the heat transfer based on the data from Liu et al.[50] (Subsec. 5.4.5) and effects of different channel orientations (Subsec. 5.4.6).

### 5.4.1 Comparison of the *CFD* and Experimental Results at Reference Conditions ( $Re=20000$ $Ro=0.2$ )

Figure 5.7 reports the comparison between *CFD* predictions and experimental measurements of the time-averaged stream-tracers path in plane S5 (at  $x = 520[mm]$ ). The data provide a clear display of the main characteristics of the secondary structures that develop inside the triangular cross-section duct. The match between experiments and simulation is satisfactory and both data report a flow structure which is apparently quite similar to the simplified flow model illustrated in Fig. 1.10 and proposed by Liu et al.[50] and Liu et al.[49]. However, some difference can be observed:

- the main direction along which the secondary flows develop is not horizontal (i.e. parallel to the direction of rotation), but depends on the cross-section shape;
- on the leading/trailing sides of the channel there is no separation/reattachment point whose existence might have a strong influence on the thermal field.

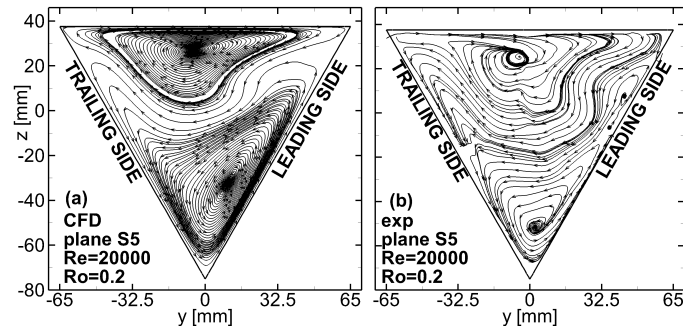


FIGURE 5.7 – *CFD* (a) and experimental(b)time-averaged stream-tracers in plane *S5* for  $Re = 20000$  and  $Ro = 0.2$ .

Although these observations might appear as a minor issue, they have a relevant impact on the development of both flow and thermal fields. The reasons of this can be understood by taking a closer look at the physics causing the appearance of the secondary structures. The phenomenon is dominated by the characteristics of the three boundary layers that develop on the channel walls and which can be considered, to some extent, as Ekman layers. An Ekman layer is a boundary layer flow that develops a particular velocity distribution (Holton and Hakim [38]) because of the combined effect of a pressure gradient and Coriolis forces.

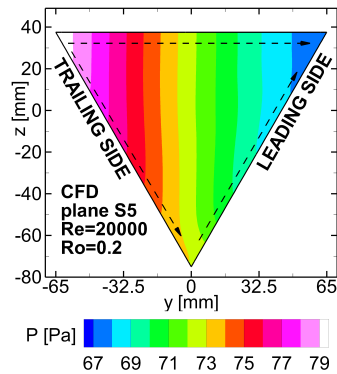


FIGURE 5.8 – *CFD* contour map of the pressure distribution on the channel cross-section in *S5* plane at  $Re = 20000$  and  $Ro = 0.2$ .

In the present case, a pressure gradient aligned along  $y$  direction (Fig. 5.8) and pointing towards the channel trailing side is induced by the  $y$  component of the Coriolis force that acts on the bulk flow (force per unit mass) (Bons and Kerrebrock[15], Hart [37], Lezius and Johnston [46], Speziale [64] and Speziale and Thangam [63]). This pressure gradient is not balanced by the Coriolis forces inside the slower boundary layers and, consequently, the near wall flow is forced to move towards the lower pressure region, i.e. towards the channel leading side (see the arrows in Fig. 5.8), as demonstrated by the paths of the near wall stream-tracers in Fig. 5.7. Therefore, no separation or reattachment can occur on the channel's walls, in contrast with the hypothesis suggested by the flow model of Fig. 1.10. Conversely, separation and reattachment are possible only at the channel apices, as shown again by the stream-tracers in Fig. 5.7. Further evidence of the near wall flow deviation imposed by the combined effect of pressure gradient and Coriolis forces, and the resulting Ekman velocity spiral, is provided by Fig. 5.9, where examples of velocity vectors distributions along the directions normal to the three channel walls are reported for both experimental and *CFD* data.

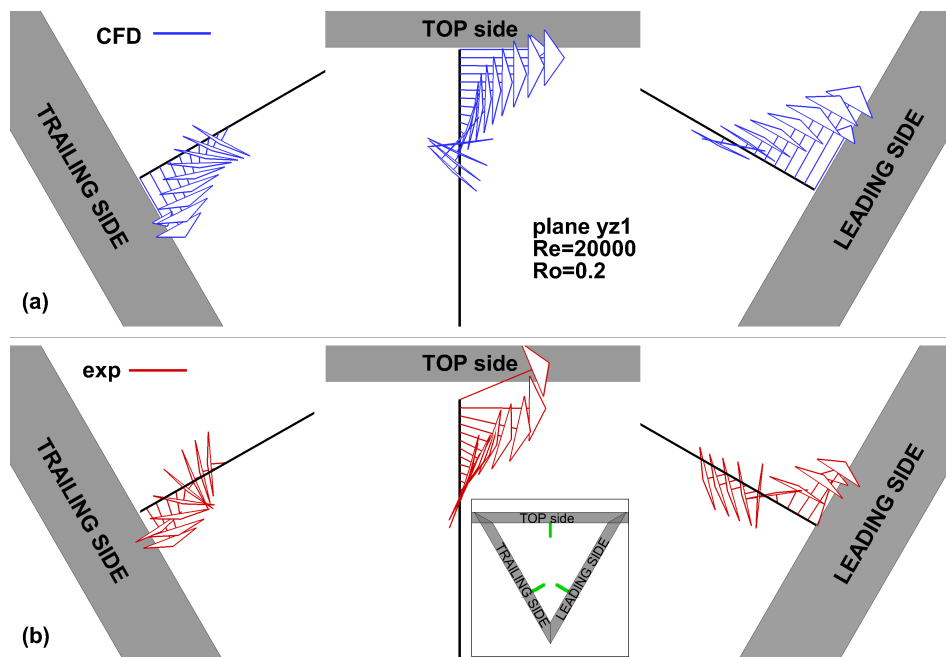


FIGURE 5.9 – *CFD* (a) and experimental(b) 3-D view of the velocity distribution inside the Ekman layer.

It should be now clearer why the secondary structure measured or computed inside the present channel geometry has the particular shape depicted in Fig. 5.7. Moreover, the physical explanation provided above will also allow to explain the development of these structures along the stream-wise direction of the channel, as it will be discussed later on.

### 5.4.2 Stream-Wise Velocity Distribution

Based on the considerations that was made in Subsec. 1.3.3 concerning orthogonal rotating radial channel with outward flow (Bons and Kerrebrock[15], Speziale [64] and Speziale and Thangam [63]), the stream-wise velocity distribution on the channel cross-section turns out to be more complicated and rather different from what might be expected by applying directly the specific knowledge about squared channels to this peculiar geometry.

Figure 5.10 shows the comparison between the *CFD* (Fig. 5.10 (a)) and experimental (Fig. 5.10 (b)) time-averaged contour maps of the stream-wise velocity  $U$  in plane *S5* at  $x = 520[mm]$ . A good match between experiments and *CFD* predictions is found. They both show two velocity peaks located near the top wall and in proximity of the lower apex, concurrent with a velocity deficit near the top-right (leading) corner.

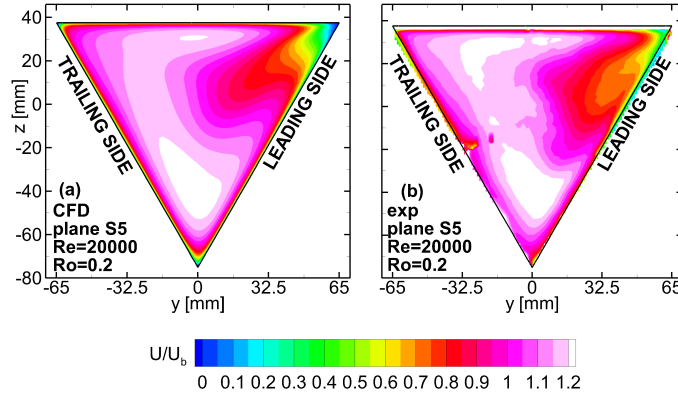


FIGURE 5.10 – *CFD* (a) and experimental (b) time-averaged stream-wise velocity contour map in plane *S5*,  $Re = 20000$ - $Ro = 0.2$ .

In order to better describe this behavior, Fig. 5.11 shows contour maps of the stream-wise ( $U$ , Fig. 5.11(a)) and transverse ( $V$ , Fig. 5.11(b)) velocity components at different  $x$  positions extracted from the *CFD* data. In order to make the data interpretation easier, six ad-hoc chosen volumetric stream tracers are added to the representation. The flow pertaining to the *Stream-Tracers (str)A* (representative of the bulk flow) has almost the same  $U$  velocity along all the channel (Fig. 5.11(a)), while its  $V$  velocity is low and slightly negative (Fig. 5.11(b)) and its path is therefore displaced towards the trailing side and  $z < 0[mm]$  because of the secondary flows direction previously observed (see Fig. 5.7). Conversely, along *strB* (near wall flow at the top side), the  $U$  velocity increases as a consequence of the acceleration induced by the  $x$  component of the Coriolis force, which is higher for *strB* than for *strA* as a result of the higher, and positive,  $V$  velocity associated to the secondary flow motion found close to the top wall (see Figs. 5.11(a,b) from *S3* to *S5*).

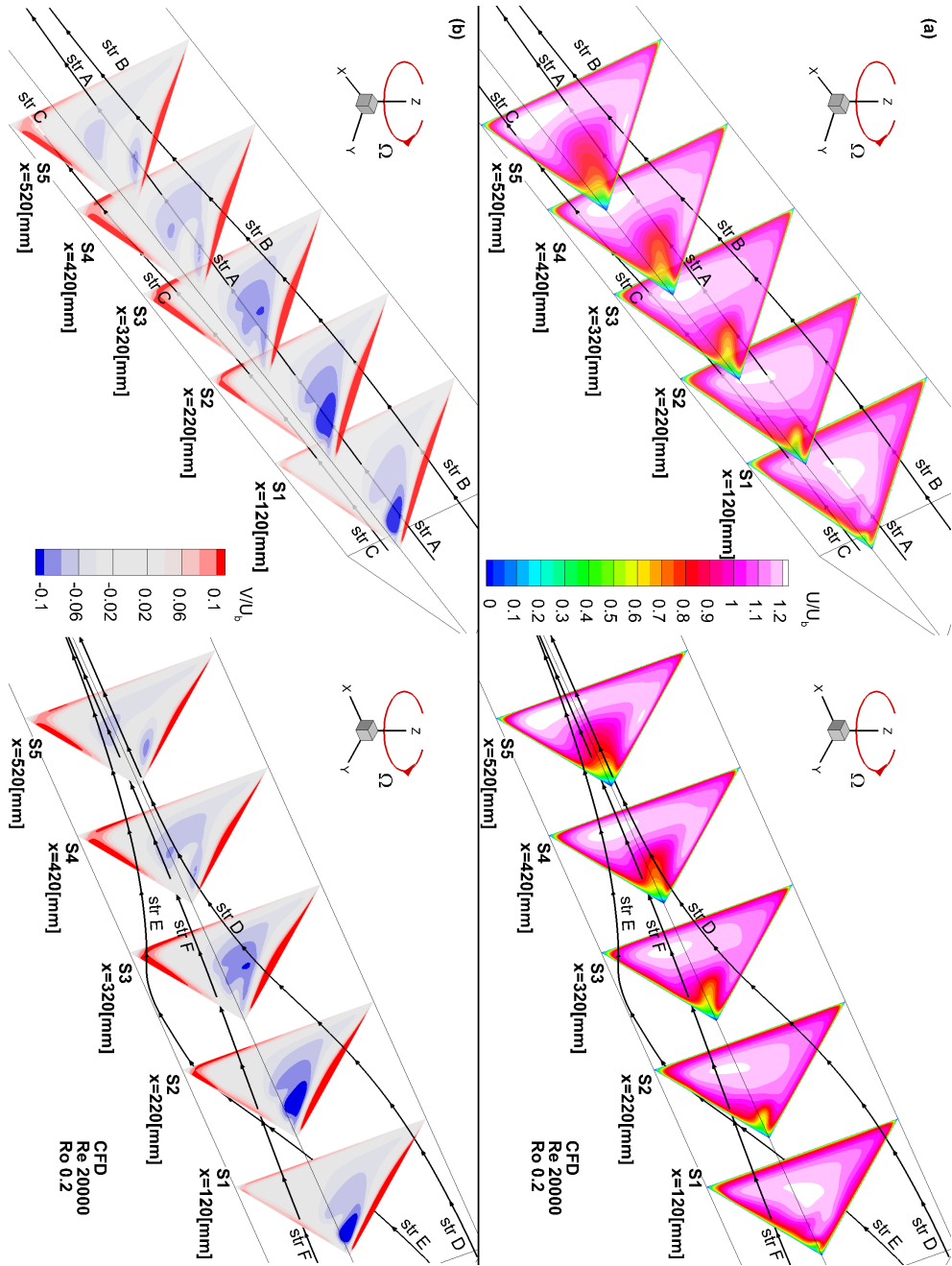


FIGURE 5.11 – Contour maps of the stream-wise (a) and span-wise (b) velocities at different channel locations from *CFD* at  $Re = 20000$ ,  $Ro = 0.2$ .

In the bottom apex the effects of the secondary flows and the stream-wise acceleration occur together, yielding to the highest acceleration coupled with a deflection even towards the leading side (see the path and the corresponding velocity levels of *strC* in Fig. 5.11). Meanwhile, in Fig. 5.11 (a) it can be observed that there is also the formation of a low  $U$  velocity region close to the leading side apex, whose dimension increases as the flow develops. This behavior is related to the velocity peak displacement towards the trailing side previously observed, resulting from the displacement of low momentum fluid in the near wall layers towards  $y > 0$  [mm] as shown by *strD*, *strE*, and *strF* and the  $V$  contour plots in Fig. 5.11 (b).

### 5.4.3 Effect of $Ro$ and $Re$

In comparison to what was observed for  $Ro = 0.2$  the flow field is further complicated if the rotation rate is increased, resulting in even more relevant discrepancies in comparison to the flow model Fig. 1.10.

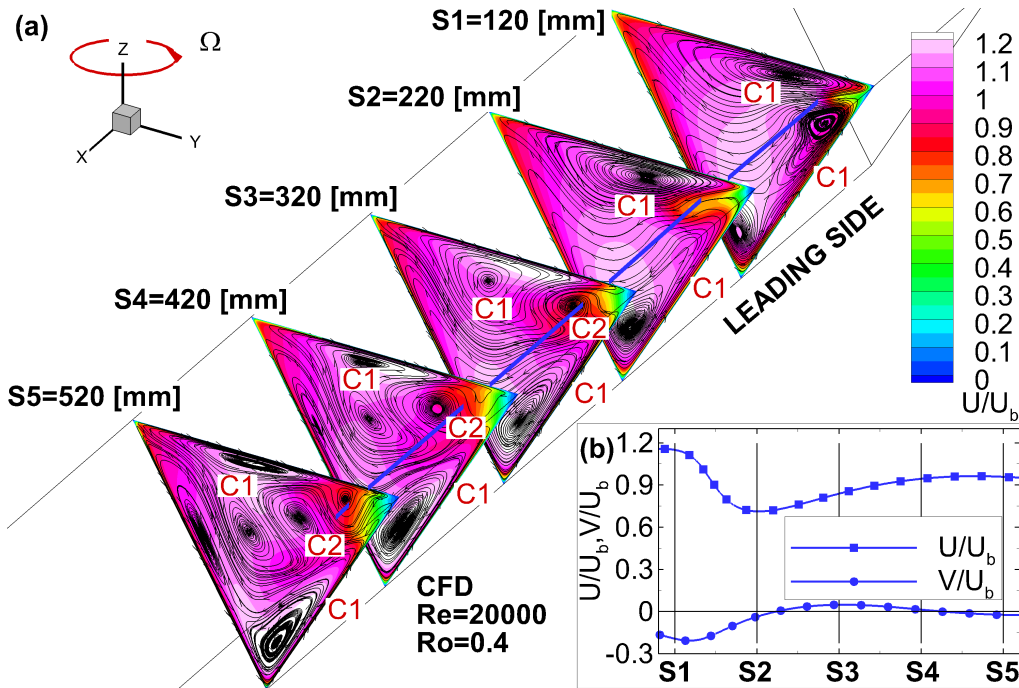


FIGURE 5.12 – *CFD* contour maps of the stream-wise velocity and stream-tracers at different channel locations (a); evolution along the channel of the stream-wise and span-wise velocities at point  $y = 38$  [mm],  $z = 24$  [mm] (b) (see the blue line in Fig. 5.12(a)). The data are at  $Re = 20000$ ,  $Ro = 0.4$ .

Figure 5.12 reports the stream-tracers and the stream-wise velocity distribution in five  $yz$

planes obtained by *CFD* at  $Re = 20000$  and  $Ro = 0.4$ , which highlights an unexpected flow behavior characterized by the appearance of a third vortex cell near the top-right corner (anti-clockwise structure *Vortex Cell (C)C2* in Fig. 5.12(a)). In order to understand the development of this structure, Fig. 5.12(b) reports the evolution of the  $\mathbf{U}$  and  $\mathbf{V}$  velocities along the blue line in Fig. 5.12(a), which indicates to a point on the channel cross-section at  $y = 38[mm]$ ,  $z = 24[mm]$ . As already commented when Fig. 5.11 was introduced, the secondary flow displaces low momentum fluid towards the top-right (leading) corner. Consequently, starting from the first part of the channel, the velocity deficit region becomes wider (compare contour maps in *S1* and *S2* of Fig. 5.12(a)) and the  $\mathbf{U}$  velocity decreases (Fig. 5.12(b)). At a certain position (about *S2*), the  $\mathbf{U}$  velocity close to the leading corner decreases below a value that is comparable to the one found in the viscous layers close to the walls. Therefore the span-wise pressure gradient in this region acts in the same way as in the boundary layers, that is displacing fluid towards the leading side (see positive  $\mathbf{V}$  velocities after position *S2* in Fig. 5.12(b)). This is the trigger for the development of the counter clockwise rotating roll cell *C2*. At this point it should be remembered that the stream-wise component of the Coriolis forces,  $A_{cx}$ , determines an acceleration of the flow layers in which the  $\mathbf{V}$  velocity component is positive (Fig. 5.12(b), position *S3*). Therefore, the flow starts accelerating along the stream-wise direction ( $\mathbf{U}$  in Fig. 5.12(b) downstream *S3*) and meanwhile structure *C2* is advected towards the trailing side by the secondary flow main cells (*C1*). Therefore, sufficiently downstream the entry section, a velocity distribution as the one at the entrance is re-established, with high  $\mathbf{U}$  velocity associated to negative  $\mathbf{V}$  velocity (position *S5* in Fig. 5.12(b)). Consequently, the phenomenon just described can have a new genesis starting from this point and thus the flow will not reach a steady state within the channel length.

The appearance of *C2*-like rolls has been observed also by Speziale [64] in a rectangular channel at intermediate rotation rates: they were found in the low velocity region at mid-height of the channel's leading side. It is important to note that these structures must develop whichever the cross-section shape is, as they are a consequence of the convective flows resulting from the Coriolis acceleration. However, in contrast with the work of [64], in the present case only a secondary roll cell (*C2*) develops, while a couple was found in a rectangular channel. Indeed, in the present case the pressure gradient is not aligned along an axis of symmetry of the geometry, unlike what occurs in a rectangular cross-section channel.

If the rotation rate is further increased to  $Ro = 0.6$ , the development of the Coriolis roll cells and of the secondary cells previously commented occurs at decreasing radial ( $\mathbf{x}$ ) positions inside the channel (compare Fig. 5.12(a) and Fig. 5.13), consistently with a higher pressure gradient because of the rotation. This suggests that the effects observed at higher  $Ro$  are possible also at  $Ro = 0.2$  if the channel is sufficiently long. Furthermore, at the highest  $Ro$ , because of the faster development of the anti-clockwise rolls *C2*, the extension of the separation region tends to remain constant along the channel's length, and however lower than that observed at  $Ro = 0.2$  (compare Fig. 5.11 and Fig. 5.13).

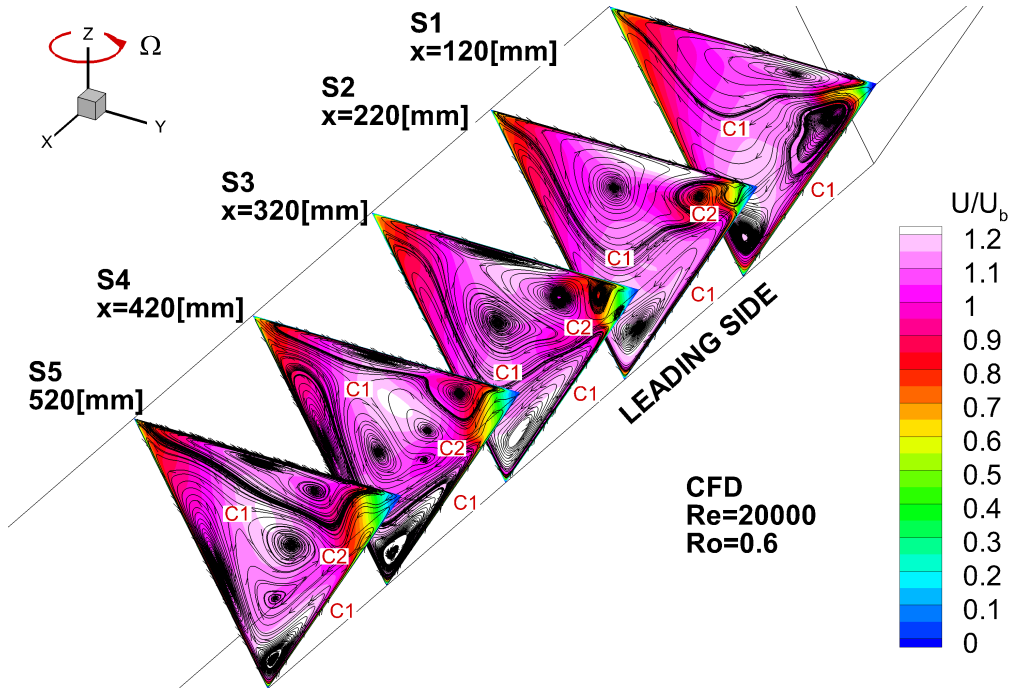


FIGURE 5.13 – *CFD* contour maps of the stream-wise velocity and stream-tracers at different channel locations at  $Re = 20000$ ,  $Ro = 0.6$ .

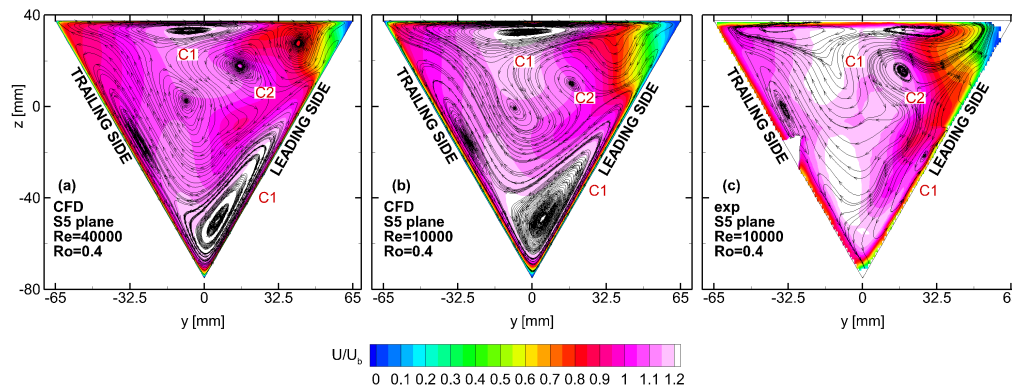


FIGURE 5.14 – *CFD* (a,b) and experimental (c) contour maps of the stream-wise velocity and stream-tracers in plane *S5*. *CFD* data at  $Ro = 0.4$  and  $Re = 40000$  (a) and  $Re = 10000$  (b), experimental data at  $Ro = 0.4$  and  $Re = 10000$  (c).

A last observation must be provided about the dependence of these flow features on the  $Re$  number. To discuss the sensibility to the  $Re$ , a set of additional *CFD* simulations

were performed at  $Ro = 0.4$  and different values of  $Re$ , namely 10000 and 40000. Experimental data were also collected at  $Re = 10000$  and  $Ro = 0.4$  and were used to provide a reference for  $CFD$  validation. Figure 5.14 sums up the information obtained from these data, reporting the stream-tracers and contour maps of the  $\mathbf{U}$  velocity in plane S5 obtained by means of both  $CFD$  and experimental data. Once again, a good agreement between experimental and  $CFD$  data can be noticed by comparing the stream-tracers and the  $\mathbf{U}$  velocity contour maps in Figs. 5.14(b,c). Finally, comparing Figs. 5.14 (a,b) no substantial differences can be observed varying the  $Re$  numbers from 10000 to 40000; it can therefore be concluded that the secondary flows development depends solely on the angular velocity, at least in the investigated range of  $Re$ .

#### 5.4.4 Turbulence intensity

Rotation can influence the flow also by modifying the transport proprieties of the shear layers associated with the mutual orientation of the flow vorticity (i.e. the vorticity of the shear and/or boundary layers) and the background vorticity ( $\Omega$ , rotation vorticity), resulting in a stabilizing/destabilizing effect on the shear layers associated with a reduction/augmentation in the their turbulence content and mixing, which are of prime interest for the heat transfer process inside cooling channels. Stabilization effects were discussed for the first time discussed by [17] and more recently by [40], where the focus was mainly related to turbomachinery flows.

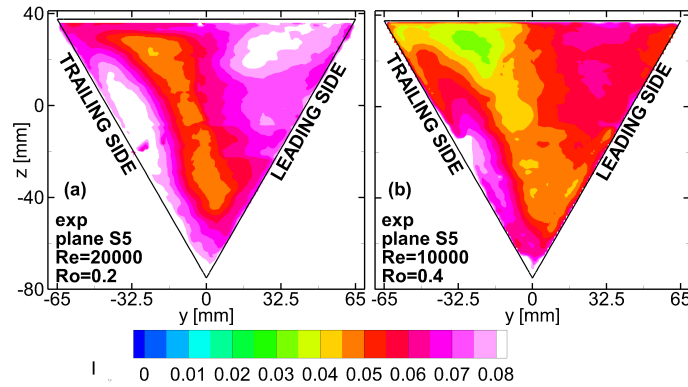


FIGURE 5.15 – Experimental contour maps of flow turbulence intensity in plane S5 for  $Re = 20000$ ,  $Ro = 0.2$  (a) and  $Re = 10000$ ,  $Ro = 0.4$  (b).

In the present channel configuration, the boundary layers that develop on the leading and trailing channel side walls experience different stabilization effects in accordance with the observations reported in [40]. The experimental contours of the Turbulence intensity  $I$  in plane S2 can be observed in Fig. 5.15. The stabilizing/destabilizing effect on the leading/trailing side walls is clearly evident:  $I$  values at the leading side are lower (stabilization of the boundary layer) than at the trailing side (destabilization of

the boundary layer). This effect becomes more noticeable if the rotation number is increased (compare Figs. 5.15(a,b)). High turbulence levels characterize also the flow at the leading side apex, consistently with the presence of the separation region observed in the time-averaged velocity field because of the confluence of the Eckman layer flows at the top and leading walls.

When looking at the *CFD* turbulence intensity (see Fig. 5.16), it is possible to observe that the comparison with the experimental data is not satisfactory (compared Figs. 5.15 vs 5.16). The overall shape of the turbulence field is captured while the computed levels are much lower than the measured ones. The reasons of this have to be found in the assumptions made in the *CFD* computations, where isotropic turbulence is assumed (as in all the two-equation turbulence models), while the experimental results show a strong anisotropy (see Fig. 5.15).

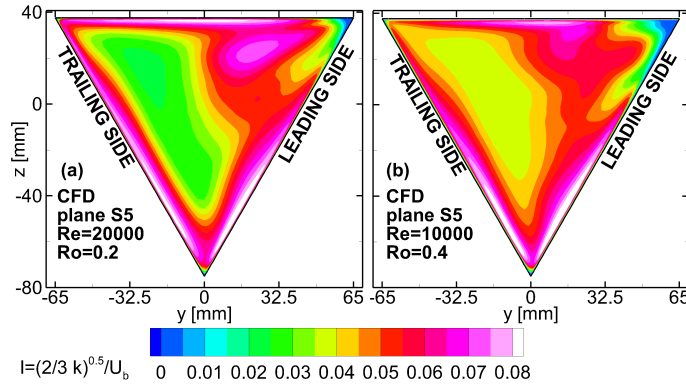


FIGURE 5.16 – *CFD* contour maps of flow turbulence intensity in plane *S5* for  $Re = 20000$ ,  $Ro = 0.2$  (a) and  $Re = 10000$ ,  $Ro = 0.4$  (b).

#### 5.4.5 Thermal effects

After providing a complete description of the time-averaged flow features developing in a rotating channel with triangular cross-section, thanks to the data available in Liu et al.[50], a further discussion can be addressed concerning the effects of the flow features described above about the thermal field, therefore providing a better explanation of the thermal behavior of this kind of devices. Figure 5.17 reports the thermal data by Liu et al.[50] for a set of flow conditions that are comparable to those considered in the present work, including also the values at  $Ro = 0$ . The plots show the distribution of the *Nu* number enhancement,  $\frac{Nu}{Nu_0}$ , extracted along the channel length at different positions on the lateral walls. In Fig. 5.17, *L1/ T1* refer to the half portion of the leading/trailing side close to the bottom apex, while *L2/ T2* pertain to the upper half of the leading/trailing sides in proximity to the upper apexes.

The first observation refers to the *Nu* enhancement that occurs at the trailing side. In comparison to the static conditions (empty symbols in Fig. 5.17), both *T1* and *T2* po-

sitions show the highest heat transfer enhancement at all rotational speeds, consistently with the presence of the Coriolis secondary rolls, which are responsible for a continuous flow renewal on the near wall flow layers. A second observation is that the ratio  $\frac{Nu}{Nu_0}$  is slightly decreasing with the radial direction at  $Ro = 0.14$  and  $Ro = 0.18$  while it is almost constant, with oscillations about a mid value, at higher rotations rates ( $Ro = 0.28$  and  $Ro = 0.56$  in Fig. 5.17). This is the consequence of the faster development of the complex flow structure commented above as the  $Ro$  number is increased (see Subsec. 5.4.3).

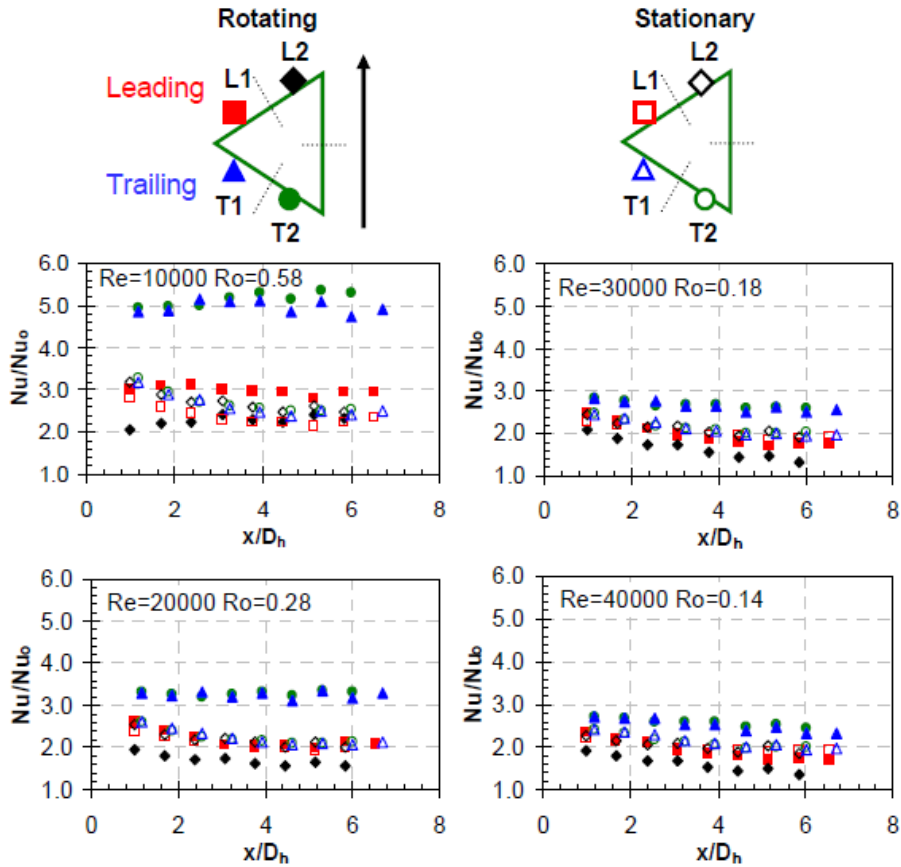


FIGURE 5.17 – Heat transfer data from Liu et al.[50].

It should be noted that the heat transfer data at the lower (L1) and upper (L2) portions of the leading side have different behaviors as  $Ro$  varies. Indeed, while the upper portion

**L2** shows an enhancement factor always smaller than the static case, the lower one (**L1**) shows always comparable or even greater values. This is the consequence of the uneven flow conditions previously observed for the two different portions of the leading side. The upper one (**L2**) is exposed in proximity to the low momentum flow region which develops at the leading upper apex and, consequently, the heat transfer is penalized unlike in the lower (**L1**) portion where the flow remains attached to the wall. Furthermore, the growth of the separation region as the coolant flows in the channel observed from the *CFD* data at  $Ro = 0.2$  is responsible for the bigger difference between the  $Nu$  enhancement values between **L1** and **L2**, which is evident at  $Ro = 0.18$  in Fig. 5.17. Conversely, the **L2** data at  $Ro = 0.58$  show an opposite trend, which has to be related to the smaller extension of the separation structure compared to  $Ro = 0.2$  and the appearance of **C2** roll cell, as previously commented Subsec. 5.4.3. Finally, the present analysis allows also the identification of the reason why the ratio  $\frac{Nu}{Nu_0}$  at **L1** position is comparable to (see  $Ro = 0.14, 0.18, 0.28$  in Fig. 5.17) or even higher ( $Ro = 0.58$  in Fig. 5.17) than the one for the static case. This is due to the presence of the highest stream-wise velocity peak which is displaced towards the lower half of the channel section when rotation occurs (see Fig. 5.10 and Fig. 5.11), causing an increase in the local  $Re$  values. As  $Ro$  increases, the velocity peak is further displaced closer to the lower portion of the leading wall (see Fig. 5.12 and Fig. 5.13) and, therefore, determines higher velocity resulting in higher heat transfer rates compared to the lower rotating condition or the static case.

#### 5.4.6 Effects of the Channel Orientation

In this subsection the flow field numerical results obtained for different channel orientations namely  $\gamma = 22.5[^\circ]$  and  $\gamma = 45[^\circ]$  will be presented.

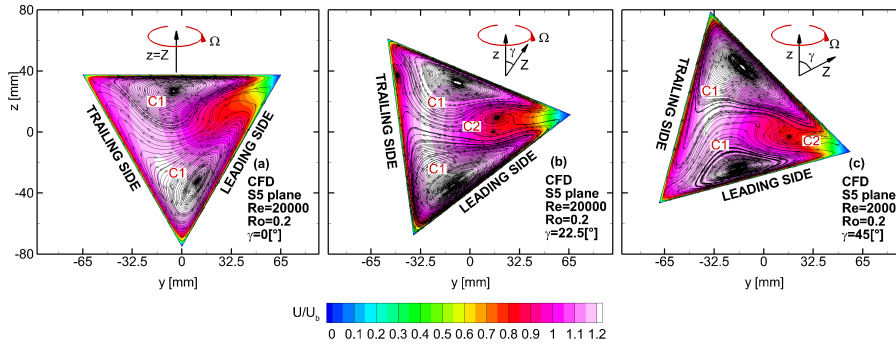


FIGURE 5.18 – *CFD* contour maps of the stream-tracers velocity in plane **S5** for different channel orientation  $\gamma = 0[^\circ]$ (a),  $\gamma = 22.5[^\circ]$ (b) and  $\gamma = 45[^\circ]$ (c), at  $Re = 20000$  and  $Ro = 0.2$ .

Figure 5.18 reports the stream-tracers and the stream-wise velocity distribution  $U$  in **S5** plane at different channel orientations ( $\gamma = 0[^\circ]$  Fig. 5.18(a),  $\gamma = 22.5[^\circ]$  Fig. 5.18(b) and  $\gamma = 45[^\circ]$  Fig. 5.18(c)) obtained by means of the *CFD* code at  $Re = 20000$  and

$Ro = 0.2$  (reference condition). As can be seen, the data provide a clear display of the main characteristics of the secondary structures that develop inside the triangular cross-section duct as  $\gamma$  increases. Apparently, this flow behavior is quite similar to the one illustrated in Fig. 1.11 proposed by Huang and Liu [39]. However, some differences can be observed:

- the main direction along which the secondary flow develops is not parallel with the direction of rotation, consistently with the results obtained for  $\gamma = 0^\circ$  (see Subsec. 5.4.1);
- on the leading/trailing sides of the channel there is no separation/reattachment point whose existence might have a strong influence on the thermal field as discussed in Subsec. 5.4.1
- at  $\gamma = 45^\circ$  (see Fig. 5.18(c)) the stream-tracers in proximity of the trailing side point towards the upper/left apex, hence in the opposite direction to  $\gamma = 0^\circ$  and  $\gamma = 22.5^\circ$ .

The reasons of this can be understood if a close look is given (as in Subsec. 5.4.1) to the pressure gradient induced by the  $y$  component of the Coriolis force as  $\gamma$  increases Fig. 5.19. It should be remembered that the channel's  $z$  axis is not aligned with the rotational axis  $Z$ , as shown in Figs. 5.18 and 5.19.

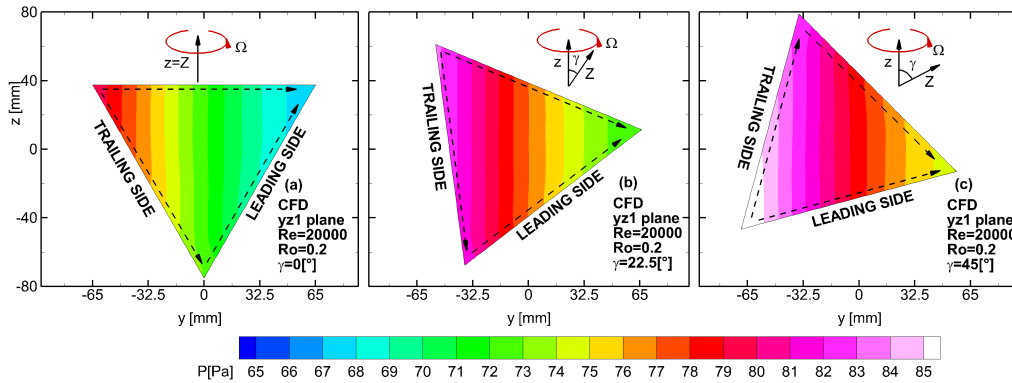


FIGURE 5.19 – CFD contour map of the pressure distribution on the channel cross-section in  $S5$  plane at different channel orientation  $\gamma = 0^\circ$ (a),  $\gamma = 22.5^\circ$ (b) and  $\gamma = 45^\circ$ (c), at  $Re = 20000$  and  $Ro = 0.2$ .

The pressure gradient is not balanced by the Coriolis forces inside the slower boundary layers and, consequently, the near wall flow is forced to move towards the lower pressure region, (see the arrows in Fig. 5.19). Moreover, when  $\gamma$  is equal to  $45^\circ$  (see Fig. 5.19 (c)) the pressure gradient on the trailing side points towards the upper/left vertex, opposite to the channel's orientations  $\gamma = 0^\circ$  and  $\gamma = 22.5^\circ$  (see Figures 5.19 (a,b) vs (c)), as clearly demonstrated by the paths of the near wall stream-tracers in Fig. 5.18. Hence, no separation or reattachment can be found on the channel walls, in contrast with the

hypothesis suggested by the flow model Fig. 1.11 developed by Huang and Liu [39]. Indeed, separation and reattachment are only possible at the channel apexes, as confirmed again by the stream-tracers in Fig. 5.19.

Moreover, as  $\gamma$  increases a  $3^{rd}$  vortex cell appears near the top right corner  $C2$  (see Figs. 5.4.1 (b,c)) and there is no evidence of this for  $\gamma = 0[^\circ]$  at  $Ro = 0.2$  (see Fig. 5.4.1 (a)). Indeed, as demonstrated in Subsec. 5.4.3 for  $\gamma = 0[^\circ]$ , the development of this vortex cell ( $C2$ ) starts at  $Ro > 0.2$ .

If the rotation rate is further increased to  $Ro = 0.4$  Fig. 5.20 or  $Ro = 0.6$  (Fig. 5.21) the flow behavior becomes completely different from the one in the model (Fig. 1.11) developed by Huang and Liu [39] but it is consistent with the descriptions in Subsec. 5.4.3.

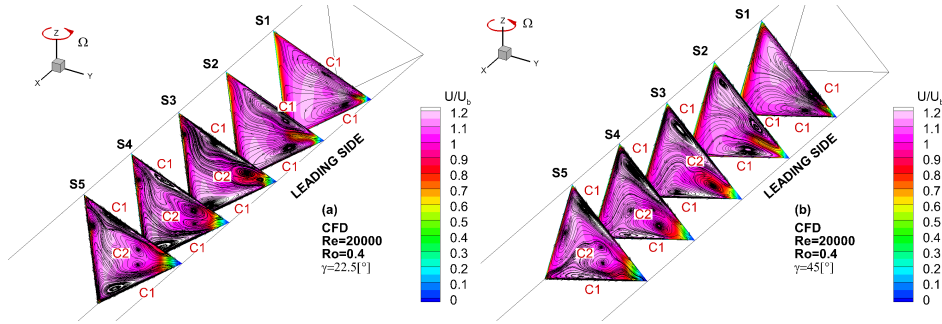


FIGURE 5.20 – CFD contour maps of the stream-wise velocity and stream-tracers at different channel locations at  $Re = 20000$   $Ro = 0.4$   $\gamma = 22.5[^\circ]$  (a) and  $\gamma = 45[^\circ]$ (b).

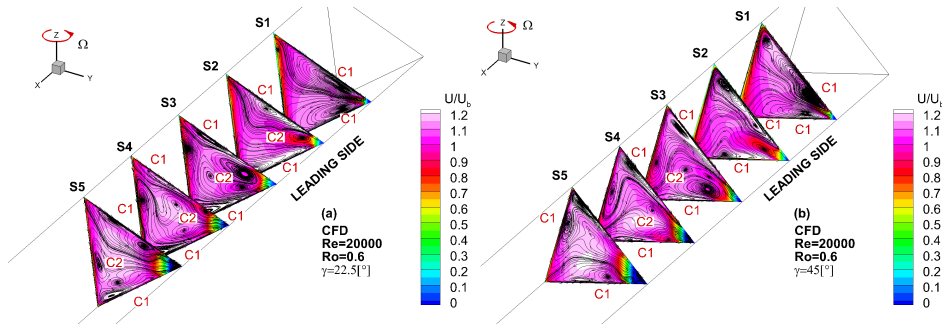


FIGURE 5.21 – CFD contour maps of the stream-wise velocity and stream-tracers at different channel locations at  $Re = 20000$   $Ro = 0.6$   $\gamma = 22.5[^\circ]$  (a) and  $\gamma = 45[^\circ]$ (b).

Indeed, as a result  $\gamma = 0[^\circ]$ (see Figs. 5.12 and 5.13) because of the secondary flows displacing the low momentum fluid towards the top-right (leading) apex (for more details see Subsec. 5.4.3), the rotating cell  $C2$  develops. Moreover, if  $Ro$  is equal to 0.6, the Coriolis roll cells  $C1$  and the secondary cell  $C2$  develop at smaller radial ( $x$ ) position inside the channel (compare Figs. 5.20 and 5.21), consistently again with an higher

pressure gradient resulting from the increased rotation. The only differences from  $\gamma = 0[^\circ]$  channel orientation (compare Figs. 5.12 vs 5.20 and Figs. 5.13 vs 5.21) are the positions of the  $C1$  and  $C2$  cells produce by the misalignment between the peripheral velocity  $Y$  axis and the channel width direction  $y$  axis.

## 5.5 Summary

The effects of rotation and channel orientations on the flow field inside a radial channel with triangular shaped cross-section were investigated in a wide range of working conditions that pertain to turbomachinery applications, namely the internal cooling of the turbine blades leading edge.

The secondary flow structures induced by rotation and different channel orientations turn out to be more complex than the flow models (Figs. 1.10 1.11) commonly accepted by scientific community to address the thermal behavior of these devices.

An explanation about the growth and development of the secondary structures was provided by looking at the physical mechanisms behind:

- the rotational effects;
- different channel orientations namely  $\gamma = 22.5[^\circ]$  and  $\gamma = 45[^\circ]$ .

The main flow features at  $\gamma = 0[^\circ]$  as  $Ro$  increases can be summarized as follows:

- near wall flows must be always deflected towards the leading side, therefore, separation and reattachment cannot occur on the channel lateral walls but are found at leading/trailing apices, respectively;
- a region of low momentum fluid is localized at the channel leading apex, while the highest stream-wise velocity peak is found in the lower apex and displaced towards the leading side;
- inside the low momentum fluid region, a third vortex cell can appear between the two main ones depending on the position along the channel and the rotation number;
- the overall structure does not develop towards a steady configuration along the channel length. This behavior is stressed by an increase in the rotation number while it turned out to be independent from  $Re$ , at least in the investigated range.

Turbulence intensity has been also investigated under rotation, and the stabilizing/destabilizing effects of rotation on the boundary layers have been well highlighted by the experimental data. The *CFD* code is also able to capture the main features of the spatial distribution and the effects of rotation. However, the computed levels turn out to be much lower than the experimental ones as a result of the strong limitations imposed by the isotropic turbulence assumption made in all the two-equation turbulence models. Moreover, the deep understanding gained through this analysis of the flow field behavior

(at  $\gamma = 0^\circ$  as  $Ro$  increases) allows a precise justification of the heat transfer performances in rotation that are available in the literature ([50]) on the same geometry. Finally, the effect of different channel orientations, namely  $\gamma = 22.5^\circ$  and  $\gamma = 45^\circ$ , have been numerically investigated. These results provide a further confirmation of the description of flow field behavior at  $\gamma = 0^\circ$  and show again that a thorough flow field analysis is essential in order to have a deeperr understanding of the thermal behavior in the internal cooling channels.



---

# 6

## Concluding Remarks

### 6.1 Achieved Objectives

The present work addresses aspects of the suitability of *CFD* for predicting the aero-thermal performances inside cooling channels designed for two portions of the blade, namely *trailing edge* and *leading edge*, in static and rotating conditions by varying the channel orientation. The main achieved objectives will be summarized hereafter.

#### 6.1.1 Quantification of the Numerical Accuracy

The quantification of the numerical accuracy was obtained as follows:

- with the established method for evaluation of discretization errors (*GCI* see Apx. C), for the trailing edge geometries (see Subsecs. 3.3.1, 3.4.1, 3.5.1, 4.2.1 and 4.3.1);
- by comparing the velocity results of three similar meshes characterized by different spatial resolutions, for the leading edge geometry (see Subsec. 5.3).

Under both these methods an accurate quantification of the uncertainty was the prerequisite for a meaningful conclusion about mesh sensitivity and for a correct interpretation of results. Indeed, this evaluation is important in order to provide information about the most sensitive region to the mesh resolution. Such information is often impossible to estimate a priori.

#### 6.1.2 Assessment of the Capabilities of the CFD Predictions

After the evaluation of discretization errors, an assessment of the prediction obtained by means of the *SST* turbulence model developed on ANSYS CFX ®v14.0 was undertaken comparing the numerical results with experimental data obtained from literature review (see Subsecs. 3.3.3, 3.4.3, 3.5.3, 4.2.2, 4.3.2, 5.4.1, 5.4.2, 5.4.3 and 5.4.4). Only in one rib-roughened configuration (*G1* trailing edge) four more turbulence models were tested (in static condition  $Ro = 0$ ) in order to enhance all computational results. The data obtained show that 90[°]ribs still represent one of the greatest challenges for the *RANS* formulation (see for further details Subsec. 3.4.4) because of the assumption of

isotropic turbulence which is made in all two-equations models (as demonstrated when Fig. 4.32 was introduced). However, in all *trailing edge* configurations in static condition, the *CFD* code predicts correctly the complex flow field inside the *IP* passages but always over-estimates the peaks of heat transfer in this area because of the excessive production of turbulence kinetic energy as shown in Apx. E. Nevertheless, despite these limitations, the comparison between experimental and numerical average heat transfer levels is good because the averaged-numerical values are within the measurements uncertainty as demonstrated in Sec. 3.6.

Subsequently the comparison between experimental and numerical results was extended in orthogonal rotating condition for two *trailing edge* configurations (namely *G0 G1*) and the *leading edge* cooling channel showing that *SST* turbulence model developed inside ANSYS CFX ®v14.0 is able to predict successfully the main rotational effects inside these particular geometries.

### 6.1.3 Exploitation of the CFD tool in Engine-Like Conditions

In Subsecs. 4.2.3, 4.2.4, 4.3.3 and 4.3.4 5.4.3 the analysis was numerically extended to engine-like condition, i.e. by increasing *Ro* and varying the channel orientation  $\gamma$  with respect to the *Z* axis. Moreover, for the *leading edge* channel the effect of different *Re* was accounted for as well. The numerical predictions obtained enable an easier and faster analysis of the aero-thermal behavior and make it possible to extend the study to a wider range of test conditions in order to make up for the lack of literature available. Indeed, for both geometries the analyses demonstrates the need of a deep understanding of both flow field and heat transfer data in engine-like condition in order to provide necessary information to close the lack in the literature available assumed by the research/industrial community.

## 6.2 Recommendations for Future Research

The result obtained in the present thesis allowed to derive some advices for future research which can be divided in two main fields: numerical work (see Subsec. 6.2.1) and physical effects (Subsec. 6.2.2).

### 6.2.1 Numerical Work

The numerical predictions of the aero-thermal performances of internal cooling channel designed for gas turbine engines can be obtain strongly benefits from improvements in turbulence modelling. For two-equation models one major issue is the generation of too high levels of turbulence kinetic energy in the stagnation zone. In the turbulence model based on  $k-\omega$  Wilcox's formulation ([70]) developed on ANSYS CFX ®v14.0 limiters are placed in the computation of the turbulence kinetic energy (for further details see Subsec. 2.3.2) in order to fix this problem. These limits require improvements because (as shown by Figs. 3.17, 3.27 and 3.40) the match between experimental and numerical flow field data is fully achieved; conversely the heat transfer generated in these area is always

over-predicted by the *CFD* code (see Figs. 3.11, 3.22 and 3.34). These discrepancies in the *CFD* have to be ascribed to an over-prediction of the turbulence kinetic energy as illustrated in Apx.E. However, limiters for the production rate  $P_k$  are difficult to develop without specific modifications which would implied generality to be lost. Another problem identified in this work is the incapability of the commercial software ANSYS CFX ®v14.0 to predict the flow field and, hence, heat transfer for one static configuration (see Sec. 3.4). In this situation only improvements that take into account for the transition from laminar to turbulent flow and vice-versa can be done in order to fix these issues, namely the correct computations of transition/turbulent reattachment.

### 6.2.2 Physical Effects

The *CFD* code was exploited to simulate the aero-thermal behavior in two significant configurations which resemble the *trailing-edge* and *leading-edge* cooling channels for blades of stator/rotor gas turbine engines. The next step to improve the analysis of both geometries is to add the effect of the buoyancy parameter so as to obtain data which are closer to the physical phenomena occurring in real engines. This analysis should be performed following the same steps as in this thesis, i.e. using experimental data for the numerical validation purpose and subsequently, obtaining an easier and faster study exploiting the *CFD* commercial software. In addition for the *leading-edge* cooling channel it would be useful to gradually analyze the effects of turbulators, impingement cooling and more engine-similar cross-sections, in order to firstly analyze the capabilities of the *CFD* commercial tool and, eventually - if the validation between experimental and numerical data is achieved - numerically extend the study to more engine-like conditions by increasing  $Ro$  and varying the channel orientation.



---

# Bibliography

- [1] M. Amro, B. Weigand, R. Poser, and M. Schnieder. An experimental investigation of the heat transfer in a ribbed triangular cooling channel. *International Journal of Thermal Sciences*, 46(5):491–500, May 2007.
- [2] J. Anderson. *Computational Fluid Dynamics*. McGraw-Hill, 1995.
- [3] L. Andrei, A. Andreini, L. Bonanni, and A. Facchini. Heat Transfer in Internal Channel of a Blade: Effects of Rotation in a Trailing Edge Cooling System. *Journal of Thermal Science*, 21(3):236–249, June 2012.
- [4] Ansys. ANSYS CFX-14.0 User Guide. Tech. Rep., ANSYS Inc., 2012.
- [5] A. Armellini, L. Casarsa, and C. Mucignat. Flow Field Analysis Inside a Gas Turbine Trailing Edge Cooling Channel Under Static and Rotating Conditions. *International Journal of Heat and Fluid Flow*, 32(6):1147–1159, December 2011.
- [6] A. Armellini, F. Coletti, T. Arts, and C. Scholtes. Aerothermal Investigation of a Rib-Roughened Trailing Edge Channel With Crossing-JetsPart I: Flow Field Analysis. *Journal of Turbomachinery*, 132(1):11009–1–11009–9, January 2010.
- [7] A. Armellini, Casarsa L., and C. Mucignat. Experimental Assessment of the Aero-Thermal Performance of Rib Roughened Trailing Edge Cooling Channels for Gas Turbine Blades. *Applied Thermal Engineering*, 58(1-2):455–464, September 2013.
- [8] A. Armellini, C. Mucignat, L. Casarsa, and P. Giannatasio. Flow field investigations in rotating facilities by means of stationary PIV systems. *Measurement Science and Technology*, 23(2):025302, February 2012.
- [9] D. R. Ballal and J. Zelina. Time-depeident and time-averaged turbulence structure near the nose of a wing-body junction. *Journal of Aircraft*, 41(1):43–50, January 2004.
- [10] F. Ballio, C. Bettoni, and S. Franzetti. A Survey of Time-Averaged Characteristics of Laminar and Turbulent Horseshoe Vortices. *Journal of Fluids Engineering*, 120(2):233–242, February 1998.
- [11] G. Barigozzi and S. Ravelli. Effects of Trailing Edge Film Cooling on the Aerodynamic Performance of a Nozzle Vane Cascade. In *9TH European Turbomachinery Conference*, Istanbul, Turkey, 2011.
- [12] G. Barigozzi, S. Ravelli, and A. Perdichizzi. Pressure side and cutback trailing edge film cooling in a linear nozzle vane cascade at different mach numbers. *Journal of Turbomachinery*, 134(5):051037–1/051037–10, September 2012.

- [13] C. Bianchini, B. Facchini, F. Simonetti, L. Tarchi, and S. Zecchi. Numerical and Experimental Investigation of Turning Flow Effects on Innovative Pin Fin Arrangements for Trailing Edge Cooling Configurations. *Journal of Turbomachinery*, 134(2):021005–1–021005–8, March 2012.
- [14] L. Bonanni, C. Carcasì, B. Facchini, and L. Tarchi. Heat transfer measurements and effect of rotation in a trailing edge cooling system. In *66 Congresso Nazionale ATI*, pages 5–9, Rende (Cosenza), 2011.
- [15] J. P. Bons and J. L. Kerrebrock. Complementary Velocity and Heat Transfer Measurements in a Rotating Cooling Passage With Smooth Walls. *Journal of Turbomachinery*, 121(4):651–662, October 1999.
- [16] J. Boussinesq. Essai sur la thorie des eaux courantes. In *Mmoires prsents par divers savants*, volume 23, pages 1–680, Acadmie des Sciences Paris, 1877.
- [17] P. Bradshaw. The analogy between streamline curvature and buoyancy in turbulent shear. *Journal of Fluid Mechanics*, 36:177–191, 1969.
- [18] P.P. Bradshaw, B.E. Launder, and J.L. Lumley. Collaborative Testing of Turbulence Models. *Journal of Fluids Engineering*, 118(2):243–247, June 1996.
- [19] R. S. Bunker. The Effects of Manufacturing Tolerances on Gas Turbine Cooling. *Journal of Turbomachinery*, 131(4):041018, October 2009.
- [20] R.S. Bunker. *Cooling Design Analysis*. In: *The Gas Turbine Handbook*. US Department of Energy, National Energy Technology Laboratory, 2006.
- [21] R.G. Casado, M. Thierry, R. Fedrizzi, A. Di-Sante, and T. Arts. PIV investigation of internal cooling channels for gas turbines, with 45 degrees inclined ribs. In *Proceedings of 12th International Symposium on Application of Laser Techniques to Fluid Mechanics*, Lisbon (Portugal), 2004.
- [22] I. B. Celik, U. Ghia, P. Roache, C.J. J. Freitas, H. Coleman, and P.E. Raad. Procedure for Estimation and Reporting of Uncertainty Due to Discretization in CFD Applications. *Journal of Fluids Engineering*, 130(2):78001, July 2008.
- [23] S.W. Chang, T.M. Liu, S.F. Chiou, and S.F. Chang. High Rotation Number Heat Transfer of Rotating Trapezoidal Duct With 45-deg Staggered Ribs and Bleeds from Apical Side Wall. *Journal of Heat Transfer*, 130(6):061702, June 2008.
- [24] T.J. Chung. *Computational Fluid Dynamics*. Cambridge University Press, 2002.
- [25] F. Coletti, A. Armellini, T. Arts, and C. Scholtes. Aerothermal Investigation of a Rib-Roughened Trailing Edge Channel With Crossing Jets - Part II: Heat Transfer Analysis. *Journal of Turbomachinery*, 133(3):031024–1–031024–8, July 2011.
- [26] F. Coletti, T. Maurer, and T. Arts. Flow field investigation in rotating rib-roughened channel by means of particle image velocimetry. *Experiments in Fluids*, 52(4):1043–1061, April 2012.

- [27] F.J. Cuhna, M.T. Dahmer, and M.K. Chyu. Analysis of Airfoil Trailing Edge Heat Transfer and Its Significance in Thermal-Mechanical Design and Durability. *Journal of Turbomachinery*, 128(4):738–746, October 2006.
- [28] W. J. Davenport and R. L. Simpson. Time-depeident and time-averaged turbulence structure near the nose of a wing-body junction. *Journal of Fluid Mechanics*, 210(1):23–55, January 1990.
- [29] A. Di Sante, R. Theunissen, and R.A. Van den Braembussche. A new facility for time-resolved PIV measurements in rotating channels. *Experiments in Fluids*, 44(2):179–188, February 2008.
- [30] N. Domaschke, J. von Wolfersdorf, and K. Semmler. Heat Transfer and Pressure Drop Measurements in a Rib Roughened Leading Edge Cooling Channel. *Journal of Turbomachinery*, 134(6):061006–1–061006–9, November 2012.
- [31] S. Dutta, J.C. Han, and P.C. Lee. A new facility for time-resolved PIV measurements in rotating channels. *International Journal of Heat and Mass Transfer*, 39(4):707–715, March 1996.
- [32] K. Elebiary and M. Taslim. Experimental/Numerical Crossover Jet Impingement in an Airfoil Leading-Edge Cooling Channel. *Journal of Turbomachinery*, 135(1):011037–1/011037–12, January 2013.
- [33] J.H. Ferziger and M. Peric. *Computational Methods for Fluid Dynamics*. Springer, 2002.
- [34] A. Haasenritter and B. Weigand. Heat transfer in triangular rib-roughened channels. In *ASME NHTC'01 National Heat Transfer Conference NHTC2001-20245*, Anaheim (California), 2001.
- [35] J.C. Han. Recent Studies in Turbine Blade Cooling. *International Journal of Rotating Machinery*, 10(6):443–457, June 2004.
- [36] J.C. Han, S. Dutta, and S. Ekkad. *Gas Turbine Heat Transfer and Cooling Technology, Second Edition*. Taylor and Francis, 2012.
- [37] J.E. Hart. Instability and Secondary Motion in a Rotating Channel Flow. *Journal of Fluid Mechanics*, 45(2):341–351, 1971.
- [38] J. Holton and G. J. Hakim. *An Introduction to Dynamic Meteorology*. Academic Press, 2012.
- [39] S.Z. Huang and Y.H. Liu. High Rotation Number Effect On Heat Transfer In a Leading Edge Cooling Channel with Three Channel Orientations. In *ASME Turbo Expo 2012 GT2012-68389*, Copenhagen (Denmark), 2012.
- [40] J.P. Johnston. Effects of System Rotation on Turbulence Structure: A Review Relevant to Turbomachinery Flows. *International Journal of Rotating Machinery*, 4(4):97–112, April 1998.

- [41] W. P. Jones and B. E. Launder. The prediction of laminarization with a two-equation model of turbulence. *International Journal of Heat and Mass Transfer*, 15(2):301–314, February 1972.
- [42] S.J. Kline and F.A. McClintok. Describing Uncertainties in Single Sample Experiments. *Mechanical Engineering*, 75(1):3–8, January 1953.
- [43] B. Lakshminarayana. *Fluid Dynamics and Heat Transfer of Turbomachinery*. Wiley-Interscience, 1995.
- [44] B. Launder, G. Reece, and W. Rodi. Progress in the development of a Reynolds-stress turbulence closure. *Journal of Fluid Mechanics*, 68(3):537–566, March 1975.
- [45] B.E. Launder and Spalding D.B. Collaborative Testing of Turbulence Models. *The numerical computation of turbulent flows*, 3(2):269–289, March 1974.
- [46] D. K. Lezius and J.P. Johnston. Instability and Secondary Motion in a Rotating Channel Flow. *Journal of Fluid Mechanics*, 77(1):153–176, 1976.
- [47] P. Ligrani. Heat Transfer Augmentation Technologies for Internal Cooling of Turbine Components of Gas Turbine Engines. *International Journal of Rotating Machinery*, 2013(2013):1–33, January 2013.
- [48] Y.H. Liu, M. Huh, and J.C. Han. High rotation number effect on heat transfer in a trailing edge channel with tapered ribs. *International Journal of Heat and Fluid Flow*, 33(1):182–192, February 2012.
- [49] Y.H. Liu, M. Huh, J.C. Han, and H.K. Moon. High Rotation Number Effect on Heat Transfer in a Triangular Channel With 45 deg, Inverted 45 deg, and 90 deg Ribs. *Journal of Heat Transfer*, 132(7):071702–09, July 2010.
- [50] Y.H. Liu, M. Huh, D.H. Rhee, J.C Han, and H.K. Moon. Heat Transfer in Leading Edge, Triangular Shaped Cooling Channels With Angled Ribs Under High Rotation Numbers. *Journal of Turbomachinery*, 131(4):041017–11, October 2009.
- [51] W.H. Lowdermilk, W.F. Weiland, and J.N.B. Livingood. Measurement of heat-transfer and friction coefficients for flow of air in noncircular ducts at high surface temperatures. *Naca Research Memorandum*, RM E53J07(1954):1–35, January 1954.
- [52] Giovanni Lozza. *Turbine a gas e cicli combinati*. Società Editrice Esculapio, Bologna, 2006.
- [53] F.R. Menter. Ansys Inc. Unpublished documentation. In -, volume -, -, -.
- [54] F.R. Menter. Two-equation eddy-viscosity turbulence models for engineering applications. *AIAA Journal*, 32(8):1598–1605, August 1994.
- [55] D. E. Metzger and R.P. Vedula. Measurement of heat-transfer and friction coefficients for flow of air in noncircular ducts at high surface temperatures. *Experimental Heat Transfer*, 1(1):31–44, January 1987.

- [56] C. Mucignat, A. Armellini, and L. Casarsa. Flow Field Analysis Inside a Gas Turbine Trailing Edge Cooling Channel Under Static and Rotating Conditions : Effect of Ribs. *International Journal of Heat and Fluid Flow*, 42(8):236–250, August 2013.
- [57] A.P. Rallabandi, Y.H. Liu, and J.C. Han. Heat Transfer in Trailing Edge Wedge-Shaped Pin-Fin Channels With Slot Ejection Under High Rotation Numbers. *Journal of Thermal Science and Engineering Applications*, 3(2):021007, June 2011.
- [58] L. Richardson and A. Gaunt. The deferred approach to the limit. Part I. single lattice. Part II. interpenetrating lattices. *Philos. Trans. R. Soc. London Sect. A*, 226:299–361, 1927.
- [59] P. J. Roache. A method for uniform reporting of grid refinement studies. *Journal of Fluids Engineering*, 116(3):405–413, March 1994.
- [60] P. J. Roache. Conservatism of the grid convergence index in finite volume computations on steady-state fluid flow and heat transfer. *Journal of Fluids Engineering*, 125(4):731–732, July 2003.
- [61] F. G. Schmitt. About Boussinesq’s turbulent viscosity hypothesis: historical remarks and a direct evaluation of its validity. *Comptes Rendus Mecanique*, 335(9–10):617–627, April 2007.
- [62] C. G. Speziale, S. Sarkar, and T. B. Gatski. Modelling the pressure-strain correlation of turbulence—an invariant dynamical system approach. *Journal of Fluid Mechanics*, 227(6):245–272, June 1991.
- [63] C. G. Speziale and S. Thangam. Numerical Study of Secondary Flows and Roll-Cell Instabilities in Rotating Channel Flow. *Journal of Fluid Mechanics*, 130:377–395, 1983.
- [64] C.G Speziale. Numerical Study of Viscous Flow in Rotating Rectangular Ducts. *Journal of Fluid Mechanics*, 122:251–271, 1982.
- [65] M.E. Taslim, T Li, and S.D. Spring. Measurements of heat transfer coefficients in rib-roughened trailing-edge cavityies with crossover jets. In *ASME-IGTI Turbo expo 98 Stockholm ASME Paper NO-98GT-435*, Stockholm (Sweden), 1998.
- [66] M.E. Taslim and Nogsang. Experimental and Numerical Cross-Over Jet Impingement in an Airfoil Trailing-Edge Cooling Channel. *Journal of Turbomachinery*, 133(4):041009–1–041009–10, October 2011.
- [67] UNI-ISO. ISO 5167 UNI EN 2004 - Measurement of fluid flow by means of pressure differential devices inserted in circular cross-section conduits running full.
- [68] D. Walker and J. Zausner. Rans evaluations of internal cooling passage geometries: ribbed passages and 180 degree bend. In *ASME Turbo Expo 2007 GT2007-278*, Montreal (Canada), 2007.

- 
- [69] B. Weigand, K. Semmler, and J. Von Wolfersdorf. Heat Transfer Technology for Internal Passages of Air-Cooled Blades for Heavy-Duty Gas Turbines. *Heat Transfer in Gas Turbine Systems*, 5(934):179–193, May 2001.
- [70] D.C. Wilcox. Multiscale model for turbulent flows. *AIAA Journal*, 26(11):1311–1320, November 1988.
- [71] D.C. Wilcox. *Turbulence Modelling for CFD*. DCW Industries Inc., 1993.
- [72] Y.M. Zhang, W.Z. Gu, and J.C. Han. Augmented heat transfer in triangular ducts with full and partial ribbed walls. *Journal of Thermophysics and Heat Transfer*, 8(3):574–579, July 1994.

---

# A

## Experimental Uncertainty Analysis

### A.1 PIV Uncertainty Analysis

The experimental flow field data used in the present thesis for the validation of the *CFD* predictions have been obtained by means of 2-D and Stereo-*PIV* measurements. All the details about the *PIV* experimental set-up and the *PIV* processing procedure are available in literature (see.[5] and [56]) therefore a brief description of the uncertainty analysis on the basis of the work of Armellini et al.[8] is reported hereafter. In this approach, the sampling error is considered to be larger than the other error sources that affect the *PIV* instantaneous data, and this is due to the limited number of samples (1000) used to compute the flow statistics. Consequently, the sampling error can be considered as the overall upper bound estimate for the *PIV* data uncertainty. Assuming a 95% confidence level, the uncertainty in the mean velocities for the 2-D *PIV* measurements turned out to be less than 2% with respect to  $U_b$ . This value applies as an uncertainty upper limit to the most part of the velocity fields, with the exception of those limited regions affected by very low velocities and high fluctuations, as inside zones of separated flow. Under the same assumptions, the maximum uncertainty in the estimate of the *r.m.s* velocities is below 5% of  $U_b$ . Concerning the accuracy of the Stereo-*PIV* measurements, it was indirectly checked by a cross-comparison with 2D data and turned out to be  $\leq 5\%$  of  $U_b$ , as demonstrated in [5] for the same Stereo-*PIV* set-up and methodology.

### A.2 LCT Uncertainty Analysis

The experimental heat transfer data used in the present thesis for the validation of the *CFD* predictions have been obtained by means of *LCT*. All the experimental details are available in [3],[14] and [7] therefore, a brief description of the uncertainty analysis is reported hereafter. Following the error propagation approach proposed by Kline and Mc-Clintock [42], and under the assumption of a 95% confidence level, the uncertainty

on the  $Nu$  turned out to be equal to 4% and 11% for the highest and the lowest heat exchange regions, respectively. The assessment was performed considering an uncertainty of  $\pm 0.5[K]$  for the surface temperature determination (the value considers both the accuracy of the  $LCT$  calibration procedure and the slight variation of the viewing angle over the camera field of view) and an uncertainty of about 20% in the determination of the thermal losses

---

# B

## High Resolution Scheme

In ANSYS CFX  $\text{\textcircled{R}}$ v14, the code automatically decides on the order of spatial discretization depending on an internal boundedness criterion [4]. In the regions where a strong gradient is found the order of the spatial discretization is reduced automatically. The example shown in Fig. B.1 for the *GO* configuration in *IP* passage *P4* confirm all the previous comments. Indeed the contour plots represent the local distribution of  $\iota$  for the velocity components in *x* direction (Fig. B.1(a)) in *y* direction (Fig. B.1(b)) and in *z* direction (Fig. B.1(c)). A value of  $\iota = 1$  corresponds to second-order spatial discretization, whereas  $\iota = 0$  represents use of the first-order upwind scheme. As can be seen the second-order spatial discretization is used for most of the fluid region. Conversely, in the zone of large gradients, the scheme is blended into the first-order scheme.

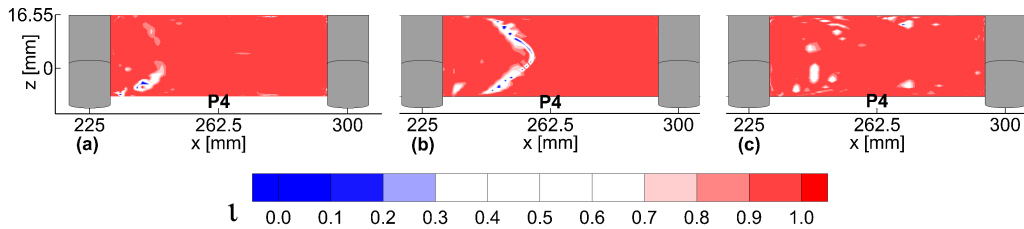
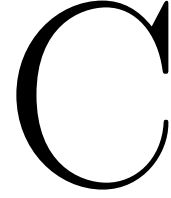


FIGURE B.1 – Automatic blending functionality of the high-resolution scheme.





## Description of the GCI

This method applies to a wide range of *CFD* problems and it is based on a generalized formulation of the Richardson extrapolation theory ([58]) made by Roache ([59], [60]). The method allows to compute a Grid Convergence Index (*GCI*), i.e. discretization error bands for the computed variables and, therefore, it can be regarded as standardized method to report on grid refinement studies. It is however obvious that, by its definition, the *GCI* method cannot account for more general modelling errors (e.g. a wrong choice of boundary conditions or turbulence model see Subsec. 2.2.4) but only for errors associated to an insufficient spatial resolution.

Starting from a fine mesh used for the computations, the *GCI* method requires to compare its results with the ones obtained from two coarser meshes obtained through a uniform reduction of the spatial resolution. In agreement with [22], the scale factor used for the determination of the number of elements of the intermediate and coarse meshes is about 1.3. The first step is to define a representative mesh size  $h^*$ , which is defined as:

$$h^* = \frac{1}{N} \left[ \sum_{i=1}^N (\Delta V_i) \right]^{\frac{1}{3}}, \quad (\text{C.1})$$

where  $N$  is the total number of elements and  $\Delta V_i$  is the volume of the  $i^{\text{th}}$  element. From representative mesh size of the grids, the refinement factor  $r$  must be determined as follows:

$$r = \frac{h^*_{\text{coarse}}}{h^*_{\text{fine}}}. \quad (\text{C.2})$$

In agreement with [22], the scale factor  $r$  used for the determination of the number of elements of the intermediate and coarse meshes should be greater than 1.3. The next step involves the calculation of the apparent order of the method,  $pp$ , using the equations:

$$pp = \frac{1}{\ln(r_{21})} \left[ \ln \left| \frac{\Lambda_{32}}{\Lambda_{21}} \right| + q(pp) \right] \quad (\text{C.3})$$

$$q(pp) = \ln \left( \frac{r_{pp}^{21} - t}{r_{pp}^{32} - t} \right) \quad (\text{C.4})$$

$$t = 1 \operatorname{sign} \left( \frac{\Lambda_{32}}{\Lambda_{21}} \right) \quad (\text{C.5})$$

with the index 1 representing the finest grid

$$\frac{\Lambda_{32}}{\Lambda_{21}} = \Xi_3 - \Xi_2 \quad (\text{C.6})$$

where  $\Xi$  stands for the solution variable for which the discretization error is to be determined, e.g. Nu values (see Subsec. 3.3.1, 3.4.1, 3.5.1) or the velocity  $C_{xyz}$  (see Subsec. 4.2.1, 4.3.1) at certain location, and  $\Xi_i$  denotes the solution on the  $i^{\text{th}}$  grid. Equations C.4, C.5 and C.6 can be solved using fixed-point iteration with equation C.4 as initial guess. The extrapolated values  $\Xi_{ext}^{21}$  and  $\Xi_{ext}^{32}$  can then be calculated from:

$$\Xi_{ext}^{21} = \frac{r_{21}^{pp} \Xi_1 - \Xi_2}{r_{21}^{pp} - 1} \quad (\text{C.7})$$

with the calculation of  $\Xi_{ext}^{32}$  being straightforward. The approximate relative error can then be given as

$$e_{app}^{21} = \left| \frac{\Xi_1 - \Xi_2}{\Xi_1} \right| \quad (\text{C.8})$$

the extrapolated error is:

$$e_{ext}^{21} = \left| \frac{\Xi_{ext}^{12} - \Xi_1}{\Xi_{ext}^{12}} \right| \quad (\text{C.9})$$

and the fine grid convergence index can be determined as:

$$GCI_{fine}^{21} = \frac{1.25 e_{app}^{21}}{r_{21}^p - 1} \quad (\text{C.10})$$

---

# D

## Inflow Conditions

In order to provide the correct boundary conditions for the *CFD* simulations, experimental measurements [5] [56] were carried out at the inlet channel along the symmetry planes *xy* and *xz*. Figure D.1 shows the profiles of the time-averaged *U* velocity component extracted in these planes at  $x = -69.8[\text{mm}]$ .

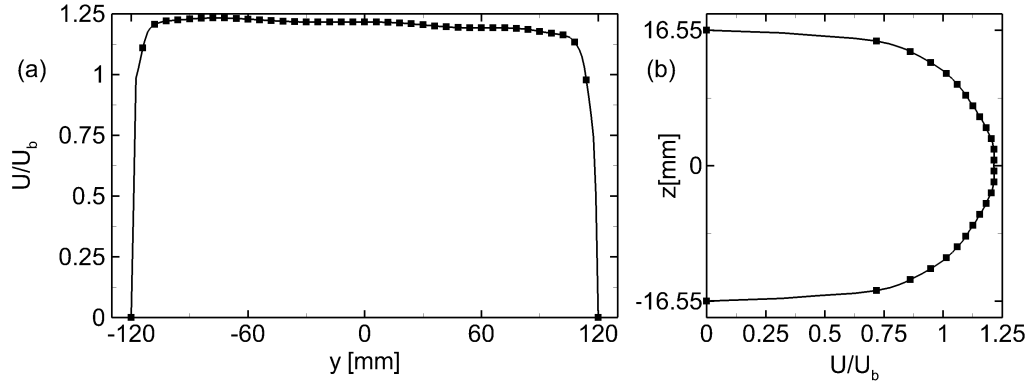


FIGURE D.1 – Experimental [5] [56] *U* velocity profiles in-planes *xy*(a) and *xz*(b) at  $x = -69.8[\text{mm}]$ .

These profiles are the basis to impose the correct inlet boundary conditions for the numerical analysis. In fact 2-D interpolation was performed to create the normal velocity map of the inlet face as follows:

$$U_{IN}(x, z) = \frac{U(x, 0) \cdot U(0, z)}{U(0, 0)} \quad (\text{D.1})$$

where  $U(x, 0)$  and  $U(0, z)$  are respectively the inlet velocity profiles along *x* and *z* axis.



# E

## Local Distribution of Turbulence Kinetic Energy in the P4 IP Passage

Figures 3.11, 3.22 and 3.34 show differences between experimental and *CFD* *Nu* in the *IP* area ( $-240 < y < -120$ ), namely the numerical data show an over-prediction of the *Nu* peaks. Conversely, compared to the problem discussed in Figs. 3.24 and 3.30 about the *IR* region, the present discrepancies are not due to a wrong estimation of the mean flow field structure. Indeed, Figs. E.1 (a,b) illustrate the comparison between experimental [56] and *CFD* time-averaged stream-tracers and in-plane velocity modulus  $C_{xz}$  in the *xzi* plane inside the 4<sup>th</sup> *IP* passage for configuration *G1*.

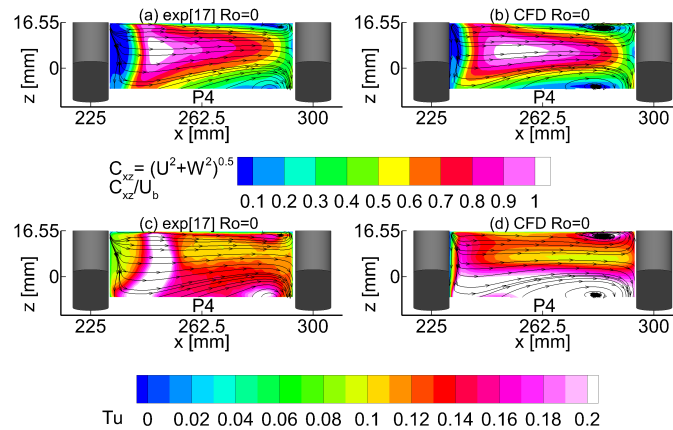


FIGURE E.1 – Experimental(a,c) [56] and *CFD*(b,d) time-averaged stream-tracers and contour plots of the velocity  $C_{xz}$  (a,b) and turbulence intensity *I* (c,d) inside the 4<sup>th</sup> *IP* passage (*P4*) in-plane *xzi*, *G1* configuration.

As can be seen the *CFD* computations correctly predict the existence and the extension of the horseshoe at the junction between the downstream pedestal (i.e. the one at  $x = 300[mm]$ ) and the channel walls. Moreover, also the contour levels of the in-plane velocity modulus  $C_{xz}$  are in a good match. Conversely, more relevant differences can be found if the comparison is extended to the experimental [56] and *CFD* turbulence intensity  $I$ , as reported in Figs. E.1(c,d). Indeed, quite higher values of  $I$  characterize the *CFD* prediction of the horseshoe vortex branch and hence causing a possible over-prediction of the heat transfer mechanism in this area.

---

# Publications

The present thesis is based on the work contained in the following publications

## Archival Publications

Pascotto, M., Armellini, A., Mucignat, C. and Casarsa, L..”Coriolis Effects On The Flow Field Inside Rotating Triangular Channel For Leading Edge Cooling”. Journal of Turbomachinery, 136(3), 031019-1/031319-12, March 2014.(<http://turbomachinery.asmedigitalcollection.asme.org/article.aspx?articleid=1746042>)

Pascotto, M., Armellini, A., Casarsa, L., Mucignat, C. and Giannatasio, P..”Effects of Rotation at Different Channel Orientations on the Flow Field Inside a Trailing Edge Internal Cooling Channel”. International Journal of Rotating Machinery, 2013(2013), 10.1155/2013/765142, 2013.(<http://www.hindawi.com/journals/ijrm/2013/765142/>)

## Conference Proceedings

Pascotto, M., Spring, S., Armellini, A. and Casarsa, L..”Numerical Aero-Thermal Analysis of a Rib-Roughened Trailing Edge Cooling Channel at Different Rotation Numbers and Channel Orientations”. ASME Paper GT2014-25479, ASME Turbo Expo 2014, Dusseldorf, Germany,2014.

Pascotto, M., Armellini, A., Casarsa, L., Giannatasio, P. and Mucignat, C..”Effects Of Rotation and Channel Orientation on the Flow Field Inside a Trailing Edge Internal Cooling Channel”. ASME Paper GT2012-68050, ASME Turbo Expo 2012, Copenhagen, Denmark, 2012.(<http://proceedings.asmedigitalcollection.asme.org/proceeding.aspx?articleid=1694384#!>)



---

# Curriculum Vitae

Name: Matteo Pascotto  
Date and place of birth: 18.10.85 in Pordenone  
Nationality: Italian

## Studies

2011–2013 Ph.D Candidate in Environmental and Energy Engineering Sciences at Università degli Studi di Udine, (Italy).  
Nov.2011/May 2012 Education and training abroad at Institute of Aerospace Thermodynamics (ITLR), Stuttgart (Germany).  
Mar.2010 Master's degree in Mechanical Engineering, Energy and Environment at Università degli Studi di Udine, (Italy).  
Oct.2009/Feb.2010 Short training program at The Von Karman Institute for Fluid Dynamics, Rhode-St-Gense (Belgium).  
Nov.2007 Bachelor's degree in Mechanical Engineering at Università degli Studi di Udine, (Italy).

## References

Jens von Wolfersdorf  
Institute of Aerospace Thermodynamics (ITLR), Deputy  
University of Stuttgart, Germany  
[jens.vonwolfersdorfaetitlr.uni-stuttgart.de](mailto:jens.vonwolfersdorfaetitlr.uni-stuttgart.de)

Luca Casarsa  
Dipartimento di Ingegneria Elettrica, Gestionale e Meccanica, Research Associate  
Università degli Studi di Udine, Italy  
[luca.casarsa@uniud.it](mailto:luca.casarsa@uniud.it)

